Improvement in Rheological Response of Transition Metal Oxide Based Magnetic Fluids

Thesis submitted for the award of the degree of

Doctor of Philosophy
in

Physics (Experimental)
by

Priyanka Saha

Department of Physics
University of Calcutta
Kolkata, India
2021

Dedicated to Maa and Baba…

Acknowledgement

Foremost, I would like to convey my sincere gratitude to my supervisor Prof. Kalyan Mandal for his immense help, inspiration, valuable discussions, and humble guidance. He always encouraged and motivated me to think and execute my research work independently in challenging areas. Without his wisdom, patience, and support, any of my research work would not be successful. Thank you Sir for providing me with the opportunity to work in your laboratory and making my PhD life very much enjoyable.

I am grateful to S. N. Bose National Centre for Basic Sciences (SNBNCBS), Kolkata, and Department of Science and Technology (DST), India, for providing a beautiful campus, advanced instrumental facilities, wonderful research environment, and INSPIRE (DST) fellowship.

I would like to thank Ms. Mousumi Majumder and Ms. Moumita Sha from CSIR-Central Glass & Ceramic Research Institute, Kolkata for providing Magnetorheological measurements facility. I am also obliged to the ex-director of SNBNCBS, Prof. Samit Kumar Ray increasing the experimental facility at the centre, which has proved to be a boon for our research work. I thank all the staff members, the security men, the cleaner, the cook, and the gardener for their sincere cooperation which makes this residential campus beautiful. I would also like to thank all the technical staff members: Urmi Chakraborty, Amit Chanda, Samik Roy Moulik, Joy Bandopadhyay, Shakti Nath Das, Dipayan Banerjee, Debarghya Ghosh and Sourav Sinha for their help in sample characterization.

I must acknowledge my seniors and labmates: Dr. Madhuri Mandal, Dr. Rupali Rakshit, Dr. Souvanik Talukdar, Dr. Indranil Chakraborty Dr. Mahebub Alam, Dr. Keshab Karmakar, Dr. Deblina Majumdar, Dr. Dipika Mandal, Dr. Subrata Ghosh, Dipanjan Maity, Anupam Gorai, Swarnali Hait, Soham Saha, Ishita Jana, Shridhar Mohanty and Saheli Samanta for providing me with a homely and cheerful environment in the lab. I thank them for their patience and helping attitude. I must specially thank Rupali Di for being a great source of knowledge, expertise, technical assistance and constant motivation. I am also thankful to Souvanik Da, Indranil Da and Deblina Di for their support in accepting the challenges of research work.

I am thankful to my seniors and friend Arghya Da, Subhadip Da, Arnab Da, Sumanta Da, Subrata Da, Abhishek Da and Anirban for helping me in questioning things and having a beautiful perspective of life. I also thank my friends: Sumanti, Subhamita, Rahul Da, Anulekha Di, Rituparna, Debayan, Dhiraj Da, Alik Da, Anish, Daisy, Abhik, Vishal, Samrat Da, Neeraj, Suraka Di, Shinjini, Varsha, Ankita, Subham, Shantanu, Ananda and Imadul for providing joyous company in several instances. I must name our SNB dance group members Ria, Amrita, Sreya, Anwesha, Subhajit, Athira, Shaili Di, Sucheta Di, Tania, Snehamoyee, Kankana, Swarnali, Anupam, Anish, Debayan, Dhiraj Da and Indrani for the memorable moments of colorful cultural activities in this Centre. I express my heartful thanks to Subhamita for this group and for introducing the rhythm of dance again in my life. I am thankful to Rahul Da, Anulekha Di, Alik Da, Anirban, Rituparna, Indranil Da and Deblina Di for their support and company during the tough COVID lockdown period.

I am, especially, thankful to Souvanik Da for being the biggest critic, for always pushing towards the things I love to do and for helping me in becoming a better version of myself. I am

thankful to my best buddies in S. N. Bose Centre, Deblina Di, Debayan and Dhiraj Da. They make my life more beautiful and helped me cheer up my mood even on the worst days. No thanks would be enough for their love, support, tolerance, and forgiveness. They help me to figure out my confusion, and shared various glorious as well as miserable moments over the last three years. They supported me at every work as well as personal annoyance. These people are family to me.

I am grateful to all of my school teachers, especially Mrs. Mina Saha, Mrs. Sutapa Tikadar Tewari, Mrs. Anindita Saha, Mrs. Sarbani Chanda, Mrs. Basudha Biswas and Mrs. Shubhra Baidya of Karimpur Girls' High School (H.S.), my college teachers, Dr. Ram Narayan Deb and Dr. Bishwajit Pal of Krishnagar Govt. College for making Physics enjoyable, and my university teachers, Dr. Syed Minhaz Hossain, Dr. Sampad Mukherjee, Dr. Dipali Banerjee, Dr. Bichitra Kumar Guha, Dr. Debasis Ray and Dr. Mojammel Haque Mondal of Indian Institute of Engineering Science and Technology, Shibpur, for motivating me towards research. I must thank Mr. Abhijit Dutta, Mr. Prabir Kundu, Mr. Rathin Mandal, Mr. Rajat Sarkar, Mr. Basudeb Swarnakar, Dr. Tapas Kumar Modak and Dr. Jyotirmoy Guha for being my philosopher and guide, and paving my life towards success.

I must name my college and university friends (Souvik, Dibakar, Surojit, Ishita, Amartya, Sayani, Sanchaita, Rayeesa and Subhankar) for their colorful company. I am thankful to my childhood friends Imon, Tanmay, Arghya, Somnath, Sattwik, Rituparna, and Barun for being the friends for life and all the beautiful moments we shared.

Finally, I express my intense gratitude to my beloved parents (Mrs. Chaina Saha and Mr. Paresh Saha), for their sacrifice, moral support, inspiration, affection, love, and guidance. They are my best teachers and I am grateful to them for being my Maa and Baba. I thank my sister (Ms. Puja Saha) for her unconditional love, cheerful company and strong support in all difficult moments of my life. They always ignore my irresponsible and uninvolved behavior and boost me to work hard with dedication. I am grateful to my late grandparents (Mr. Palan Chandra Saha and Mrs. Malati Saha) for a colorful childhood. My sweet sister, youngest member of our family, Koushani Saha, also deserves special mention for adding vibrant colors to my life. I am also thankful to my late maternal grandfather (Mr. Rabindra Nath Saha) and grandmother (Mrs. Shefali Saha) for always believing in me. I am blessed to have the enjoyable company of my aunts, (Mrs. Tandra Saha, mamoni), uncles (Mr. Pradip Saha, Nishith Kaku, Krishna Mama), and cousins, Raja, Badu, and Monu.

Priyanka Saha

Publications

*1. ***P. Saha***; R. Rakshit; K. Mandal,

"Enhanced magnetic properties of Zn doped Fe_3O_4 nano hollow spheres for better bio-medical applications"

Journal of Magnetism and Magnetic Materials, 2019*, 475, 130*

*2. ***P. Saha***; R. Rakshit; M. Alam; K. Mandal,

"Magnetic and Electronic Properties of Zn-Doped Fe_3O_4 Hollow Nanospheres"

Physical Review Applied, 2019*, 11, 024059*

*3. ***P. Saha;*** S. Mukherjee; K. Mandal,

"Rheological response of magnetic fluid containing Fe_3O_4 nano structures"
Journal of Magnetism and Magnetic Materials, 2019, *484, 324*

*4. ***P. Saha;*** R. Rakshit; M. Pal; K. Mandal,

"Shear response of magnetorheological fluid with Zn0.2Fe2.8O4 sub-micron hollow spheres"

Journal of Applied Physics 2021*, 129, 033901*

5. R. Rakshit; E. Khatun; M. Pal; S. Talukdar; D. Mandal; ***P. Saha***; K. Mandal,

"Influence of functional group of dye on the adsorption behaviour of $CoFe_2O_4$ nano-hollow spheres"
New Journal of Chemistry, 2017*,41, 9095*

6. R. Rakshit; S. K. Kadakuntla; P. Agarwal; S. Sardar; ***P. Saha***; K. Mandal; D. S. Rana,
'' Surface Electronic States Induced High Terahertz Conductivity of Co_3O_4 Microhollow Structure''
ACS Applied Material and Interfaces, 2018*, 10, 19189*

7. S. Talukdar; ***P. Saha***; I. Chakraborty; K. Mandal,

"Surface functionalized $CoFe_2O_4$ nano-hollowspheres: Novel properties"

Journal of Magnetism and Magnetic Materials, 2020, *513, 167079*

8. S. Talukdar; ***P. Saha***; K. Mandal,

"Folate modified zinc ferrite nano-hollowspheres for drug delivery and intrinsic fluorescence"

AIP Conference Proceedings 2020, *2265, 030131*.

*9. ***P. Saha***; R. Rakshit; A. Garai; D. Mandal; K. Mandal,

"Unusual Dielectric Properties of hollow magnesium ferrite nano-spheres: a potential lightweight microwave absorber"

Manuscript under review.

*10. ***P. Saha***; K. Mandal,

"Magnetic field stimulated dielectric, electronic and thermal properties of magnetite nano-hollow spheres based magnetic fluids"

Manuscript under review.

11. R. Rakshit; S. K. Kadakuntla; P. Agarwal; ***P. Saha;*** S. Sardar; D. S. Rana; K. Mandal'

"Exceptional surface conducting states in insulating $MnFe_2O_4$ nanostructures"

Manuscript under review.

***** These publications are included in this thesis.

Contents **Page**

Acronyms

NSs: Nanostructures

NMs: Nanomaterials

NPs: Nanoparticles

NHSs: Nano hollow spheres

SD: Single domain

MD: Multi-domain

SPM: Superparamagnetic

CFSE: Crystal field splitting energy

EM: Electromagnetic

EMI: Electromagnetic Interference

EMA: Electromagnetic Absorption

RL: Reflection Loss

TEM: Transverse Electromagnetic Wave

TE: Transverse Electric Waves

TM: Transverse Magnetic Waves

NRW: Nicholson-Ross-Weir

VNA: Vector Network Analyzer

SE: Shielding Efficiency

MR: Magnetorheological

BP: Bingham Plastic

HB: Herschel-Bulkley

CI: Carbonyl Iron

XRD: X-ray diffraction

FESEM: Field emission scanning electron microscope

TEM: Transmission electron microscope

HRTEM: High resolution transmission electron microscope

EDX: Energy dispersive X-ray

SAED: Selected area electron diffraction

AFM: Atomic force microscopy

C-AFM: Conductive Atomic force microscopy

DC: Direct current

AC: Alternating current

VSM: Vibrating sample magnetometer

SQUID: Superconducting quantum interference device

MEMS: micro-electromechanical systems

BSE: back scattered electrons

SE: scattered electrons

EELS: electron energy loss spectroscopy

DUT: device under test

PDF: pressure driven flow

DS: Direct Shear

DE: Double Exchange Interaction Energy

SE: Super Exchange Interaction Energy

ZFC: Zero-field-cooled

FC: Field-cooled

GB: grain boundary

MW: Maxwell-Wagner

RT: Room Temperature

RL: Reflection Loss

LLG: Landau–Lifshitz–Gilbert

HTF: Heat Transfer Fluids

Table of Symbols

M_s: Saturation magnetization

M_r: Remanence

H_c: Coercivity

X: Susceptibility

T_B: Blocking temperature

T_c: Curie temperature

E_A: Magnetocrystalline anisotropy energy

K: Magnetocrystalline anisotropy constants

θ : Angle

r: Radius

D: Diameter

D: Grain size

R: Distance

V: Volume

A: Area

t: Thickness

V: Voltage

I: Current

d: Thickness

d: Crystal plane spacing

L: Length

eV: Electron volt

k_B : Boltzmann constant

T: Temperature

Z: Impedance

Y: Admittance

L: Inductance

C: Capacitance

E: Electric field

J: Cyrrent density

η: Impedance of a medium

η_0: Impedance of free space

δ: Skin depth

α : Attenuation constant

β : Phase constant

Φ_0: Flux

m: Magnetic moment

H: Magnetic field strength

D: Electric displacement

P: Polarization

M: Magnetization

ε: Electric permittivity

ε_0: Free space permittivity

μ: Magnetic permeability

μ_0: Free space permeability

σ: Electric conductivity

c: Velocity of light in free space

k: Wave vector

ω: Angular frequency

λ: Wavelength

T: Transmission Coefficient

Γ: Reflection coefficient

ρ : Charge density

t_m: Thickness

δ : Inversion degree

T_g : Spin freezing temperature

ν : Phono vibration frequency

M: Madelung constant

τ: Relaxation time

τ: Shear Stress

τ_y: Yield stress

$\dot{\gamma}$: Shear rate

η: Viscosity

Mn: Mason number

δ: Phase shift

G: Shear modulus

Chapter 1 Introduction

This introductory chapter involves the thorough literature review of numerous research works that motivate to work in this explicit field, a brief summary of entire work, and the theoretical facets that help to elucidate the findings.

1.1. Importance of Nano

The concept of "nano-technology" was first discussed by Richard P. Feynman in 1959 in his talk entitled "*There is plenty of room at the bottom*" describing the possibility of manipulation of atoms. K. Eric. Drexler used nanotechnology in his book "*Engines of creation: The coming era of nanotechnology*" in 1986, being inspired by Richard Feynman[1]. Nanomaterials (NMs) drew enormous attention of researchers due to the improvement of numerous properties in contrast to their bulk counterpart and the evolution of new phenomena in nanoscale. By definition, NMs should have as a minimum one dimension within the range of 1-100 nm (1nm = 10^{-9} m). NMs interact differently with the surrounding substances, light, magnetic and electric filed, offering unique properties due to its higher surface to volume ratio and the presence of a large number of atoms on the surface, compared to bulk. Upon moving from bulk to nanoscale the density of states (D(E)) of the electrons fluctuates from a continuous function ($D(E) \propto E^{1/2}$) to discontinuous delta function, shown in Figure 1.1, leading to constrained movements of electron within an infinite potential well of very small particles.

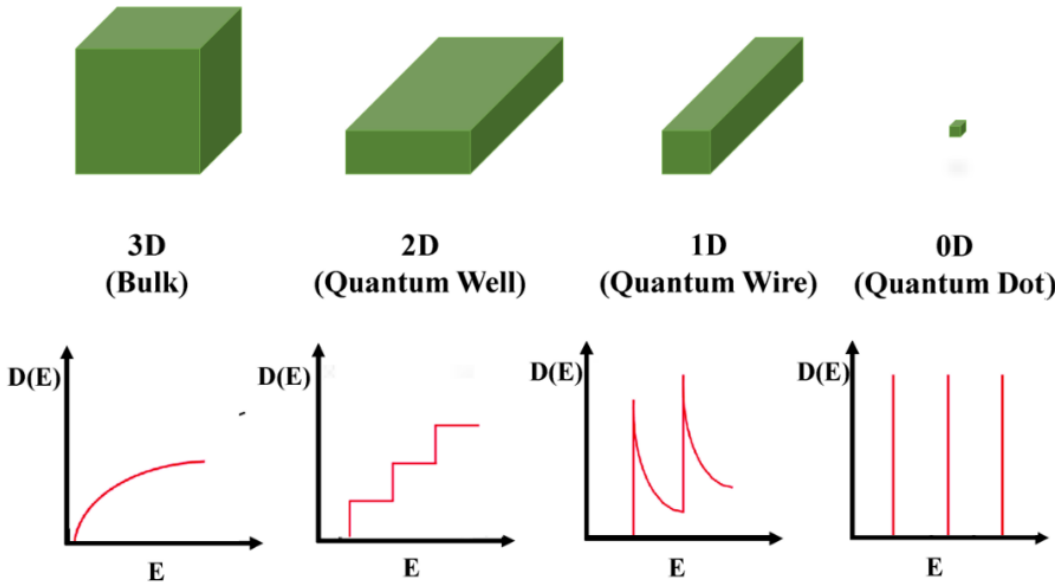

Figure 1.1: Variation of the density of states of electron in nanomaterials with decreasing size (from bulk to quantum well to quantum wire to quantum dot).

Moreover, the increased surface to volume ratio in nanomaterials increases various properties of the material by enhancing the number of active surface atoms.

Variation of surface to volume ratio with particle size in nm scale is shown in Figure 1.2. It gives rise to a wide variety of new phenomena by affecting the macroscopic properties of the NMs. When the size of the NMs becomes less than or comparable to particular length scales such as carrier mean free path, superconducting coherence length, magnetic domain wall width etc., various novel properties arise in the NMs, which are absent in their bulk counterpart[2]. The size of metal and semiconductor nanoparticles (NPs) greatly influences the magnetic property, electronic excitation, chemical reactivity, optical property, conductivity etc[3]. Rhodium in nanoscale shows ferromagnetic or ferrimagnetic ordering, whereas bulk Rhodium is Pauli paramagnet[4]. It has been observed that metals show a non-metallic band-gap upon size reduction, showing electronic absorption spectra. Moreover, clusters of non-magnetic bulk materials are found to display magnetic properties at nanoscale[5].

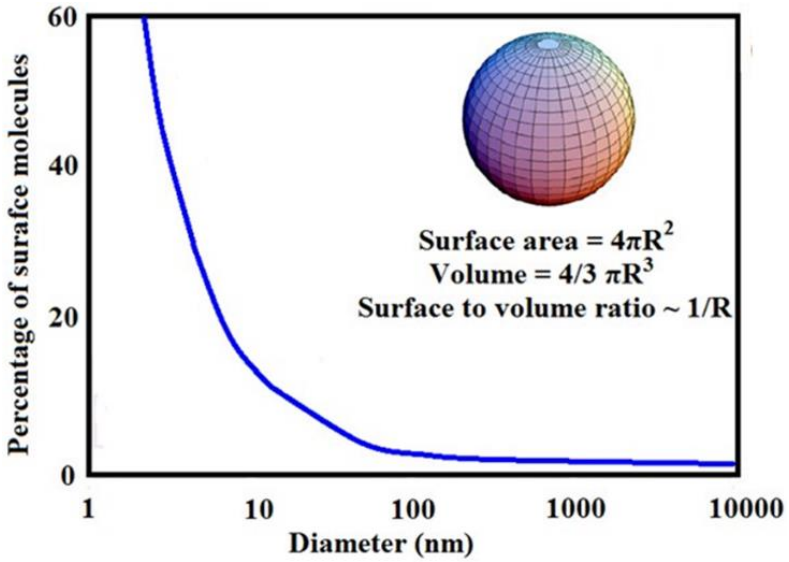

Figure 1.2: Graphical presentation of variation of surface atom percentage with particle diameter.

1.2. Nanostructures

Various NMs are synthesized to date with huge chemical diversity consisting of metals[6], metal oxides[7], semiconductors[8,9], polymers[10], and carbonaceous materials[11,12]. Owing to their novel optical, magnetic, thermal, electrochemical, electrical properties, these NMs have become a promising candidate to solve challenges in the field of medicine, energy storage, catalysis, sensing, and information technology[13–21]. The novel properties of NMs

can also be tuned employing their nanoscale building blocks[2]. NMs with the same composition but different morphologies, such as sphere, cube, sheet, disc, rod, wire, tube[22-27] etc. are found to show different properties.

Among these NSs, nano-hollow spheres (NHSs) attracted material scientists over the last few years because of their hollow interior, enhanced surface area, low density, high compressibility giving rise to unique properties[28–30]. Contrary to the definition of nano, these NHSs with diameter more than 100 nm show unique nano-scale properties due to their hollow cavity and thin shell thickness < 100 nm. D. Sarkar *et al*[31] showed NHSs of diameter 350 nm show single domain nature, whereas for NPs single domain is visible up to a few nm only. These hollow structures offer several applications in controlled drug delivery[32], bio-medical imaging[33], light weight microwave absorbers[34], magnetorheological fluids[35], light fillers[36], low dielectric materials[37], photonic crystals[38], energy storage[39] etc. The large void space of these NHSs can be used to encapsulate drugs, DNA and cosmetics and also helps in their controlled release[40]. In addition, owing to their low density these NHSs show better dispersibility in liquid medium for bio-medical applications. Mandal *et al*[41] showed excellent microwave absorption properties of these hollow structured NMs due to multiple reflections of electromagnetic (EM) waves inside the hollow cavity of the NHSs. Moreover, the presence of two surfaces in the shell region of these NHSs offers unique electrical and magnetic properties[42], making this special morphology interesting for basic understanding of physics, as well as for technological applications.

1.3. Transition Metal Oxide Based Magnetic Nanomaterials

Unusual properties of magnetic NMs such as abnormally high magnetocaloric effect, giant magnetoresistance drew the attention of researchers in this field. In addition to that magnetic NMs offers unique magnetic properties such as magnetostriction, blocking temperature (T_B), magnetocrystalline anisotropy, relaxation times (Neel relaxation and Brown relaxation) and magnetic saturation (M_s). 3-dimensional transition metal oxide-based magnetic materials e.g., magnetite (Fe_3O_4), zinc ferrite ($ZnFe_2O_4$), magnesium ferrite ($MgFe_2O_4$) drew enormous attention compared to metallic and alloy-based magnetic materials due to their higher chemical and mechanical stability, non-toxicity, low cost, easy synthesis procedure and high Curie temperature (T_c). Detailed and long-term research on these ferrite NMs reveals that these materials have excellent bio-medical and technological

applications such as information storage, biosensors, bio-separation, hyperthermia, molecular imaging, EM wave shielding, magnetorheology because of their outstanding magnetic, optical, electronic, catalytic, dielectric and EM properties[43–49]. In bio-sensing, EM absorption and magnetorheology, magnetic NMs with high M_s are preferred, whereas in information storage NPs with high H_c are required. The necessity of specific magnetic property for a particular field of application brings the perception of tuning the magnetic properties of the NMs for desired applications.

Magnetic properties of NMs depend on several factors such as chemical composition, crystal defects, particle size, shape, morphology, interaction of the particle with the surrounding matrix. M_s is found to vary proportionally with the size of the NPs up to a threshold value of the size and beyond which M_s becomes nearly constant reaching close to bulk value, shown in Figure 1.3(a). On the other hand, H_c varies differently. For larger crystals H_c increases with reduction in particle size and reaches maximum at a critical diameter (D_c). Below this critical diameter, the particle becomes single domain and H_c decreases. With further decrease in the size of the NPs the particles reach superparamagnetic (SPM) state and H_c becomes zero. Variation of H_c with particle size is shown in Figure 1.3(b).

Apart from the size and morphology doping is found to be an excellent method to tune the magnetic response of the magnetic NMs. Among the transition metal oxides, Fe_3O_4 is found to be an age-old versatile compound used as MRI contrast agent for early stage cancer detection[50], in high-frequency components owing to its low eddy current loss due to high resistivity[51,52]. The magnetic and electrical properties of Fe_3O_4 can be tuned further more with divalent cation doping depending on the desired field of application. For example, substitution of Co^{2+} in place of Fe^{2+} in Fe_3O_4 increases H_c, making $CoFe_2O_4$ a hard magnet[53], whereas $ZnFe_2O_4$ is a soft magnet[54]. $Mn_{0.7}Mg_{0.3}Fe_2O_4$ exhibits unusual behavior such as field-induced metamagnetic transition due to spin reversal[55]. Focusing on transition metal-based ferrite with general formula $M_xFe_{3-x}O_4$ (M=Zn, Mg, Mn, Co, Ni) can be an excellent way to tune the magnetic properties of these magnetic NMs for bio-medical as well as technological applications. Co *et al* reported improved M_s (~81 emu/gm) of sulfur-doped coral-like cobalt ferrite NPs with an average size ~90-100 nm[56]. Pal *et al*[57] prepared micelle coated $CoFe_2O_4$ NPs (diameter ~16 nm), showing enhanced coercivity in comparison to bare $CoFe_2O_4$. Besides, ferrites with the combination of high magnetic

permeability (μ) and dielectric permittivity (ε) show excellent EM wave absorption properties compared to traditional metallic and carbon-based materials[41,58,59].

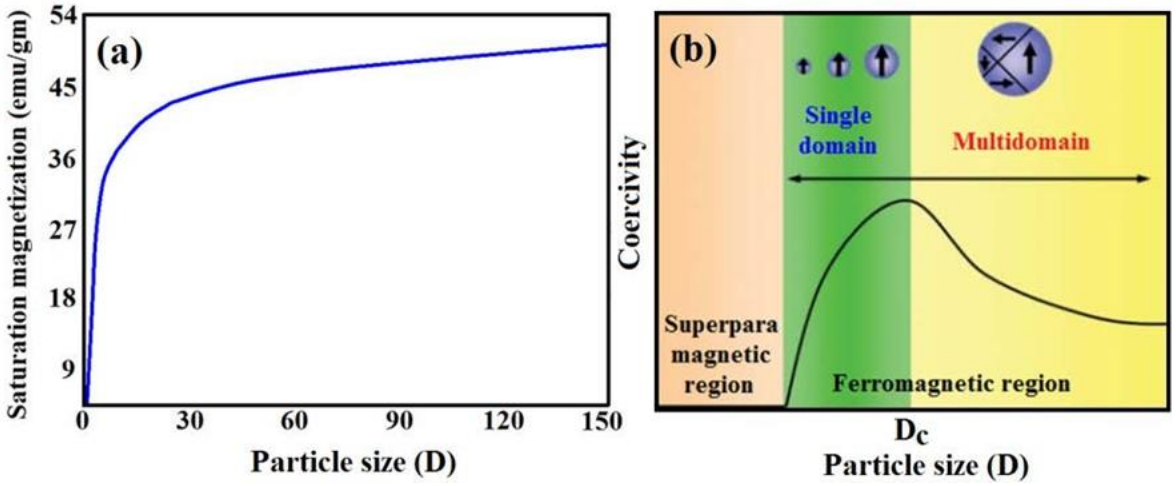

Figure 1.3. Variation of (a) M_s, and (b) H_c of magnetic NMs with particle diameter.

In addition, the magnetic properties are also found to show a vital role in determining the magnetorheological (MR) response of MR fluids. MR fluid is the suspension of nano- micrometer sized magnetic particles in carrier fluids, which shows MR response by forming chain under the application of external magnetic field and increases the overall viscosity of the material, reversibly, i.e, upon removing the external field the MR fluids return to the initial state. For good MR response, the magnetic particles should possess high M_s and low M_r. Metallic magnetic materials such as carbonyl iron have been studied mostly so far, owing to its high magnetic saturation, for commercial applications. However, due to the high density, low chemical stability and high cost of synthesis of iron NPs, researchers tried replacing the metallic magnetic particles with economic tradition transition metal oxide-based ferrites NSs with lower density and magnetic properties comparable with metallic magnetic NSs. Fe_3O_4 is found to be an excellent replacement of non-economic carbonyl iron particles for magnetorheology due to its chemical stability, controllable size and low density[60,61]. However, low M_s of Fe_3O_4 in comparison to Fe, lead material scientists to improve the magnetic response of transition metal oxide-based ferrites by doping, varying morphology and by tuning the size of the nanostructures (NSs). Anupama and her co-workers have prepared Li–Zn ferrite ($Li_{0.4}Zn_{0.2}Fe_{2.4}O_4$) particles and improved the MR response due to increases M_s[62]. G. Wang et al. reported improved MR response in $CaFe_2O_4$ nanocrystal clusters [63]. Apart from magnetic properties the surface area

and surface friction also play a crucial role in determining the strength and applicability of an MR fluid. Thus surface modification is also an effective method to improve the MR response. J. Wei showed better MR response of Fe_3O_4-TiO_2 nanocomposite[64]. Hence a detailed study on the structural, dielectric, magnetic and magnetorheological properties of the 3d transition metal oxides based magnetic NSs become of immense importance.

1.4. Crystal Structure

Ferrites can be classified into three categories depending on their structures, i) Spinels, ii) Garnets and iii) Hexaferrites. 3d transition metal oxide-based magnetic NMs with general formula MFe_2O_4 (M=Fe, Zn, Mg, Ni etc.) are spinel ferrites of the Fd3m space group. The cubic unit call contains total of 56 atoms, where 32 oxygen anions are distributed in the cubic closed pack structure, and amid the other 24 atoms, 8 cations fill the 64 available tetrahedral sites (A sites) and the rest 16 cations are distributed in the 32 available octahedral sites (B sites)[65], shown in Figure 1.4[66].

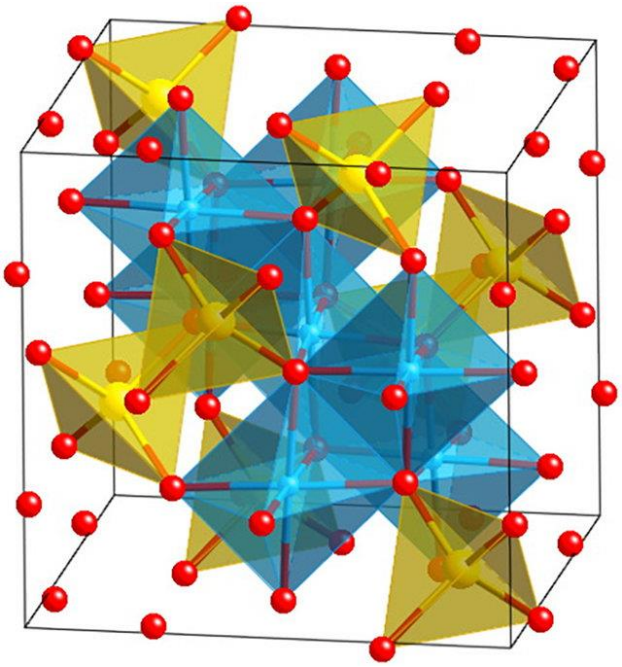

Figure 1.4: Schematic diagram of Spinel Ferrite structure showing Oxygen anions in red, octahedral sites in blue and tetrahedral sites in yellow.

In this oxygen closed pack configuration forming the face centered cubic (FCC) lattice structure, the corners are occupied by the anions and the cations fill the voids created

by those oxygen anions. The structural formula of a spinel ferrite of general formula MFe_2O_4 can be written as[67]

$$[M_{(1-\delta)}Fe_{\delta}]^{A}[M_{\delta}Fe_{(2-\delta)}]^{B}O_4 \quad (1.1)$$

where the amount in brackets signify the average occupancy of A and B sites and δ is the inversion degree parameter. The cation distribution on the A and B sites depends on the cation size and the crystal filed stabilization energy (CFSE). Depending on the cation distribution the spinel structures can be normal, inverse or mixed[68]. Both the cationic size and the value of CFSE determine the preferential site occupancy by the cations. For example, cations with a high value of CFSE occupy the higher coordination sites, i.e, the B sites. Fe_3O_4, $CoFe_2O_4$, $NiFe_2O_4$ form inverse spinel structure, whereas in $ZnFe_2O_4$ and $MnFe_2O_4$ there is a possibility of forming normal, inverse and mixed spinel structures. However, depending on the size of the NSs, method of synthesis or fabrication and doping content normal, inverse or mixed spinel structure formation is observed. Depending on the cation distribution among the A and B sites, the magnetic and dielectric properties of the materials can be altered and tuned. For example, in Zn doped Fe_3O_4 the magnetic saturation and electric conductivity of the material is altered due to non-magnetic Zn doping, as a result of cation distribution[69].

1.4.1.Normal Spinel Structure

In normal spinel structure, M^{2+} occupies the tetrahedral A site with the structural formula $M^{2+}[Fe_2^{3+}]O_4^{2-}$. In normal spinel structure, all the 8 bivalent cations are distributed in the A sites and the 16 trivalent cations occupy the B sites, where δ=0. Normal spinel structure formation is observed in Zn ferrites $Zn^{2+}[Fe^{3+}Fe^{3+}]O_4^{2-}$. This type of structure formation is schematically presented in Figure 1.5(a).

1.4.2. Inverse Spinel Structure

Inverse spinel structure, where all M^{2+} are in B sites and Fe^{3+} are equally distributed between A and B-sites, with the structural formula $Fe^{3+}[M^{2+}Fe^{3+}]O_4^{2-}$, where δ=1. In the inversed ferrites, Fe^{3+} ions are distributed between A and B sites in alternative arrangements, shown in Figure 1.5(b). Fe_3O_4, $CoFe_2O_4$, $NiFe_2O_4$ are an example of inverse spinel structure.

1.4.3. Mixed Spinel Structure

Mixed spinel structures are formed when the M^{2+} and Fe^{3+} cations occupy both the tetrahedral and the octahedral sites. The structural formula of these ferrites is $M_{(1-\delta)}^{2+}Fe_{\delta}^{3+}[M_{\delta}^{2+}Fe_{(2-\delta)}^{3+}]O_4^{2+70}$. The degree of inversion δ lies between 0< δ <1 for mixed spinel. The formation of mixed spinel is schematically represented in Figure 1.5(c). $MgFe_2O_4$ is found to form mixed spinel structure.

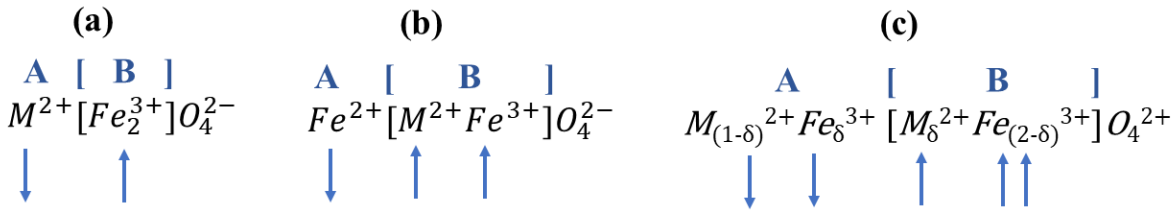

Figure 1.5: Schematic of cation distribution in (a) normal, (b) inverse and (c) mixed spinel.

1.5. Magnetic properties of Nanomaterials

In this section, various magnetic properties of transition metal oxide-based spinel NSs will be discussed under ac and dc applied magnetic field conditions. Magnetism in a material originates due to the magnetic moments of the atoms' electrons and nuclei. Nuclear magnetic moments are negligible in the context of magnetic properties of materials due to their thousands times smaller value compared to electronic magnetic moments. All materials exhibit some sort of magnetism and these materials can be classified depending on their bulk susceptibility (χ) values. Substances showing negative susceptibility are classified as diamagnetic, whereas materials with positive magnetic susceptibility are called paramagnet. Diamagnetism is developed due to the change in orbital motion of electron, whereas paramagnetism has its origin in the spin and orbital motion of individual electron, shown schematically in Figure 1.6(a). Pierre Curie in 1895 showed that χ varies inversely with absolute temperature (T)

$$\chi = \frac{C}{T} \tag{1.2}$$

The modified and more accurate form of the above equation is

$$\chi = \frac{C}{T-\theta} \qquad (1.3)$$

where, C is constant and θ is Curie temperature, below which the material show spontaneous magnetization i.e, ferromagnetism and above θ the material is paramagnet. Equation 1.3 is known as Curie-Weiss law[71].

In ferromagnets in addition to atomic moments there exists small regions called magnetic domains, where the magnetic moments are oriented in a preferential crystallographic direction. Spontaneous magnetization exists in each of these domains. In 1928 Heisenberg 1st explained the origin of ferromagnetism in terms of exchange integral, which is a quantum mechanical effect and electrostatic in nature[72]. According to Heisenberg's theory, antiferromagnetic or ferromagnetic order can occur depending on the exchange of interaction energy between the spins. In antiferromagnets, the forces between two adjacent atomic dipoles have signs opposite to those in ferromagnets. Materials that consist of two or more types of magnetic ions are called ferrimagnet, where all the magnetic ions are ordered in a mixed scheme of ferromagnetic or anti-ferromagnetic arrangement, resulting in a net magnetization. The schematic presentation of ferromagnetic, antiferromagnetic and ferrimagnetic ordering are shown in Figures 1.6(b-d).

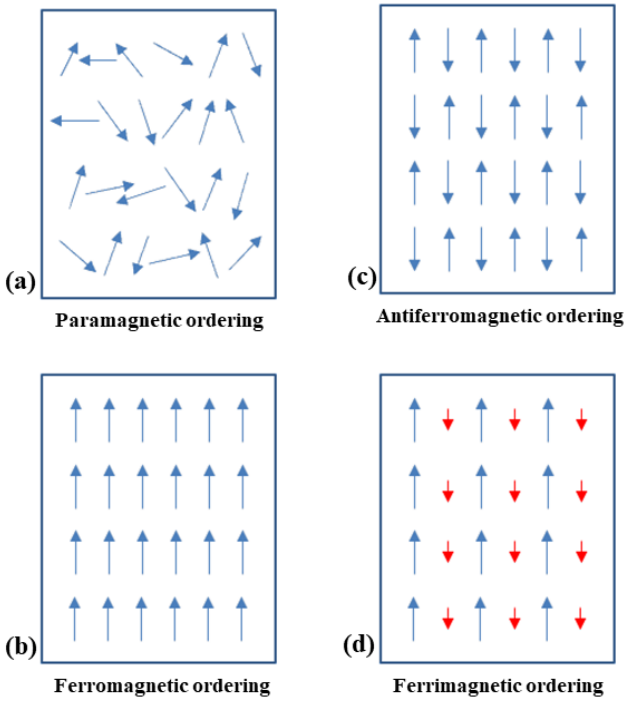

Figure 1.6: Schematic presentation of (a) paramagnetic, (b) ferromagnetic, (c) antiferromagnetic and (d) ferrimagnetic ordering.

Loadstone or Fe_3O_4 (magnetite) is the most common naturally obtained substance belonging to this class of magnetic materials and commonly known as ferrites. The variation of magnetization (M) with an applied magnetic field (H) for various kinds of magnetic materials is presented in Figure 1.7, showing saturation magnetization (M_s, maximum induced magnetization), remanent magnetization (M_r, remaining magnetization after the magnetic field is removed) and coercivity (H_c, magnetic field required to demagnetize the material).

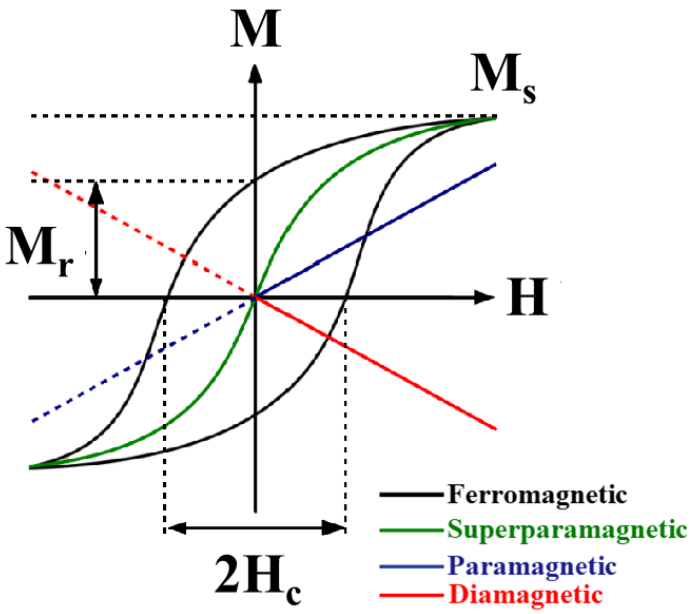

Figure 1.7: Magnetic behavior of materials under applied magnetic field.

In cubic spinel structure, the divalent and trivalent cations on the octahedral (B) site interact directly with each other, whereas the interaction between the cations between the octahedral and tetrahedral (A) sites are mediated through the oxygen anions. In inverse spinel ferrites MFe_2O_4 (M=Fe, Ni) the Fe^{3+} ions in A sites are aligned in antiparallel arranged with respect to the B sites, due to the strong superexchange interaction, J_{AB} between these two sites. The divalent cations (M^{2+}) having unpaired electrons incline to align themselves parallelly with the adjacent Fe^{3+} ions in the octahedral site. Thus the M^{2+} ions are in ferromagnetic arrangement and contribute in the net magnetization due to the nullification of magnetic contribution from the Fe^{3+} ions in A and B sites. The exchange interaction J_{AB} can be determined by Bloch's theorem[31], which we will discuss later on.

The magnetic properties of NMs are determined by two key issues, finite-size

effects and surface properties, giving rise to various exceptional features. Magnetic domains size, ranging between 10-1000 nm, are comparable to the size of nanocrystals. If the crystal size of ferromagnetic material reaches SD upon scaling down the size of the NMs, demagnetization becomes harder as the spins get aligned with each other. For particle size lesser than SD dimension, the material show superparamagnetization as the force needed for spin alignment is not enough to overcome the thermal randomization in absence of an external field. We will discuss suparamagnetic behavior in detail later.

The surface anisotropy in nanoscale is one order of magnitude higher than that in contrast to bulk materials. This is due to the presence of a large number of superficial ions in nanoparticles[73]. These disordered surface-spins are originated as they reside within an uncompensated coordination sphere due to broken bonds and vacancies, thus resulting in a magnetically harder surface layer than the core of NMs. Various kind of magnetic anisotropy is discussed below, including surface anisotropy.

1.5.1. Magnetic Anisotropy

Magnetic anisotropy represents an energetically favorable direction for spontaneous magnetization relative to the exchange interaction and the crystal axis. In the absence of an external magnetic field this spontaneous magnetization direction is called the 'easy axis' and the associated energy is named anisotropy energy. In a magnetic material, the magnetic anisotropy may arise due to the symmetry of crystalline lattice and also from the shape of a specific nanostructured material. Various sources of magnetic anisotropy are discussed below.

1.5.1.1. Magnetocrystalline Anisotropy

Magnetocrystalline anisotropy is an intrinsic property of a material and the most prominent contribution to the magnetic anisotropy originated from the symmetry axis of the local atomic structure. It arises because of the spin-orbit interaction of the electrons and also depends on the crystal field splitting energy[74]. Two models describe the magnetic anisotropy; (a) Neel model, which defines that magnetic anisotropy arises due to magnetic spin pair interactions between two magnetic ions[75] and (b) Single-ion or crystal field model which describes crystal field interactions with atoms that are not essentially magnetic[76]. The magnetocrystalline energy being associated with the relative orientation of the total

magnetization with respect to the magnetic easy axis of the crystal, i.e. θ, the magnetocrystalline anisotropy energy can be expressed as,

$$E_A = V(K_0 + K_1 sin^2\theta + K_2 sin^4\theta) \quad (1.4)$$

where, K_n (n= 0, 1, 2 …) are the magnetocrystalline anisotropy constants. K_0 is θ independent, arbitrary and thus an irrelevant parameter.

In Fe_3O_4 (cubic crystal), the magnetocrystalline anisotropy can be expressed as a series expansion in terms of cube axes and magnetization direction, where only the 1st two terms of the series expansion (K_1 and K_2) are sufficient to express the anisotropy energy in any arbitrary direction. Depending on the crystallographic orientation of the material, it reaches saturation at a different applied magnetic field. In hexagonal crystals, like hematite (α-Fe_2O_3), the weak ferromagnetism lies in the basal plane, which is an easy plane of magnetization. Magnetization generally lies along the c-axis, which is the hard direction, leading to its antiferromagnetic behavior at a lower temperature. It is extremely difficult to flip the magnetization out of the basal plan into the direction of the c-axis. With significant thermal excitation, these spins can tilt slightly along the basal plane, giving rise to ferromagnetic behavior of the material.

1.5.1.2. Shape Anisotropy

In polycrystalline material has no crystalline anisotropy due to the absence of any preferred direction. If the material is perfectly spherical, then the externally applied magnetic field will magnetize the material in every possible direction to the same extent. However, for material having non-spherical shape and preferential growth direction, it is easy to magnetize the material along the long axis in comparison to the short one. This kind of anisotropy is called shape anisotropy. Shape anisotropy becomes important in thin films and often produces in-plane alignment of moments. Here demagnetization field plays a significant role, determining the actual field inside a sample. For shape anisotropy $K_1 = \mu_0(1 - 3D_m)M_s^2/4$, where D_m is the demagnetization factor, which has values 0, 1/3 and 1 for long cylinders, spheres and plates respectively[77].

1.5.1.3. Surface Anisotropy

Surface anisotropy, first introduced by Néel[75], is related to surface and interfaces of

NMs and is observed in materials with complicated structures and morphologies such as monolayer transition metal films, multi-layers, rough surfaces, and especially in smaller particles. As mentioned earlier, surface anisotropy in NPs is one order of magnitude higher compared to that in bulk, because of the randomization of surface spins[78]. The effective anisotropy energy, K_{eff}, for a spherical particle can be expressed as, $K_{eff}=K_b+(6/D)K_s$, where K_b and K_s are the bulk (or volume) and surface anisotropy constants, respectively, and D is the diameter of the particle.

1.5.2. Saturation Magnetization (M_s)

M_s represents the maximum probable magnetization of a magnetic material under an externally applied high magnetic field. Saturation magnetization is the characteristic of ferromagnetic and ferrimagnetic material. Assuming each atom has an equal magnetic moment, M_s depends on the magnitude of magnetic moment and the density of atoms. The size and synthesis procedure of NMs are also found to affect M_s. For various reasons M_s in NMs decreases as the material dimension moves from bulk to nano. Gangopadhay *et al*[79] showed that the M_s reduction is due to the formation of a disordered nonmagnetic shell layer over the magnetically aligned core in NMs. On the other hand, Parker *et al*[80] showed that the spin canting occurs in nanoscale due to quantum size effects. Besides, temperature dependence of M_s is found to follow Bloch's $T^{3/2}$ law in bulk material, but NMs show deviation from this $T^{3/2}$ behavior.

1.5.3. Exchange Interaction and Bloch's Theorem

In spinel ferrites, the intra-site interactions (J_{AA}, A-O-A and J_{BB}, B-O-B) are direct-exchange types and the inter-site interaction (J_{AB}, A-O-B) is super-exchange type, where the interactions between 3d cations are mediated through the non-magnetic oxygen anions. In inverse spinel ferrite, such as Fe_3O_4, in addition to antiferromagnetic exchange interaction, there is ferromagnetic double-exchange interaction mediated by the spin-down t_{2g} electrons hopping between mixed-valent Fe ions on the B sites, shown schematically in Figure 1.8. As pointed out by Néel[81] in the simplest model ferrimagnetism in Fe_3O_4 with high T_C is obtained without any DE interaction for large $J_{AB}>>J_{BB}$, J_{AA} forcing an antiparallel alignment of the moments on the A and B sites. The net magnetization in Fe_3O_4 is contributed by the divalent Fe cations due to the nullification of magnetic contribution from

antiferromagnetically coupled Fe^{3+} ions. Later on, Néel model has been extended by Yafet and Kittel[82], suggesting the B sublattice to be subdivided into two Fe_B^{2+} and Fe_B^{3+} sublattices. They showed that on weakening J_{AB} and strengthening J_{BB}, the B site magnetic moments are no longer rigidly parallel to the A site moments. The stronger B-O-B super-exchange interaction results in spin canting expressed by a finite Yafet-Kittel angle, thus reducing M_s. Hence it is understood that the magnetic properties of spinel ferrites can be tuned and well understood by taking into account the ferromagnetic double-exchange interaction of the B sublattice competing with the antiferromagnetic super-exchange interaction.

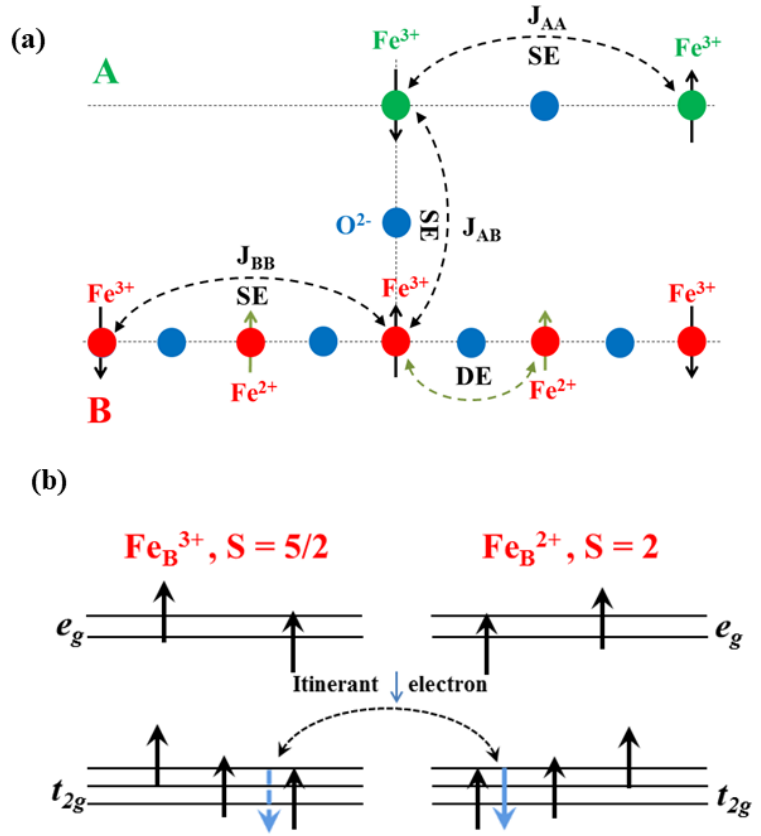

Figure 1.8: Schematic diagram of (a) antiferromagnetic interaction in Fe_3O_4 and (b) the spin-down t_{2g} electron hopping between mixed-valent Fe ions on the B sites.

J_{AB} can be calculated experimentally from the fitting of Bloch's law in M_s vs temperature curve. In general, at temperatures well below T_C, the temperature dependence of M_s follows Bloch's law,

$$M_s = M_s(0)(1 - BT^b) \qquad (1.5)$$

where $M_s(0)$ is M_s at T=0 K, B is the Bloch constant and b is the Bloch exponent which is 3/2 for a three dimensional system[83,84]. In small nanoparticles, a deviation from Bloch's law is observed. Bloch exponent is found to be strongly dependent on the size of the particles, their chemical composition and synthesis route but independent of the structure of the nanoparticles. From the B values, the exchange constant between A and B sites (J_{AB}) can be calculated using the following equation[31,85]

$$J_{AB} = \frac{16\, k_B(S_{B1}+S_{B2}-S_B)}{11 S_A(S_{B1}+S_{B2})}\left[\frac{0.05864}{4B(S_{B1}+S_{B2}-S_A)}\right]^{2/3} \quad (1.6)$$

where, for Fe_3O_4, S_A and S_{B1} are the spins of Fe^{3+} ions (S=5/2) and S_{B2} is the spin of Fe^{2+} ions (S=2).

1.5.4. Magnetic Domain Theory and Superparamagnetism

The ultimate perception of ferromagnetism and ferrimagnetism is dependent on magnetic domains. Each magnetic material consists of small regions with uniform magnetization i.e, the magnetic moments in each domain are aligned in the same direction. Each domain has a size ~1-100's μm and they are separated by domain walls, where the magnetic moments much change direction from one domain to that in the other one. Magnetic domain walls are of finite size and it depends on the exchange and magnetocrystalline energy. Depending on the size of the domain, magnetic behavior can be divided into three ranges[86].

Large-sized particles contain multidomain (MD) configuration and with an increase in size, they behave as bulk material. In these MD particles, the main reasons behind the magnetization reversal are domain wall motion and nucleation. With a decrease in particle size, the domain or grain size also reduces and a critical size is achieved, where the grain cannot accommodate a boundary. Below this critical size, the grain contains an SD. An SD grain is uniformly magnetized to saturation and magnetically hard with high H_c and M_r. If the grain size is reduced further with the SD regime, another critical threshold is reached below which H_c and M_r become zero. In this condition the domain or grain becomes superparamagnetic (SPM), where the magnetic relaxation can be characterized by Néel-Arrhenius equation[78,87], expressed as

$$f = f_0 \exp\left(-\frac{KV}{k_B T}\right) \quad (1.7)$$

where, f_0 is the Larmour frequency ranging between 10^9-10^{12} s^{-1}, K is anisotropy constant, V, particle volume, k_B, Boltzmann constant and T is the absolute temperature. As the size of the particles is too small, small anisotropy energy (E_A=KV) permits the magnetization to fluctuate between energetically favorable up and down states under slight thermal agitation. This means SPM particles behave paramagnetically, however, their magnetization is much higher than characteristic paramagnets and hence the term superparamagnetism, denoting a much higher susceptibility as compared to simple paramagnet, as shown in Figure 1.7. In SPM particles, the total magnetic moment in absence of any magnetic field and at T > 0 K will average to Zero.

The exponential dependence of the relaxation time on V and T makes it possible to define a T_B (at constant volume), or blocking volume V_B, (at constant temperature) at which the magnetization goes from an unstable condition ($1/ f_0 << t$) to a stable one ($1/ f_0 >> t$). Superparamagnetism is identified by three characteristics of magnetization curves. A SPM magnetization curve has zero H_c and M_r, the existence of T_B below which ferromagnetic order reappears and magnetization curves superimpose when plotting as H/T above T_B.

1.5.5. Hysteresis

Magnetic hysteresis loop is the plot of magnetization under an applied magnetic field. The hysteresis behavior i.e., the inability to trace back the same magnetization curve is related to the presence of domain in the material and it is the most common method to study the bulk property of that particular material. When the magnetic domains are magnetized in a certain direction, some energy is needed to turn them back again. This property is important for memory capacity of devices for audio recording or magnetic storage of data on computer disks. The easy magnetization directions in an SD particle depends on the magnetic anisotropy and these easy directions are separated by an energy barrier. These barriers are easily overcome by thermal fluctuations on atomic scale. However, on nano or macroscopic length scale excitations are too weak to overcome the energy barrier and this is defined as hysteresis. H_c represents the magnetic field strength required to reduce M_r to zero. The most useful information obtained from the hysteresis

loop is the maximum energy product, i.e., the product of maximum field (H_{max}) and maximum magnetization (M_{max}), which is a measure of maximum work done by a magnetic material. For SD non-interacting particles, Stoner and Wohlfarth theoretically showed that H_c is related to M_s and K, following the relation, $H_c=2K/M_s$ [88].

1.5.6. Magnetic Relaxation

Magnetic relaxation is the approach of a magnetic system to equilibrium upon removal or changing of the applied magnetic field. In nanoscale, this spin flipping to the steady-state condition and the reversal time depends on several parameters such as temperature, frequency in case of ac magnetic field, anisotropy energy etc. Magnetic relaxation is interesting to study the ability of a material to store the magnetization in time duration, for example in permanent magnets. For an assembly of magnetic particles, magnetic relaxation time (τ) is found to follow the Néel-Arrhenius equation

$$\tau = \tau_0 \exp(\frac{E_a}{k_B T}) \quad (1.8)$$

where, τ_0 is the Arrhenius pre-factor. By fitting equation 1.8 in the ac susceptibility vs T curve the relaxation time of the magnetic particles can be determined. However, Néel-Arrhenius law is applicable for independently relaxing magnetic particles assembly. For interacting magnetic particles systems forming magnetic cluster or spin-glass system another model was proposed, Vogel-Fulcher law[89], expressed as

$$\tau = \tau_0 \exp[\frac{E_a}{k_B(T-T_0)}] \quad (1.9)$$

τ_0 is the characteristic relaxation time and T_0 is the characteristic temperature, which is the measure of the interparticle interaction energy. By analyzing the fitting parameters the relaxation mechanism of the magnetic particles assembly and their temperature and frequency dependence of magnetic behavior can be understood.

1.6. Dielectric Properties

Since the introduction of ferrites as high permeability core materials, due to their high resistivity and low eddy current loss, magnetic properties of ferrites have attracted

immense interest from material scientists. Their dielectric characteristics become important because of the expanding interests of ferrites in microwave frequencies (1-40 GHz). Materials can be classified into conductor, semiconductor and insulator depending on their conductivity, whereas depending on the polarizability they are characterized into dielectric, paraelectric and ferroelectric[90]. In general, ferrites belong to the semiconductor and dielectric range. The study of complex dielectric properties of materials in the radio frequency (RF) and microwave frequency range is very important due to its relevance in communication technology, microwave circuit design and bio-medical fields[91]. Besides, ac measurements provide insights into the ionic conduction mechanism of the systems, which cannot be obtained from the less informative dc measurements. Thus ac techniques are employed to study the material properties such as bulk conductivity, grain and grain-boundary effect, ionic transport and double-layer formation at the electrode/sample interface[92]. Dielectric properties of a material such as dielectric permittivity, conduction and relaxation mechanisms depend both on external parameters such as frequency, temperature, pressure, humidity as well as the on the internal parameters like molecular structure, surface effects and orientation of the material[93,94]. For instance, Fe_3O_4 shows high conductivity as compared to $ZnFe_2O_4$ due to the presence of both divalent and trivalent Fe ions on the octahedral sites in Fe_3O_4, whereas the high resistivity in $ZnFe_2O_4$ is attributed to the occupation of Zn^{2+} ions replacing Fe^{2+} ions on B sites and thus reducing conductivity due to reduced hopping between $Fe^{2+} \leftrightarrow Fe^{3+}$ ions[69]. In the following section, important aspects related to the dielectric properties of a material is discussed.

1.6.1. Impedance Spectroscopy

Impedance spectroscopy is a powerful technique for determining the dielectric property of a material by analyzing its dielectric permittivity (ε), ac conductivity (σ_{ac}), impedance (Z), admittance (Y), transport phenomena, interfacial capacitance and mobility of charge carriers[95]. In this technique, dielectric property of a material is measured as a function of frequency, based on the interaction of the electric dipoles of the sample with the externally applied electric field. It involves phase-sensitive measurement of current and the corresponding voltage applied to the material under test. Under the application of an ac electric field with strength far less than the breakdown voltage is applied, the impedance (Z) of the sample in the time domain can be expressed as a ratio of voltage (V) and current

(I), following Ohm's law.

$$V(t) = V_0 \exp(j\omega t) \quad (1.10)$$

$$I(t) = I_0 \exp(j\omega t) \quad (1.11)$$

$$Z(\omega) = |Z|Cos\theta + j\,|Z|Sin\theta = Z' + jZ'' \quad (1.12)$$

Z' and Z'' are the real and imaginary parts of impedance, respectively, named as resistance and reactance. Impedance (Z) is defined as the total opposition a material offers to the flow of an alternating current at a given frequency. Impedance can be expressed using the rectangular coordinate form, as shown in equation 1.12 or in terms of magnitude and phase angle, |Z| and θ respectively. The mathematical relation between Z′, Z″, |Z| and θ can be expressed as

$$Z = \sqrt{Z'^2 + Z''^2} \quad (1.13)$$

$$\theta = tan^{-1}\frac{Z''}{Z'} \quad (1.14)$$

The reciprocal of impedance is called admittance (Y) and can be expressed as

$$Y = \frac{1}{Z} = \frac{1}{Z' + jZ''} \quad (1.15)$$

Impedance is practically useful for representing a series connection of resistance and reactance, where Z can be expressed as a sum of these two parameters, whereas for parallel connection of Z′ and Z″, Z can be expressed using the flowing equation

$$Z = \frac{Z'X^2}{Z'^2 + X^2} + j\frac{Z'^2 X}{Z'^2 + X^2} \quad (1.16)$$

There are two types of reactance, capacitive (Z''_C) and inductive (Z''_L), where $Z''_C = 1/(2\pi fC)$ and $Z''_L = 2\pi fL$. Here f is the frequency, C represents capacitance and L is the inductance.
To find the impedance we need to measure at least two values, one real and another imaginary and these values are then converted to the desired parameters such as |Z|, θ, Z′, Z″, C, L. We have studied the variation of |Z| and θ with the applied electric field frequency and calculated the dielectric properties of the sample specimen by analyzing Z′, Z″, real and imaginary parts of dielectric permittivity (ε′ and ε″ respectively), dielectric loss (tanδ) and ac conductivity (σ_{ac}). The dielectric parameters can be calculated by utilizing the following

equations

$$\varepsilon' = \frac{Z''}{\omega C_0 (Z'^2 + Z''^2)} \quad (1.17)$$

$$\varepsilon'' = \frac{Z'}{\omega C_0 (Z'^2 + Z''^2)} \quad (1.18)$$

$$\tan\delta = \frac{\varepsilon''}{\varepsilon'} \quad (1.19)$$

$$\sigma_{ac} = \omega \varepsilon_0 \varepsilon'' \quad (1.20)$$

where, ω is the angular frequency, $\omega = 2\pi f$, C_0 is the capacitance of air, defined as $C_0 = \frac{\varepsilon_0 A}{d}$ (A and d is the area and thickness of the sample respectively) and ε_0 is the permittivity of vacuum.

ε' represents the amount of dipole or charge alignment due to polarization and ε'' represents the energy amount to align the dipoles or move the ions. Loss tangent (tanδ) is the measure of the amount of energy loss in the process of polarization and dielectric relaxation in the material.

Frequency dispersion of dielectric permittivity can be expressed by Debye's dispersion equation

$$\varepsilon' = \varepsilon'_\infty + \frac{(\varepsilon'_0 - \varepsilon'_\infty)}{(1+\omega^2\tau^2)} \text{ and } \varepsilon'' = \frac{(\varepsilon'_0 - \varepsilon'_\infty)\omega\tau}{(1+\omega^2\tau^2)} \quad (1.21)$$

where, ε'_∞ and ε'_0 are the dielectric permittivity values at high and low frequencies respectively and τ is the relaxation time constant. ε' decreases with an increase in ω due to the mismatch between dipole characteristic frequency and the applied electric field frequency. However ε'' becomes maximum at $\omega = 1/\tau$, where the oscillating dipoles are coupled with the oscillating electric field and absorb maximum electric energy. There are non-Debye type materials that do not follow the ideal Debye dispersion showing a broad dielectric loss peak. This non-Debye type behavior can be explained by Cole-Cole, Davidson-Cole and Havriliak-Negami empirical expression[96]. Dielectric permittivity of a material increases with an increase in temperature due to the increased dipolar characteristic frequency at high temperatures. The dielectric polarization of ferrites is discussed below in detail.

1.6.2. Dielectric Polarization

When a dielectric material is placed in an electric field, the electric charges do not flow similar to conductor, instead, the positive and negative ions or charge-centers shift from their equilibrium position casing polarization. The positive charges move in the direction of the electric field and the negative charges in the opposite direction, causing an internal electric field in the material and thus reducing the overall electric field within the dielectric. In spinel ferrites, the cations are surrounded by closed pack oxygen anions. Due to the applied oscillating electric field, the center of cations gets shifted with respect to the center of anions in oscillating motion[97]. The anions and cations displace or drift through the grain regions and accumulate in the grain boundary resulting in polarization. The migration of charge carriers as well their accumulation, hence various dielectric properties of spinel ferrites, depends on the cation placement in A and B sites. Besides, the hopping of charge carriers between the divalent and trivalent cations in the B sites may contribute to dielectric polarization[91]:

$$M^{3+} + Fe^{2+} \leftrightarrow M^{2+} + Fe^{3+} + E_a \quad (1.22)$$

where, E_a is the activation energy required for the electron to hop the energy barrier.
There are various sources of dielectric polarization in spinel ferrites, as discussed below.

1.6.2.1. Electronic Polarization

Electron clouds displace relative to the nucleus upon applied electric field causing polarization. The required time for this type is the lowest (~10^{-15} s) and thus it occurs at high-frequency range at ~ 10^{15} Hz.

1.6.2.2. Atomic Polarization

Atomic polarization takes place when adjacent positive and negative ions 'stretch' under an applied electric field. This is also a fast process with a required response time ~ 10^{-13} s, effective at THz and microwave frequencies. Along with dielectric relaxation, at high frequency, resonance-type dielectric response takes place in the dielectric system[98].

1.6.2.3. Dipolar Polarization

Dipolar polarization occurs when permanent dipoles respond to the applied

electric field. This is also called orientation polarization and typically requires 10^{-9} s response time.

1.6.2.4. Interfacial Polarization

Interfacial or space-charge polarization takes place due to the accumulation of charge carriers at the interface or boundary of the inhomogeneous dielectric material. With an increase in temperature, this kind of polarization enhances due to the accumulated more thermally activated charge carriers at the interfaces. The operating frequency range of space charge polarization is below 10^7 Hz at room temperature and it can be described best with the Maxwell-Wagner model and Cole-Cole plot or Nyquist plot, described later on.

As the electric frequency increases the slow mechanism drops out leaving the fast mechanisms to contribute to dielectric permittivity. The frequency dependence of ε with its real and imaginary components is shown in Figure 1.9.

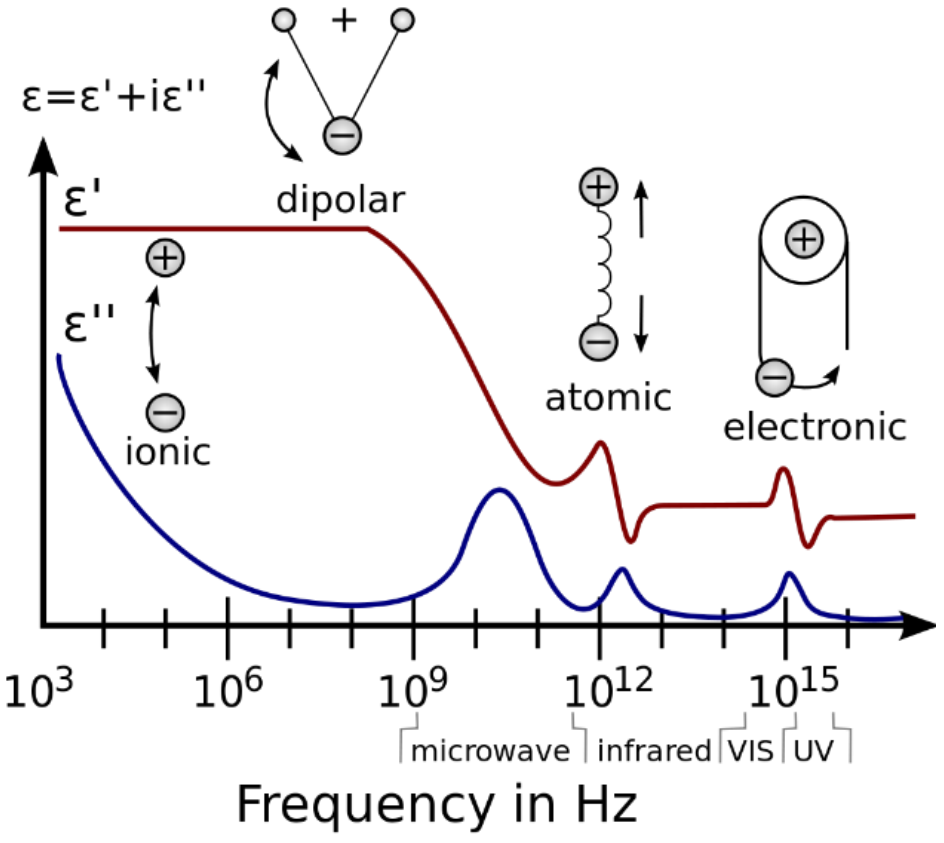

Figure 1.9: Variation of real and imaginary parts of dielectric permittivity with frequency.

1.6.3. Maxwell-Wagner Model

C.G. Koops[99] suggested a simple model to describe the frequency dispersion of

dielectric polarization for inhomogeneous dielectric material, showing the well-conducting grains in ferrites are separated by low conducting boundaries, shown in Figure 1.10, which was introduced by Maxwell-Wagner. Under the application of an external electric field, the charge carriers easily drift through the grains and accumulate at the resistive grain boundaries, producing high ε′ at low frequencies. The opposition to the charge movement would cause relaxation of dipoles to the polarizing field which causes a finite phase difference with the field. After a sufficiently high characteristic cut off frequency, the phase lag becomes prominent and hence ε′ decays.

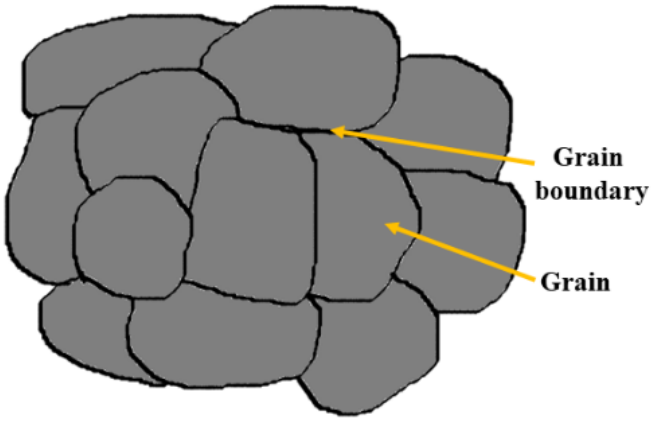

Figure 1.10: Schematic of Maxwell-Wagner grain and grain boundary model.

1.6.3.1. Cole-Cole Plot and Equivalent Circuit Model

Cole-Cole plot (plot of Z′ vs Z′′) portrays the Maxwell-Wagner two-layer model. It represents the electrical processes taking place within the system and also suggests the relaxation mechanisms. A Cole-Cole plot or Nyquist plot of Fe_3O_4 NHSs system is shown in Figure 1.11. For Debye type material perfect semicircular curves are obtained. However for non-Debye type systems, distorted semicircles can be observed, where the contributions from measuring leads are also may be present. The Z′ vs Z′′ plots can be fitted with an equivalent circuit model as shown in the inset of Figure 1.11. From the fitting parameters, the resistive and capacitive effect of the grains and grain boundaries can be obtained.

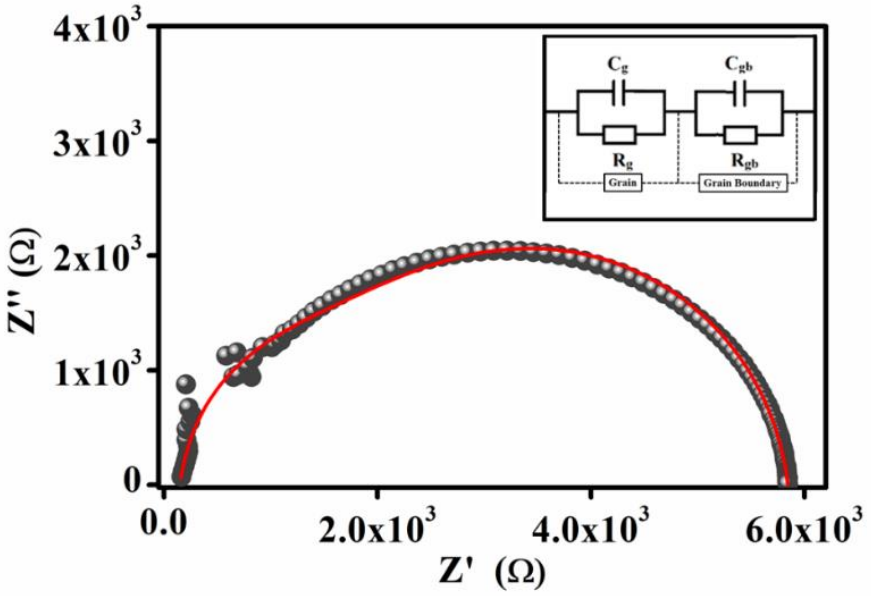

Figure 1.11: Cole-Cole plot between the real and imaginary part of impedance, fitted with equivalent circuit model shown in the inset.

1.6.4. Conductivity

In ferrites, electrical conduction takes place due to the hopping of spin-down itinerant electrons between the divalent and trivalent cations. As the applied electric field frequency increase, conducting grains become active and hopping becomes more prominent, thus gradually increasing the ac conductivity with frequency. As the conduction becomes prominent due to hopping polarization decreases. The frequency dependence of σ_{ac} can be expressed using Johnson's universal power law[100]

$$\sigma_{ac}(\omega, T) = \sigma_{dc}(T) + A\omega^{n}(T) \tag{1.23}$$

Here, σ_{dc} is the frequency-independent dc part of conductivity where conduction takes place due to drifting of the charge carriers, A is a material dependent parameter and n is a temperature-dependent parameter. Values of n vary between $0 < n < 1$, depending on the mechanism of conduction. Thermal excitation facilitates hopping of charges by increasing mobility of charge carriers and carrier concentration. At high temperatures along with electron hopping polaron hopping may also take place. From the nature of variation of n with temperature, the conduction mechanism in the dielectric system can be obtained. The activation energy for electrical conduction can be obtained from the ln σ_{dc} vs 1/T plot, fitted

with Arrhenius law.

1.7. Microwave Absorption Properties

The demand for ferrites is increasing rapidly for high-frequency applications with the evolution of technology from wireless information transfer to radar communication[41,101]. The frequency band designation of EM spectra is shown in Figure 1.12. This high demand for ferrites is owed to their high electrical resistivity. Unlike metallic magnetic particles, ferrites allow penetration of EM waves inside the material and provide low eddy current loss by increasing the scope of application in high-frequency regime. For the application of ferrites as microwave absorbers, lossy materials with broad resonance bandwidth and proper matching of relative permittivity ($\varepsilon = \varepsilon' - i\varepsilon''$) and *permeability* ($\mu = \mu' - i\mu''$) is required.

With the advancement of technology the usage of high-frequency electromagnetic devices various unwanted side effects such as electromagnetic interference (EMI) became an issue to be concerned for[102]. This is not only harmful to birds, but also affect human health. Thus electromagnetic absorbers (EMA) are needed to reduce electromagnetic pollution and shield unwanted EM waves. From the 19th century, there is enormous use of EMA material in military field for 'stealth technology' to make the aircraft and ships invisible towards radar detection[103,104]. However, the main drawback of EMA materials is the heavy weight of ferrite fillers in the polymer matrix, whereas for practical applications thin, lightweight, inexpensive efficient EMA materials are desired[105]. To achieve this, ferrites with nano-hollow spherical morphology can be an excellent candidate for EMA due to their low density and excellent magnetic, and dielectric properties.

Over the years various methods have been developed to measure permeability and permittivity, which include open-ended co-axial probe method, free-space method, cavity resonators, full-body resonance techniques, and transmission line techniques[106]. Each method has its range of applicability with some intrinsic limitations. Among these transmission-line techniques are the simplest and relatively accurate way of measuring the permeability and permittivity of EMA materials. Outline of the transmission line technique along with the related EM theory is discussed in the following section.

Approximate Band Designations	
High frequency (HF)	3 MHz–30 MHz
Very high frequency (VHF)	30 MHz–300 MHz
Ultra high frequency (UHF)	300 MHz–3 GHz
L band	1–2 GHz
S band	2–4 GHz
C band	4–8 GHz
X band	8–12 GHz
Ku band	12–18 GHz
K band	18–26 GHz
Ka band	26–40 GHz
U band	40–60 GHz
V band	50–75 GHz
E band	60–90 GHz
W band	75–110 GHz
F band	90–140 GHz

Figure 1.12: Frequency band designation of EM wave spectra.

1.7.1. Related Electromagnetic Theory

Maxwell's equations provide a foundation for practical applications of guided waves and transmission line. Moreover, the propagation of EM waves in a material can be described by Maxwell's equations, expressed as:

$$\vec{\nabla}.\vec{D} = \rho \tag{1.24a}$$

$$\vec{\nabla}.\vec{B} = 0 \tag{1.24b}$$

$$\vec{\nabla} \times \vec{E} = -\frac{\partial \vec{B}}{\partial t} \tag{1.24c}$$

$$\vec{\nabla} \times \vec{H} = \vec{J} + \frac{\partial \vec{D}}{\partial t} \tag{1.24d}$$

Here, $\vec{D} = \varepsilon_0\vec{E} + \vec{P} = \varepsilon\vec{E}$, is the electric flux density, $\vec{B} = \mu_0(\vec{H} + \vec{M}) = \mu\vec{H}$, is the magnetic flux density, ρ is the free charge density and $\vec{J} = \sigma\vec{E}$ represents the current density. Orientation of $\vec{E}, \vec{H}, \vec{k}$ vectors for a general plane wave is shown schematically in Figure 1.13. $\vec{H}$ can be expressed in terms of $\vec{E}$ as,

$$\vec{H} = -\frac{1}{i\omega\mu_0}\vec{\nabla} \times (\overrightarrow{E_0}e^{-i\vec{k}.\vec{r}})$$

$$= \frac{1}{\omega\mu_0}\vec{k} \times \overrightarrow{E_0} e^{-i\vec{k}.\vec{r}}$$

$$= \sqrt{\frac{\varepsilon_0}{\mu_0}}(\hat{n} \times \vec{E}) \quad (1.25)$$

Considering $\vec{E} = E_0 \cos(\omega t + \varphi)\,\hat{x}$, Maxwell's equations can be written as,

$$\vec{\nabla}.\vec{D} = \rho \quad (1.26a)$$

$$\vec{\nabla}.\vec{B} = 0 \quad (1.26b)$$

$$\vec{\nabla} \times \vec{E} = -i\omega\vec{B} \quad (1.26c)$$

$$\vec{\nabla} \times \vec{H} = \vec{J}\omega\vec{D} + \vec{J} \quad (1.26d)$$

For the propagation of ac EM wave in a material, permittivity becomes complex. In this scenario eq. 1.26(d) can be written as

$$\vec{\nabla} \times \vec{H} = \vec{J}\omega(\varepsilon' - i\varepsilon'')\vec{E} + \sigma\vec{E} \quad (1.27)$$

and dielectric loss tangent can be defined as

$$\tan\delta_\varepsilon = \frac{(\sigma + \omega\varepsilon'')}{\varepsilon'} \quad (1.28)$$

Solving for E and H from equations 1.26(c) and 1.26(d) gives Helmholtz equations

$$\vec{\nabla} \times \vec{\nabla} \times \vec{E} = -j\omega\mu\vec{\nabla} \times \vec{H} = \omega^2\mu\varepsilon\vec{E} \quad (1.29a)$$

$$\nabla^2\vec{E} + \omega^2\mu\varepsilon\vec{E} = 0 \quad (1.29b)$$

$k = \omega\sqrt{\mu\varepsilon}$ is defined as the propagation constant (also known as the phase constant or wave number) of the material medium. For plane wave in a lossy medium the general wave equation for E becomes,

$$\nabla^2\vec{E} + \omega^2\mu\varepsilon\left(1 - i\frac{\sigma}{\varepsilon\omega}\right)\vec{E} = 0 \quad (1.30)$$

The complex propagation constant for the medium can be defined as

$$\gamma = \alpha + j\beta = j\omega\sqrt{\varepsilon\mu}\sqrt{1 - j\frac{\sigma}{\omega\varepsilon}} \tag{1.31}$$

Where α is the attenuation constant and β is the phase constant. When an EM wave enters the EMA material, the wave decays exponentially with distance z by the factor $e^{-\alpha z}$. In low conductive ferrites α can be expressed as

$$\alpha + j\beta = j\frac{2\pi f}{c}\sqrt{(\mu'\varepsilon' - \mu''\varepsilon'') - j(\mu'\varepsilon'' + \mu''\varepsilon')} \tag{1.31}$$

$$\alpha = \frac{\sqrt{2}\pi f}{c}\sqrt{(\mu''\varepsilon'' - \mu'\varepsilon') + \sqrt{(\mu''\varepsilon'' - \mu'\varepsilon')^2 + (\mu''\varepsilon' + \mu'\varepsilon'')^2}} \tag{1.32}$$

From eq. 1.25 and the modified Helmholtz equation, relation between magnetic and electric field can be expressed as,

$$\vec{\mathrm{H}} = \frac{\gamma}{j\omega\mu}\vec{\mathrm{E}} \tag{1.33}$$

Here $\eta = \frac{j\omega\mu}{\gamma}$ is the intrinsic impedance of the conducting medium. In materials with high conductivity e.g., metal, the EM wave cannot penetrate the material due to the occurrence of much lower skin depth $\delta = 1/\alpha = \sqrt{\frac{2}{\omega\mu\sigma}}$. The average power ($P_l$) dissipated in a lossy medium due to conductivity, dielectric and magnetic losses is

$$P_l = \frac{\sigma}{2}\int E^2 dv + \frac{\omega}{2}\int (\varepsilon'' E^2 + \mu'' H^2) dv \tag{1.34}$$

It is to be kept in mind that the contribution from domain wall resonance and magnetic hysteresis is less important in low field and high frequencies (f >100 MHz in ferrites). However, the eddy current loss and characteristic ferromagnetic resonance are much prominent in GHz range[107].

When an EM wave, propagating in the z-direction, incidents on a material surface, some part of the wave reflects from the surface and some passes through the medium. For normal incidence (as shown in Figure 1.14) the expressions for an incident (E_i, H_i), reflected (E_r, H_r) and transmitted (E_t, H_t) waves will be,

(at z < 0)

$$\vec{\mathrm{E}}_i = \hat{x}E_0 e^{-jk_0 z} \quad (1.35a)$$

$$\vec{\mathrm{H}}_i = \hat{y}\frac{1}{\eta_0}E_0 e^{-jk_0 z} \quad (1.35b)$$

$$\vec{\mathrm{E}}_r = \hat{x}\Gamma E_0 e^{jk_0 z} \quad (1.35c)$$

$$\vec{\mathrm{H}}_r = -\hat{y}\frac{\Gamma}{\eta_0}E_0 e^{jk_0 z} \quad (1.35d)$$

(at z>0)

$$\vec{\mathrm{E}}_t = \hat{x}TE_0 e^{-\gamma z} \quad (1.35e)$$

$$\vec{\mathrm{H}}_t = \hat{y}\frac{T}{\eta}E_0 e^{-\gamma z} \quad (1.35f)$$

Here Γ is the reflection coefficient, T is the transmission coefficient and η_0 represents the intrinsic impedance of free space (~377 Ω). Applying boundary conditions to make the tangential components at z=0 continuous, we obtained

$$1 + \Gamma = T \quad (1.36a)$$

$$1 - \frac{\Gamma}{\eta_0} = \frac{T}{\eta} \quad (1.36b)$$

By solving equations 1.36a and 1.36b, Γ and T can be expressed as

$$\Gamma = \frac{\eta - \eta_0}{\eta + \eta_0} \quad (1.37a)$$

$$T = \frac{2\eta}{\eta + \eta_0} = 1 + \Gamma \quad (1.37b)$$

Reflection loss (RL) related to the reflected power from the material is defined from Γ value and can be expressed as $RL(\text{ in dB}) = -20\log|\Gamma|$. The sign of RL is taken negative in this thesis as per convention.

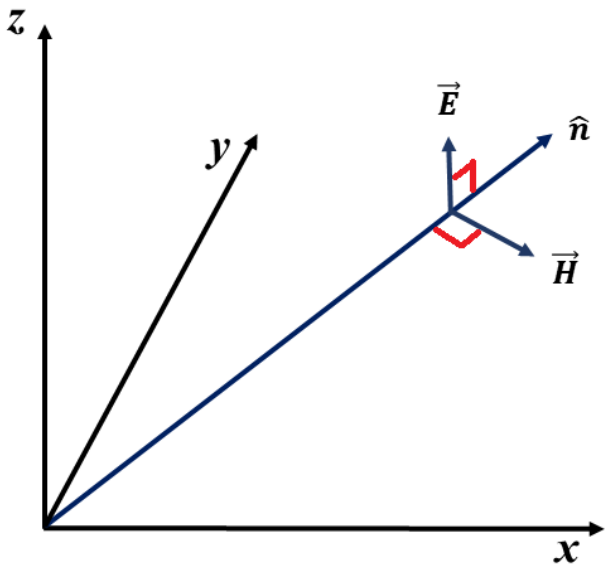

Figure 1.13: Orientation of the $\vec{E}, \vec{H}, \vec{k} = k\hat{n}$ vectors for a general plane wave.

1.7.2. Transmission Line Analogy

When the EM wave gets confined to a waveguide, resonator or optical fibre, different transverse modes are associated considering the boundary conditions of transmission lines. These transmission lines consist of one or more conducting lines. The circuit elements related to such lines are series resistance (R), series inductance (L) from the conductors, shunt capacitance (C) for the parallelly placed lines and an addition shunt conductance (G) from added load[108]. In transmission lines, the voltage and current can vary appreciably over its length, in terms of magnitude and phase. Besides, transmission lines are compact, economic, and can be easily integrated with active circuit devices, making it important for microwave circuits and devices analysis. Transmission lines consisting of two or more conductors can support only transverse electromagnetic (TEM) waves, characterized by the lack of longitudinal components. However, the waveguides consisting of a single conductor, support transverse electric (TE) and/or transverse magnetic (TM) waves, with the presence of longitudinal electric and magnetic components respectively.

1.7.2.1. Rectangular Waveguide

The dominant propagation mode in a rectangular waveguide with breadth 'a' and width 'b' (a > b) is the TE_{10} mode and it depends on the longer side 'a'. TM mode can also

propagate through the rectangular waveguide, but its cut off frequency is much higher than the TE mode. However, it cannot support TEM mode being a closed conductor. Rectangular waveguides are generally used to transfer large amount of power in high-frequency and materials properties can be achieved more accurately in this kind of waveguides. A rectangular waveguide and field propagation through the waveguide are shown schematically in Figure 1.15.

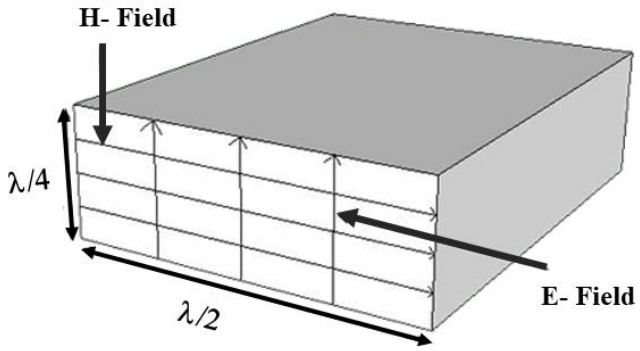

Figure 1.15: Geometry of a rectangular waveguide and field lines for TE10 mode.

1.7.2.2. Coaxial Airline

The coaxial airline is a broad band waveguide with no restrictions in frequency. Both TE and TM can propagate through a coaxial airline. More interestingly, TEM mode has no cut-off frequency in this kind of waveguide and it is the dominant propagation mode. Furthermore, coaxial airline is also shielded like rectangular waveguides and can be used at high frequencies. Field lines in the coaxial waveguide are shown in Figure 1.16.

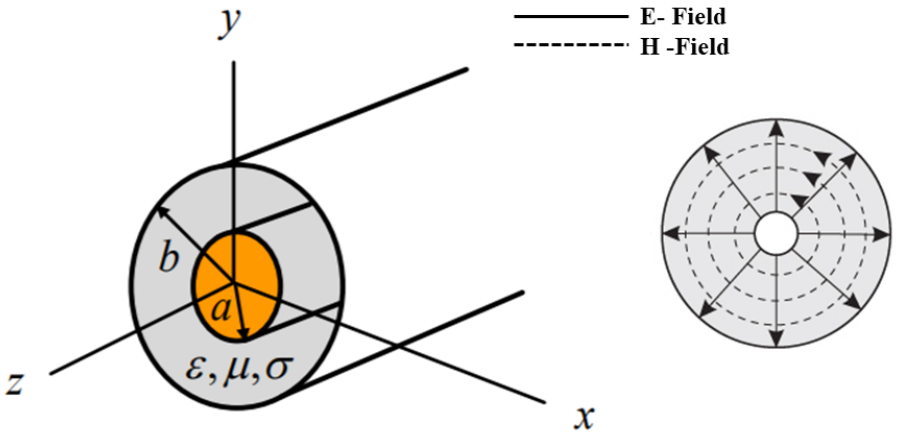

Figure 1.16: Geometry of a coaxial line and field lines for TEM mode.

1.7.3. Scattering Parameters

Microwave network analysis interconnects both the EM field theory and circuit analysis. At microwave frequencies, as the measurement of voltage or current is difficult, a clearly defined terminal pair is desired. Impedance, admittance, scattering matrices of circuit theory are usually incorporated as these terminal or port quantities. For a multiple-port network, impedance, admittance and scattering parameters in matrix form are expressed respectively,

$$[V] = [Z][I] \tag{1.39a}$$

$$[I] = [Y][V] \tag{1.39b}$$

$$[V^-] = [S][V^+] \tag{1.39c}$$

For transmission lines, at microwave frequencies, direct measurement of Y or Z parameters is tough due to the inaccessibility of apparatus to measure port current and voltage directly, and difficulty of obtaining perfect opens or shorts. Under these circumstances, direct measurements with the concepts of incident, reflected, and transmitted waves are given by the scattering matrix. A specific element of the scattering matrix can be obtained as,

$$S_{ij} = \left.\frac{V_i^-}{V_j^+}\right|_{V_k^+=0, k\neq j} \tag{1.40}$$

S_{ij} is the ratio of reflected or transmitted wave amplitude V_i^- coming out of port i, while the incident wave at port j is voltage V_j^+. For a two-port network, the scattering parameters (S parameters) are S_{11}, S_{21}, S_{12} and S_{22}. A schematic representation of a 2-port network defining the S parameters is shown in Figure 1.16. The expression for 2-port S-parameters is,

$$\begin{bmatrix} b_1 \\ b_2 \end{bmatrix} = \begin{bmatrix} S_{11} & S_{12} \\ S_{21} & S_{22} \end{bmatrix} \begin{bmatrix} a_1 \\ a_2 \end{bmatrix} \tag{1.41}$$

Here S_{11} and S_{22} are the forward and reverse reflection coefficients and S_{21} and S_{12} are the forward and reverse gains respectively.

1.7.4. Nicholson-Ross-Weir Algorithm

Microwave properties measurements using reflection or transmission line technique involves the analysis of two-port S parameters in a vector network analyser (VNA), by placing the sample in a section of a waveguide or coaxial airline. The conversion of S parameters to complex permittivity and permeability is calculated by solving equations using different algorithms. Nicholson-Ross-Weir (NRW) method is the most commonly used algorithm for measuring both μ and ε values. The determination of μ and ε values usually proceeds by solving a transcendental equation that involves the sample length, sample position, and reflection coefficient[109].

The phase ambiguity is the main problem of the NRW method which makes the solution not entirely analytical. Difficulties such as numerical singularities can occur at frequencies corresponding to integral multiples of one half wavelength (λ/2). This problem can be solved by using very thin samples. Besides, air gap and over-molding are two major issues in transmission line techniques[106]. Among the possible ways to rectify the problems, the polynomial fitting technique is a newer method that assumes a functional relationship between the material properties and the measurement frequency. The functional relationship is assumed to be an nth order polynomial.

Gaps between the sample holder and sample either may be corrected with gap-correction formulas or a conducting paste can be applied to external surfaces of the sample that are in contact with the sample holder. Air gaps in between interfaces can be considered as layered capacitors[106]. This approach assumes that the gaps between the transmission line and sample are effectively modelled by a set of capacitors in series.

For a coaxial line,

$$C = \frac{2\pi\varepsilon l}{\ln\frac{R_2}{R_1}} \tag{1.42}$$

Solving for ε provides,

$$\varepsilon_c' = \varepsilon_m' \frac{L_2}{L_3 - \varepsilon_m' L_1} \tag{1.43a}$$

$$\varepsilon_c'' = \left(\varepsilon_c' \times \frac{\varepsilon_m''}{\varepsilon_m'}\right) \frac{L_3}{L_3 - L_1 \varepsilon_m' \left(1 + \left[\frac{\varepsilon_m''}{\varepsilon_m'}\right]^2\right)} \tag{1.43b}$$

Modelling transmission line as a series of inductors for the E-field gap,

$$L_c = L_m - L_{air} \tag{1.44}$$

Where c, m and air represents corrected value, measured value and air space. For a coaxial line,

$$L = \frac{1}{2\pi}\mu' \ln\left(D_3/D_2\right) \tag{1.45}$$

Thus the corrected permeability can be written as,

$$\mu_c' = \mu_m' \frac{L_3 - L_1}{L_2} \tag{1.46a}$$

$$\mu_c'' = \mu_m'' \frac{L_3}{L_2} \tag{1.46b}$$

Where,

$$L_1 = \ln \frac{D_2}{D_1} + \ln \frac{D_4}{D_3} \tag{1.47a}$$

$$L_2 = \ln \frac{D_3}{D_2} \tag{1.47b}$$

$$L_3 = \ln \frac{D_4}{D_1} \tag{1.47c}$$

At higher frequencies, a frequency-dependent term should be included with this correction. For, rectangular waveguide, considering the same models and H-field gap, the corrected values for μ and ε are,

$$\varepsilon_c' = \varepsilon_m' \frac{d}{b-(b-d)\varepsilon_m'} \tag{1.48a}$$

$$\varepsilon_c'' = \varepsilon_c' \left(\frac{\varepsilon_m''}{\varepsilon_m'}\right) \frac{b}{b-(b-d)\varepsilon_m'} \tag{1.48b}$$

$$\mu_c' = \mu_m' \left(\frac{b}{d}\right) - \left(\frac{b-d}{d}\right) \tag{1.48c}$$

$$\mu_c'' = \mu_m'' \frac{b}{d} \tag{1.48d}$$

1.7.5. EM Absorption By A Single Layer Shielding Material

Shielding efficiency (SE) of an EM absorbing material is defined as the amount of EM energy obstructed by the material while passing through it. The diagram of an EM wave

normally incident on an absorber and possible interactions with the material is shown in Fig. 1.17. A normally incident EM wave (E_I) usually (a) partially reflects at the air-absorber interface, denoted as E_R, which can be detected by $S_{11\text{-OPEN}}$, (b) partially penetrates through the material, labelled as E_T and detected by S_{21}, and (c) partially attenuates in the material, E_A. Thus the whole attenuation process is contributed by reflection, transmission and total internal reflection and the corresponding shielding efficiencies are denoted as SE_R, SE_A and SE_M respectively[105,110]. Hence the total SE can be expressed as,

$$SE(dB) = 10\log\left(P_t/P_I\right) = SE_A + SE_R + SE_M \tag{1.49}$$

Where P_t and P_I represent the transmitted and incident power of the EM wave respectively. The SE components are defined as,

$$SE_R(dB) = 10\log\left(1 - R\right), [\text{ where}, R = |S_{11}|^2] \tag{1.50a}$$

and

$$SE_A(dB) = 10\log\left[(T/(1 - R)\right], [\text{ where}, T = |S_{21}|^2] \tag{1.50b}$$

Combining equations 1.49 and 1.50, and neglecting the minute effects of total internal reflections, SE can be written as,

$$SE(dB) = 20\log|S_{21}| \tag{1.51}$$

SE_R is related to the relative impedance mismatching between the material and EM wave. On the other hand, absorption loss is caused by the ohmic loss and heating due to the induced current in the material. The RL property can be directly measured from $S_{11\text{-SHORT}}$, which is in accordance with the value calculated from the transmission line theory[111]. At a quarter wavelength thickness of the absorbing material, EM waves interfere destructively. This matching thickness (t_m) is important for fabricating the proper thickness of the absorber material with maximum shielding. This thickness can be interpreted from the quarter wavelength model as,

$$t_m = \frac{nc}{4f_m\sqrt{|\varepsilon_r\mu_r|}}(n = 1,3,5, \dots) \tag{1.52}$$

where for odd values of n, reflected waves from two interfaces of the absorber become out of phase. Therefore, by optimizing the material parameters and thickness, RL can be tuned

for particular frequencies. Throughout the years, various materials such as carbons, metal powders, ferrites, oxides or polymers are merged, coated, doped into each other to get essential features, and even different fabrication techniques and synthesis procedures are verified to tune the characteristic parameters[41,112–117].

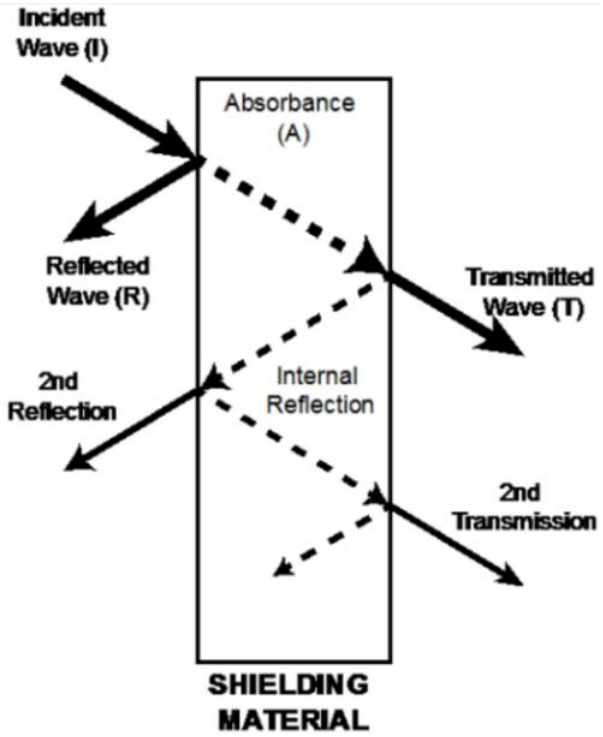

Figure 1.17: Schematic diagram of reflected and transmitted waves when an EM wave is incident on an EMA material.

1.8. Magnetorheology

1.8.1. Magnetorheological Fluid and Magnetorheological Effect

The term Rheology comes from the Greek word "*rheos*", which means flow. Rheology is the study of flow and deformation of a material under externally applied force and describes the liaison between force, deformation and time. In magnetorheology, the external force is magnetic. MR fluid is a classic smart material consisting of suspended micron-sized magnetic particles in the carrier fluid. These smart fluids undergo reversible and very fast (in a fraction of millisecond) changes in viscosity up to several orders of magnitude under applied magnetic field conditions from liquid to solid-like state, called

MR effect[118]. This unique property makes MR fluid an excellent candidate for application in mechanical systems where active control of vibration and transmission of torque is required, such as shock absorbers, brake, clutch, seismic vibration control, limb joints[119–124]. This outstanding property of MR fluids is also applied in a magnetic field controlled heat transfer[125,126], bio-medical applications[127], polishing devices[128–130], sound propagation[131], isotheral magnetic advection[132] and chemical sensing applications[133–135].

MR fluids are prepared by dispersing large amounts (up to 50 vol%) of solid magnetic particles with high saturation magnetization in a non-magnetic carrier liquid. Carbonyl iron particles are the most commonly used component of MR fluids due to its high saturation magnetization[136–144]. Typical carrier liquid includes mineral oil, silicone oil, polyethers, polyesters, water and synthetic hydrocarbons. Due to density mismatch between the magnetic particles and base fluids, sedimentation stability is the most faced problem in MR suspensions. To overcome sedimentation and particles aggregation, as well as to provide additional lubricating properties some additives are added to the MR fluids. These incorporate thixotropic agents, surfactants and polymers.

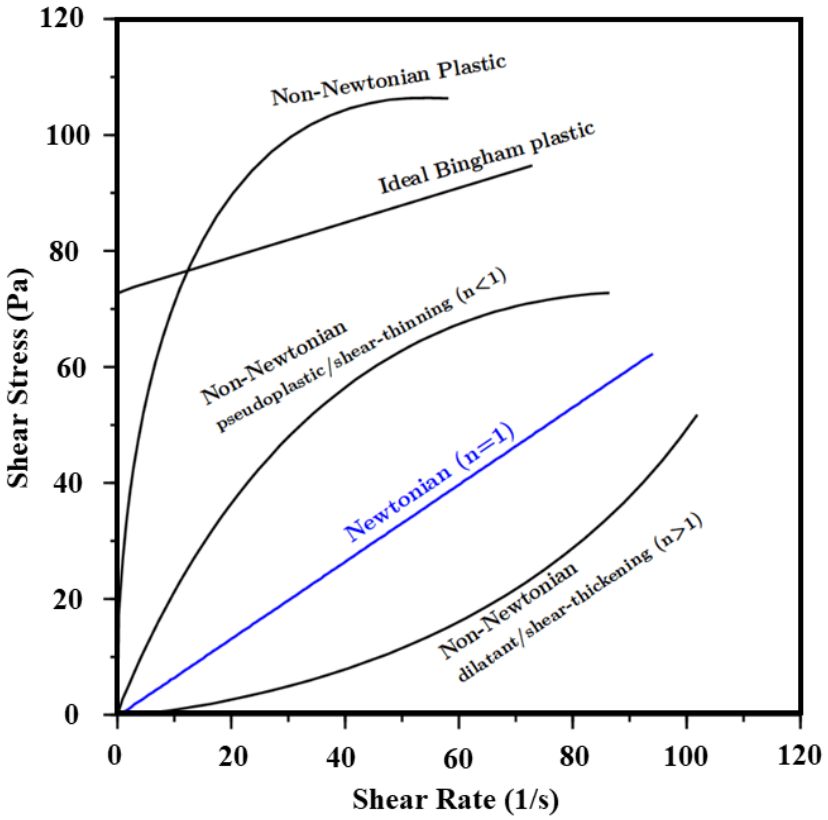

Figure 1.18: Shear stress vs shear rate curves of Newtonian and different types of non-

Newtonian fluids.

In the absence of a magnetic field, MR suspensions have low viscosity and behave like Newtonian fluids. When a magnetic field is applied the suspended particles attract one another along the field line and form asymmetric chains. The shear stress vs shear rate curves for Newtonian and various kinds of non-Newtonian fluids are shown in Figure 1.18. The mechanical behavior of MR fluids is determined by magnetic field induced percolated structures and characterized by the parameter yield stress (τ_y). Resistance of the particle network against the applied mechanical stress is defined in terms of field-dependent yield stress[145]. A pictorial representation of the development of apparent yield stress in MR fluid is shown in Figure 1.19.

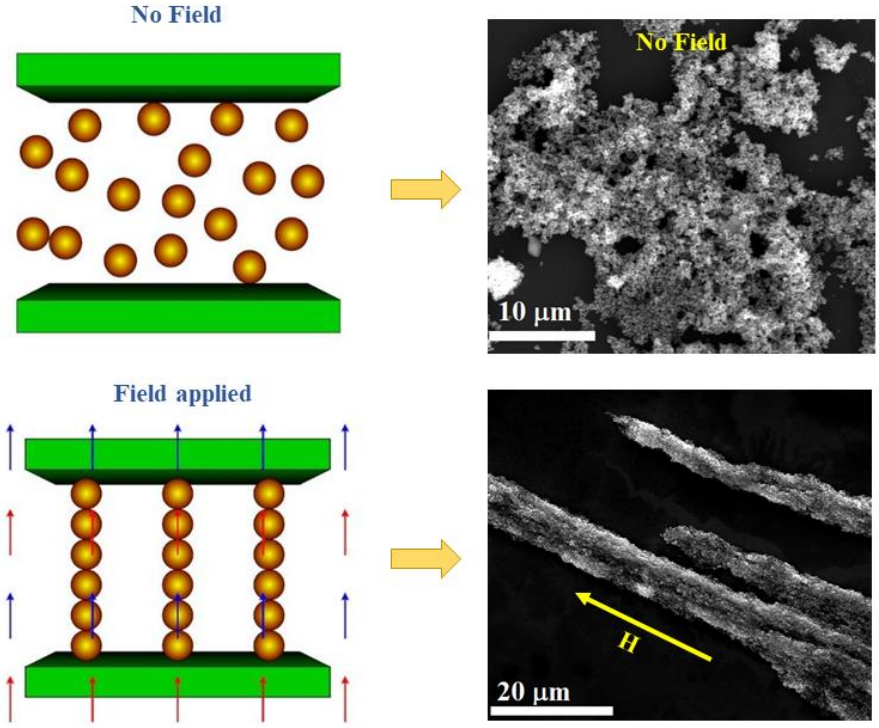

Figure 1.19: Schematic presentation of chain formation in MR fluid under applied field condition (left). Right side Figures show the chain formation process in scanning electron micrographs.

Flow in the MR suspension takes place only when the percolated structures are broken. τ_y is the critical point after which the MR suspension can no longer resist the mechanical stress and the percolated networks are raptured. If the stress level in the MR material is below this critical level, the material is predominantly elastic. An ideal MR fluid should possess the following properties: stable against settling, non-corrosive, wide active

temperature range, high magnetic saturation, small coercivity and remanent magnetization, stable against chemical degradation and oxidation, high field-induced yield stress and low apparent viscosity in the absence of field. Under applied magnetic field conditions MR fluids show yielding, shear-thinning and viscoelastic behavior. These properties are discussed below in brief.

1.8.2. Yield Stress

Yield stress is the minimum stress value essential for the onset of flow. It is proportional to the force required to break the field-induced particle networks. Upon increasing the magnetic field, the strength of the MR fluids i.e. the yield stress increases. The time scale related to particle rearrangement is driven by the magnetic forces[145]. The main motivation in MR fluid technology is to achieve excellent MR effect and therefore highest possible τ_y.

Yield stress models published in literature can be classified into two groups: i) macroscopic and ii) microscopic models. Macroscopic models assume homogeneous structures formation in the suspensions and are based on magnetization energy minimization principles. In this model, only the shape anisotropy of the particles aggregates are taken into account under small deformations[146]. On the other hand, in the microscopic model the interparticle interactions are also taken into account[147,148]. In most yield stress models, the shear stress is found to be subjugated by magnetostatic interactions and interactions between the field-induced particle chains are ignored, hence limiting the applicability of these models to low particle concentration MR suspensions only. Other yield stress models elaborated in literature involve percolation theory[149] and fractal aggregate concepts[150]. In percolation theory, an anisotropic microstructural network formation is considered in place of chain-like networks, when the particle concentration is above the percolation threshold. The application of magnetic field strengthens the particle network, without affecting its shape. The macroscopic model cannot reproduce the experimental yielding behavior in conventional MR fluids. However, the microscopic model involving dipolar magnetostatic interactions provide reasonable agreement with the experimental data[148].

At small applied field value, τ_y is proportional to the square of the magnetic field strength[151]. As the magnetic field increases the particle magnetization increases reaching

towards saturation, where τ_y can be expressed as

$$\tau_y = \sqrt{6\emptyset\mu_0 M_S^{1/2} H_0^{3/2}} \quad (1.53)$$

where, $\mu_0 = 4\pi \times 10^{-7}$ N/A^2 is the permeability of vacuum, $\emptyset$ is the particle volume fraction. Eventually, as the field strength increases further τ_y becomes independent of applied magnetic field value[148],

$$\tau_y = 0.086\emptyset\mu_0 M_S^2 \quad (1.54)$$

All micromechanical models based on the gap-spanning single-particle width chains i.e. the fibrillation formation envisage yield stress that increases linearly with particle concentration for any applied field strength. However, literature survey reveals that this linear behavior is valid only for diluted MR fluids at low magnetic fields[152]. For concentrated conventional MR fluids a more rapid that linear increment is observed due to thick and robust columnar structures formation.

Experimentally yield stress is calculated in steady shear mode or by oscillatory tests[153]. Three kinds of yield stresses can be defined from the shear flow experiments[154]: the elastic-limit yield stress, static yield stress and dynamic yield stress. The elastic-limit yield stress represents the maximum stress that can be applied without disturbing the particle structures and on removing the stress the structure is completely recoverable. The static yield stress is the minimum stress required to initiate the flow. This yield stress is frequently related to slip of the aggregated fluid rather than breaking the structures. The static yield stress is experimentally estimated by using creep tests, the so-called tangent method. Dynamic yield stress represents the stress needed to continuously break the aggregates with reform in the presence of magnetic interaction once the static yield stress is exceeded. It can be calculated by taking into account the viscoplastic rheological models such as Bigham-Plastic model, Herschel-Bulkley fluid model or Casson model, discussed in section 1.8.3.

1.8.3. Physical Mechanisms and MR Models

The relation between shear stress (τ) and shear rate ($\dot{\gamma}$) of MR fluids can be described by the non-Newtonian fluid model, where the fluid viscosity is a function of the shear rate. The most commonly used model in literature to understand the MR behavior is

Bigham-Plastic (BP) model[155]

$$\tau = \tau_y + \eta\dot{\gamma} \tag{1.55}$$

where η is the plastic viscosity.

MR studies probing a wider range of shear rate is found to be better fitted with Herschel-Bulkley (HB) model[156],

$$\tau = \tau_y + k\dot{\gamma}^n \tag{1.56}$$

where n is the power index and k is the consistency index. For n<1 the fluid is shear-thinning, whereas for n>1 it is shear-thickening. If n=1 and τ_y=0 it reduces to Newtonian fluid model.

Casson rheological model[157] is also used by researchers to describe the shearing behavior, expressed as

$$\sqrt{\tau} = \sqrt{\tau_y} + \sqrt{\eta_c\dot{\gamma}} \tag{1.57}$$

where, η_c is the Casson viscosity.

In HB and Casson models the whole region of the shear stress and shear rate curve (flow curve) is fitted for various magnetic field values. Whereas in the BP model only the high shear rate linear region is fitted to get τ_y. With different magnetic fields, the nature of flow curves change, thus it is difficult to fit the whole region by a single model.

To understand the MR field-induced anisotropic interaction, the particle magnetization model is the widely accepted mechanism. According to this model the magnetic moments in MR suspensions are field-induced and the thermal forces exerted by the solvent molecules ($\propto kT$), i.e. the Brownian motion, are negligible compared to magnetic and hydrodynamic forces. Due to large particle size in MR fluids, the magnetic particles behave as multidomain. A considerable simplification is achieved in this model by neglecting multibody magnetostatic interactions. The rheological effect is attributed to the permeability discrepancy between the continuous and dispersed phases. In the linear magnetization region an isolated magnetic sphere of radius 'a' shows magnetic moment

$$m = 4\pi\mu_0\mu_{cr}\beta a^3 H_0 \tag{1.58}$$

where, $\mu_0 = 4\pi \times 10^{-7}$ N/A^2 is the permeability of vacuum, μ_{cr} is the relative permeability of continuous phase, $\beta = (\mu_{pr} - \mu_{cr})/(\mu_{pr} + 2\mu_{cr})$ is the coupling parameter, μ_{pr} is the relative permeability of the particles, and H_0 is the magnetic field strength. At high field, when the particle magnetization reaches saturation, magnetic moment is independent of field strength and can be expressed as,

$$m = \frac{4}{3}\pi\mu_0\mu_{cr}a^3M_S \tag{1.59}$$

The magnetic interaction energy between two magnetic moments relative to the thermal energy, in the linear regime, can be designated by λ parameter[158],

$$\lambda = \frac{\pi\mu_0\mu_{cr}\beta^2a^3H_0^2}{2k_BT} \tag{1.60}$$

Where $0 < \beta < 1$ for conventional strong MR fluids and $-0.5 < \beta < 0$ for weak MR fluids or inverse ferrofluids. When the λ parameter is large enough magnetostatic interactions between the suspended particles is sufficient to overcome the thermal motion, resulting in chain-like percolated structures formation. For small values of λ the chain-like structures are absent due to the domination of Brownian motion. The particle structure formation is determined by particle volume fraction, $\emptyset$ and λ159. Not only that, experimentally it has been observed that the final structure formation is greatly impacted by the container size and rate of field increase[160]. Labyrinth like structure formation has also been recognized when the rate of field increases is high. Moreover, Promislow and Gast[161] showed that a DC field increased at a very slow rate does not produce the lowest energy suspension structure. Instead, they used pulsed magnetic fields to investigate the structuration in the absence of flow.

Mason number (Mn) is another dimensionless number, which is relevant when the MR fluid is subjected to flow. For steady shear flow Mn can be defined as the ratio of hydrodynamic drag (estimated as Stokes drag) and magnetostatic forces (dipolar interaction force) acting on the particles[162]:

$$Mn = \frac{8\eta_c\dot{\gamma}}{\mu_0\mu_{cr}\beta^2H^2} \tag{1.61}$$

where, η_c is the continuous phase viscosity.

Mn and λ parameters are related to Peclet number $Pe = 6\pi\eta_c\dot{\gamma}a^3/k_BT$ as $Mn\ \lambda=2Pe/3$. It is also worth noting that apart from hydrodynamic and magnetostatic other forces such as Van der Waals, frictional and body forces play a significant role in the redispersibility and offset properties of MR fluids[163–165]. However, the properties of MR fluids for short-range negligible forces depend on $\emptyset$, λ and Mn.

1.8.4. Viscoelasticity

Oscillatory shear provides valuable information for understanding the structures of MR fluids. In comparison to steady unidirectional shear, oscillatory shear testing can provide less ambiguous results in determining the yield stress and also gives access to a wide range of temporal scales. Besides, from the application point of view, most of the MR devices work in oscillatory mode. So understanding the viscoelastic properties from oscillatory shear measurements is important.

At small strain amplitude, MR fluid system exhibits linear viscoelasticity. Parthasarathy and Klingenberg[166] characterized the transition from linear to non-linear viscoelastic region by defining a critical strain. For higher strain, a transition from non-linear viscoelastic to viscoplastic regime is observed, associated with a second critical strain. At a very high frequency or amplitude of the applied oscillatory strain, MR fluids behave as Newtonian fluid. Thus for understanding the viscoelastic nature of MR suspensions, a small amplitude oscillatory strain is applied in the elastic region of the material.

When the MR suspension is subjected to a sinusoidal oscillatory shear of amplitude γ_0 and angular frequency ω, the resulting stress is also sinusoidal in nature of same frequency with amplitude τ_0 and phase shift δ. From the in-phase and out of phase components of the response, storage modulus G′ and loss modulus G′′ can be calculated respectively, as :

$$G' = \frac{\tau_0}{\gamma_0}\ cos\delta \tag{1.62}$$

$$G'' = \frac{\tau_0}{\gamma_0}\ sin\delta \tag{1.63}$$

In the presence of magnetic field large value of G′ appears, which is associated with the field-induced structures and is at least one order magnitude larger than G′′. The storage

modulus, G′, gives information about the amount of structure present in a material. It represents the energy stored in the elastic structure of the MR fluids. With the removal of the applied shear, this elastic nature helps the material to return back to its original shape. G′′ represents the viscous part or the amount of energy dissipated as heat in the sample. The micromechanical models discussed in section 1.8.2 are used in literature to predict G′ values under the assumption that stresses are exclusively determined by magnetic field and thus the dissipation is neglected. For the lower strain limit G′ is calculated from τ/γ ratio. Ginder *et al*[148] predicted that for intermediate field strength $G' = 3\emptyset\mu_0 M_S H$. As the particle magnetization begins to saturate non-quadratic dependence of G′ on-field strength arises. At high field strength when the particles′ magnetization is completely saturated G′ becomes independent of field strength given as $G' = 0.3\emptyset\mu_0 M_S^2$. These behaviors are in accordance with experimental reports. In some cases, the manifestation of multibody or multipolar interactions is also found in literature[167].

Amplitude sweep tests divulge a small linear viscoelastic region (strain amplitudes in the range of ~0.01 to 0.1%) that shifts to lower strain amplitudes with an increase in the magnetic field strength. Besides, the dependence of viscoelastic moduli on the applied strain varies with the variation of particle volume fraction. MR suspension below the percolation transition show particle rearrangement under the applied field condition leading to viscoelastic enhancement. On the other hand, for highly concentrated MR fluids flocculation exists even in the absence of magnetic fields. Thus upon shearing, the network structure disrupts and viscoelasticity decreases[168].

Apart from amplitude sweep test, frequency sweep test is also another method to understand the viscoelastic nature of MR fluids. The frequency dependence of linear viscoelastic material functions is not quite understandable. Numerous experiments and simulations suggest that G′ and G′′ can remain constant, reaching a maximum, or reduce or upsurge depending on the MR system under test. Chin *et al*[169] reported a frequency-independent loss tangent with corresponds to a gelation transition point. The magnetic field strengths lying below gel transition, a 2: 1 power-law dependence of G′ and G′′ on the oscillation frequency indicates that the relaxation times accompanying the self-similar structure reside within this frequency range.

Understanding of the non-linear regime, i.e. the large-amplitude oscillatory shear, is also important because of the small linear viscoelastic region limited to very small strain

amplitude and hence limited space for practical applications. McKinley and co-workers used a microscopic visco-elastoplastic model based on a classical soft-glassy rheological model to predict the large amplitude oscillatory shear behavior of MR suspensions[170].

1.8.5. Magnetometry: MR Fluids Operational Mode

There are three basic operational modes for MR fluids based devices: (a) pressure-driven flow mode (fixed poles), (b) direct-shear mode (relatively moveable poles), and (c) squeeze-film mode (relatively moveable poles), shown schematically in Figure 1.20.

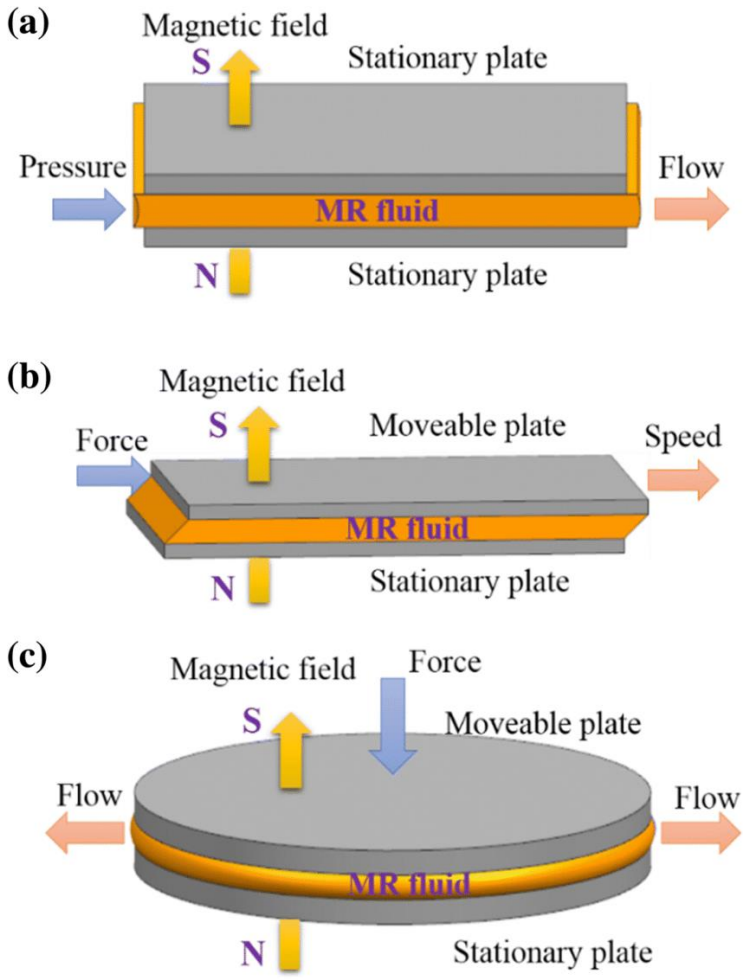

Figure 1.20: Schematic diagram of basic operational modes of MR fluids, (a) pressure-driven flow mode, (b) direct-shear mode and (c) squeeze-flow mode.

Pressure driven flow mode devices include dampers, shock absorbers and servo-valves. Whereas, clutches, brakes, chucking and locking devices operate in direct-shearing mode. The third operational mode appears in slow motion and/or high force

applications[171]. Direct shear mode has been studied thoroughly throughout the years by various researches[172] and numerous commercial products are available in market. However, less attention has been paid to the pressure-driven flow mode in spite of the fact that much larger shear rates can be applied to the MR suspensions in this operational mode (~20000 s^{-1}) in comparison to conventional rotational rheometry, which encompasses shear rates up to a few thousand s^{-1} only[173]. Moreover, this mode is most common in current applications such as in automotive dampers. In squeeze-film mode, much higher shear stress can be obtained compared to the other two modes, but there are very limited results available in literature regarding this mode[174–177].

1.8.6. MR Materials

MR fluids are comprised of three main components: magnetic particles, carrier fluid and additives. Most commonly used carbonyl iron (CI) particles with high permeability and saturation magnetization, are obtained from the chemical vapor deposition of iron pentacarbonyl. The shape of carbonyl iron particles is spherical as it helps in reducing the wear effect on the container wall and also on the MR fluid device. However, fiber shaped particles show better MR response, i.e. yield stress, and low off-state viscosity in contrast to spherical particles[178]. The concentration of carbonyl iron particles in carrier fluid ranges between 20-40 vol% with particle size maintained between 0.1 and 10 μm. Though apparently, it appears that with an increase in the magnetic particle concentration the MR response will increase, but 50 vol% is the upper limit of particle concentration in carrier oils. Above that limit the MR response decreases[179].

As the density of the ferromagnetic particles is much higher than that of the carrier fluids, which would certainly cause apparent sedimentation, limit the rheological properties of MR fluids and decrease the adjustability and shock absorption capacity of MR fluid devices. Thus, many researchers suggested numerous methods as a remedy to the sedimentation problem. Kormann *et al*[180] prepared nanometer-sized magnetic particles which improved the MR response, as well as the response time. Du *et al*[181] adopted the hydrophilic-lipophilic balance theory to choose the surfactant and showed that surfactants could improve the sedimentation stability of MR fluids, while the magnetic properties of the suspended particles and thus the rheological properties of MR fluids decrease to some degree. Dong *et al*[182] introduced a novel MR fluid to improve the MR properties by dispersing

$Fe_{76}Cr_2Mo_2Sn_2P_{10}B_2C_2Si_4$ amorphous alloy particles in silicon oil and discovered that the MR effect and sedimentation stability properties of MR fluids containing amorphous magnetic materials show improved MR response at lower field intensities. Arief *et al*[183] prepared CTAB surfactant coated CoNi hexagonal nanoplates to reduce the sedimentation problem. Kim and Choi *et al*[184] mixed PEO in distilled water and developed an MR suspension from the distribution of carbonyl iron particles in a polymeric solution, however, the mismatching of magnetic particles and the carrier liquid still persisted to be overcome in order to make considerable breakthroughs in improving the sedimentation stability of MR fluids. Besides, oxidation of iron particles takes place in the presence of air and moisture, which severely affect the MR response. Wahid *et al*[185] speculated due to oxidation of the iron particles it causes in use thickening of the MR fluids owing to prolonged use. This increases the solid volume fraction of the magnetic particles in the carrier fluid and also reduces the magnetic response of the iron particles, hence the performance of the MR fluids deteriorates abruptly. Thus iron or carbonyl iron-based MR fluids are nan-economic for commercial application.

As a remedy to the oxidation problem, Jang *et al*[186] suggested organic coating on the iron particles, which will reduce the exposure of the particles to the atmosphere. But the organic coating reduces magnetic saturation of the iron particles, thus reducing the yield stress. Organic and polymer coating as a measure to reduce the density mismatch between the magnetic particles and carrier liquid was also anticipated by some researchers. Liu *et al*[187] reported MR behavior of silica-coated carbonyl iron core-shell particles. Fang *et al*[188] fabricated carbonyl iron embedded polycarbonate composite particles for improved MR response and stability. Hajalilou *et al*[189] coated the surface of the iron particles with silver nanoparticles. This method improved the stability of the MR fluid in carrier oil. However, the yield stress reduces in Ag coated CI-based MR fluids compared to bare CI-based ones, due to the reduced magnetic saturation of CI as a result of Ag coating. Thus, surface coating to improve the stability of MR suspension leads to delayed MR response.

Apart from surface coating the alternative method of reducing the sedimentation problem is the addition of anti-sedimentation surfactant or other additives. Rabbani *et al*[190] reported 92% improvement in stability by the addition of 3 weight % stearic acid. Jang et al. added magnetic γ-Fe_2O_3 nanoparticle additives to micrometer-sized CI-based MR fluids to improve the yield stress and lower the sedimentation of the fluid. Nanosilica particles

addition also improves the stability of MR fluids[179]. There are two mechanisms explaining the effect of silica particles on the stability of MR fluids. First, silica–silica interparticle hydrogen bonding enables the formation of a thixotropic grid that averts the sedimentation and eventually reduces redispersion difficulties. Secondly, a silica particle may adhere to the CI particle by acid-base reaction in non-polar medium. In the presence of the magnetic field, the shell of adsorbed silica will partially screen the magnetic interactions between iron particles, thus reducing the MR effect. Nonetheless, due to the additives and coatings, the MR response gets compromised and noneconomic.

An alternate method to improve the MR response is to incorporate spinel ferrites with tunable size, better chemical and oxidation stability, low density compared to metallic magnetic particles. More interestingly, this method of production is highly economical, which is industry-friendly. Unlike metallic (such as Fe and CI) particles, the preservation of the ferrite sample is easy. MR fluids containing oxide ferrite samples provide excellent sedimentation stability due to the low density of these ferrimagnetic particles. Wang *et al*[191] reported $CaFe_2O_4$ nanocluster based MR fluids with excellent sedimentation stability. However, the yield stress value was quite low (~400 Pa) due to 25 wt% particle fraction of $CaFe_2O_4$, as well as its low saturation magnetization. A. V. Anupama[192] and her group showed that $Ni_{0.5}Zn_{0.5}Fe_2O_4$ powder (M_s=62.4 emu/g and 40% particle weight fraction) is an excellent MR material with $\tau_y = 7.8\, kPa$. This inconsistency is due to the physical presence of porous-network structures of powder particles occupying more volume fraction of magnetic particles in the fluid, thus enhancing the shear stress. This also suggests that the MR performance of ferrites based MR fluids can be enhanced by using porous magnetic particles. Not only this will help in improving the yield stress, but also the sedimentation stability due to low density of these porous structures in contrast to their solid counterpart. Ruan *et al*[35] reported Fe_3O_4 hollow nanospheres based MR fluids with improved sedimentation stability. However, very low yield stress value (~80 Pa) for 20 wt% particle fraction. It suggests that along with using porous structures, it is also important to improve the saturation magnetization of the material by some means. It is a challenge in the field of magnetorheology, to improve both the stability and yield stress values by using ferrite as the magnetic component. A brief review of the available MR materials is attempted in Table 1.1 below.

Table 1.1: Magnetorheological properties of different magnetic materials

Magnetic materials	Base fluid	Particle concentration	Additives	Yield stress	Drawback	Reference
CI particles with poly(vinyl butyral) (PVB) shell	mineral oil (MO, Aldrich)	20 vol %	NA	10.5 kPa	High M_r	193
Ag-coated CI particles	Polyalpha olefin oil	30 vol %	oleic acid	12.7 kPa	Reduced yield stress compared to bare CI particles	189
Iron NPs	Silicone oil	40 vol%	NA	4 kPa	High M_r and H_c	194
Fe_3O_4 hollow nanospheres	Water	10 wt%	NA	80 Pa	Poor yield stress	35
$CaFe_2O_4$ nanocrystal	Silicone oil	20 wt%	NA	400 Pa	Low yield stress	63
CI particles and Fe nanowires	Silicone oil	60 wt% CI and 6 wt% Fe	stearic acid	34.71 kPa	Low oxidation stability	195
Fe_3O_4 micro-octahedrons	Silicone oil	40 wt%	NA	3.5 kPa	None	196

1.9. Motivation and Objective of Thesis

Magnetorheological fluids have tremendous applications in biomedical as well as technological fields such as MR damper, brake, clutch, seismic vibration control, robotics. Moreover, the lightweight body armors based on MR fluid is the future of the military and defense field. Till now CI and Fe based metallic alloys are found to be the best magnetic materials for MR fluids based commercial applications owing to their high saturation magnetization. However, the poor sedimentation and chemical stability make these metallic

magnetic particles based MR fluids impractical and expensive for wide applications. Ferrites with low density and better oxidation stability can be an excellent replacement of non-economic metallic magnetic particles. Thus, if by any means we can enhance the magnetic response of ferrites those problems will be solved. In this context, ferrites for their synergistic magnetic and dielectric properties are the superior choice for high-frequency applications and devices as well.

Ferrites NHSs with hollow core and thin shell region is an excellent candidate for MR fluids due to its low density, better compressibility, and dispersibility. Not only that, due to the presence of two surfaces in the shell region ferrites NHSs contributes to unique electrical and dielectric properties. NHSs is a new drift towards lightweight and size efficient high-frequency communication technology and EM shielding devices. Besides, owing to the unique properties of nanostructured materials in contrast to their bulk counterpart, it is easy to tune the magnetic and dielectric properties of nanomaterials by varying the morphology and size. In this thesis, various methods such as chemical doping, morphology and size control are introduced to tune the magnetic, electronic and dielectric response of spinel ferrites. Finally, these materials are used in MR fluids to study their MR response and MR fluids based applications, and in EM shielding.

The key focus of this thesis is,

- We have prepared various transition metal oxides (Fe_3O_4, $ZnFe_2O_4$, $MgFe_2O_4$) based magnetic NSs (NPs and NHSs) by solvothermal synthesis procedure.
- We have tailored the magnetic and dielectric response of these 3D transition metal oxide-based magnetic NSs.
- We have studied their EM responses in high-frequency microwave regions since they show high permeability as well as unique dielectric response.
- We have studied the MR response of these magnetic NSs based MR fluids by adding 50wt% of magnetic materials in silicon oil. We showed experimentally that sedimentation stability plays a key role in determining the MR response.
- We have developed a theoretical model based on magnetic dipolar interactions to understand the yielding behavior of the NHSs based MR fluids.
- We have applied the MR fluids to externally tune the thermal transport and dielectric properties by magnetic stimulation.

1.10. Organization of Thesis

The entire thesis is divided into eight chapters. A brief sketch of the outline is given below.

Chapter 1 gives a brief introduction about the transition metal oxide-based ferrite NSs with their crystal structure, magnetic, electric, dielectric, microwave absorption and magnetorheological properties. Here we have discussed the necessity of tuning the magnetic and electronic properties of ferrites NSs. The frequency dependence of magnetic and dielectric properties are incorporated as well. Moreover, the motivation of the thesis work and the outline of the work performed are also discussed.

Chapter 2 is focused on the synthesis procedure of various NSs and different instrumental techniques for the characterization of the prepared NSs and their measurements.

Chapter 3 describes the preparation of Zn doped Fe_3O_4 NHSs with various doping concentrations of Zn, to tune the magnetic and dielectric response of Fe_3O_4 with chemical doping. Detailed investigation of the experimental data on structural, magnetic and dielectric measurements reveal the improved magnetization of Zn doped Fe_3O_4 NHSs up to a certain doping percentage of Zn and more interestingly reduced conductivity for the same doping content. Owing to its improved permittivty and reduced conductivity, $Zn_{0.2}Fe_{2.8}O_4$ NHSs is found to show excellent microwave absorption properties.

Chapter 4 demonstrates synthesis and structural, magnetic, and dielectric response of Mg-doped Fe_3O_4 NHSs with different doping content of Mg. Finally, the microwave absorption properties of $Mg_{0.3}Fe_{2.7}O_4$ is studied owing to its unique magnetic and dielectric properties. Interestingly, $Mg_{0.3}Fe_{2.7}O_4$ NHSs is found to be an excellent lightweight and broadband EMA material.

Chapter 5 exhibits the synthesis of Fe_3O_4 NHSs and NPs based MR fluids to study the effect of size and morphology on magnetorheological response. Fe_3O_4 NHSs is found to show better MR response compared to their solid counterpart and a suitable replacement of metallic magnetic particles to improve the MR response and sedimentation stability of MR fluids.

Chapter 6 shows the MR response, MR mechanism and viscoelastic properties of Zn doped Fe_3O_4 NHSs based MR fluids. Further, a theoretical model is developed to understand the yielding behavior and magnetorheological mechanism of ferrites NHSs based MR fluids depending on magnetic dipolar interaction.

Chapter 7 reports the preparation of water and ethylene glycol-based MR fluids with various concentrations of Fe_3O_4 NHSs. The effect of particle concentration and base fluids on the external magnetic field stimulated dielectric, electrical and thermal conduction properties of the MR fluids are studied in detail. Further, it is demonstrated that the thermal transport properties can be controlled by orientation and strength of the external magnetic field.

Chapter 8 concludes the thesis with an idea about the scope for future work in this direction.

Bibliography

1. Drexler, K. E. Engines of creation 2.0." The Coming Era of Nanotechnology. *Anchor Books-Doubleday* **1986**, 576 (2006).
2. Martín, J. I. *et al.* Ordered magnetic nanostructures: fabrication and properties. *JMMM* **256**, 449–501 (2003).
3. Bose, S. *et al.* Size induced metal-insulator transition in nanostructured niobium thin films: intra-granular and inter-granular contributions. *J. Phys.: Condens. Matter* **18**, 4553–4566 (2006).
4. Cox, A. J., Louderback, J. G. & Bloomfield, L. A. Experimental observation of magnetism in rhodium clusters. *Physical Review Letters* **71**, 923 (1993).
5. Cox, A. J., Louderback, J. G., Apsel, S. E. & Bloomfield, L. A. Magnetism in 4*d*-transition metal clusters. *Physical Review B* **49**, 12295 (1994).
6. Lopez-Sanchez, J. A. *et al.* Facile removal of stabilizer-ligands from supported gold nanoparticles. *Nature Chemistry 2011 3:7* **3**, 551–556 (2011).
7. Brollo, M. E. F. *et al.* Compact Ag@Fe3O4 Core-shell Nanoparticles by Means of Single-step Thermal Decomposition Reaction. *Scientific Reports 2014 4:1* **4**, 1–6 (2014).
8. Del Alamo, J. A. Nanometre-scale electronics with III–V compound semiconductors. *Nature 2011 479:7373* **479**, 317–323 (2011).
9. Erwin, S. C. *et al.* Doping semiconductor nanocrystals. *Nature 2005 436:7047* **436**, 91–94 (2005).
10. CJ, C., GT, T., JK, S.-S. & WM, S. A holistic approach to targeting disease with polymeric nanoparticles. *Nature reviews. Drug discovery* **14**, 239–247 (2015).
11. Ren, W. & Cheng, H.-M. The global growth of graphene. *Nature Nanotechnology 2014 9:10* **9**, 726–730 (2014).
12. Novoselov, K. S. *et al.* A roadmap for graphene. *Nature 2012 490:7419* **490**, 192–200 (2012).
13. Juliano, R. Nanomedicine: is the wave cresting? *Nature Reviews Drug Discovery 2013 12:3* **12**, 171–172 (2013).
14. Veiseh, O., Tang, B. C., Whitehead, K. A., Anderson, D. G. & Langer, R. Managing diabetes with nanomedicine: challenges and opportunities. *Nature Reviews Drug Discovery 2014 14:1* **14**, 45–57 (2014).
15. Larcher, D. & Tarascon, J.-M. Towards greener and more sustainable batteries for electrical energy storage. *Nature Chemistry 2014 7:1* **7**, 19–29 (2014).
16. Aricò, A. S., Bruce, P., Scrosati, B., Tarascon, J.-M. & van Schalkwijk, W. Nanostructured materials for advanced energy conversion and storage devices. *Nature Materials 2005 4:5* **4**, 366–377 (2005).
17. Hashmi, A. S. K. & Hutchings, G. J. Gold Catalysis. *Angewandte Chemie International Edition* **45**, 7896–7936 (2006).
18. Grunwaldt, J. D., Kiener, C., Wögerbauer, C. & Baiker, A. Preparation of Supported Gold Catalysts for Low-Temperature CO Oxidation via "Size-Controlled" Gold Colloids. *Journal of Catalysis* **181**, 223–232 (1999).
19. Garadkar, K. M., Ghule, L. A., Sapnar, K. B. & Dhole, S. D. A facile synthesis of ZnWO4 nanoparticles by microwave assisted technique and its application in photocatalysis. *Materials Research Bulletin* **3**, 1105–1109 (2013).
20. Zhang, W. *et al.* Multifunctional glucose biosensors from Fe3O4 nanoparticles modified chitosan/graphene nanocomposites. *Scientific Reports 2015 5:1* **5**, 1–9 (2015).

21. Corr, S. A. Metal oxide nanoparticles. 180–207 (2012) doi:10.1039/9781849734844-00180.
22. Xu, Y., Sherwood, J., Qin, Y., Holler, R. A. & Bao, Y. A general approach to the synthesis and detailed characterization of magnetic ferrite nanocubes. *Nanoscale* **7**, 12641–12649 (2015).
23. Shen, J., Zhu, Y., Jiang, H. & Li, C. 2D nanosheets-based novel architectures: Synthesis, assembly and applications. *Nano Today* **11**, 483–520 (2016).
24. Zou, G. *et al.* Magnetic Fe3O4 nanodisc synthesis on a large scale via a surfactant-assisted process. *Nanotechnology* **16**, 1584 (2005).
25. Heurlin, M. *et al.* Continuous gas-phase synthesis of nanowires with tunable properties. *Nature 2012 492:7427* **492**, 90–94 (2012).
26. Pérez-Juste, J., Pastoriza-Santos, I., Liz-Marzán, L. M. & Mulvaney, P. Gold nanorods: Synthesis, characterization and applications. *Coordination Chemistry Reviews* **249**, 1870–1901 (2005).
27. Ebbesen, T. W. & Ajayan, P. M. Large-scale synthesis of carbon nanotubes. *Nature 1992 358:6383* **358**, 220–222 (1992).
28. Mandal Goswami, M. Synthesis of Micelles Guided Magnetite (Fe3O4) Hollow Spheres and their application for AC Magnetic Field Responsive Drug Release. *Scientific Reports 2016 6:1* **6**, 1–10 (2016).
29. Rakshit, R. *et al.* Evaluation of SiO2@CoFe2O4 nano-hollow spheres through THz pulses. *AIP Conference Proceedings* **1728**, 020084 (2016).
30. Guo, P., Zhang, G., Yu, J., Li, H. & Zhao, X. S. Controlled synthesis, magnetic and photocatalytic properties of hollow spheres and colloidal nanocrystal clusters of manganese ferrite. *Colloids and Surfaces A: Physicochemical and Engineering Aspects* **395**, 168–174 (2012).
31. Sarkar, D., Mandal, M. & Mandal, K. Domain controlled magnetic and electric properties of variable sized magnetite nano-hollow spheres. *Journal of Applied Physics* **112**, 064318 (2012).
32. Y, Z., L, L., F, T. & J, R. Controlled drug delivery system based on magnetic hollow spheres/polyelectrolyte multilayer core-shell structure. *Journal of nanoscience and nanotechnology* **6**, 3210–3214 (2006).
33. Souvanik Talukdar, Rupali Rakshit, André Krämer, A. Müller, F. & Kalyan Mandal. Facile surface modification of nickel ferrite nanoparticles for inherent multiple fluorescence and catalytic activities. *RSC Advances* **8**, 38–43 (2018).
34. Xu, H.-L., Bi, H. & Yang, R.-B. Enhanced microwave absorption property of bowl-like Fe3O4 hollow spheres/reduced graphene oxide composites. *Journal of Applied Physics* **111**, 07A522 (2012).
35. Ruan, X., Pei, L., Xuan, S., Yan, Q. & Gong, X. The rheological responds of the superparamagnetic fluid based on Fe3O4 hollow nanospheres. *Journal of Magnetism and Magnetic Materials* **429**, 1–10 (2017).
36. Lapčík, L. *et al.* Hollow spheres as nanocomposite fillers for aerospace and automotive composite materials applications. *Composites Part B: Engineering* **106**, 74–80 (2016).
37. Park, S. S. & Ha, C. S. Polyimide/hollow silica sphere hybrid films with low dielectric constant. *Composite Interfaces* **23**, 831–846 (2016).
38. Rengarajan, R., Jiang, P., Colvin, V. & Mittleman, D. Optical properties of a photonic crystal of hollow spherical shells. *Applied Physics Letters* **77**, 3517 (2000).
39. Liu, T., Zhang, L., Cheng, B. & Yu, J. Hollow Carbon Spheres and Their Hybrid Nanomaterials in Electrochemical Energy Storage. *Advanced Energy Materials* **9**, 1803900 (2019).

40. Zhao, D. *et al.* Hollow structures as drug carriers: Recognition, response, and release. *Nano Research 2021* 1–19 (2021) doi:10.1007/S12274-021-3595-5.
41. Mandal, D., Gorai, A. & Mandal, K. Electromagnetic wave trapping in NiFe2O4 nano-hollow spheres: An efficient microwave absorber. *Journal of Magnetism and Magnetic Materials* **485**, 43–48 (2019).
42. Rakshit, R. *et al.* Surface Electronic States Induced High Terahertz Conductivity of Co3O4 Microhollow Structure. *ACS Applied Materials & Interfaces* **10**, 19189–19196 (2018).
43. Zhao, Z. *et al.* Octapod iron oxide nanoparticles as high-performance T2 contrast agents for magnetic resonance imaging. *Nature Communications 2013 4:1* **4**, 1–7 (2013).
44. Li, C. *et al.* Phase and composition controllable synthesis of cobalt manganese spinel nanoparticles towards efficient oxygen electrocatalysis. *Nature Communications 2015 6:1* **6**, 1–8 (2015).
45. Xiao, J. *et al.* Ultrahigh relaxivity and safe probes of manganese oxide nanoparticles for in vivo imaging. *Scientific Reports 2013 3:1* **3**, 1–7 (2013).
46. M, Z., M, de R. & H, F. Time-resolved observations of water oxidation intermediates on a cobalt oxide nanoparticle catalyst. *Nature chemistry* **6**, 362–367 (2014).
47. Hankare, P. P., Pandav, R. S., Patil, R. P., Vader, V. T. & Garadkar, K. M. Synthesis, structural and magnetic properties of copper substituted nickel manganite. *Journal of Alloys and Compounds* **544**, 197–202 (2012).
48. Blanco-Andujar, C., Ortega, D., Southern, P., Pankhurst, Q. A. & Thanh, N. T. K. High performance multi-core iron oxide nanoparticles for magnetic hyperthermia: microwave synthesis, and the role of core-to-core interactions. *Nanoscale* **7**, 1768–1775 (2015).
49. Kim, D. K. *et al.* Energy absorption of superparamagnetic iron oxide nanoparticles by microwave irradiation. *Journal of Applied Physics* **97**, 10J510 (2005).
50. Wang, L., Neoh, K. G., Kang, E. T., Shuter, B. & Wang, S.-C. Superparamagnetic Hyperbranched Polyglycerol-Grafted Fe3O4 Nanoparticles as a Novel Magnetic Resonance Imaging Contrast Agent: An In Vitro Assessment. *Advanced Functional Materials* **19**, 2615–2622 (2009).
51. Guan, P. F., Zhang, X. F. & Guo, J. J. Assembled Fe3O4 nanoparticles on graphene for enhanced electromagnetic wave losses. *Applied Physics Letters* **101**, 153108 (2012).
52. Rakshit, R. *et al.* Acoustic vibration induced high electromagnetic responses of Fe3O4 nano-hollow spheres in the THz regime. *Journal of Physics D: Applied Physics* **48**, 245301 (2015).
53. Ding, J., McCormick, P. G. & Street, R. Magnetic properties of mechanically alloyed CoFe2O4. *Solid State Communications* **95**, 31–33 (1995).
54. Wu, J. *et al.* Partially inverse spinel ZnFe2O4 with high saturation magnetization synthesized via a molten salt route. *Applied Physics Letters* **99**, 202505 (2011).
55. Sláma, J., Jozef, P., Šoka, M. & Lokaj, J. Metamagnetic properties in Mn0.7Mg0.3Fe2O4 ferrite. *Physica B: Condensed Matter* **576**, 411705 (2020).
56. Cao, D. *et al.* Nonmetal sulfur-doped coral-like cobalt ferrite nanoparticles with enhanced magnetic properties. *Journal of Materials Chemistry C* **4**, 951–957 (2016).
57. Pal, D. *et al.* Micelles induced high coercivity in single domain cobalt-ferrite nanoparticles. *Journal of Applied Physics* **108**, 124317 (2010).
58. Sisi Dai *et al.* Porous-carbon-based Mo 2 C nanocomposites as excellent microwave absorber: a new exploration. *Nanoscale* **10**, 6945–6953 (2018).

59. Zhou, B. *et al.* Submicron carbonyl iron particles as an efficient microwave absorber in the low frequency band. *Journal of Physics D: Applied Physics* **50**, 475001 (2017).
60. Jung, H. S. & Choi, H. J. Hydrothermal fabrication of octahedral-shaped Fe3O4 nanoparticles and their magnetorheological response. *Journal of Applied Physics* **117**, 17E708 (2015).
61. Chang, H., Tsai, K. L. & Tsung, T. T. A Study on Dynamic Stability of the Fe3O4 Magnetorheological Fluid. *Materials Science Forum* **561–565**, 2175–2178 (2007).
62. V. Anupama, A., V. Kumaran & B. Sahoo. Magnetorheological fluids containing rod-shaped lithium–zinc ferrite particles: the steady-state shear response. *Soft Matter* **14**, 5407–5419 (2018).
63. Wang, G. *et al.* Synthesis of calcium ferrite nanocrystal clusters for magnetorheological fluid with enhanced sedimentation stability. *Powder Technology* **322**, 47–53 (2017).
64. Wei, J. H. *et al.* Synthesis and magnetorheological effect of Fe3O4-TiO2 nanocomposite. *Journal of Physics: Conference Series* **149**, 012083 (2009).
65. Verwey, E. J., Haayman, P. W. & Romeijn, F. C. Physical Properties and Cation Arrangement of Oxides with Spinel Structures II. Electronic Conductivity. *The Journal of Chemical Physics* **15**, 181 (2004).
66. Kefeni, K. K. & Mamba, B. B. Photocatalytic application of spinel ferrite nanoparticles and nanocomposites in wastewater treatment: Review. *Sustainable Materials and Technologies* **23**, (2020).
67. Sickafus, K. E., Wills, J. M. & Grimes, N. W. Structure of Spinel. *Journal of the American Ceramic Society* **82**, 3279–3292 (1999).
68. Harris, V. G. *et al.* Cation distribution in NiZn-ferrite films via extended x-ray absorption fine structure. *ApPhL* **68**, 2082–2084 (1996).
69. Saha, P., Rakshit, R., Alam, M. & Mandal, K. Magnetic and Electronic Properties of Zn - Doped Fe3 O4 Hollow Nanospheres. *Physical Review Applied* **11**, (2019).
70. Mathew, D. S. & Juang, R. S. An overview of the structure and magnetism of spinel ferrite nanoparticles and their synthesis in microemulsions. *Chemical Engineering Journal* **129**, 51–65 (2007).
71. Kittel, C., McEuen, P. & John Wiley & Sons. Introduction to solid state physics.
72. Chikazumi, S. Physics of magnetism. 554 (1964).
73. Shao, H., Huang, Y., Lee, H., Suh, Y. J. & Kim, C. O. Effect of PVP on the morphology of cobalt nanoparticles prepared by thermal decomposition of cobalt acetate. *Current Applied Physics* **Supplement 1**, e195–e197 (2006).
74. Bethe, H. Termaufspaltung in Kristallen. *Annalen der Physik* **395**, 133–208 (1929).
75. Néel, L. Anisotropie magnétique superficielle et surstructures d'orientation. *J. Phys. Radium* **15**, 225–239 (1954).
76. Skomski, R. *Permanent magnetism*. (Institute of Physics Pub., 1999).
77. Osborn, J. A. Demagnetizing Factors of the General Ellipsoid. *Physical Review* **67**, 351 (1945).
78. Sarkar, D. & Mandal, M. Static and Dynamic Magnetic Characterization of DNA-Templated Chain-Like Magnetite Nanoparticles. *Journal of Physical Chemistry C* **116**, 3227–3234 (2012).
79. Gangopadhyay, S. *et al.* Magnetic properties of ultrafine iron particles. *Physical Review B* **45**, 9778 (1992).
80. Parker, F. T. & Berkowitz, A. E. Field response of surface spins on Co-adsorbed γ-<span class. *Physical Review B* **44**, 7437 (1991).
81. Néel, M. L. Propriétés magnétiques des ferrites ; ferrimagnétisme et antiferromagnétisme.

Annales de Physique **12**, 137–198 (1948).
82. Yafet, Y. & Kittel, C. Antiferromagnetic Arrangements in Ferrites. *Physical Review* **87**, 290 (1952).
83. Gang Xiong, * *et al.* Preparation and Magnetic Properties of CoCrFeO4 Nanocrystals. *Chemistry of Materials* **13**, 1943–1945 (2001).
84. Taylor, P. Dekker Encyclopedia of Nanoscience and Nanotechnology , Second Edition Nanoceramics Nanoceramics. 37–41 (2009).
85. Barbeta, V. B., Jardim, R. F., Kiyohara, P. K., Effenberger, F. B. & Rossi, L. M. Magnetic properties of Fe3O4 nanoparticles coated with oleic and dodecanoic acids. *Journal of Applied Physics* **107**, 073913 (2010).
86. Abari, R. *et al.* INTRODUCTION TO MAGNETIC MATERIALS.
87. Néel, L. Théorie du traînage magnétique des ferromagnétiques en grains fins avec application aux terres cuites. *Annales de géophysique* **5**, 99--136 (1949).
88. Stoner, E. C. & Wohlfarth, E. P. A mechanism of magnetic hysteresis in heterogeneous alloys. *Philosophical Transactions of the Royal Society of London. Series A, Mathematical and Physical Sciences* **240**, 599–642 (1948).
89. Tholence, J. L. On the frequency dependence of the transition temperature in spin glasses. *Solid State Communications* **35**, 113–117 (1980).
90. Kong, L. B., Huang, H. & Li, S. Fundamentals of Ferroelectric Materials. (2018).
91. Datt, G. & Abhyankar, A. C. Dopant driven tunability of dielectric relaxation in MxCo(1-x)Fe2O4 (M: Zn2+, Mn2+, Ni2+) nano-ferrites. *Journal of Applied Physics* **122**, 034102 (2017).
92. Ramana, C. v., Kolekar, Y. D., Bharathi, K. K., Sinha, B. & Ghosh, K. Correlation between structural, magnetic, and dielectric properties of manganese substituted cobalt ferrite. *Journal of Applied Physics* **114**, 183907 (2013).
93. Brantley, W., Berzins, D., Iijima, M., Tufekçi, E. & Cai, Z. Structure/property relationships in orthodontic alloys. *Orthodontic Applications of Biomaterials* 3–38 (2017) doi:10.1016/B978-0-08-100383-1.00001-1.
94. Deshmukh, K. *et al.* Dielectric Spectroscopy. *Spectroscopic Methods for Nanomaterials Characterization* **2**, 237–299 (2017).
95. Ozturk, T., Güneşer, M. T. & Tahir Güneşer, M. Measurement Methods and Extraction Techniques to Obtain the Dielectric Properties of Materials Provisional chapter Measurement Methods and Extraction Techniques to Obtain the Dielectric Properties of Materials. (2016) doi:10.5772/intechopen.80276.
96. Jonscher, A. K. Dielectric relaxation in solids. *Journal of Physics D: Applied Physics* **32**, R57 (1999).
97. Rezlescu, N. & Rezlescu, E. Dielectric properties of copper containing ferrites. *physica status solidi (a)* **23**, 575–582 (1974).
98. Tang, R. *et al.* Dielectric relaxation, resonance and scaling behaviors in Sr3Co2Fe24O41 hexaferrite. *Scientific Reports 2015 5:1* **5**, 1–11 (2015).
99. Koops, C. G. On the Dispersion of Resistivity and Dielectric Constant of Some Semiconductors at Audiofrequencies. *Physical Review* **83**, 121 (1951).
100. JONSCHER, A. K. Physical basis of dielectric loss. *Nature 1975 253:5494* **253**, 717–719 (1975).
101. Wang, F. *et al.* Template free synthesis and electromagnetic wave absorption properties of monodispersed hollow magnetite nano-spheres. *Journal of Materials Chemistry* **21**, 4314–4320

(2011).
102. Ding, Y. *et al.* Reduced Graphene Oxide Functionalized with Cobalt Ferrite Nanocomposites for Enhanced Efficient and Lightweight Electromagnetic Wave Absorption. *Scientific Reports 2016 6:1* **6**, 1–9 (2016).
103. Bai, X., Zhai, Y. & Zhang, Y. Green Approach To Prepare Graphene-Based Composites with High Microwave Absorption Capacity. *Journal of Physical Chemistry C* **115**, 11673–11677 (2011).
104. Liu, J. *et al.* Microwave Absorption Enhancement of Multifunctional Composite Microspheres with Spinel Fe3O4 Cores and Anatase TiO2 Shells. *Small* **8**, 1214–1221 (2012).
105. Panigrahi, R. & Srivastava, S. K. Trapping of microwave radiation in hollow polypyrrole microsphere through enhanced internal reflection: A novel approach. *Scientific Reports 2015 5:1* **5**, 1–10 (2015).
106. EtlD, A., Baker-Jarvis Michael Janezic John H Grosvenor, J. D. & Richard Geyer V, J. G. Transmission/Reflection and Short-Circuit Line Methods for Measuring Permittivity and Permeability. (1993).
107. Jun-Zhe He, Xi-Xi Wang, Yan-Lan Zhang & Mao-Sheng Cao. Small magnetic nanoparticles decorating reduced graphene oxides to tune the electromagnetic attenuation capacity. *Journal of Materials Chemistry C* **4**, 7130–7140 (2016).
108. Pozar, D. M. Microwave Engineering, 4th Edition. *John Wiley &Sons, Inc* 1–756 (2012).
109. Vicente, A. N., Dip, G. M. I. & Junqueira, C. The step by step development of NRW method. *SBMO/IEEE MTT-S International Microwave and Optoelectronics Conference Proceedings* 738–742 (2011) doi:10.1109/IMOC.2011.6169318.
110. Vineeta Shukla. Review of electromagnetic interference shielding materials fabricated by iron ingredients. *Nanoscale Advances* **1**, 1640–1671 (2019).
111. Wang, T. *et al.* Reflection loss mechanism of single layer absorber for flake-shaped carbonyl-iron particle composite. *Journal of Applied Physics* **112**, 104903 (2012).
112. Li, X. *et al.* Morphology-controlled synthesis and electromagnetic properties of porous Fe3O4 nanostructures from iron alkoxide precursors. *Journal of Physical Chemistry C* **115**, 12350–12357 (2011).
113. Zhang, J., Shi, C., Ji, T., Wu, G. & Kou, K. Preparation and Microwave Absorbing Characteristics of Multi-Walled Carbon Nanotube/Chiral-Polyaniline Composites. *Open Journal of Polymer Chemistry* **04**, 62–72 (2014).
114. Ali, N. N. *et al.* Design of lightweight broadband microwave absorbers in the X-band based on (polyaniline/MnNiZn ferrite) nanocomposites. *Journal of Magnetism and Magnetic Materials* **453**, 53–61 (2018).
115. Feng, Y. B., Qiu, T. & Shen, C. Y. Absorbing properties and structural design of microwave absorbers based on carbonyl iron and barium ferrite. *Journal of Magnetism and Magnetic Materials* **318**, 8–13 (2007).
116. Wang, Y. *et al.* Hybrid of MoS_2 and Reduced Graphene Oxide: A Lightweight and Broadband Electromagnetic Wave Absorber. *ACS applied materials & interfaces* **7**, 26226–26234 (2015).
117. Mandal, D. & Mandal, K. Enhancement of electromagnetic wave absorption in MnFe2O4 nano-hollow spheres. *Journal of Applied Physics* **129**, 074902 (2021).
118. Rabinow, J. The magnetic fluid clutch. *Electrical Engineering* **67**, 1167–1167 (2013).
119. Klingenberg, D. J. Magnetorheology: Applications and challenges. *AIChE Journal* **47**, 246–

249 (2001).
120. Milecki, A. & Hauke, M. Application of magnetorheological fluid in industrial shock absorbers. *Mechanical Systems and Signal Processing* **28**, 528–541 (2012).
121. Kumbhar, B. K., Patil, S. R. & Sawant, S. M. Synthesis and characterization of magneto-rheological (MR) fluids for MR brake application. *Engineering Science and Technology, an International Journal* **18**, 432–438 (2015).
122. Bucchi, F., Forte, P., Frendo, F. & Squarcini, R. A magnetorheological clutch for efficient automotive auxiliary device actuation. *Pierburg Pump Technology Italy S.p.A., Via S.Orlando* **23**, 57123 (2013).
123. Aly, A. M. Vibration control of buildings using magnetorheological damper: A new control algorithm. *Journal of Engineering (United Kingdom)* **2013**, (2013).
124. Oh, J. S. & Choi, S. B. State of the art of medical devices featuring smart electro-rheological and magneto-rheological fluids. *Journal of King Saud University - Science* **29**, 390–400 (2017).
125. Heine, M. C., Vicente, J. de & Klingenberg, D. J. Thermal transport in sheared electro- and magnetorheological fluids. *Physics of Fluids* **18**, 023301 (2006).
126. Reinecke, B. N., Shan, J. W., Suabedissen, K. K. & Cherkasova, A. S. On the anisotropic thermal conductivity of magnetorheological suspensions. *Journal of Applied Physics* **104**, 023507 (2008).
127. Liu, J., Flores, G. A. & Sheng, R. In-vitro investigation of blood embolization in cancer treatment using magnetorheological fluids. *Journal of Magnetism and Magnetic Materials* **225**, 209–217 (2001).
128. Kordonski, W. & Golini, D. Multiple Application of Magnetorheological Effect in High Precision Finishing: *http://dx.doi.org/10.1106/104538902026104* **13**, 401–404 (2016).
129. Jha, S. & Jain, V. K. Design and development of the magnetorheological abrasive flow finishing (MRAFF) process. *International Journal of Machine Tools and Manufacture* **10**, 1019–1029 (2004).
130. Kordonski, W. I., Shorey, A. B. & Tricard, M. Magnetorheological Jet (MR JetTM) Finishing Technology. *Journal of Fluids Engineering* **128**, 20–26 (2006).
131. Donado, F., Carrillo, J. L. & Mendoza, M. E. Sound propagation in magneto-rheological suspensions. *Journal of Physics: Condensed Matter* **14**, 2153 (2002).
132. Solis, K. J. & Martin, J. E. Isothermal Magnetic Advection: Creating functional fluid flows for heat and mass transfer. *Applied Physics Letters* **97**, 034101 (2010).
133. Read, D. H. & Martin, J. E. Strain-Tunable Chemiresistor. *Analytical Chemistry* **82**, 2150–2154 (2010).
134. Read, D. H. & Martin, J. E. Analyte Discrimination from Chemiresistor Response Kinetics. *Analytical Chemistry* **82**, 6969–6975 (2010).
135. Read, D. H. & Martin, J. E. Field-Structured Chemiresistors. *Advanced Functional Materials* **20**, 1577–1584 (2010).
136. Liu, Y. D., Lee, J., Choi, S. B. & Choi, H. J. Silica-coated carbonyl iron microsphere based magnetorheological fluid and its damping force characteristics. *Smart Materials and Structures* **22**, 065022 (2013).
137. F, F. F., J, C. H. & S, C. W. Two-layer coating with polymer and carbon nanotube on magnetic carbonyl iron particle and its magnetorheology. *Colloid Polym. Sci.* **288**, 359–363 (2010).
138. F, F. F., J, C. H. & Y, S. Sequential coating of magnetic carbonyliron particles with

polystyrene and multiwalled carbon nanotubes and its effect on their magnetorheology. *ACS Appl. Mater. Interfaces* **2**, 54–60 (2010).
139. M, S. *et al.* Rheological properties of magnetorheological suspensions based on core–shell structured polyaniline-coated carbonyl iron particles. *Smart Mater. Struct.* **19**, 115008 (2010).
140. C, M. *et al.* Rheology of aqueous magnetorheological fluid using dual oxide-coated carbonyl iron particles. *J. Am. Ceram. Soc.* **94**, 2386–2392 (2011).
141. D, L. Y., F, F. F. & J, C. H. Core–shell-structured silica-coated magnetic carbonyl iron microbead and its magnetorheology with anti-acidic characteristics. *Colloid Polym. Sci.* **289**, 1295–1298 (2011).
142. B, C. H., L, Z., H, S. J., J, Z. Q. & M, W. N. Magnetorheology and sedimentation behavior of an aqueous suspension of surface modified carbonyl iron particles. *J. Appl. Phys.* **107**, 09b507 (2010).
143. D, L. Y. & J, C. H. Carbon nanotube-coated silicated soft magnetic carbonyl iron microspheres and their magnetorheology. *J. Appl. Phys.* **111**, 07B502 (2012).
144. Vinod, S., John, R. & Philip, J. Magnetorheological properties of sodium sulphonate capped electrolytic iron based MR fluid: A comparison with CI based MR fluid. *Smart Materials and Structures* **26**, (2017).
145. Bossis, G., Khuzir, P., Lacis, S. & Volkova, O. Yield behavior of magnetorheological suspensions. *Journal of Magnetism and Magnetic Materials* **Complete**, 456–458 (2003).
146. Bossis, G., Lemaire, E., Volkova, O. & Clercx, H. Yield stress in magnetorheological and electrorheological fluids: A comparison between microscopic and macroscopic structural models. *Journal of Rheology* **41**, 687 (1998).
147. Klingenberg, D. J. & IV, C. F. Z. Studies on the steady-shear behavior of electrorheological suspensions. *Langmuir* **6**, 15–24 (2002).
148. GINDER, J. M., DAVIS, L. C. & ELIE, L. D. RHEOLOGY OF MAGNETORHEOLOGICAL FLUIDS: MODELS AND MEASUREMENTS. *http://dx.doi.org/10.1142/S0217979296001744* **10**, 3293–3303 (2012).
149. Zimmerman, D. T., Bell, R. C., II, J. A. F., Karli, J. O. & Wereley, N. M. Elastic percolation transition in nanowire-based magnetorheological fluids. *Applied Physics Letters* **95**, 014102 (2009).
150. C, G., J, P., D, C. & B, C. Electrorheological properties and microstructure of silica suspensions. *Journal of colloid and interface science* **273**, 658–667 (2004).
151. Ramos, J., Klingenberg, D. J., Hidalgo-Alvarez, R. & Vicente, J. de. Steady shear magnetorheology of inverse ferrofluids. *Journal of Rheology* **55**, 127 (2010).
152. Felt, D. W., Hagenbuchle, M., Liu, J. & Richard, J. Rheology of a Magnetorheological Fluid: *http://dx.doi.org/10.1177/1045389X9600700522* **7**, 589–593 (2016).
153. Mezger, T. G. European Coatings Tech Files The Rheology Handbook 3 rd Revised Edition. (2011).
154. Bonnecaze, R. T. & Brady, J. F. Yield stresses in electrorheological fluids. *Journal of Rheology* **36**, 73 (1998).
155. Wereley, N. M. *et al.* Bidisperse Magnetorheological Fluids using Fe Particles at Nanometer and Micron Scale: *http://dx.doi.org/10.1177/1045389X06056953* **17**, 393–401 (2016).
156. Lee, D.-Y. & Wereley, N. M. Quasi-Steady Herschel-Bulkley Analysis of Electroand Magneto-Rheological Flow Mode Dampers: *http://dx.doi.org/10.1106/E3LT-LYN6-KMT2-VJJD* **10**,

761–769 (2016).
157. Casson N. *Rheology of Disperse System*. vol. Chapter 5 (London, UK: Pergamon Press, 1959).
158. Rosensweig, R. E. Ferrohydrodynamics. (2013).
159. Furst, E. M. & Gast, A. P. Dynamics and lateral interactions of dipolar chains. *Physical Review E* **62**, 6916 (2000).
160. Mohebi, M., Jamasbi, N. & Liu, J. Simulation of the formation of nonequilibrium structures in magnetorheological fluids subject to an external magnetic field. *Physical Review E* **54**, 5407 (1996).
161. Promislow, J. H. E. & Gast, A. P. Magnetorheological Fluid Structure in a Pulsed Magnetic Field. *Langmuir* **12**, 4095–4102 (1996).
162. Volkova, O., Bossis, G., Guyot, M., Bashtovoi, V. & Reks, A. Magnetorheology of magnetic holes compared to magnetic particles. *Journal of Rheology* **44**, 91 (1999).
163. de Vicente, J., Durán, J. D. G., Delgado, A. v., González-Caballero, F. & Bossis, G. EFFECT OF MAGNETIC HYSTERESIS OF THE SOLID PHASE ON THE RHEOLOGICAL PROPERTIES OF MR FLUIDS. *http://dx.doi.org/10.1142/S0217979202012682* **16**, 2576–2582 (2012).
164. Korshunov, M. M. *et al.* Effects of nonmagnetic interparticle forces on magnetorheological fluids. *Journal of Physics: Conference Series* **149**, 012063 (2009).
165. Zheng, J.-N. *et al.* Redispersibility in magnetorheological fluids: Surface interactions between iron powder and wetting additives. *Journal of Physics: Conference Series* **149**, 012038 (2009).
166. Parthasarathy, M. & Klingenberg, D. J. Large amplitude oscillatory shear of ER suspensions. *Journal of Non-Newtonian Fluid Mechanics* **81**, 83–104 (1999).
167. de Vicente, J., López-López, M. T., Durán, J. D. G. & Bossis, G. A slender-body micromechanical model for viscoelasticity of magnetic colloids: Comparison with preliminary experimental data. *Journal of Colloid and Interface Science* **282**, 193–201 (2005).
168. Hao, T. & Xu, Y. Microstructure-Confined Mechanical and Electric Properties of the Electrorheological Fluids under the Oscillatory Mechanical Field. *Journal of Colloid and Interface Science* **185**, 324–331 (1997).
169. Chin, B. D. & Winter, H. H. Field-induced gelation, yield stress, and fragility of an electro-rheological suspension. *Rheologica Acta 2002 41:3* **41**, 265–275 (2002).
170. Deshmukh, S. S. 1978-. Development, characterization and applications of magnetorheological fluid based "smart" materials on the macro-to-micro scale. (2006).
171. MR Jolly & M Nakano. Actuator 98. in *6th Int Conf. on New Actuators* 411–416 (1998).
172. Olabi, A. G. & Grunwald, A. Design and application of magneto-rheological fluid. *Materials & Design* **28**, 2658–2664 (2007).
173. Wang, X. & Gordaninejad, F. Study of magnetorheological fluids at high shear rates. *Rheologica Acta* **45**, 899–908 (2006).
174. Chen, P., Bai, X. X., Qian, L. J. & Choi, S. B. A magneto-rheological fluid mount featuring squeeze mode: analysis and testing. *Smart Materials and Structures* **25**, 055002 (2016).
175. Zhang, H., Zou, Z. & Choi, S.-B. Modeling of magnetorheological fluid in quasi-static squeeze flow mode. *Smart Materials and Structures* **27**, 065022 (2018).
176. McIntyre, E. C. & Filisko, F. E. Squeeze Flow of Electrorheological Fluids Under Constant Volume: *http://dx.doi.org/10.1177/1045389X07083130* **18**, 1217–1220 (2016).
177. Zhang, X. Z., Gong, X. L., Zhang, P. Q. & Wang, Q. M. Study on the mechanism of the

squeeze-strengthen effect in magnetorheological fluids. *Journal of Applied Physics* **96**, 2359 (2004).
178. de Vicente, J., Klingenberg, D. J. & Hidalgo-Alvarez, R. Magnetorheological fluids: a review. *Soft Matter* **7**, 3701–3710 (2011).
179. Kumar, J. S., Paul, P. S., Raghunathan, G. & Alex, D. G. A review of challenges and solutions in the preparation and use of magnetorheological fluids. *International Journal of Mechanical and Materials Engineering* **14**, 1–18 (2019).
180. Kormann, C., Laun, H. M. & Richter, H. J. MR FLUIDS WITH NANO-SIZED MAGNETIC PARTICLES. *http://dx.doi.org/10.1142/S0217979296001604* **10**, 3167–3172 (2012).
181. Du, C., Chen, W. & Wan, F. Influence of HLB Parameters of Surfactants on Properties of Magneto-Rheological Fluid. *Advanced Materials Research* **97–101**, 843–847 (2010).
182. Dong, X. F. *et al.* Properties of magneto-rheological fluids based on amorphous micro-particles. *Transactions of Nonferrous Metals Society of China* **22**, 2979–2983 (2012).
183. Arief, I. & Mukhopadhyay, P. K. Two-step yielding in novel CoNi nanoplatelet-based magnetic fluids under oscillatory rheology. *Materials Letters* **167**, 192–196 (2016).
184. Kim, J. E. & Choi, H. J. Magnetic carbonyl iron particle dispersed in viscoelastic fluid and its magnetorheological property. *IEEE Transactions on Magnetics* **47**, 3173–3176 (2011).
185. Wahid, S. A., Ismail, I., Aid, S. & Rahim, M. S. A. Magneto-rheological defects and failures: A review. *IOP Conference Series: Materials Science and Engineering* **114**, 012101 (2016).
186. Jang, I. B. *et al.* Role of organic coating on carbonyl iron suspended particles in magnetorheological fluids. *Journal of Applied Physics* **97**, 10Q912 (2005).
187. Liu, Y. D., Hong, C. H. & Choi, H. J. Polymeric colloidal magnetic composite microspheres and their magneto-responsive characteristics. *Macromolecular Research 2012 20:12* **20**, 1211–1218 (2013).
188. Fang, F. F., Yang, M. S. & Choi, H. J. Novel magnetic composite particles of carbonyl iron embedded in polystyrene and their magnetorheological characteristics. *IEEE Transactions on Magnetics* **44**, 4533–4536 (2008).
189. Hajalilou, A., Kianvash, A., Shameli, K. & Lavvafi, H. Carbonyl iron based magnetorheological effects with silver nanoparticles via green-assisted coating. *Applied Physics Letters* **110**, 261902 (2017).
190. Rabbani, Y., Ashtiani, M. & Hashemabadi, S. H. An experimental study on the effects of temperature and magnetic field strength on the magnetorheological fluid stability and MR effect. *Soft Matter* **11**, 4453–4460 (2015).
191. Wang, G. *et al.* Synthesis of calcium ferrite nanocrystal clusters for magnetorheological fluid with enhanced sedimentation stability. *Powder Technology* **322**, 47–53 (2017).
192. Anupama, A. v., Kumaran, V. & Sahoo, B. Steady-shear magnetorheological response of fluids containing solution-combustion-synthesized Ni-Zn ferrite powder. *Advanced Powder Technology* **29**, 2188–2193 (2018).
193. Jang, I. B. *et al.* Role of organic coating on carbonyl iron suspended particles in magnetorheological fluids. *Journal of Applied Physics* **97**, 10Q912 (2005).
194. Zhu, W., Dong, X., Huang, H. & Qi, M. Iron nanoparticles-based magnetorheological fluids: A balance between MR effect and sedimentation stability. *Journal of Magnetism and Magnetic Materials* **491**, 165556 (2019).
195. Jiang, W., Zhang, Y., Xuan, S., Guo, C. & Gong, X. Dimorphic magnetorheological fluid with improved rheological properties. *Journal of Magnetism and Magnetic Materials* **323**, 3246–

3250 (2011).
196. Anupama, A. v., Khopkar, V. B., Kumaran, V. & Sahoo, B. Magnetic field dependent steady-state shear response of Fe 3 O 4 micro-octahedron based magnetorheological fluids. *Physical Chemistry Chemical Physics* **20**, 20247–20256 (2018).

Chapter 2 Experimental Details

This chapter describes solvothermal synthesis technique of 3d transition metal oxide-based magnetic nanostructures along with the preparation method of these materials based magnetorheological fluids. Various techniques to characterize their physical, magnetic, dielectric, microwave absorption and magnetorheological properties are also presented herein.

2. Material Synthesis and Characterization Techniques

2.1. Preamble

In this chapter, a brief overview of the solvothermal method to synthesize various 3d transition metal oxide-based magnetic nanostructures (NSs) along with the procedure of preparing these magnetic NSs based magnetorheological (MR) fluids are described. The characterization techniques employed to investigate the physical, optical, magnetic, dielectric and electromagnetic (EM) properties are presented here. In addition, the magnetorheological, dielectric and thermal conduction properties of the MR fluids are depicted.

The phase and morphological characterization of as-synthesized NSs are performed using X-ray Diffraction (XRD), Field Emission Scanning Electron Microscope (FESEM), Transmission Electron Microscope (TEM), High-Resolution Transmission Electron Microscope (HRTEM), Selected Area Electron Diffraction (SAED). The surface topography and nanoscale electrical properties of magnetic nanomaterials (NMs) are characterized by Atomic Force Microscopy (AFM) and Conductive Atomic Force Microscopy (C-AFM). Spectroscopic analysis is carried out through Fourier Transformed Infrared (FTIR) Spectrometer. The magnetic characterizations are studied employing Vibrating Sample Magnetometer (VSM) and Superconducting Quantum Interference Device (SQUID). Impedance analyzer and LCR meter are used to carry out the dielectric properties of the magnetic NSs and the MR fluids. For the EM characterization and microwave absorption of the magnetic NSs a Vector Network Analyzer (VNA) is incorporated. The MR properties of the MR fluids are studied in a parallel plate magneto-rheometer MCR-301, whereas the thermal conduction properties of these MR fluids are analyzed in a laboratory made setup.

2.2. Synthesis of Nanostructures

Numerous techniques for the fabrication of different nanostructured materials can be categorized into two categories, (1) top-down (i.e. bulk to nano) and (2) bottom-up (i.e. atom to nano) approaches.

2.2.1.Top-Down Approach

The top-down approach represents the consecutive cutting of bulk material to obtain nanomaterials. Milling is a distinctive top-down technique of producing nanoparticles (NPs). However, the drawback of milling is the imperfection of surface structure and substantial crystallographic defect which leads to additional challenges in device designing and fabrication. The advantage of this approach is bulk production of NMs. Numerous types of lithographic techniques (e.g., photo-, ion beam-, electron- or X-ray- lithography) are also instances of top-down approaches which can overcome all the inadequacies of milling, however are still restricted by the resolution of the tools, restricting the smallest size of the NSs. Nowadays, lithography methods are greatly used for the miniaturization of electronic devices and components, such as computer chips, MEMS (micro-electromechanical systems), computer hard drives, and CD and DVD players. Nonetheless, their uses are only limited to commercial fields, due to high cost of the device and clean room environment, special arrangement to reduce the tremendous heat dissipation for smaller geometry, and wastage of materials.

2.2.2. Bottom-Up Approach

The bottom-up approach denotes the building up of material from the bottom: atom by atom, molecule by molecule or cluster by cluster. The ability to assemble nanoscale functional building blocks is a useful and flexible way for material scientists to design materials with explicit physical and chemical properties[1]. Wet chemical synthesis, self-assembly, molecular fabrication, and electrodeposition are examples of bottom-up techniques. It is an easier and more economical method and allows forming NMs of smaller geometry compared to lithography. However, there are some challenges in fabricating complex, robust NMs incorporating bottom-up techniques. An outline of synthesizing various 3d transition metal oxide-based magnetic NSs using bottom-up approach is described in detail Section 2.3.

Both the to-down and the bottom-up approaches are shown schematically in Figure 2.1.

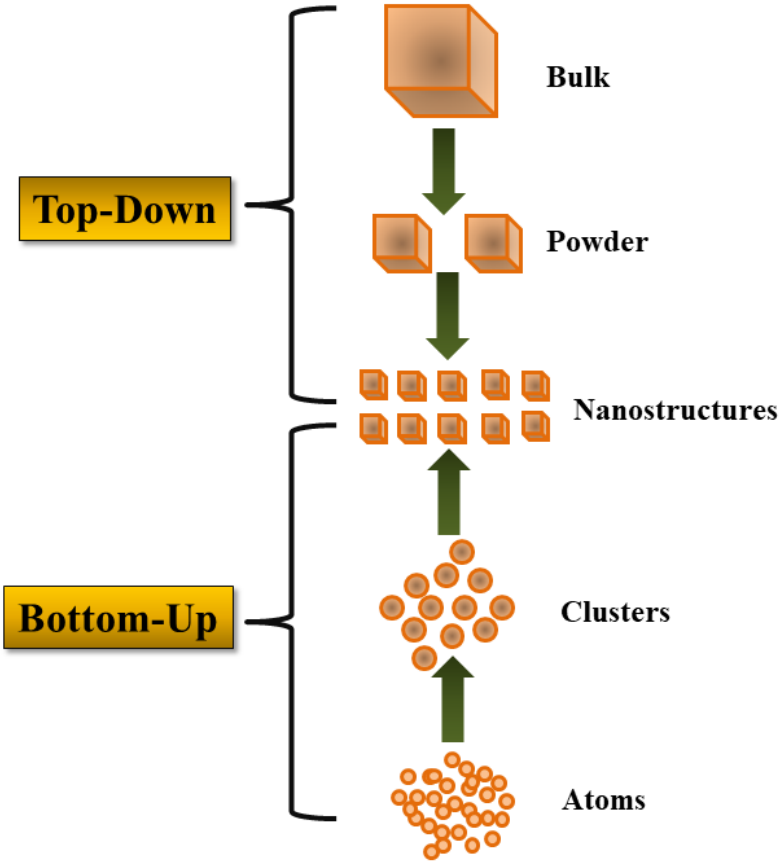

Figure 2.1: Schematic diagram of top-down and bottom-up approaches.

2.3. Fabrication Techniques of Different Nanostructures

2.3.1. Wet Chemical Method

The wet chemical method denotes a specific group of approaches where nano- or ultra- dispersed inorganic materials are prepared in aqueous or non-aqueous solutions. It is different from the conventional solid-state process in reference to that it can only be done in a liquid phase. In this method much smaller can be prepared with monodispersed grains or crystallites, at lower temperatures and have shorter phase formation duration. It is a "bottom-up" method to synthesize NMs by chemical reduction of metal salts, electrochemical trails or through controlled decomposition of various metastable organometallic complexes.

2.3.1.1. Solvothermal Method

Solvothermal technique is a method for fabrication of NSs of various metals,

semiconductors, ceramics, and also polymers from aqueous or non-aqueous medium by controlling temperature, pressure, capping agent, chemical composition, and reaction time. This process incorporates various polar (such as water, ethanol) or non-polar solvents (such as Ethylene Glycol, Benzene, Ethylene di-amine) under high pressure and temperature (above the boiling point of the solvents) to enable the interaction of precursor molecules during the synthesis.

Solvothermal reaction involves the use of a sealed reaction vessel. It helps to develop an autogenous pressure[2]. The pressure within the sealed reaction container not only depends on the reaction temperature but also varies with other experimental parameters, e.g., dissolved salts, capping agents and the percentage fill of the vessel. When the solvent is water, this technique is called hydrothermal method. Various fundamental properties of solvents are significantly affected by reaction pressure and temperature. For example, the viscosity of water reduces with an increase in temperature, e.g., at 500 °C and 10 bar, viscosity of water is 10% of its magnitude under ambient conditions[3]. Similarly, the dielectric constants of solvents also reduce considerably above the critical pressure and temperature; it has key consequences on the solubility of solid reagents under reaction conditions[2]. In this method, precursors are dissolved in the solvent by magnetic stirring or sonication. Thereafter this homogeneous mixture is shifted to a stainless steel teflon-lined autoclave chamber, as shown in Figure 2.2.

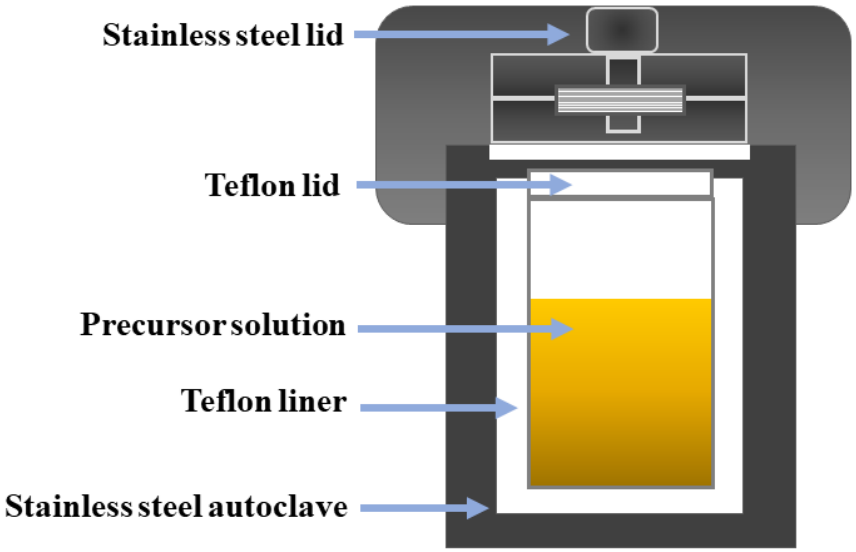

Figure 2.2: Schematic diagram of a stainless steel autoclave with a teflon-lined chamber for solvothermal synthesis.

A proper amount of the precursor solution is poured into the chamber to fill 70% of the total volume. The sealed autoclave is thereafter heated in an oven to a certain temperature. Various NSs such as particles, wires, rods, hollow spheres, spindles, cubes etc. can be synthesized in this method. The beneficial features of the solvothermal method are the formation of homogeneous materials of compound mixed metal solids, the isolation of metastable phases, which is undoable at high temperature, and the controlled crystal formation, which make the technique specifically attractive.

The MFe_2O_4 (M=Fe, Zn, and Mg) nano-hollow spheres (NHSs) and NPs are synthesized by template-free solvothermal method which involves high temperature (~200 ^{0}C) heating of metal ion salts (only Iron(III) chloride, $FeCl_3$, $6H_2O$ in case of Fe_3O_4 and addition of Magnesium (II) chloride, $MgCl_2$, $6H_2O$/Zinc (II) chloride, $ZnCl_2$ in case of $Mg_xFe_{3-x}O_4$, and $Zn_xFe_{3-x}O_4$ NHSs respectively) in a polar solvent, ethanol and non-polar solvent, ethylene glycol, for 20 h in presence of capping agents in a stainless steel teflon-lined autoclave. A brief discussion of the synthesis and growth mechanism of NHSs and NPs has been described in *Chapter 5* of this thesis. The formation of MFe_2O_4 (M=Fe) NPs is achieved by modulating the reaction time and amount of capping agent.

2.5. Fabrication of Samples for Different Measurements

As synthesized samples are given necessary shapes and forms for various measurements. Sample preparation techniques for different measurements are described in the corresponding instrumentation section. The preparation technique of magnetorheological fluid is described below.

2.5.1. Preparation of Magnetorheological Fluid

The main constituents of MR suspension are the magnetic particles, base fluids and stabilizer additives. MR fluids are prepared in a very simple method by mixing all of these constituents. The base fluid behaves like a carrier in which the magnetic particles are suspended. Magnetic particles play a key role in MR fluids. These particles sediment fast in the carriers fluids due to the density mismatch between the magnetic particles and base fluids. The stabilizer additives are added in the MR fluids to overcome the sedimentation of the magnetic particles. A simple and efficient MR fluid can be obtained by dispersing the

magnetic particles in silicon oil, with stearic acid as the stabilizer[4]. The magnetic particles are dispersed in the base fluids with mechanical stirring followed by sonication until uniformity is achieved. We have prepared Fe_3O_4 NSs and $Zn_{0.2}Fe_{2.8}O_4$ NHSs based MR fluids by dispersing them in silicon oil, without adding any stabilizer additives, shown in Figure 2.2. A brief discussion of the stability of these MR fluids has been described in *Chapter 5* of the thesis.

Figure 2.2: MR fluid prepared by dispersing Fe_3O_4 NHSs in silicon oil.

2.6. Phase and Morphology Characterization Techniques

2.6.1. X-Ray Diffractometer (XRD)

XRD is a non-destructive technique used in material science to determine the crystallographic structure of micro and NSs, thin films, and bulk samples. XRD works by diffraction of incident X-rays by atomic planes of the material in different explicit directions depending on the alignments. A 3-dimensional impression of the density of electrons within the specified crystal can be attained by measuring the angle and intensity of the diffracted beams. The mean location of the atoms in the crystalline material can be obtained as shown in Figure 2.3.

As shown in Figure 2.4, in XRD, a monochromatic beam of X-rays falls on a material. The incident X-rays produce a constructive interference that satisfies Bragg's law[5] and scatters elastically by the electrons within the crystal planes. The scattered waves interfere constructively following Equation 2.1:

$$2d \sin\theta = n\lambda \tag{2.1}$$

where d is the crystal plane spacing, θ is the diffraction angle, n is an integer, and λ is the wavelength of incident light. Using a detector, the angle and the intensity of the diffracted beams are processed and recorded electronically, resulting in an intensity vs. 2θ plot for crystalline material.

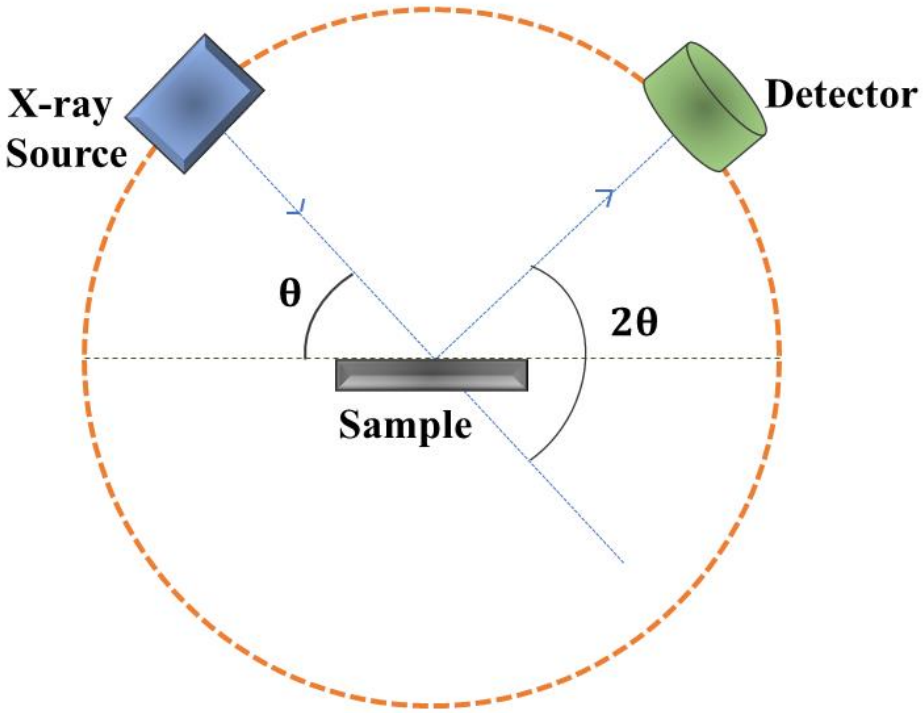

Figure 2.3: Schematic of X-ray diffractometer.

The grain size (D) of the sample can be calculated by using Debye-Scherrer Equation 2.2:

$$D = \frac{0.9\lambda}{\beta \cos\theta} \tag{2.2}$$

where β is the full width at the half maximum of the diffraction peak at a diffraction angle of 2θ. The XRD patterns of our samples were obtained by applying a scanning rate of 0.02° s^{-1} in the 2θ range from 20° to 80° by Rigaku miniflex II diffractometer equipped with Cu K_α (λ~1.54 Å) radiation (at 40 mA and 40 kV).

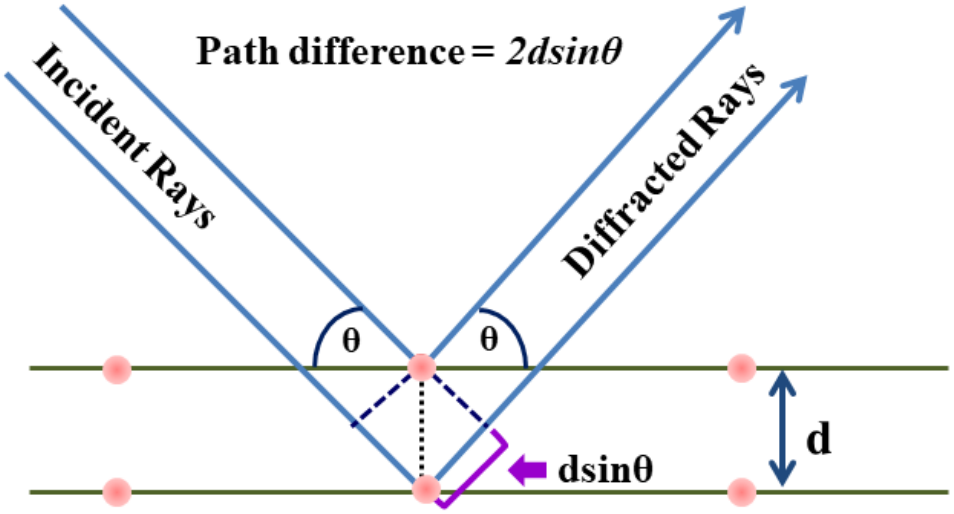

Figure 2.4: Schematic of X-ray diffraction by the crystal lattice.

2.6.2. Electron Microscopes

The type of microscope that uses a highly energetic electrons beam to illuminate a specimen and produces its magnified image is called an electron microscope. We have used two kinds of electron microscopes to investigate the as-synthesized samples as described below.

2.6.2.1. Scanning Electron Microscope (SEM)

In SEM, a tiny electron beam is focused onto the sample, formed either thermionically or by field emission[6]. While passing through a selected area of the sample under characterization, the electrons beam scan the sample and the corresponding generated signals are recorded, thus forming an image pixel by pixel, as shown in Figure 2.5.

SEM works within the voltage range of 2 to 50 kV. From SEM micrographs valuable information about morphology, composition and surface topology of the sample can be obtained. The interactions responsible for a multitude of signal types are back scattered electrons (BSEs), secondary electrons (SEs), X-rays, Auger electrons, and cathodoluminescence. Up on the interaction of incident electrons beam with the electric field of sample's electrons, inelastic events occur, resulting in transfer of energy leading to

potential expulsion of an electron from that atom as SEs. The energy of SEs is less than 50 eV. When an electron from a higher level orbital fills the vacancy created due to the formation of SE, the characteristic X-ray of that energy transition is produced. On the other hand, elastic events take place when an electron beam interacts with the electric field of the nucleus of a sample atom, resulting in change of direction of electrons without changing energy of the electron significantly (< 1eV). The backward deflected elastically scattered electrons are called BSEs, having energy between 50 eV to the energy of incident beam. The image displayed in SEM is a mapping of varying intensity of the signal produced by SEs in a position corresponding to the precise position of the beam on the sample. The characteristic X-rays are used for elemental analysis of the specimen, this method is known as EDX, as shown in Figure 2.6. Morphology of our samples was characterized by FESEM (FEI QUANTA FEG-250) operating at 5-10 keV.

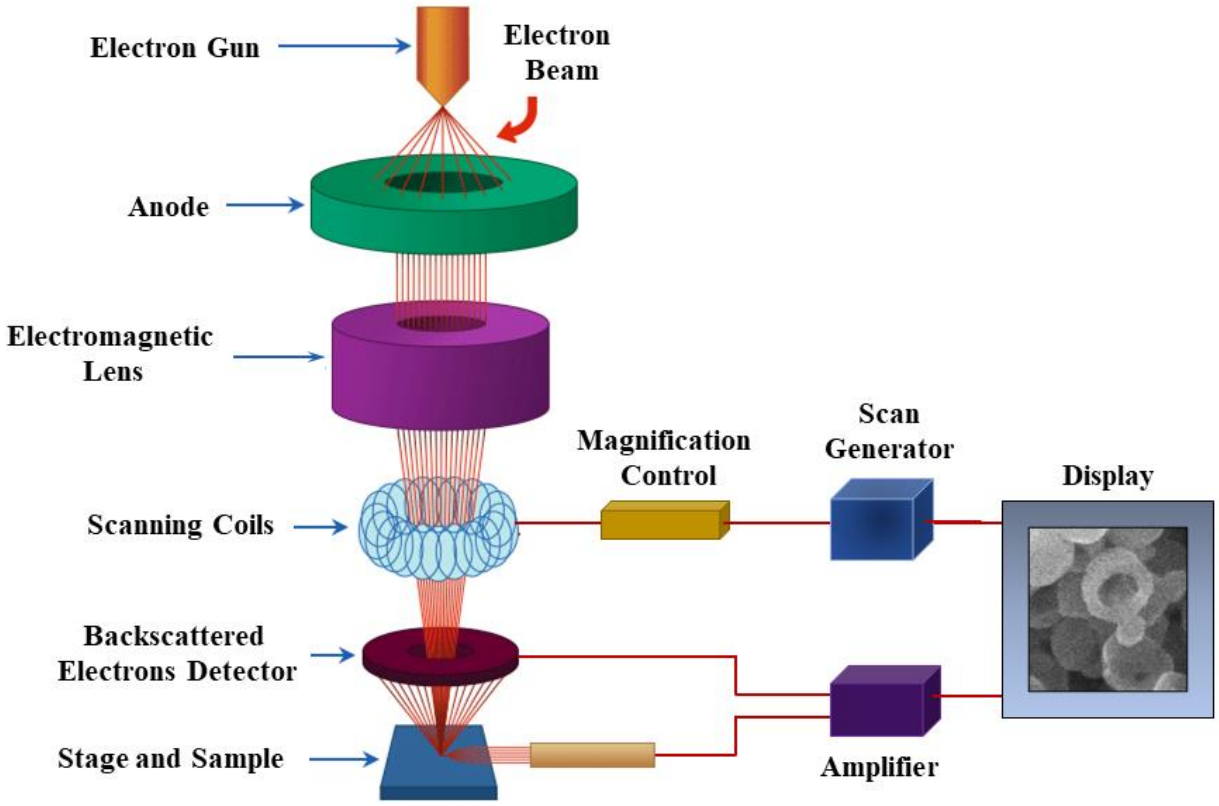

Figure 2.5: Schematic diagram of a scanning electron microscope. An SEM micrograph of Fe_3O_4 NHSs is shown in the display.

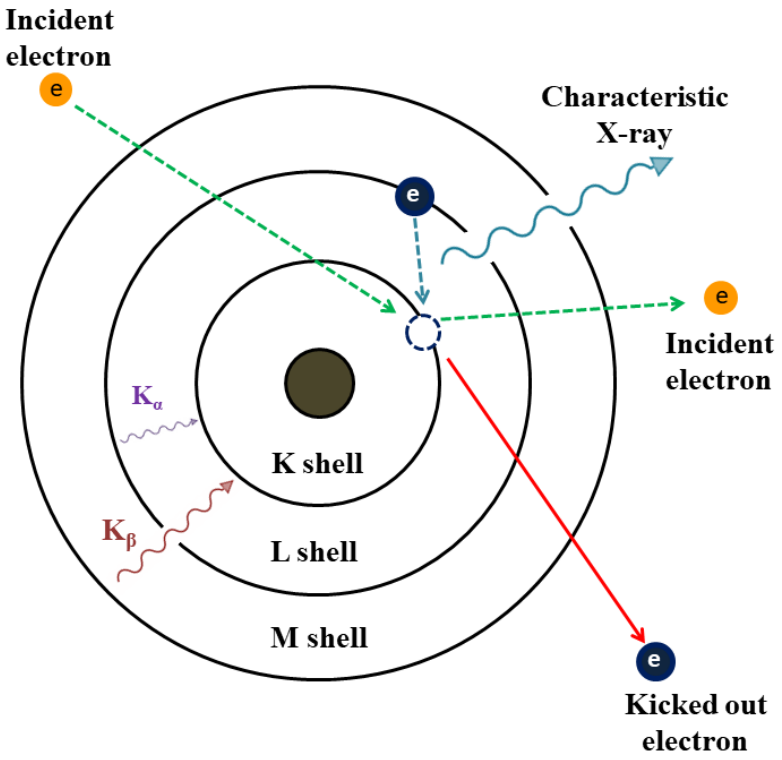

Figure 2.6: Schematic diagram of EDX principle.

2.6.2.2. Transmission Electron Microscope (TEM)

In TEM, primarily two different types of interactions are considered between the electron beam and specimen to construct an image; such as unscattered electrons (transmitted beam) and elastically scattered electrons (diffracted beam). Figure 2.7 shows the schematic diagram of a TEM. In this procedure, incident electrons are transmitted through the thin sample without causing any interaction within the material. The transmission of unscattered electrons is inversely proportional to the thickness of the sample. TEM works in bright field imaging mode, where the thick areas of the sample will have less transmitted unscattered electrons and so will appear darker; conversely, the thinner areas will have more transmitted and thus will appear lighter. This mode of operation to create contrast in image is called bright-field imaging mode.

Electron diffraction is another important mode of TEM imaging. Electron beam undergoes Bragg scattering for a crystalline specimen, in accordance with Bragg's law as expressed by equation 2.1. The incident electrons having the same energy, hence the same wavelength, enter the sample perpendicularly to the surface. The electron beams that are

scattered from the same set of parallel planes can be gathered using a magnetic lens to form a pattern of spots. Each of these spots corresponds to a specific crystalline plane or atomic spacing. This pattern can produce information about the phase, orientation, and atomic arrangements of the area under observation.

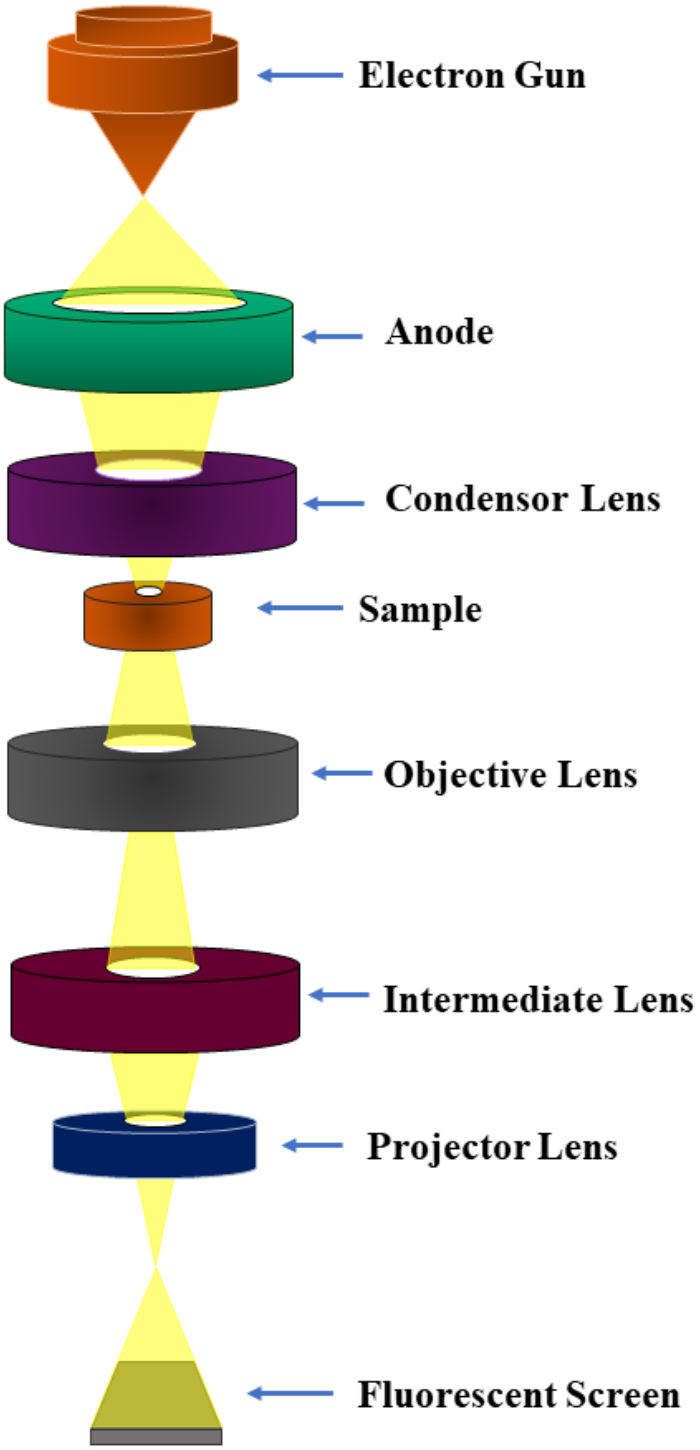

Figure 2.7: Schematic diagram of TEM.

A resolution of around 0.2 nm can be achieved in HRTEM, which is efficient for analyzing the lattice fringes of the specimen under consideration. The occurrence of transmitted electrons, elastic and inelastically scattered (energy loss) electrons, SEs, BSEs, Auger electrons and X-ray photons are originated due to the transmission of electron beams through the thin section of the specimen. TEM-based elemental analysis techniques use X-ray photons in EDX and the "energy loss" electrons or the inelastically scattered electrons in electron energy loss spectroscopy (EELS), and energy-filtered TEM (EFTEM).

For TEM analysis we prepared the samples by preparing a homogeneous mixture of NSs in ethanol, water or hexane and drop-casting it on a 300-mesh carbon-coated copper grid. The sample is air-dried overnight before the TEM measurements. Particle size was measured from TEM micrographs and elemental analysis was carried out from EDX spectrum recorded by an FEI Tecnai TF-20 field emission high-resolution TEM operating at 200 keV.

2.6.3. Atomic and Conductive Atomic Force Microscope (AFM & C-AFM)

Atomic force microscope (AFM) is a high-resolution imaging technique by exploiting the forces due to individual atoms, shown schematically in Figure 2.8. In AFM the sample surface is scanned using a silicon or silicon nitride cantilever with a sharp tip, which has a typical radius of the order of nanometer. When the cantilever tip is brought into the proximity of the sample surface, the force between the sample and the tip leads to tip defection following Hook's law[7]. The forces that are involved in AFM involve contact force, Van der Waals force, capillary force, chemical bonding, electrostatic force, magnetic force, Casimir force, solvation force etc.

There are two different modes, in which the force between the sample surface and the probe can be analyzed, in AFM, i) contact mode and ii) tapping mode. In contact mode, the tip is directly in contact with the specimen surface and the dominating interaction force in this mode is Van der Waals interaction. The tapping mode, on the other hand, is a non-contact mode. The cantilever is oscillated by a mechanical oscillator in this mode, and the interaction between the tip and specimen surface changes the oscillation amplitude or phase relative to the drive signal.

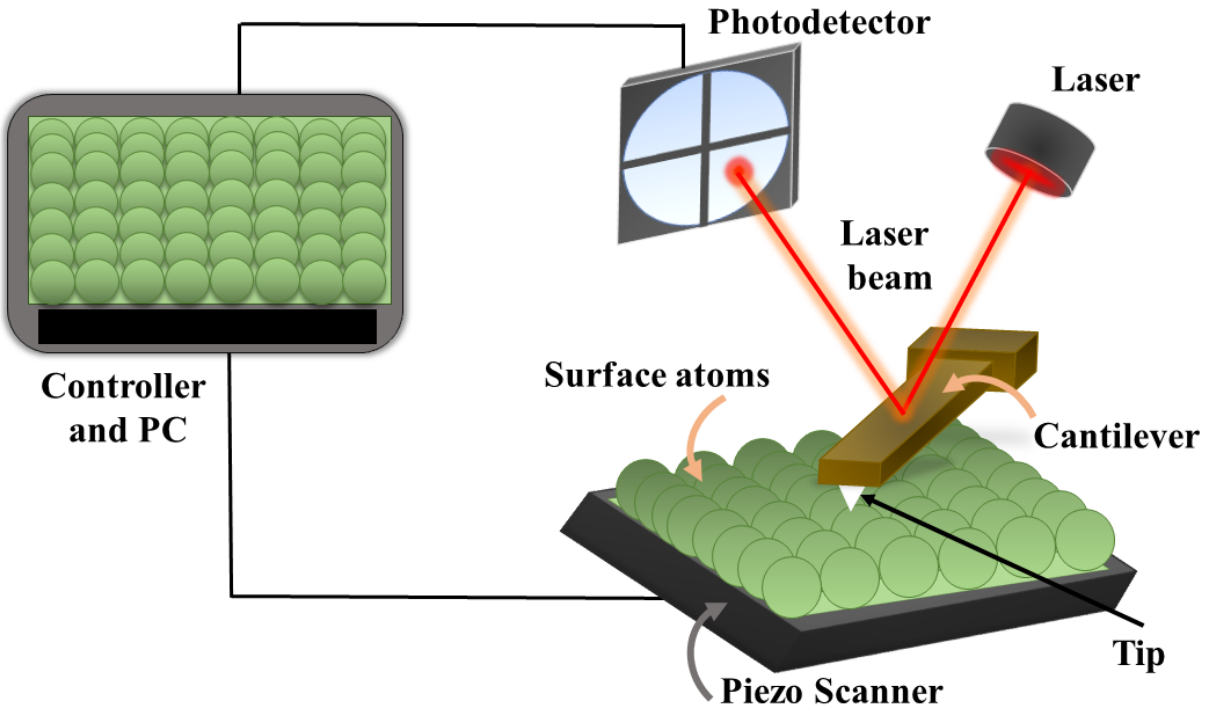

Figure 2.8: Schematic of AFM.

Conductive atomic force microscope (C-AFM) is another mode of AFM in which the specimen surface is scanned with a conductive tip. During C-AFM measurements a voltage is applied between the tip and the sample, generating a current profile. Among various kinds of C-AFM tips, conductive diamond-coated silicon is used typically. In C-AFM both the current and topographical images are taken from the same area of the sample. The tip can be moved to any desired location after acquiring the topographical image and the local current-voltage (I-V) curves can be obtained with various applied bias. From the C-AFM measurements of polycrystalline materials, the conductivity of the grain and grain boundary regions can be obtained. Due to the high spatial resolution of C-AFM over standard electrical measurements techniques, the conducting paths can be identified from C-AFM current profile. For the C-AFM measurements, the powdered samples are palettized and contact is made on one surface of the thin palette with conductive silver paste and Cu wire. Figure 2.9 shows AFM and C-AFM micrographs of Fe_3O_4 NHSs with an average diameter of 350 nm. A Bruker (di INNOVA) atomic force microscope is used for the AFM and C-AFM analysis of our samples.

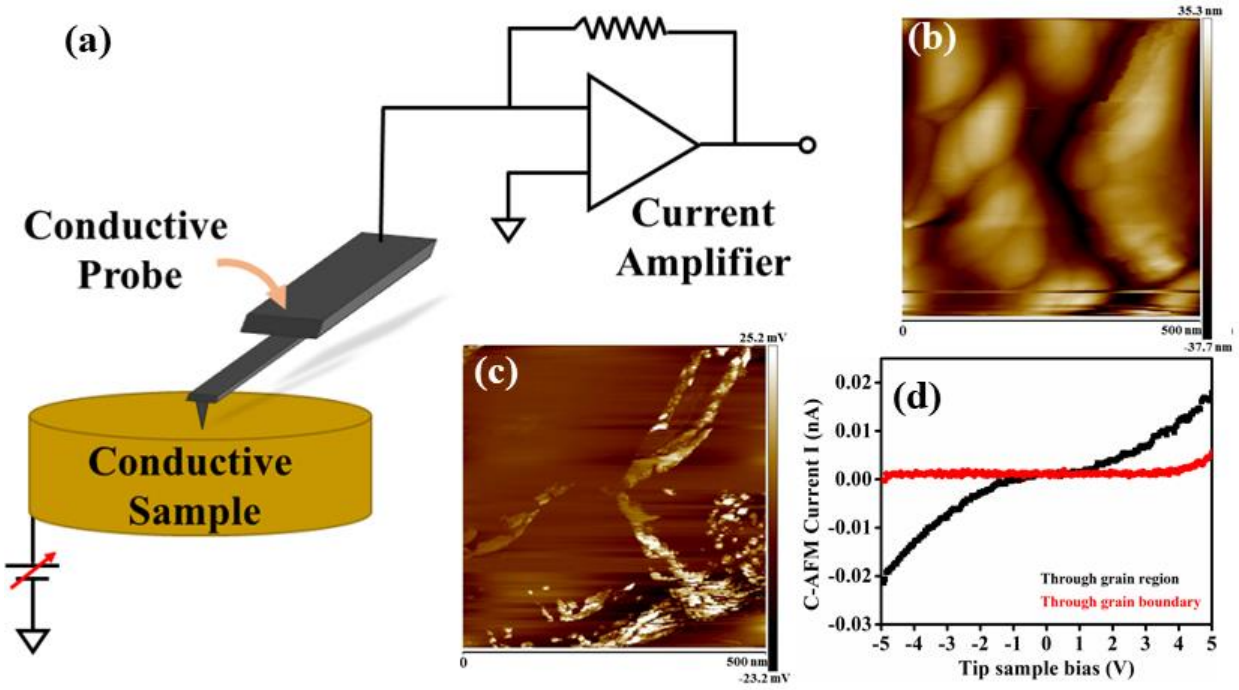

Figure 2.9: (a) Schematic of C-AFM conductive tip scan over conductive surface to study the current profile. (b) AFM and (d) C-AFM micrographs of Fe_3O_4 NHSs with the local nanoscale current voltage profile.

2.7. Optical Characterization Techniques

2.7.1. Fourier Transform infrared (FTIR) Spectroscopy

FTIR is called a molecular fingerprint. It is a powerful tool to identify the functional groups and chemical bonds within a molecule[8]. FTIR signal is obtained when the frequency of vibration of polar molecules matches the incident IR frequency. Figure 2.10. shows the schematic of the FTIR spectrometer.

The two main components of the IR spectrometer are the source and detector. The most common source of FTIR is the Nernst glower, consisting of a rod of a sintered mixture of Zirconium, Ytterbium and Erbium oxides. This rod is electrically heated to 1773 K to produce IR radiations. Sodium chloride or other alkali halides make the best cell container for FTIR, as they are transparent in the IR r egion. The collimated IR beam is partially reflected by and transmitted through the beam splitter, which is a half-silvered mirror, and it moves to the stationary and moving mirrors respectively, as shown in Figure 2.8. The reflected beam from the stationary mirror and transmitted beam from the moving

mirror interfere at the back side of the beam splitter. Depending on the wavelength of the light and the path difference introduced by the moving mirror constructive or destructive interference may take place giving rise to a resulting signal called an interferogram. Finally, the Fourier transform of this interferogram is performed to have a plot of intensity at each frequency (frequency spectrum). A JASCO FTIR-6300 spectrometer is used to perform the FTIR analysis. For the FTIR study of our materials, the powdered samples are mixed with KBr and made in a form of a pallet. For background correction, pure KBr pallet is used before each measurement.

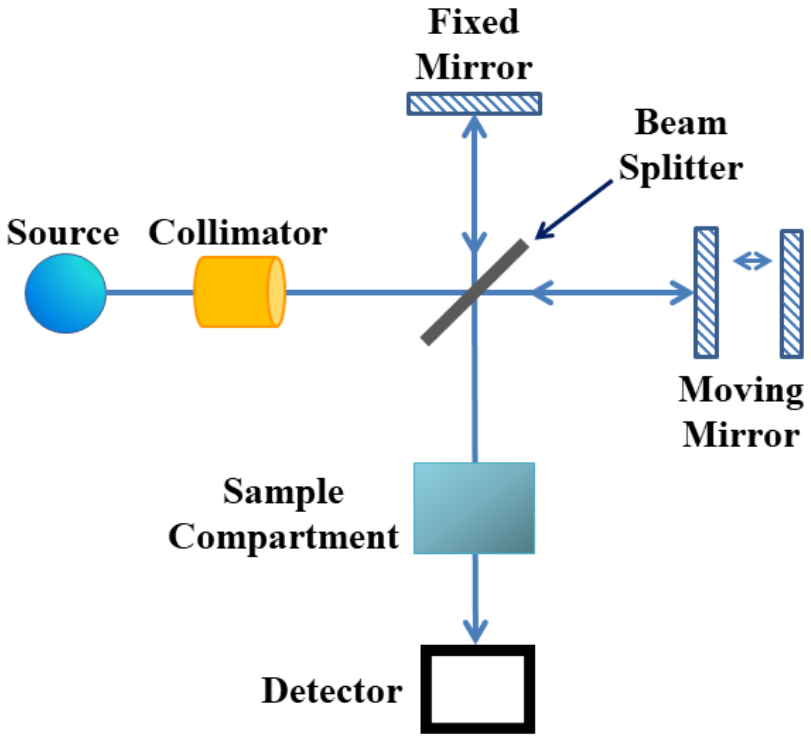

Figure 2.10: Schematic of FTIR spectrometer.

2.8. Magnetic Characterization Techniques

2.8.1. Vibrating Sample Magnetometer (VSM)

A vibrating sample magnetometer (VSM) works on Faraday's law of induction, which suggests that upon changing the magnetic field an electric field will produce. In VSM a magnetic sample is vibrated sinusoidally by placing it in a direct current (DC) magnetic field (H), which introduce a voltage in the pickup coil due to the variation of magnetic flux (B). According to Faraday's law of EM induction, the induced voltage V in the pickup coil

with N number of turns and with a cross-sectional area A can be expressed as

$$V = -NA\frac{dB}{dt} \tag{2.3}$$

where, $B = \mu_0 H$ (μ_0 is the permeability of vacuum)

If a sample with magnetization M is placed in the pickup coil, the total magnetic induction can be written as

$$B = \mu_0(H + M) \tag{2.4}$$

Therefore $\nabla B = \mu_0 M$ is the change in flux due to magnetic sample insertion. Thus equation 2.3 can be written as

$$Vdt = -\mu_0 NAM \tag{2.5}$$

The intensity of the signal is same as that of the magnetic moment of the sample, where the frequency is the sinusoidal motion at which the sample is vibrating. The schematic diagram of a VSM along with the sample holder and detection method is shown in Figure 2.11. A Lake Shore-7144 VSM equipped with an electromagnet, capable of generating a field of up to 1.6 T at 300 K is used for the magnetic study of our samples.

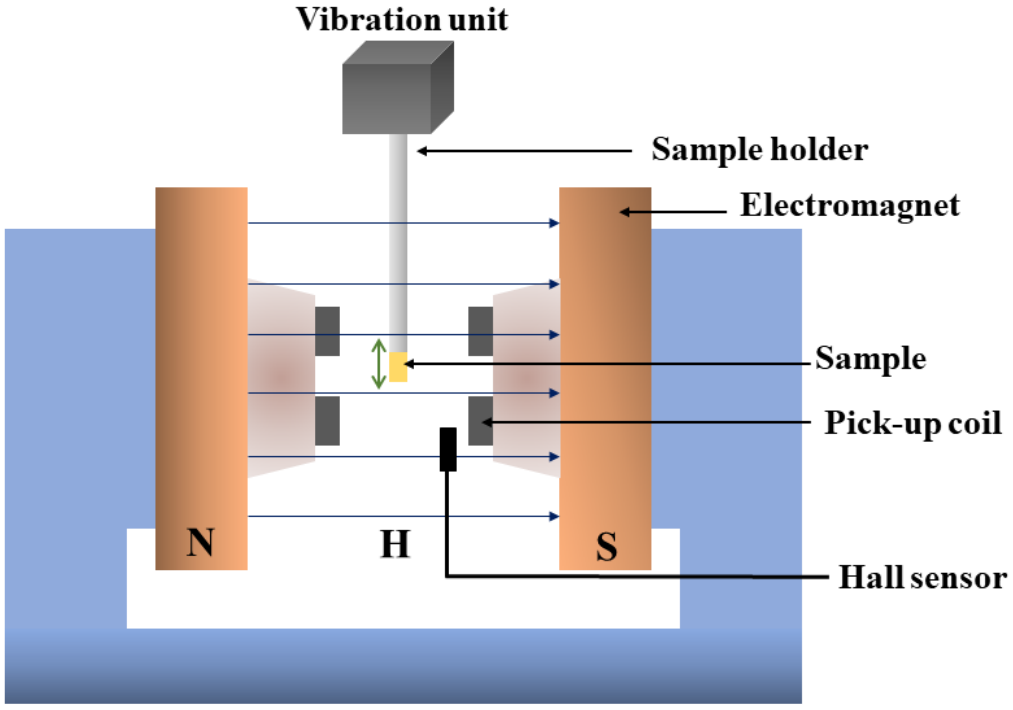

Figure 2.11: Schematic diagram of VSM.

2.8.2. Superconducting Quantum Interference Device (SQUID)

SQUID is the most effective and sensitive device that has been designed to date to detect incredibly small magnetic fields and moments, small enough to measure the magnetic field of living organisms. As shown in Figure 2.12, SQUID consists of two superconductors separated by a thin insulating layer, to form two parallel Josephson junctions, so that the cooper pairs can easily tunnel through the insulating junction.

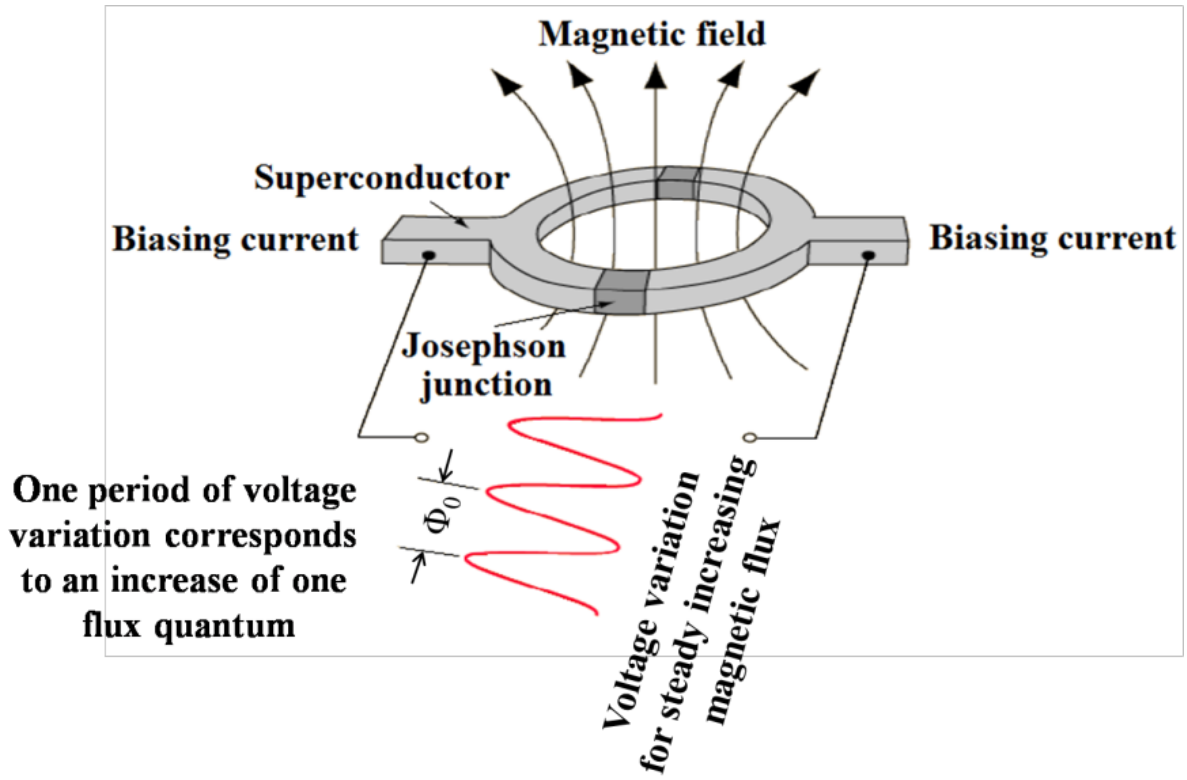

Figure 2.12: Schematic of SQUID.

The sensitivity of SQUID is associated with measuring changes in magnetic field associated with one flux quantum (Φ_0). In the absence of any external magnetic field, the biasing current 'I' splits into two branches equally. If a small external magnetic field is applied to the superconducting loop, a screening current, 'I_S', will generate in the superconductors to cancel the externally applied field, as superconductor excludes magnetic flux. In one of the branches of the superconducting loop, the induced current is in the same direction as 'I', and is opposite to 'I' in the other branch. A voltage appears across

the junction when the current in either branch overdoes the critical current, I_C, of the Josephson junction. Under the consideration that the external flux is amplified until it exceeds half the magnetic flux quantum, $\Phi_0/2$. Since the flux enclosed by the superconducting loop must be an integral number of flux quanta, instead of screening the flux, SQUID now energetically prefers to upsurge it to Φ_0 and I_S flows in the opposite direction. As a result, I_S changes direction every time the flux increases by half-integer multiples of Φ_0. SQUID detects the change in this current to measure the magnetic moment of the sample[9].

2.9. Dielectric Characterization Technique

2.9.1. Impedance Analyzer and LCR Meter

For higher accuracy and simplicity of measurement techniques LCR meter and impedance analyzer are used in low-frequency range, whereas for high-frequency range beyond 1GHz a vector network analyzer is employed for dielectric property analysis of our materials. We have used an NF corporation LCR meter (ZM2376) operating in the frequency range of 1mHz-5.5MHz, and an Agilent 4249A impedance analyzer within a frequency range 40 Hz-110 MHz. A schematic of the LCR meter is shown in Figure 2.13. In LCR meter the voltage (V) and current (I) across the material under test are measured, and subsequently, the impedance (Z) is analyzed. LCR meter can measure the inductance (L), capacitance (C), resistance (R), dissipation factor (d), quality factor, current, voltage, phase angle (θ) between the current and voltage, conductance, susceptance. Impedance of a material is the opposition to the flow of current through the material. Z is a vector quantity composed of resistance (R or Z') and reactance (X or Z''). X represents the opposition of the sample under test to the alternating (ac) current composed of capacitance and inductance components. Both in case of LCR meter and impedance analyzer the experimental sample is subjected to an ac voltage. These instruments work on auto-balancing bridge method, depending on the impedance, test frequency, connections, accuracy etc.

An LCR meter can measure impedance at spot frequencies or in a wide range of frequencies and the capacitance, inductance and resistance of the material can be calculated separately. We have studied the variation of $|Z|$ and θ with the applied electric field

frequency and calculated the dielectric properties of the sample specimen by analyzing Z′, Z″, real and imaginary parts of dielectric permittivity (ε′ and ε″ respectively), dielectric loss (tanδ) and ac conductivity (σ_{ac})[10]. The experimental set-up of impedance analyzer instrument developed in our laboratory is shown in Figure 2.13. Several parameters influence the dielectric response of a material, such as temperature, humidity, magnetic field. Temperature dependence of dielectric property is analyzed in detail in *chapter 3* and *chapter 4*. The effect of magnetic field on the dielectric response of magnetic fluids is explained in detail in *chapter 7*.

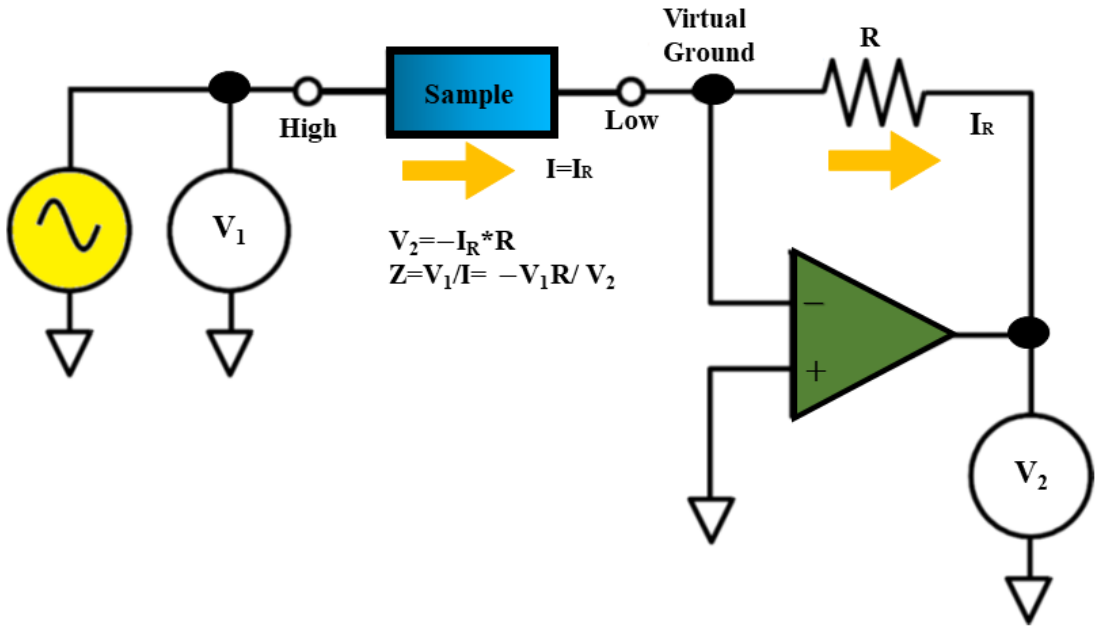

Figure 2.13: Schematic diagram of the working principle of MCR meter and impedance analyzer.

2.9.1.1. Dielectric property analysis of solid powder material

For the dielectric property analysis of solid powder material in impedance analyzer the powdered sample is palletized. On both surfaces of the pallet conducting silver adhesive paste is added and contact is made with Copper wire. For the measurements, the sample is connected with the measuring leads of the impedance analyzer. Temperature dependence of the dielectric response is studied by inserting the palletized sample in an oven.

2.9.1.2. Dielectric property analysis of magnetic fluid

For the dielectric analysis of magnetic fluids, a liquid dielectric cell is designed by incorporating a cylindrical alumina cell of inner diameter 1.8 cm, outer diameter 2.21 cm and of height 2.9 cm. Two Cu electrodes are placed maintaining a constant gap of 1.4 cm inside the dielectric cell, as shown in Figure 2.14. The liquid dielectric cell is connected to an NF corporation LCR meter ZM2376. For measuring the effect of the magnetic field on the dielectric response the dielectric cell is placed in between the coils of an electromagnetic, shown in Figure 2.15, in such a way that the direction of the magnetic field and the direction of the applied electric field are parallel.

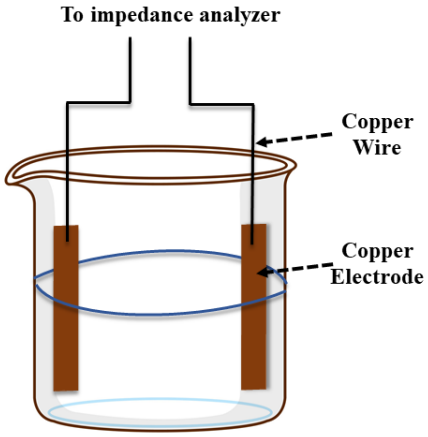

Figure 2.14. Liquid dielectric cell for impedance analysis.

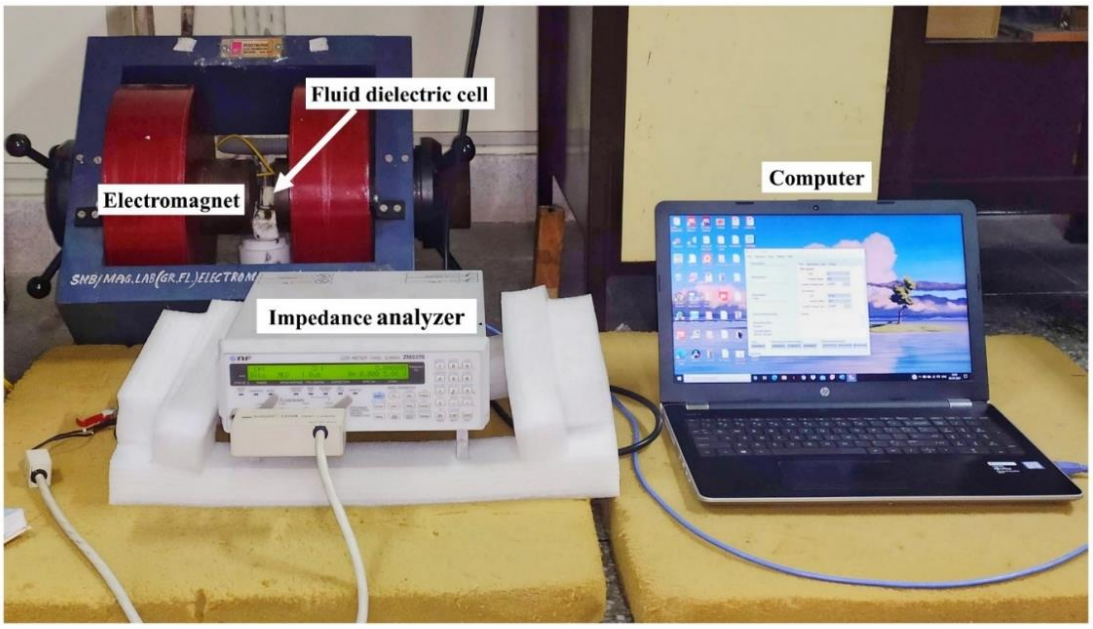

Figure 2.15. Setup for magnetic field dependent dielectric property analysis of magnetic fluid.

2.9.2. Vector Network Analyzer (VNA)

A network analyzer is an instrument used for measuring the electrical network parameters. VNA is a network analyzer that is used for radio frequency and microwave applications, which measures both the phase and amplitude of the measured parameters. VNA is implemented for characterizing both the active and passive network, in terms of network scattering parameters, known as S parameters[11]. Measuring the S parameters by analyzing the reflection and transmission of electrical networks is easy as well as accurate in the high-frequency range.

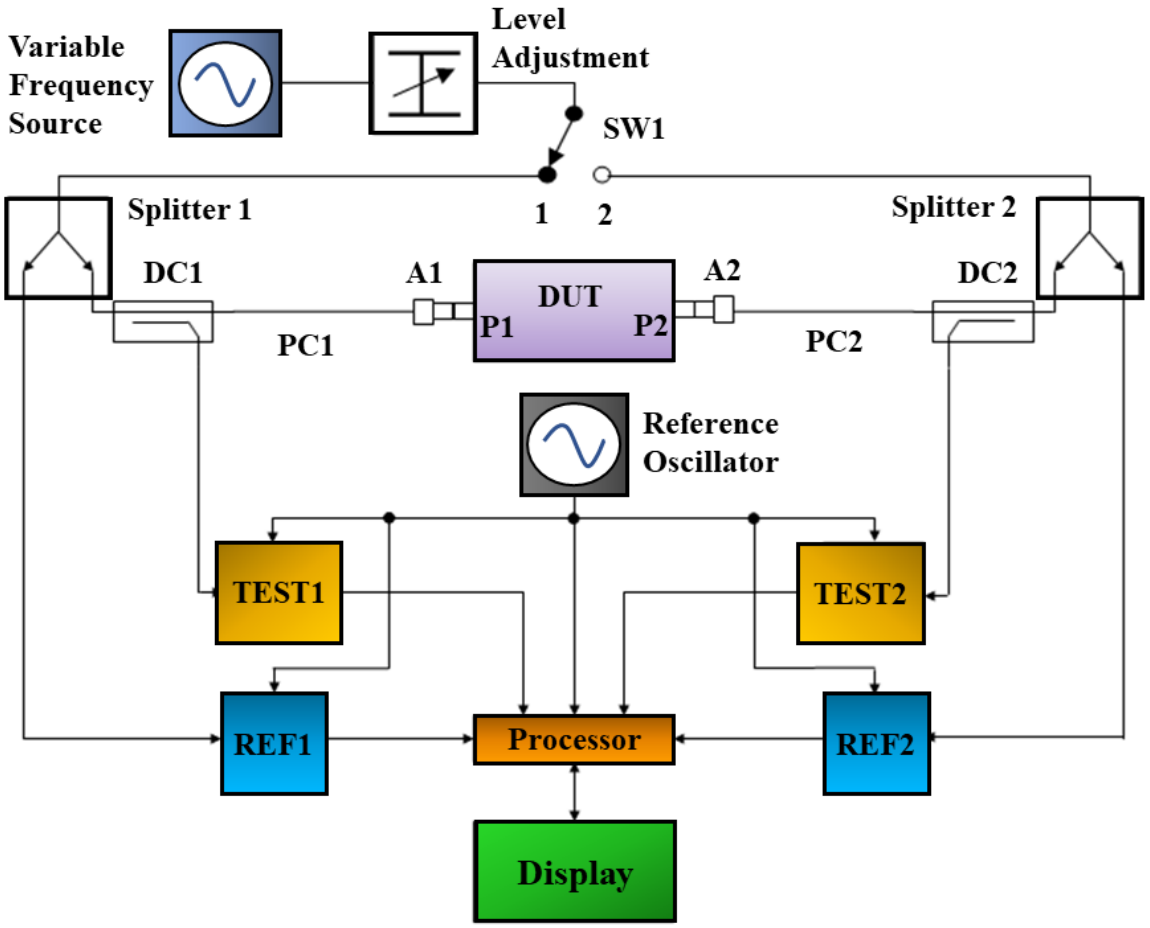

Figure 2.16: Schemtic presentation of VNA.

VNA can measure the electrical parameters of a network with any arbitrary number of ports. Here we will use VNA on a 2-port network. Figure 2.16 shows the block diagram of a 2-port VNA. Two ports of the device under test (DUT) are denoted as port 1 (P1) and port 2 (P2). PC1 and PC2 are the precision cables connected to P1 and P2 from the VNA.

For microwave measurements using coaxial airline (Maury Microwaves-8043S6) and vector network analyser (Anritsu MS46122B), the material should be of toroidal shape with outer diameter 3.5 mm and inner diameter 1.5 mm according to the dimension of coaxial line. The composite samples for microwave measurements are prepared by loading powder samples in 25 wt% in Epoxy Resin matrix and moulding this mixture in a precisely fabricated self-made Teflon mould.

2.10. Magnetorheological (MR) Property Measurements

Magnetorheological (MR) properties of MR fluids can be studied in three basic operation modes, i) valve mode or pressure-driven flow (PDF) mode, ii) direct shear (DS) mode and iii) squeeze mode. Examples of PDF mode devices include dampers, serve-valves, shock absorbers, whereas devices that work on DS mode are brakes, clutches and locking devices. The third mode of operation, squeeze mode, appears in high force and/or slow motion applications[12].

2.10.1. Study of Magnetorheological Properties in Shear Mode

The MR response of our MR fluids is studied in a parallel plate magnetorheometer AntonPaar Physica MCR 301, operating in shear mode. In this magnetorheometer the MR fluid sample is placed between two parallel plates, the lower plate is fixed and the upper plate is rotated with angular velocity to apply shear is the test fluid. An electromagnetic coil is attached to the instrument for applying a magnetic field during the MR measurements, shown in Figure 2.17(a). The magnetic particles suspended in the fluid form particle chain along the field direction, as shown in Figure 2.17(b), and try to oppose the rotation of the upper plate. As a result, shear stress is developed in the material, which is the measure of its MR performance.

For the viscoelastic property study of MR fluids, a sinusoidal oscillatory shear strain is applied to the fluid and sinusoidal shear stress is recorded to analyze the storage and loss modulus of the material.

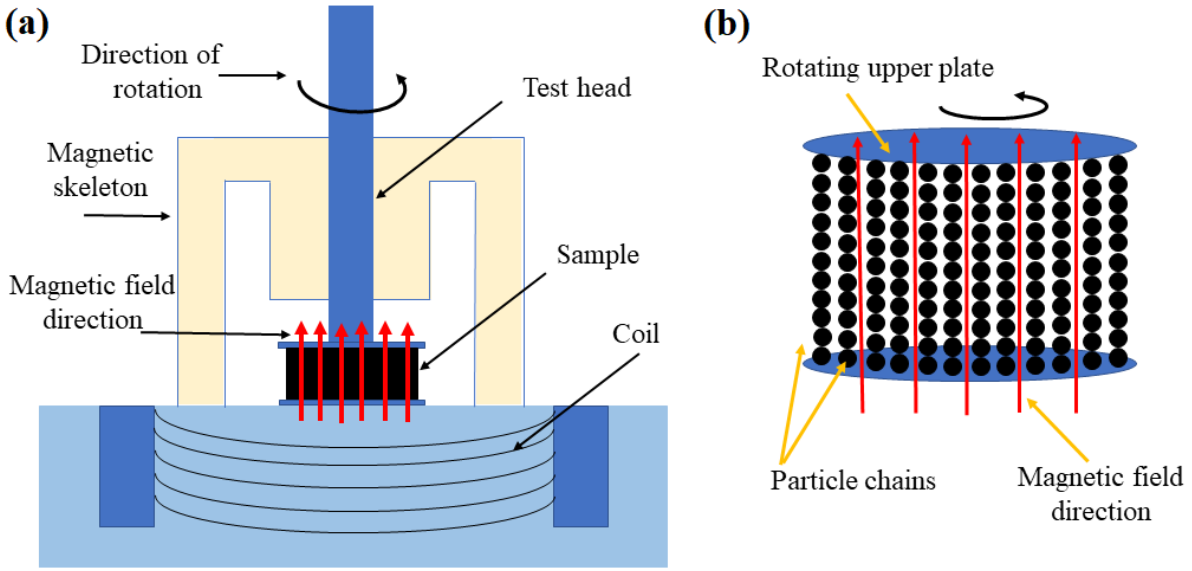

Figure 2.17: (a) Schematic of magnetorheometer operating in shear mode (b) particle chain formation between upper and lower plates of magnetorheometer under applied magnetic field.

2.11. Thermal Conduction Properties

For measuring the thermal conduction property of the MR fluids under the application of an external magnetic field an experimental setup is built in the laboratory. In a 10 ml beaker two Cu plates are placed parallelly maintaining a constant gap, as shown in Figure 2.18.

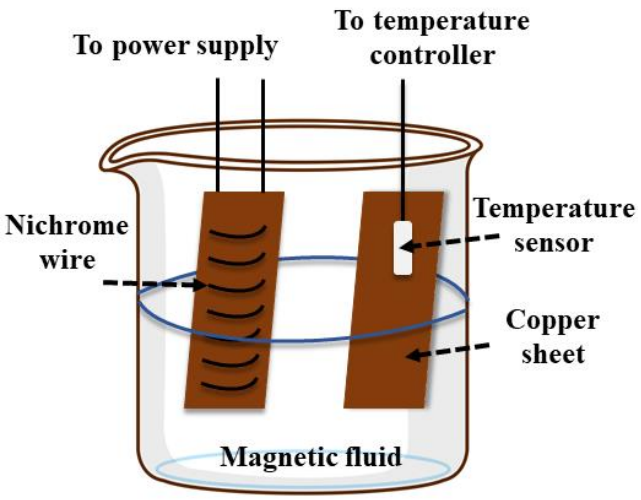

Figure 2.18: Magnetic fluid cell for thermal conduction property measurements.

On one plate (plate A) a nichrome wire is mounted to apply constant current, through Aplab 0-32 V DC power supply LQ6324, for heating the plate and on another plate

(plate B) a Pt resistant sensor PT-103 is mounted, which is connected to a 340 temperature controller unit by Lakeshore. The fluid cell is placed between the poles of an electromagnet as shown in Figure 2.19. The change in temperature of plate B with time is measured under the application of various magnetic fields.

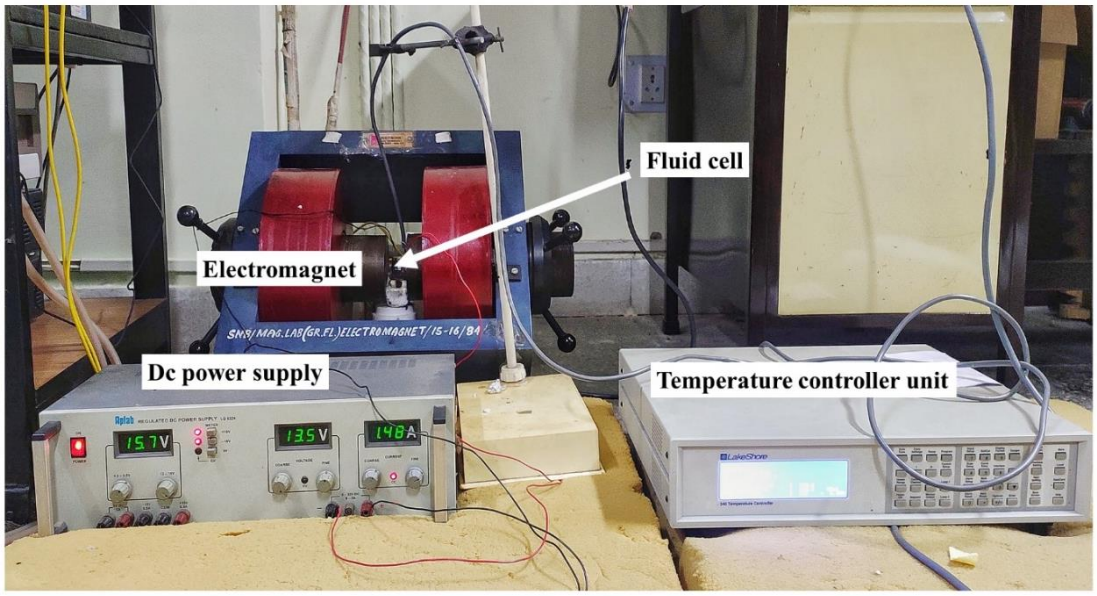

Figure 2.19: Set up for thermal conduction property analysis of magnetic fluids developed in laboratory.

Bibliography

1. Min, Y., Kwak, J., Soon, A. & Jeong, U. Nonstoichiometric Nucleation and Growth of Multicomponent Nanocrystals in Solution. *Accounts of Chemical Research* **47**, 2887–2893 (2014).
2. Walton, R. I. Subcritical solvothermal synthesis of condensed inorganic materials. *Chemical Society Reviews* **31**, 230–238 (2002).
3. Rabenau, A. The Role of Hydrothermal Synthesis in Preparative Chemistry. *Angewandte Chemie International Edition in English* **24**, 1026–1040 (1985).
4. Ashtiani, M., Hashemabadi, S. H. & Ghaffari, A. A review on the magnetorheological fluid preparation and stabilization. *Journal of Magnetism and Magnetic Materials* **374**, 716–730 (2015).
5. Kittel, C. Chapter 16 - Dielectrics and Ferroelectrics. *Introduction to Solid State Physics* 453–486 (2004).
6. Groves, T. R., Pfeiffer, H. C., Newman, T. H. & Hohn, F. J. EL3 system for quarter-micron electron beam lithography. *Journal of Vacuum Science & Technology B: Microelectronics Processing and Phenomena* **6**, 2028 (1998).
7. Cappella, B. & Dietler, G. Force-distance curves by atomic force microscopy. *Surface Science Reports* **34**, 1–3 (1999).
8. JANSSENS, M. Fundamental measurement techniques. *Flammability Testing of Materials Used in Construction, Transport and Mining* 22–62 (2006) doi:10.1533/9781845691042.22.
9. Clarke, J. SQUIDs. *Scientific American* **271**, 46–53 (1994).
10. Deshmukh, K. *et al*. Dielectric Spectroscopy. *Spectroscopic Methods for Nanomaterials Characterization* **2**, 237–299 (2017).
11. Su, C.-C. Microwave Engineering, 4th Edition.
12. Carlson, J. D. & Jolly, M. R. MR fluid, foam and elastomer devices. *Mechatronics* **10**, 555–569.

Chapter 3

Magnetic, Dielectric and Microwave Absorption Properties of $Zn_xFe_{3-x}O_4$ Nano-Hollow Spheres

This chapter demonstrates synthesis of $Zn_xFe_{3-x}O_4$ nano-hollow spheres with x=0.0, 0.1, 0.2, 0.3, 0.4 and 1.0 doping content. Variation of structural, magnetic and dielectric responses of as-synthesized different $Zn_xFe_{3-x}O_4$ nano-hollow spheres with different doping content are studied in detail. Owing to the improved magnetic permeability and decreased dielectric permittivity of $Zn_{0.2}Fe_{2.8}O_4$ hollow-spheres broadband microwave absorption properties are obtained.

A part of this chapter is already published in ***Physical Review Applied, 2019**, 11, 024059* and it is reproduced here.

3. Tuning of Magnetic and Dielectric Response of Fe_3O_4 Nano-Hollow Spheres Through Zn-Doping : An Excellent Material for High Frequency Applications

3.1. Preamble

Magnetite (Fe_3O_4) in nano scale is one of the most important magnetic materials with high permeability, 100% spin polarization, Verwey transition T_V~120 K and a very high Curie temperature, T_c ~856 K, which enable it to be a promising candidate for use in nanoscale functional spintronic devices, magnetic fluid, high density magnetic storage and bio-medical applications[1–4]. Among all their nanostructures, nano hollow spheres (NHSs) drew maximum attention because of low density, high compressibility to withstand changes in pressure and temperature and large effective surface area. Lower density of hollow spheres enables them to be better material for magnetorheological application with higher dispersibility[5]. The hollow cavity can also be used for delivering drugs[6].

In all the applications, including biomedical, high magnetization is required. However it deteriorates significantly when size is reduced from bulk to nano, because of surface effects, where magnetic order is highly disturbed due to the randomly oriented surface spins. Therefore enhancement of magnetization in Iron oxide nanostructures is a real challenge to the material scientists. Doping Fe_3O_4 with divalent cation (Zn^{2+}, Co^{2+}, Mn^{2+}, Mg^{2+}, Ni^{2+} etc.) is an effective method to enhance magnetic properties[7–11]. Among them Zn doped Fe_3O_4 nanostructures drew great interest, particularly in clinical applications due to less toxicity of Zn^{2+}. Moreover the presence of Zn helps in forming stable complexes with various Fe_3O_4drugs, polymers and organic materials according to Irving-William series[12].

In addition to large magnetic moment, high resistivity is also required for high frequency applications such as in microwave communication technology to reduce eddy current, back emf and other high frequency related negative effects[13,14]. With inclusion of Zn, the conductivity of Fe_3O_4 reduces due to the reduction in spin hopping.

Magnetite and other ferrites have attracted much attention in recent years in microwave (MW) attenuation devices. The MW attenuation materials must possess the

properties of high absorption with minimum reflection loss. To achieve complete electromagnetic (EM) wave absorption μ'/ε' should be ~1[15], where μ' is the real part of magnetic permeability and ε' is the real part of dielectric permittivity. μ' can be very high by choosing suitable materials such as ferrites. However, ferrites $\mu'/\varepsilon' << 1$, as the value of ε' is much higher than μ'. Therefore, μ'/ε' should be tuned to unity, by doping Zn, which increases μ' due to increase in magnetization. Hollow structured materials can also enhance the electromagnetic absorption due to repeated reflection at the inner surface of the hollow cavity.

The reported magnetic properties of $Zn_xFe_{3-x}O_4$ nano materials prepared by different synthesis methods are contradictory. Takaobushi et al.[16,17] reported continuous increase of magnetization (M_s) in $Zn_xFe_{3-x}O_4$ epitaxial thin films till x= 0.9. By contrast, Venkateshvaran et al.[18] observed M_s of $Zn_xFe_{3-x}O_4$ epitaxial films to increase and conductivity to decrease monotonously with x from 0 to 0.5. Matsuo et al.[19] showed the maximum M_s for x=0.2 in nanoparticles, prepared by chemical coprecipitation method. Therefore from the literature we observed that Zn doping in Fe_3O_4 up to certain percentage enhances magnetic moment, reduces conductivity and helps forming stable complexes.

In this chapter, we prepared $Zn_xFe_{3-x}O_4$ NHSs with $0.0 \leq x \leq 1.0$ to investigate the relationship of magnetic and dielectric property with Zn doping. Maximum magnetization along with significant reduction in conductivity and dielectric permittivity is observed for x=0.2. Owing to the highest saturation magnetization, reduced conductivity and dielectric permittivity, the microwave absorption property of $Zn_{0.2}Fe_{2.8}O_4$ NHSs is studied.

3.2. Experimental Section

3.2.1. Material Used

The precursor salts, Zinc Chloride ($ZnCl_2$) and Ferric Chloride ($FeCl_3$, $6H_2O$), urea (CH_4N_2O) and surfactant oleylamine ($C_{18}H_{37}N$) are obtained from Sigma-Aldrich. All the reagents are of analytical grade and used without further purification. Ethylene glycol and ethyl alcohol are used as solvents.

3.2.2. Synthesis of Nano-Hollow Spheres

$Zn_xFe_{3-x}O_4$ (x=0.0, 0.1, 0.2, 0.3, 0.4 & 1) NHSs are synthesized using a facile template free solvothermal method through proper variation of $ZnCl_2$ to maintain the stoichiometry

for different doping percentage. In the typical synthesis of $Zn_xFe_{3-x}O_4$ NHSs, 1.35 g of $FeCl_3.6H_2O$, x g of $ZnCl_2$ ($0 \leq x \leq 0.291$) and 0.53 g of urea are dissolved in 30 ml solvent mixture of 20 ml Ethylene glycol & 10 ml Ethanol, which are stirred until clear homogeneous solution was obtained. Thereafter, 1 ml of oleylamine which is a growth modifier as well as surface stabilizer was added to the solution mixture in order to restrict the particle growth in nanometer size range. The properly mixed final solution is transferred into 40 ml Teflon lined stainless steel autoclave and heated to 180°C for 20 h followed by natural cooling to room temperature. The resulting black precipitate is thoroughly washed with absolute ethanol to remove all residual reagents and separated by centrifugation. The as-obtained product is dried at 60°C for 12 h. By varying the amount of $ZnCl_2$, we have been able to prepare $Zn_xFe_{3-x}O_4$ (x=0.0, 0.1, 0.2, 0.4, 1) NHSs. At the elevated temperature urea decomposed to ammonia which produced hydroxyl groups. These hydroxyl groups precipitated the hydroxides of zinc and ferric ions and finally $Zn_xFe_{3-x}O_4$ NHSs formed.

3.2.3. Characterization

The phase of the prepared samples are characterized by a PANalytical X'Pert PRO X-ray diffractometer equipped with Cu Kα radiation (λ=1.5418 Å) radiation. Morphological analysis are performed using FEG transmission electron microscope (TEM) (80–200 kV) and a FEI QUANTA FEG 250 field-emission scanning electron microscope (FESEM) (0.2–30 kV). The magnetic measurement is performed with a vibrating sample magnetometer (VSM), Lake Shore-7144. An Agilent 4249A impedance analyzer within a frequency range 40 Hz-110 MHz is used for dielectric measurements. The electromagnetic (EM) wave absorption properties of $Zn_{0.2}Fe_{2.8}O_4$ NHSs are performed using an Anritsu MS46122B vector network analyzer and a coaxial airline (Maury Microwaves-8043S6). The composite sample for microwave measurements is prepared by loading 25 wt% powder samples in an epoxy resin matrix. The final composite is in a hollow cylindrical shape with inner diameter (d_{in}) = 1.5 mm, outer diameter (d_{out}) = 3.5 mm and thickness (d) = 3.12 mm. Analysis from 2-port scattering (S)-parameters measured in transmission line technique is performed using Nicholson-Ross-Weir algorithm.

3.3. Results and Discussion

3.3.1. Structural and Morphological Properties

The XRD patterns of as-synthesized NHSs with Rietveld refinement, shown in Figure 3.1(a), confirm the formation of face centered cubic spinel structure (JCPDS card np. 89-1397). The (311) peak (Figure 3.1 b) shifts to the lower diffraction angle up to x=0.2, beyond which it moves towards the higher angle. As the tetrahedral site (A-site) is larger than octahedral site (B-site), the nonmagnetic Zn^{2+} (0.74 Å) ions prefer to replace Fe^{3+} (0.64 Å) ions of the A-site under lower doping concentration, resulting in larger lattice parameter from 8.4 Å (for x=0.0) to 8.4084 Å (for x=0.2) and leading to the cation distribution at the A and B sites as $(Zn_x^{2+}Fe_{(1-x)}^{3+})_A[Fe_{(1-x)}^{2+}Fe_{(1+x)}^{3+}]_BO_4$. However, excess Zn^{2+} beyond x=0.2 replace Fe^{2+} ions partly at B-sites and start to form mixed ferrite as $[Zn_{(x-\delta)}^{2+}Fe_{(1-x+\delta)}^{3+}]_A[Zn_\delta^{2+}Fe_{(1-x)}^{2+}Fe_{(1+x-\delta)}^{3+}]_BO_4$ where δ is the inversion degree defined as the fraction of B-sites occupied by Zn^{2+} ions. The cation distribution, δ and lattice parameter obtained from the Rietveld refinement of the experimental XRD pattern are shown in Table I. While both the iron sites are replaced by Zn^{+2} ions, the competition between parameter b, due to cation size effect and the Madelung constant, M, starts to play a significant role in determining the lattice constant, a, following the relation $a \propto b/M$[20]. On substitution of more Zn^{2+} and replacement of Fe^{2+} causes change of repulsion potential as well as the ionic distance, resulting in the reverse trend of decreasing lattice constant beyond x=0.2. The variation of lattice constant with Zn content is shown in Figure 3.1(c).

Table 3.1: Table for cation distribution, inversion degree (δ) and lattice parameter from Rietveld refinement:

x	$Zn_xFe_{3-x}O_4$	Lattice parameter (Å)
0.0	$Fe^{3+}[Fe^{2+}\ Fe^{3+}]O_4$	8.4±0.0002
0.1	δ=0, $Zn_{0.1}^{2+}Fe_{0.9}^{3+}[Fe_{0.9}^{2+}Fe_{1.1}^{3+}]O_4$	8.4021±0.0003
0.2	δ=0.003, $Zn_{0.197}^{2+}Fe_{0.803}^{3+}[Zn_{0.003}^{2+}Fe_{0.8}^{2+}Fe_{1.197}^{3+}]O_4$	8.4084±0.0002
0.3	δ=0.03, $Zn_{0.27}^{2+}Fe_{0.73}^{3+}[Zn_{0.03}^{2+}Fe_{0.7}^{2+}Fe_{1.27}^{3+}]O_4$	8.3906±0.0003
0.4	δ=0.06, $Zn_{0.34}^{2+}Fe_{0.66}^{3+}[Zn_{0.06}^{2+}Fe_{0.6}^{2+}Fe_{1.34}^{3+}]O_4$	8.4014±0.0002
1.0	δ=0, $Zn^{2+}[Fe^{3+}]\ O_4$	8.3989±0.0004

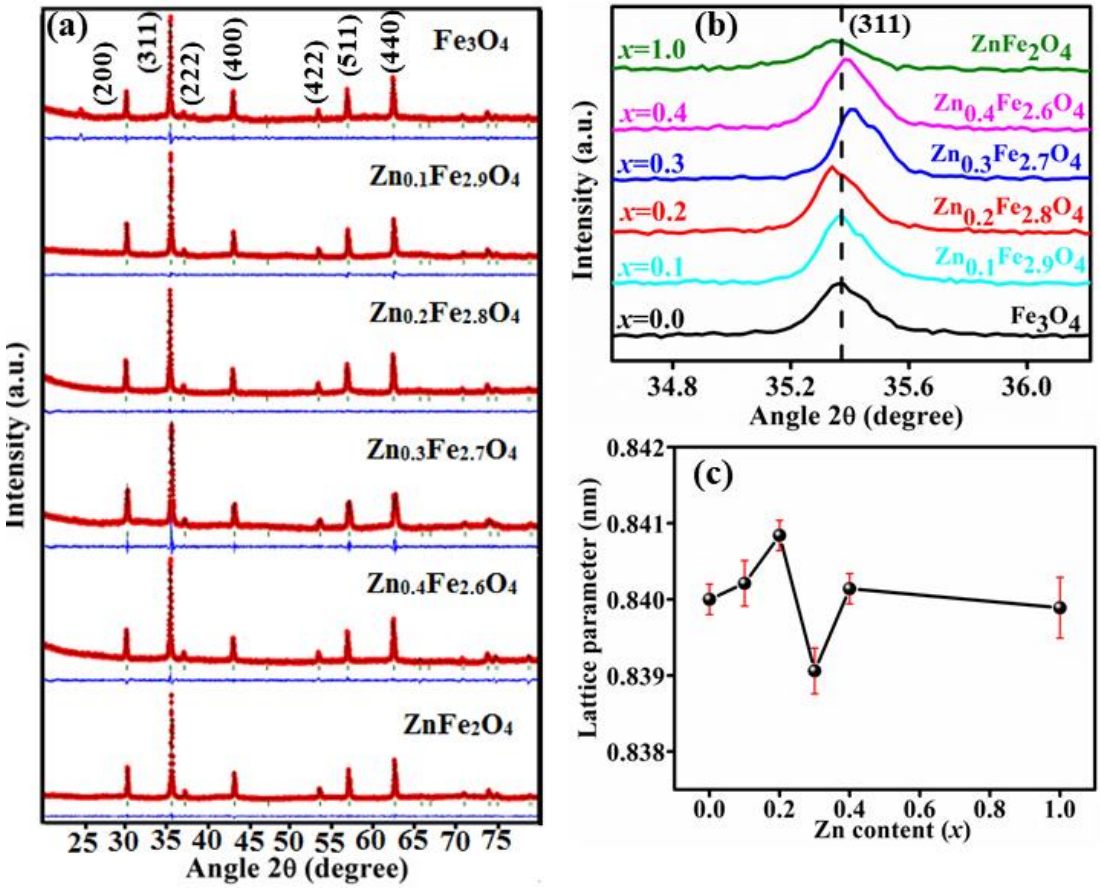

Figure 3.1: (a) XRD intensity pattern of $Zn_xFe_{3-x}O_4$ (x=0.0, 0.1, 0.2, 0.4, 1) with Rietveld refinement, (b) enlarged image of (311) reflection peak and (c) variation of lattice constant with Zn doping concentration.

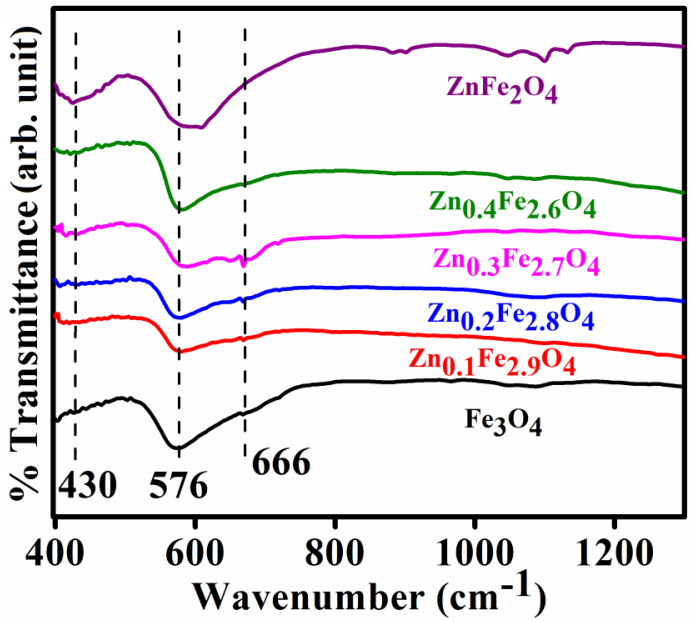

Figure 3.2: FTIR spectra of the $Zn_xFe_{3-x}O_4$ NHSs.

The FTIR spectra of the as prepared $Zn_xFe_{3-x}O_4$ (x=0, 0.1, 0.2, 0.3, 0.4, 1) NHSs is

shown in Figure 3.2. Absorption bands at 576 cm^{-1} and 666cm^{-1} are observed which are associated with Fe-O stretching vibrations of Fe^{3+} ions in octahedral and tetrahedral sites respectively, where the latter is absent for x=1.0 confirming full doping of Zn[21]. With the substitution of zinc a peak is observed at 430 cm^{-1} for Zn-O stretching vibration at tetrahedral sites, confirming Zn doping.

FESEM analysis is performed on all the as-prepared $Zn_xFe_{3-x}O_4$ samples, shown in Figure 3.3 (a-f) with size distribution curves of respective samples in the inset. From the surface morphology hollow spherical structure formation is confirmed with uniform size distribution. The average size of the NHSs calculated from FESEM images are 200-400 nm. For detail analysis of the hollow interior TEM analysis is performed.

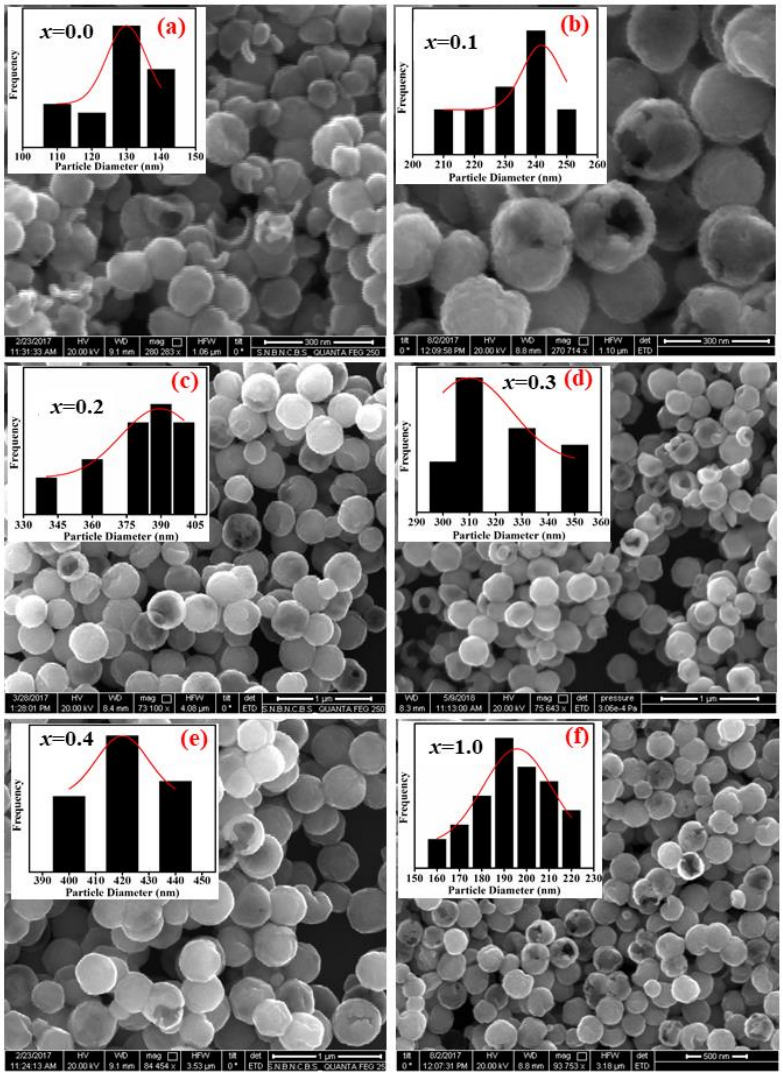

Figure 3.3: FESEM images with size distribution graph in the inset for (a) x=0.0, (b) x=0.1, (c) x=0.2, (d) x=0.3, (e) x=0.4 and (f) x=1.0 NHSs.

The intensive contrast between the dark boundary line and bright center of TEM images of all the samples clearly show the formation of NHSs with homogeneous size distribution and shell thickness in Figures 3.4 (a-f). TEM micrographs along with selected area diffraction pattern (SAED), HRTEM image of (311) plane and size distribution curve of the $Zn_xFe_{3-x}O_4$ samples are shown. From the HRTEM fringe pattern the calculated line spacing matches well with that calculated from XRD analysis shown in Table 3.1.

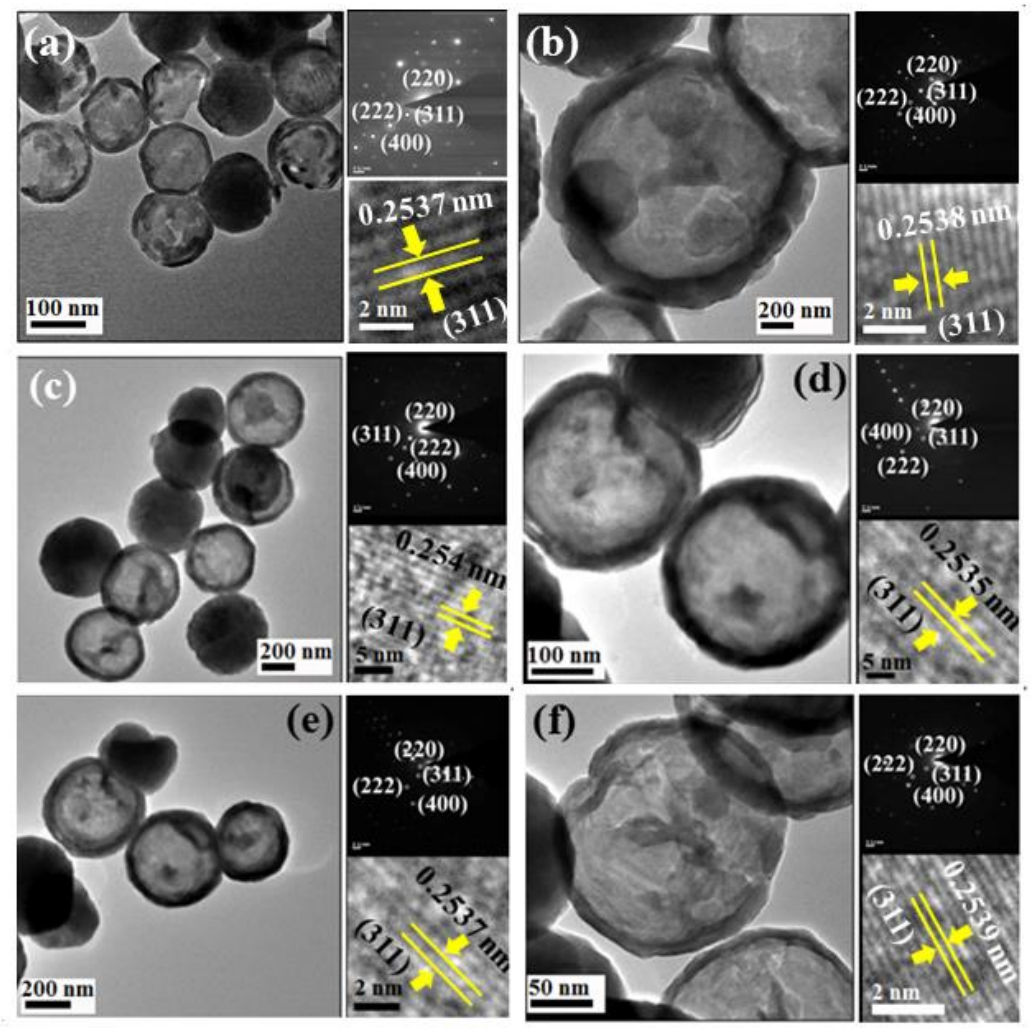

Figure 3.4: TEM, HRTEM and SAED pattern of (a) x=0.0, (b) x=0.1, (c) x=0.2, (d) x=0.3, (e) x=0.4 and (f) x=1.0 NHSs.

3.3.2. Magnetic Properties

Figure 3.5 shows the M-H hysteresis loop of the samples at temperature T= 300 K and 80 K. An increase in saturation magnetization (M_S) is observed on Zn doping with maximum M_S = 92.5 emu-g^{-1} at 300 K and 99.5 emu-g^{-1} at 80 K for x=0.2. M_s decreases on

doping more Zn beyond x=0.2. Magnetism in Fe_3O_4 arises due to the exchange interactions among the cations in inverse-spinel structure, which is governed by a combination of antiferromagnetic super-exchange (SE) and ferromagnetic double exchange (DE) interactions. In Fe_3O_4, tetrahedral A site is occupied by Fe^{3+} and in octahedral B site there is an alternate arrangement of Fe^{3+} and Fe^{2+} ions. There are three antiferromagnetic SE interactions J_{AA} (A-O-A), J_{BB} (B-O-B), and J_{AB} (A-O-B) between the Fe^{3+} ions on the A and B sites, mediated by the oxygen (O) ions. In addition, there is a ferromagnetic DE interaction mediated by the itinerant spin down t_{2g} electrons hopping between the mixed-valent Fe ions on the B sites[18].

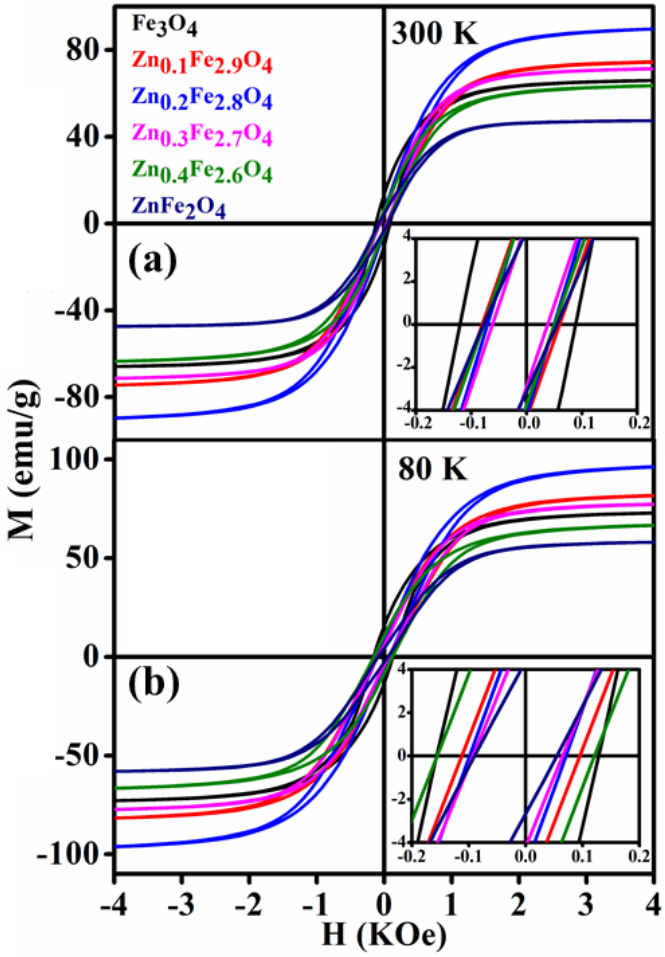

Figure 3.5: Variation of Magnetization (M_s) with applied magnetic field (H) at (a) 300 K and (b) 80 K for $Zn_xFe_{3-x}O_4$ (x=0.0, 0.1, 0.2, 0.3, 0.4, 1) NHSs. Inset figures show the enlarged version of the central region of M-H curves of the respective M-H plots.

In pure Fe_3O_4 the resultant magnetization from Fe^{3+} ions are zero due to antiferromagnetic coupling and only Fe^{2+} ions contribute to the net magnetization. On low Zn substitution Fe^{3+} ion on the A site is replaced by non-magnetic Zn^{2+} ion and it does not

affect the magnetic exchange on the B site. However for charge compensation Fe^{2+}on B site is converted to Fe^{3+} and nullification of magnetic moment from Fe^{3+} is lost. As a result M_s increases at low substitution level (x=0.2) due to contribution from Fe^{2+} as well as Fe^{3+}. For higher substitution of Zn^{2+} (x>0.2) exchange interaction J_{AB} is diluted due to nonmagnetic Zn^{2+} and saturation magnetization decreases. The variation of M_s with x is shown in Figure 3.6 (a) for both the measuring temperatures. Figure 3.6(b) shows the variation of coercivity (H_c) values for $Zn_xFe_{3-x}O_4$ NHSs with doping content x. H_c decreases with increase in Zn content up to x=0.3 and increases thereafter. Increment in H_c at 80 K for x=0.4 is rapid compared to 300 K. Besides low value of M_s for x=0.4 at lower temperature (80 K) indicates the presence of canted antiferromagnetic spins, thus enhancement in magnetic anisotropy.

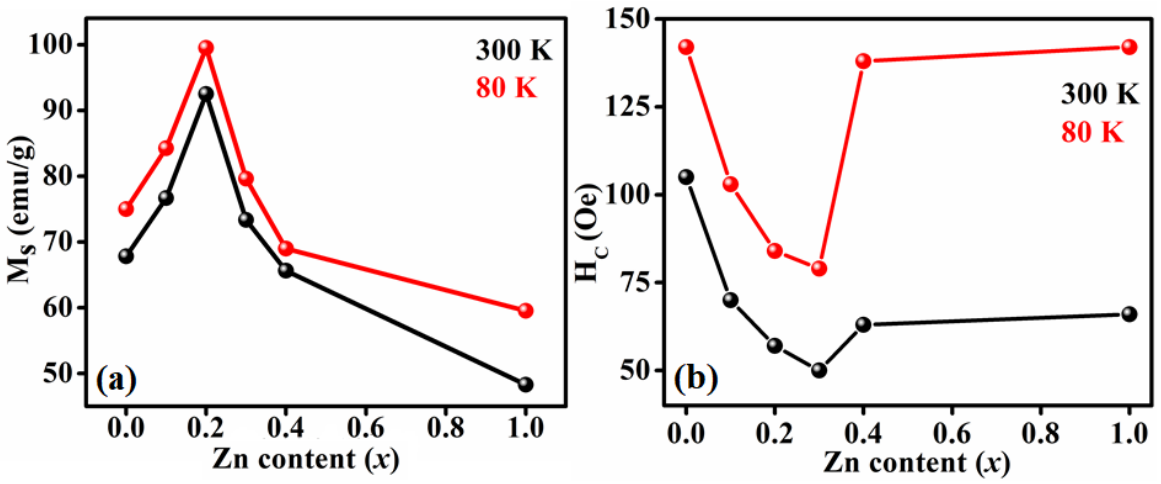

Figure 3.6: Variation of (a) M_s and (b) H_c with x at 300 K and 80 K of $Zn_xFe_{3-x}O_4$ (x=0.0, 0.1, 0.2, 0.3, 0.4, 1) NHSs.

The Zero-field-cooled (ZFC) and field-cooled (FC) χ vs T measurements are shown in Figure 3.7 for $Zn_xFe_{3-x}O_4$ NHSs with an applied field of 100 Oe. In case of ZFC curves during cooling randomness of surface spins are frozen below a certain temperature, called spin freezing temperature (T_g), leading to cusp-like maximum around 30 K. Higher magnetization of the FC curve compared to corresponding ZFC curve is attributed to the surface spins, which are frozen during cooling in the direction of external field. When non-magnetic Zn^{2+} occupies A site only (for x=0.1, 0.2, 1.0) J_{AB} is diluted and T_g reduces. For x=0.3 and x=0.4, in addition to tetrahedral site Zn^{2+} also occupies the octahedral site. This results in frustrated exchange interaction due to canted antiferromagnetic spins. The inset

of Figures show the variation of $\frac{d\chi(T)}{dT}$ with T for the respective sample for better identification of the peak positions. Figure 3.8 (a) shows the variation of T_g with Zn content (x).

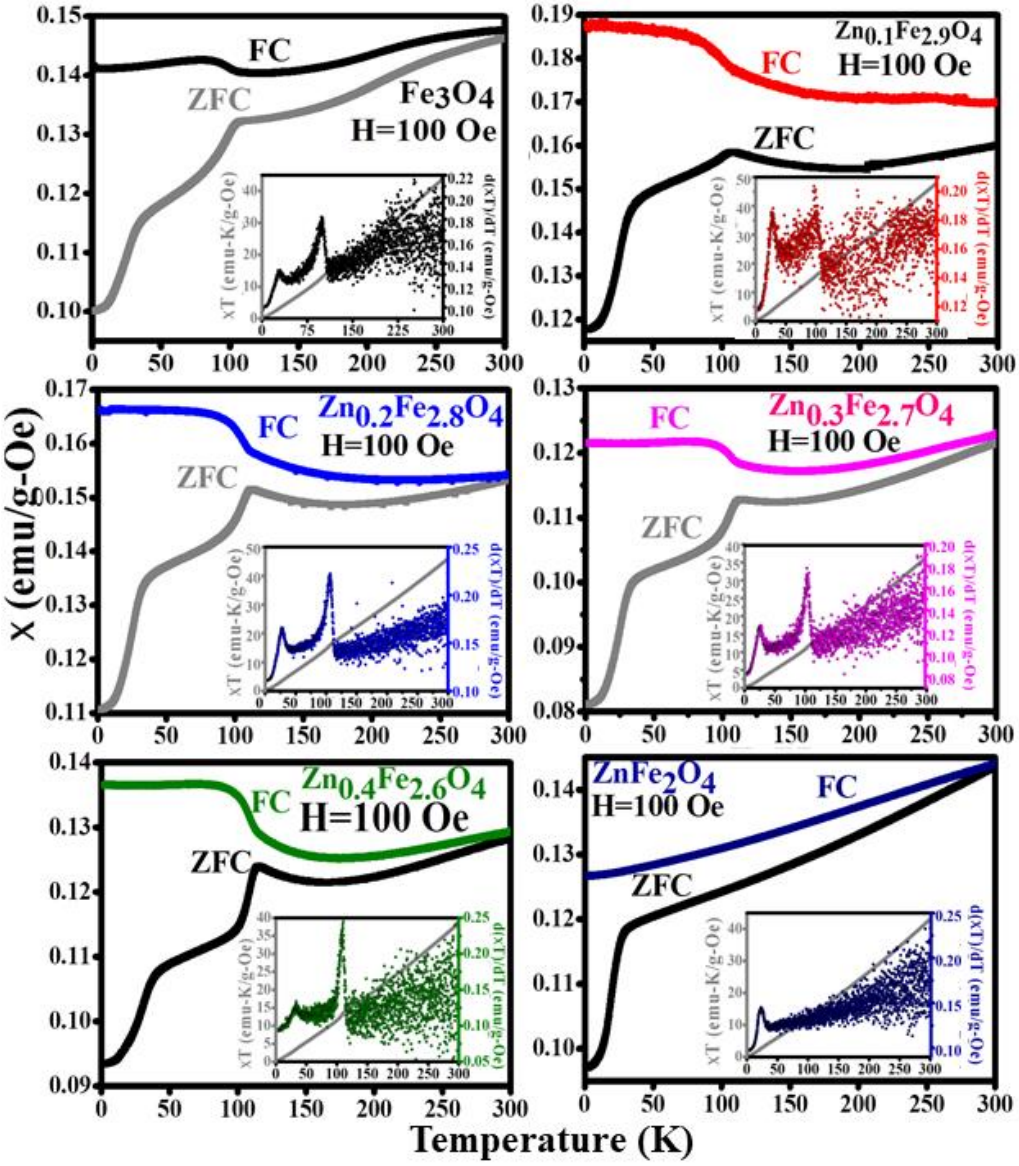

Figure 3.7: ZFC-FC curves of $Zn_xFe_{3-x}O_4$ (x=0.0, 0.1, 0.2, 0.3, 0.4, 1) NHSs.

Another cusp like maximum observed at higher temperature for all the samples, except $ZnFe_2O_4$, corresponds to the Verwey transition where structural transition from cubic to monoclinic symmetry takes place. The Verwey transition temperature (T_V) is extremely sensitive to the oxygen stoichiometry or the transition metals present in the compound. Since Zn^{2+} replaces Fe^{3+} at the A sites around which the vibrating oxygen ions are situated, the changes in frequency of phonon vibration (v) is expected. Gupta et al.[22]

showed the reduction in T_V with increasing phonon frequency. ν can be written as

$$\boldsymbol{\nu} = \frac{\mathbf{1}}{\mathbf{2}\pi}\sqrt{\frac{k}{m_r}} \tag{3.1}$$

where, the reduced mass $\boldsymbol{m_r} = \frac{m_1 m_2}{m_1 + m_2}$ and k is the bond strength.

Here, m_1 is the mass of Zn^{+2} / mass of Fe^{+3} and m_2 is the mass of O^{-2}. With increasing Zn^{2+} (65.408 Dalton), replacing Fe^{+3} (55.843 Dalton), m_r increases and hence ν decreases. On the other hand, replacement of Fe^{3+} by larger Zn^{2+} changes k in the same fashion as lattice constant, shown in Figure 3.1. The resultant effect of Zn doping on T_V is shown in Figure 3.8(b).

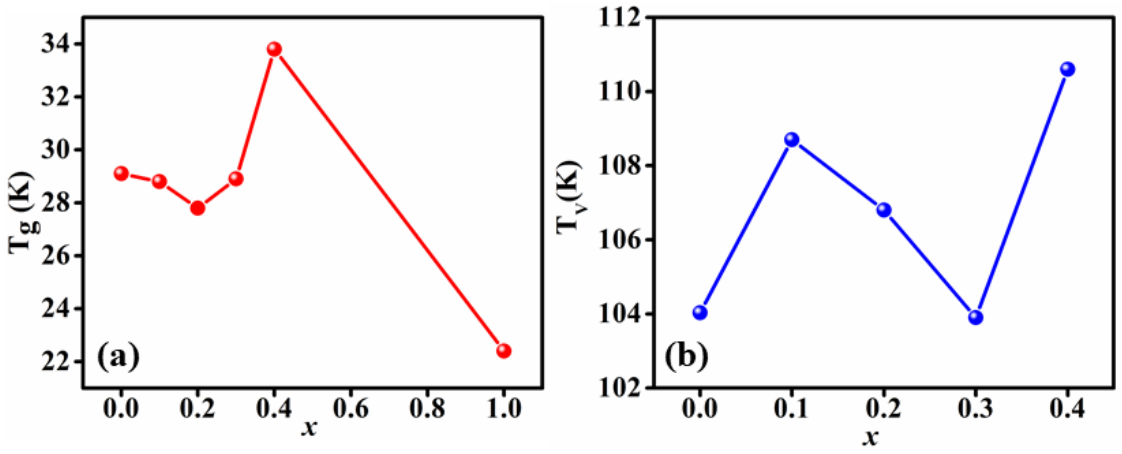

Figure 3.8: Variation of (a) T_v and (b) T_g with Zn doping content x.

For deeper understanding of the nature of spin freezing behaviour in $Zn_xFe_{3-x}O_4$ NHSs system, the AC magnetic properties are studied. The real (χ′) and imaginary (χ″) parts of AC susceptibility, for $Zn_xFe_{3-x}O_4$ (x=0.0, 0.1, 0.2, 2.3, 0.4, 1) NHSs are shown in Figure 3.9 (a-f) at four different frequencies f= 7 Hz, 83 Hz, 253 Hz & 503 Hz and in the temperature range 5 K to 400 K. We observed two peaks in the susceptibility vs temperature curves. The peak at lower temperature (T_g' for χ′ and T_g'' for χ″) corresponds to the spin freezing temperature and the second one at higher temperature (T_V' for χ′ and T_V'' for χ″) indicates the Verwey transition, which is independent of frequency[23]. With frequency χ′ does not change much except at temperatures close to and below T_g', whereas χ″ changes significantly due to the presence of magnetic dipolar interactions[24].

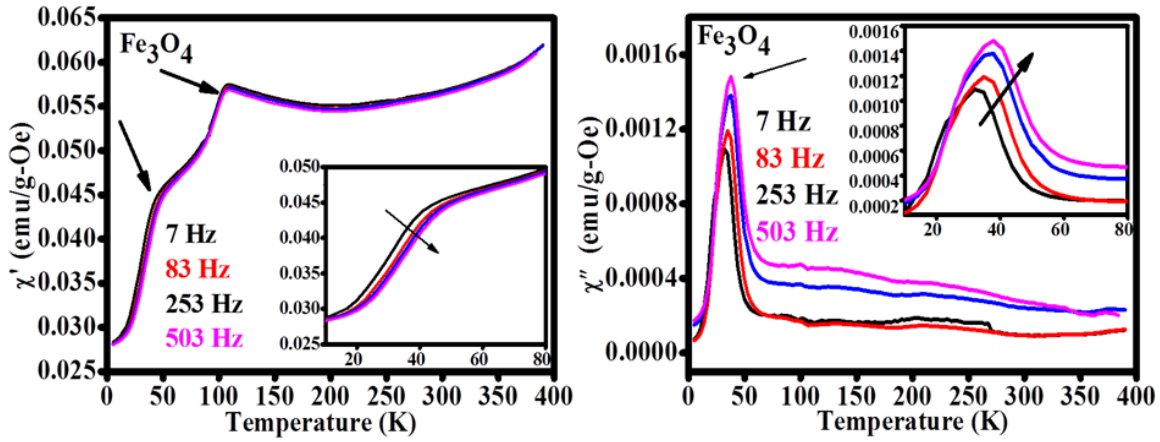

Figure 3.9 (a): Variation of χ′ and χ″ with temperature for Fe_3O_4 (x=0.0) NHSs.

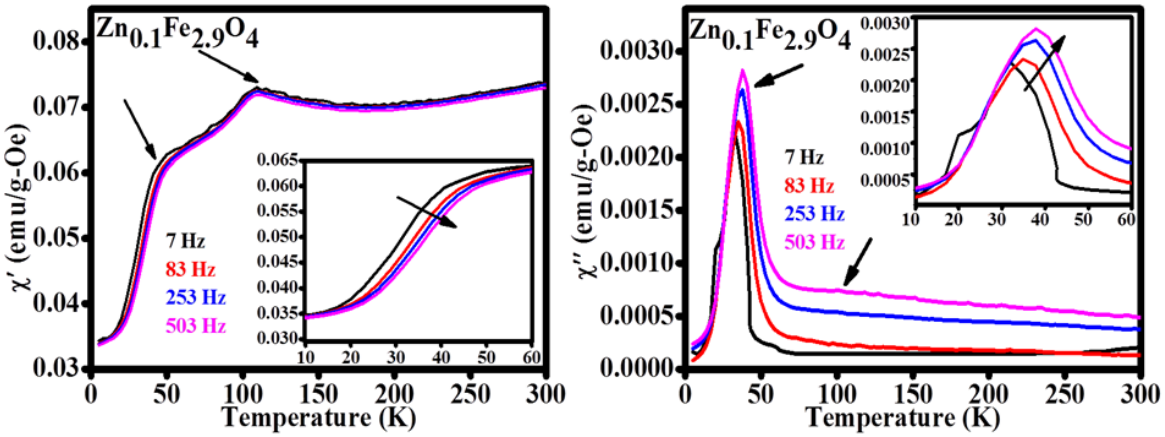

Figure 3.9 (b): Variation of χ′ and χ″ with temperature for $Zn_{0.1}Fe_{2.9}O_4$ (x=0.1) NHSs.

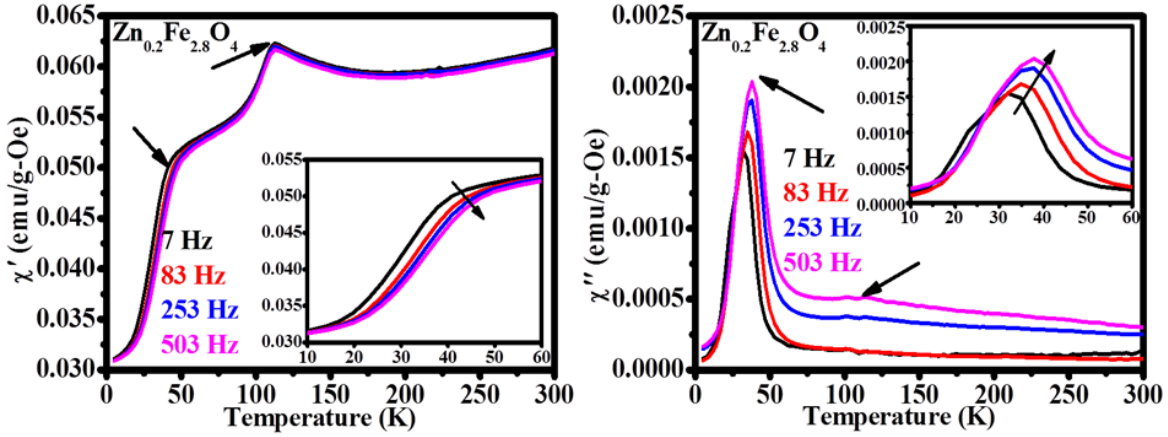

Figure 3.9 (c): Variation of χ′ and χ″ with temperature for $Zn_{0.2}Fe_{2.8}O_4$ (x=0.2) NHSs.

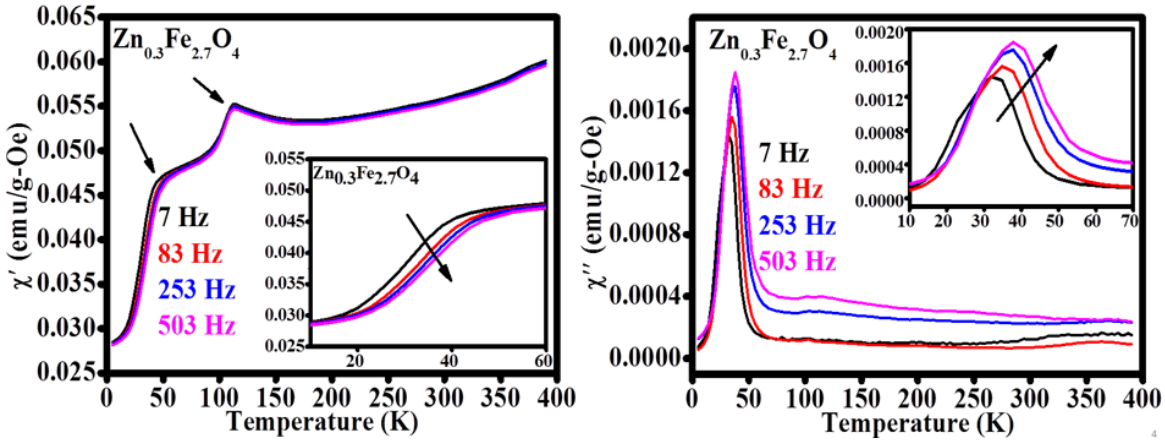

Figure 3.9 (d): Variation of χ' and χ'' with temperature for $Zn_{0.3}Fe_{2.7}O_4$ (x=0.3) NHSs.

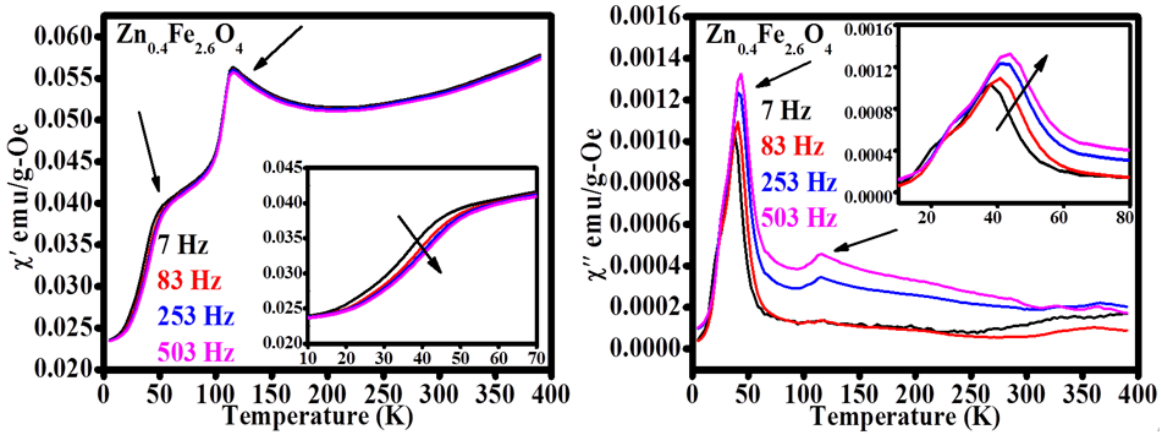

Figure 3.9 (e): Variation of χ' and χ'' with temperature for $Zn_{0.4}Fe_{2.6}O_4$ (x=0.4) NHSs.

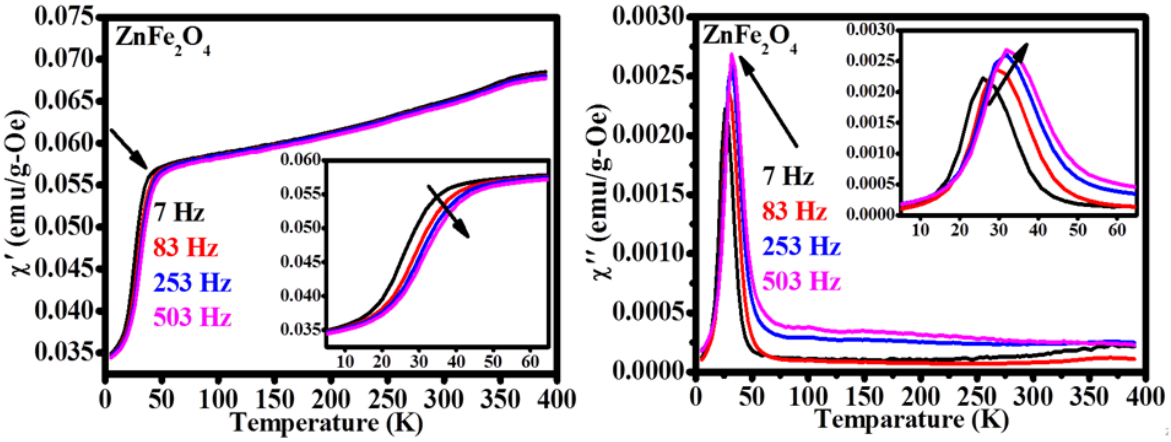

Figure 3.9 (f): Variation of χ' and χ'' with temperature for $ZnFeO_4$ (x=1.0) NHSs.

Frequency dependence of χ' for $T < T_g'$ and its frequency independence for $T > T_g'$, suggests the blocking process of the Fe_3O_4 NHSs[25]. Variation of T_g' and T_g'' with frequency is related to the relaxation of domain walls[26], which resulted in higher magnetic anisotropy as well as spin freezing temperature. The frequency dependence of T_g' can be quantified in

terms of the parameter $k=\frac{\nabla T_g'}{T_g' \nabla log f}$, which signifies the relative shift in spin freezing temperature with frequency. This relative shift parameter is also known as Mydosh parameter, which is used to identify different spin-glass system[27]. The calculated value of k for our NHSs is 0.06, except for $Zn_{0.1}Fe_{2.9}O_4$, where k=0.1. Values of k suggests higher sensitivity to frequency for all these $Zn_xFe_{3-x}O_4$ NHSs. From the values of Mydosh parameter lying between 0.02-0.06 cluster glass like system can be confirmed with slow rate of magnetic relaxation.

In order to get clear sight into the relaxation mechanism of the NHSs we fit the data of relaxation time (τ) and T_g' with Vogel- Fulcher equation[28]:

$$\tau = \tau_0 \exp[-E_a/k_B(T_g' - T_0)] \quad (3.2)$$

where, E_a is the anisotropy energy barrier, τ_0 is the characteristic relaxation time, k_B is the Boltzmann constant and T_0 is the characteristic temperature which is the measure of the interparticle interaction energy.

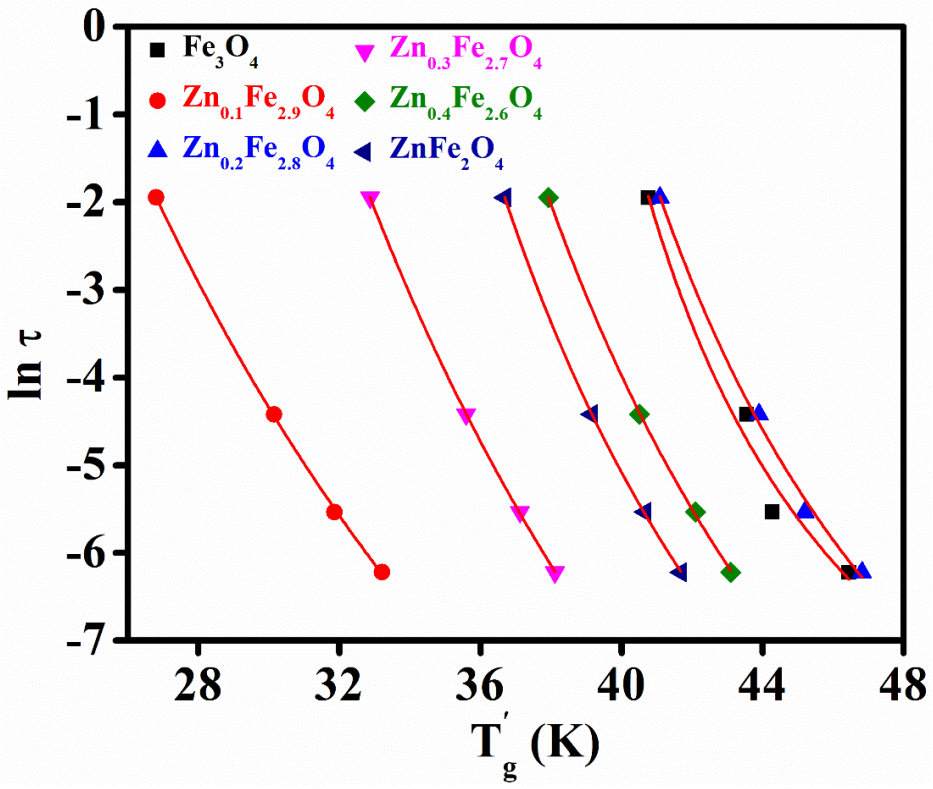

Figure 3.10: Frequency dependence of T_g' fitted to Vogel- Fulcher Law.

Table 3.2: Table for parameters obtained from Vogel-Fulcher fitting

x	τ_0 (sec)	T_0 (K)
0.0	8.5×10^{-7}	33.8±7.6
0.1	2.4×10^{-10}	3.06±0.6
0.2	4.79×10^{-7}	30.2±6.4
0.3	2.3×10^{-10}	13.2±2.2
0.4	1.9×10^{-8}	23.9±2.6
1.0	5.3×10^{-8}	24.3±1.4

The variation of relaxation time with spin-freezing temperature is fitted with Eq. (3.2), shown in Figure 3.10. The fitting parameters are shown in Figure 3.2. From the fitting parameters values, large τ_0 is obtained for interacting spin cluster[30]. T_0 can be considered to describe the temperature regime where interactions are effective and above which thermal energy is sufficient for the interactions to be overcome under the conditions of the ac-susceptibility measurement. Dipolar interaction plays an important role in governing anisotropy energy. Due to doping magnetic moment changes, which in turn changes the interparticle interaction energy. T_0 is much lower for x=0.1 compared to other doping concentration indicating activated interparticle interactions at low temperature region.

3.3.3. Dielectric Properties

Figure 3.11 shows the variation of real (ε′) and imaginary (ε″) part of dielectric constant with frequency of $Zn_xFe_{3-x}O_4$ NHSs for x=0.0 and 0.2 within the temperature range of 303 K ≤ T ≤ 573 K. Higher value of ε′ is observed for the undoped Fe_3O_4 compared to Zn-doped sample. Below 473 K, dielectric constant is almost independent of frequency, because at lower temperature thermal vibration frequency of the charge carriers does not match with the applied frequency range. With the increase in temperature when the thermal vibration is comparable to the applied electric field frequency, ε′ increases. However at very high frequency the carriers cannot follow the applied frequency and lag behind, thus reducing ε′. Dielectric constant (ε′) and dielectric loss (ε″) both show high value at low frequency and

decrease with frequency reaching a nearly saturated value indicating a frequency independent behaviour beyond 10^6 Hz. This phenomenon can be explained on the basis of Koop's theory[29] and Maxwell-Wagner model. According to this theory, the dielectric structure was said to be composed of grains and grain boundaries in which grains are conducting, while grain boundaries are non-conducting. Dielectric contribution in ferrites arise due to the oscillation of dipoles in the grain region and the accumulation of the carriers in the resistive grain boundary regions. Among the various source of polarizations dipolar (within 10^3-10^6 Hz) and interfacial polarization (below ~10^3 Hz) contribute significantly in the experimental frequency range. However these polarizations cannot follow the applied frequency beyond 10^6 Hz, leading to reduction in polarization with increasing frequency.

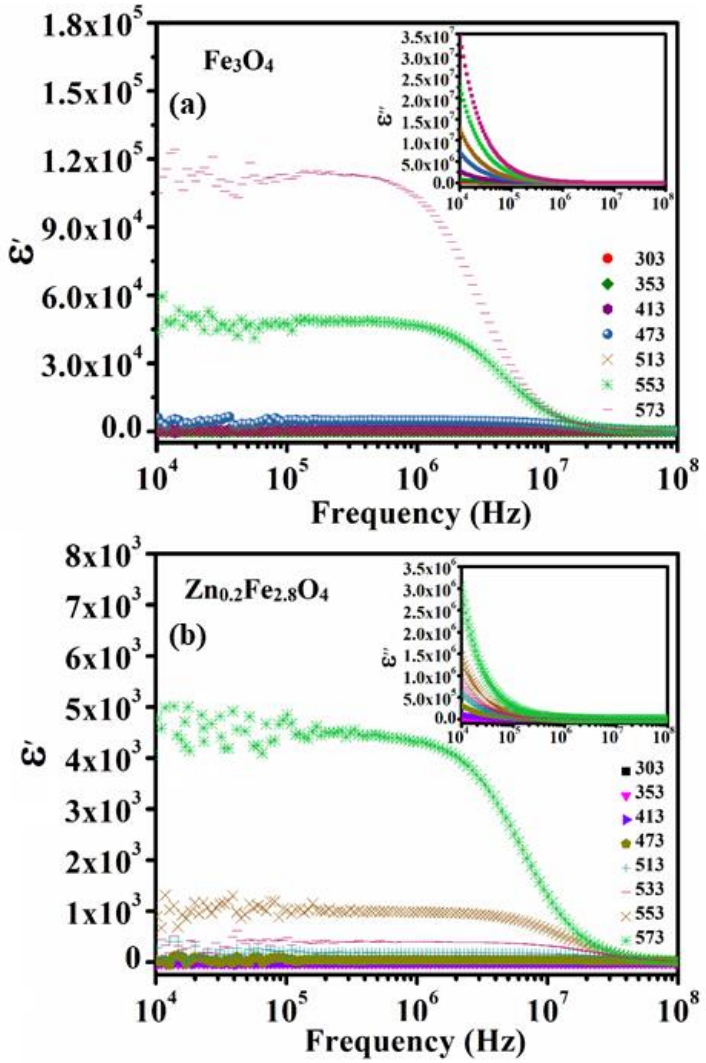

Figure 3.11: Frequency dependent variation of dielectric constant (ε′) at different temperatures for (a) Fe_3O_4 and (b) $Zn_{0.2}Fe_{2.8}O_4$ (inset figures show the dielectric relaxation behaviour over the same frequency range at different temperature values for the respective samples). The measurement temperatures are in K.

The dielectric permittivity of $Zn_{0.2}Fe_{2.8}O_4$ NHSs is less than Fe_3O_4. To understand the reason behind lower dielectric response in x=0.2, Nyquist plot or Cole-Cole plot of imaginary vs real impedance (-z″ vs z) of x=0 and 0.2 are analysed and are shown in Figures 3.12(a) and (b), respectively, at different measurement temperatures. For each temperature the -z″ vs z curves consist of distorted semicircles, suggesting non-Debye type dielectric relaxation in the NHSs systems. The low and high frequency parts of the arcs correspond to the contribution from grain boundary and grain respectively. The resistance value at a particular temperature is equal to the intercept at the x-axis of the corresponding semi-circle. These Nyquist plots are fitted with Maxwell-Wagner equivalent circuit model, shown in the inset of Figure 3.12(b), consisting of two parallel RC circuits, $R_g||C_g$ (from grain) and $R_{gb}||C_{gb}$ (from grain boundary) and R_s and L_s connected in series. R_s and L_s represent the contribution from measuring leads and electrodes.

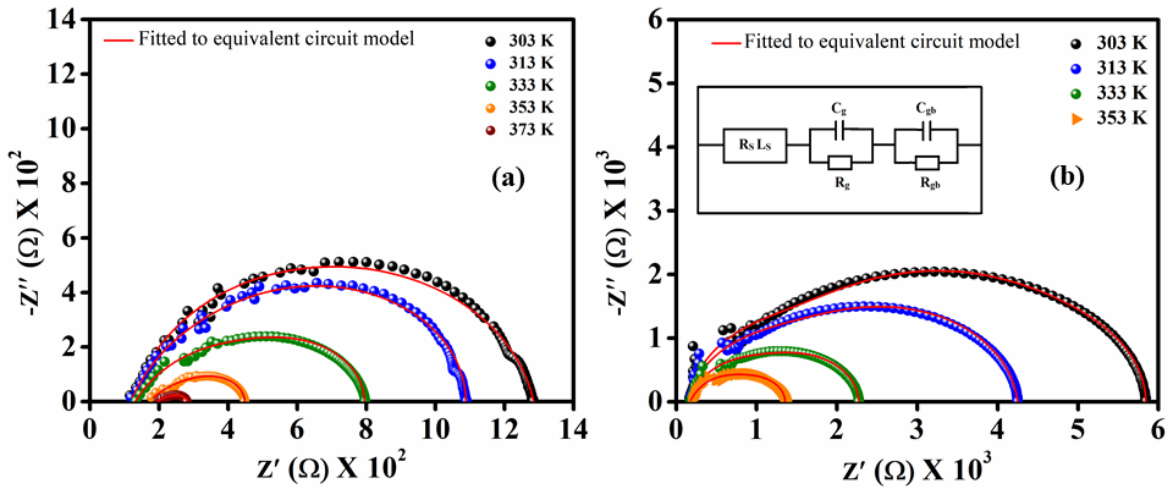

Figure 3.12: Nyquist plot of (a) Fe_3O_4 and (b) $Zn_{0.2}Fe_{2.8}O_4$ fitted with Maxwell-Wagner type equivalent circuit model (inset of (b)).

Each semicircle appearing in the Nyquist plot corresponds to the parallel RC component of the equivalent circuit. The grain resistance decreases with increasing temperature due to change in conductivity at higher temperature. The grain capacitance (C_g) is related to R_g via this equation:

$$\omega\tau = 2\pi f_{max} R_g C_g = 1 \qquad (3.3)$$

where, f_{max} is the frequency maxima of the semicircle and t is the relaxation time which

follows the Arrhenius law:

$$\tau = \tau_0 \exp\left(\frac{E_r}{k_B T}\right) \quad (3.4)$$

where, τ_0 is a pre-factor, E_r is the activation, T is absolute temperature and k_B is the Boltzmann Constant. From the slope of the plot between ln τ and 1000/T (Figure 3.13) activation energy is found out to be 0.01±0.001 eV for Fe_3O_4 and 0.07±0.009 eV for $Zn_{0.2}Fe_{2.8}O_4$. The E_r value increases with doping, which provides more hindrance to the movement of carriers through the grain regions in $Zn_{0.2}Fe_{2.8}O_4$, resulting in low dielectric response in this particular doping content compared to Fe_3O_4 NHSs.

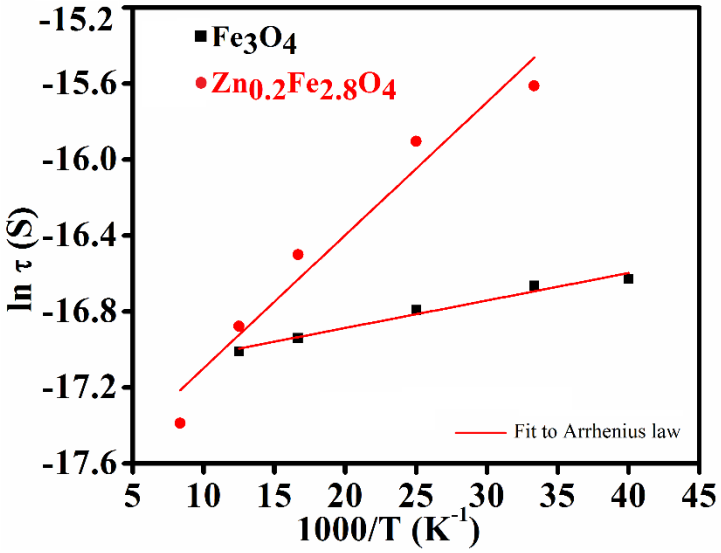

Figure 3.13: Arrhenius plot of relaxation time for Fe_3O_4 and $Zn_{0.2}Fe_{2.8}O_4$ NHSs.

Figure 3.14 shows the variation of ac conductivity (σ_{ac}) with frequency over 10 KHz to 100 MHz range at different temperature ranging from 303 K to 573 K. Below ~400 K the ac conductivity does not change significantly up to ~5 MHz and thereafter increases reaching a peak value beyond which a reduction is observed. The constant conductivity at low frequency is attributed to the inability of charge carriers to cross the energy barrier; however at higher frequency they gain sufficient energy to cross the barrier and increase conductivity. At very high frequency the carriers cannot follow the applied electric field and lag behind, resulting in reduced σ_{ac}. Above ~400 K σ_{ac} vs frequency curve does not show any peak. Instead a frequency independent flat curve indicates sufficient thermal energy to cross the energy barrier.

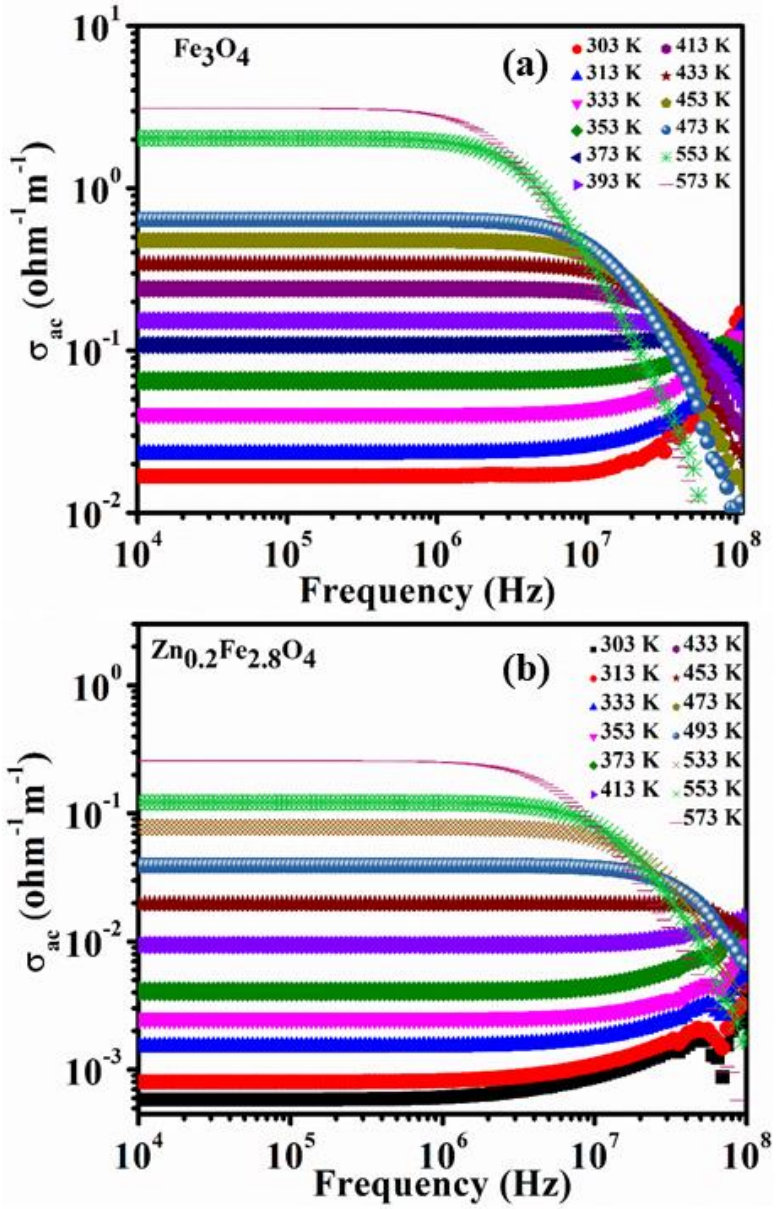

Figure 3.14: Variation of ac conductivity with frequency at different temperatures for (a) Fe_3O_4 and (b) $Zn_{0.2}Fe_{2.8}O_4$ NHSs.

From Figure 3.14 it is clear that the ac conductivity value of $Zn_{0.2}Fe_{2.8}O_4$ NHSs is lower than the undoped one, because of the reduction of both the spin hopping and itinerant (Fe^{2+}) charge carrier density in the octahedral site due to doping.

σ_{ac} of a material can be written as[30]

$$\sigma_{ac}(T) = \sigma_1(T) + \sigma_2(T) \quad (3.5)$$

Where the first term σ_1 (T) is the dc conductivity which corresponds to the drift of charge

carriers and the second one, σ_2 is the frequency dependent part of ac conductivity given by[31]:

$$\sigma_2(\omega, T) = A(T)\,\omega^{\eta}(T) \quad (3.6)$$

where, A has the unit of conductivity and η is dimensionless, which can be calculated from the slope of ln (σ_{ac}) vs. ln (ω) plot. Figure 3.15 shows the variation of η with temperature for our samples.

The nature of variation of η with temperature gives the idea of conduction mechanism in materials depending on different models[30,32–35]: (i) conduction can be explained by quantum mechanical tunnelling (QMT), when η is independent of temperature, (ii) correlated barrier hopping (CBH) is expected when η decreases with temperature and (iii) the increase in η with temperature can be correlated with small polaron conduction, while if η reaches a minimum followed by an increase with a further increase in temperature then the dominant conduction mechanism is an overlapping large polaron tunnelling (OLPT). From Figure 3.15, η decreases with increasing temperature, CBH as the conduction mechanism in undoped and Zn-doped Fe_3O_4 NHSs.

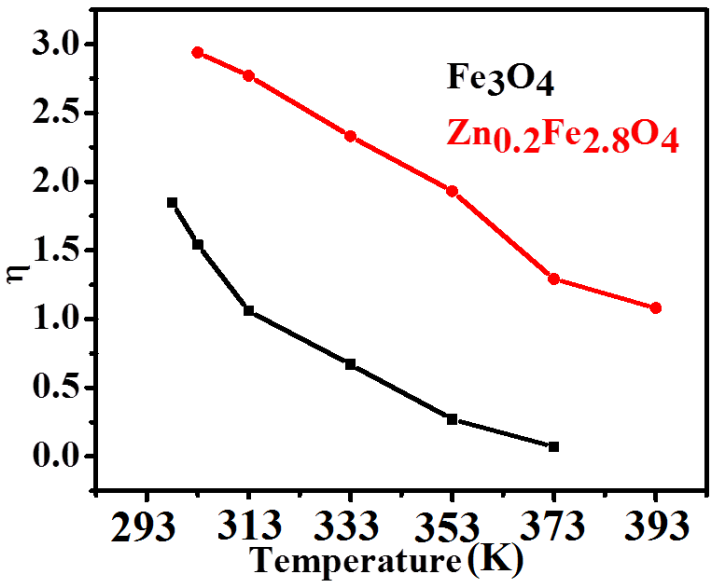

Figure 3.15: Variation of η with temperature for x=0.0 and 0.2.

3.3.4. Microwave Absorption Properties

According to the Globus equation $\mu' \propto \left(M_s^2 D/(K_1)^{1/2}\right)$, the higher saturation magnetization (M_s), larger grain size (D), and lower magnetocrystalline anisotropy constant

(K_1) may contribute to higher complex permeability. On the basis of the magnetic results, $Zn_xFe_{3-x}O_4$ NHSs with x=0.2 showing highest Ms is selected for microwave absorption (MA) measurement. The transmit-line theory relates the MA properties of a material to the frequency, thickness of the material, relative complex permittivity ($\varepsilon_r = \varepsilon' - j\varepsilon''$), and relative complex permeability ($\mu_r = \mu' - j\mu''$)). ε′ and μ′ represent the storage ability of electromagnetic (EM) energy, and ε″ and μ″ symbolize the dielectric and magnetic loss of the material. To study the MA properties of $Zn_{0.2}Fe_{2.8}O_4$ NHSs, the four EM parameters (ε′, ε″, μ′, and μ″) are measured at room temperature in the frequency range of 1–20 GHz. The frequency dependent variation of ε′, μ′ and the corresponding dielectric and magnetic tangent loss factors $\tan\delta_\varepsilon$ (=ε″/ε′), and $\tan\delta_\mu$ (=μ″/ μ′) are shown in Figure 3.16(a-b). ε′ decreases with frequency and it increases again in the frequency range of 10-18 GHz. In the experimental frequency range, dielectric polarization is originated from dipolar and interfacial polarization. The occurrence of a high-frequency peak at ~14 GHz suggests the presence of atomic polarization[36] and thus ε′ increases. From the frequency-dependent variation of $\tan\delta_\varepsilon$ in Figure 3.16(b), a dielectric relaxation peak is observed at ~9 GHz with a sufficiently high value of dielectric loss. Figure 3.16(a) shows, μ′ decreases sharply after 1 GHz followed by further increase near 18 GHz. Meanwhile $\tan\delta_\mu$ increases with an increase in frequency with occurrence of a relaxation peak at ~ 4 GHz and it increases again in the frequency range of 12-18 GHz. Typical morphology of NHSs enhances the surface magnetic anisotropy than bulk ferrites, which helps to achieve higher magnetic loss and EM wave absorption in the NHSs system[37]. Dynamic magnetic loss arises from magnetic hysteresis, domain wall resonance, eddy current effects, and natural and exchange resonance. Due to the presence of a low field in this study, the first two contributions are less effective for $Zn_{0.2}Fe_{2.8}O_4$ NHSs in the high-frequency region[38].

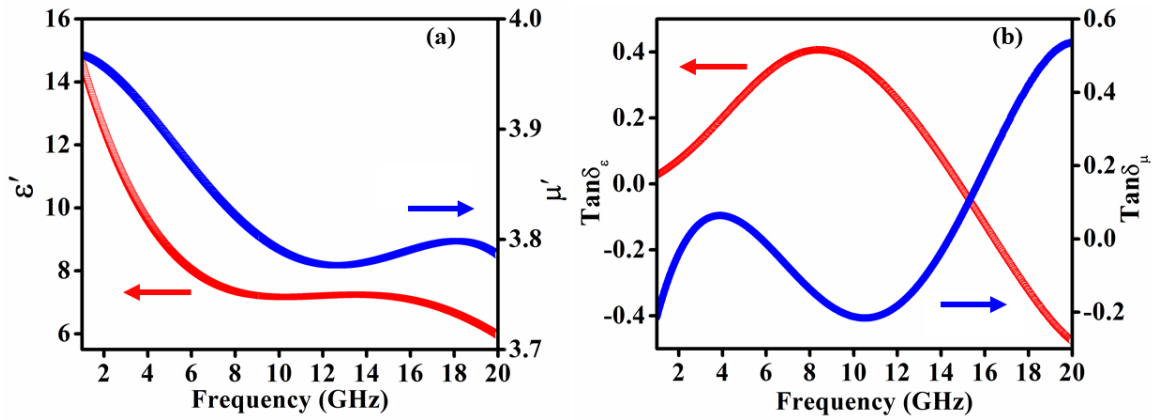

Figure 3.16: Frequency-dependent variation of (a) ε′, μ′, and (b) $\tan\delta_\varepsilon$, $\tan\delta_\mu$.

Dynamic magnetic properties of the ferrimagnets are strongly related to the parameters such as magnetic anisotropy and Saturation magnetization (MS), according to the Landau–Lifshitz–Gilbert (LLG) equation[39]. Moreover, the analysis from the Globus equation the contribution of eddy current loss to μ″ can be understood from the relation, connecting μ″ and electrical conductivity σ, expressed as $\mu'' \propto 2\pi\mu_0\mu'^2(d^2\sigma)f$, where d is the thickness of the sample (4 mm here) and μ_0 is the permeability of free space[40]. According to the above formula, if μ″ originates from eddy current loss, $\mu''(\mu')^{-2}f^{-1}$ vs f curve will show no peaks[41]. In order to understand the probable source of magnetic loss is our NHSs system frequency-dependent plot of $\mu''(\mu')^{-2}f^{-1}$ is shown in Figure 3.17, showing two visible peaks around 3.5 GHz and 18 GHz, suggesting resonance to be the main mechanism of high and low frequency magnetic losses.

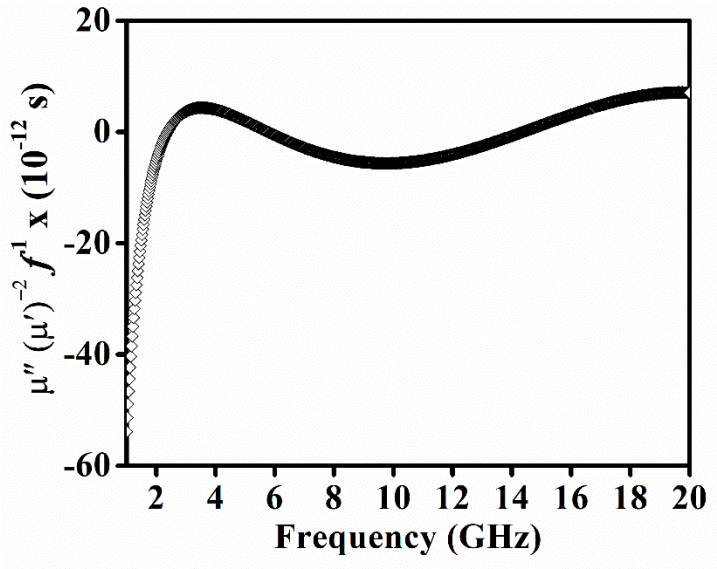

Figure 3.17: Frequency dependence of $\mu''(\mu')^{-2}f^{-1}$ in the frequency range 1-20GHz.

Reflection loss (RL) of EM waves gives insight towards the efficiency of a material to cut down the reflected waves and it is strongly correlated to the magnetic and electronic properties of the material. According to transmission line theory, RL of a microwave absorbing material can be calculated by the following formula[42–44]:

$$Z_{in} = Z_0 \sqrt{\frac{\mu_r}{\varepsilon_r}} \tanh\left[j\left(\frac{2\pi ft}{c}\right)\sqrt{\mu_r\varepsilon_r}\right] \quad (3.7)$$

$$RL = 20 \log \left|(Z_{in} - Z_0)/(Z_{in} + Z_0)\right| \quad (3.8)$$

where, *c* is the velocity of light in free space, *t*, thickness of the absorber composite, Z_0 and

Z_{in} are the impedance of free space and the input impedance of the absorber respectively.

The frequency dependence (1-20 GHz) of RL of the composite of various thicknesses (1-8 mm) made with epoxy resin and 25 wt% $Zn_{0.2}Fe_{2.8}O_4$ NHSs is shown in Figure 3.18. $Zn_{0.2}Fe_{2.8}O_4$ NHSs exhibits stronger dissipation with RL= −66.9 dB at 5.01 GHz and an effective bandwidth (BW) of ~7.71 GHz (frequency region for RL < −10 dB) at t=2.78 mm. Microwave absorption is strongly dependent on either (i) higher transmission of the incident wave that requires better impedance matching, i.e., $|Z_{in}/Z_0|$ ~1 or (ii) the dynamic combination of dielectric and magnetic loss[41,45]. The better MA property of $Zn_{0.2}Fe_{2.8}O_4$ NHSs is attributed to both the high dielectric and magnetic loss, as well as the best impedance matching achieved for t = 2.78 mm. Moreover, the incident EM waves form repeated oscillation inside the hollow cavity of the $Zn_{0.2}Fe_{2.8}O_4$ NHSs, giving rise to enhanced RL due to enhancement of the total propagation path[46,47]. The MA properties of various composite microwave absorber materials are listed in Table 3.3 and compared with $Zn_{0.2}Fe_{2.8}O_4$ NHSs.

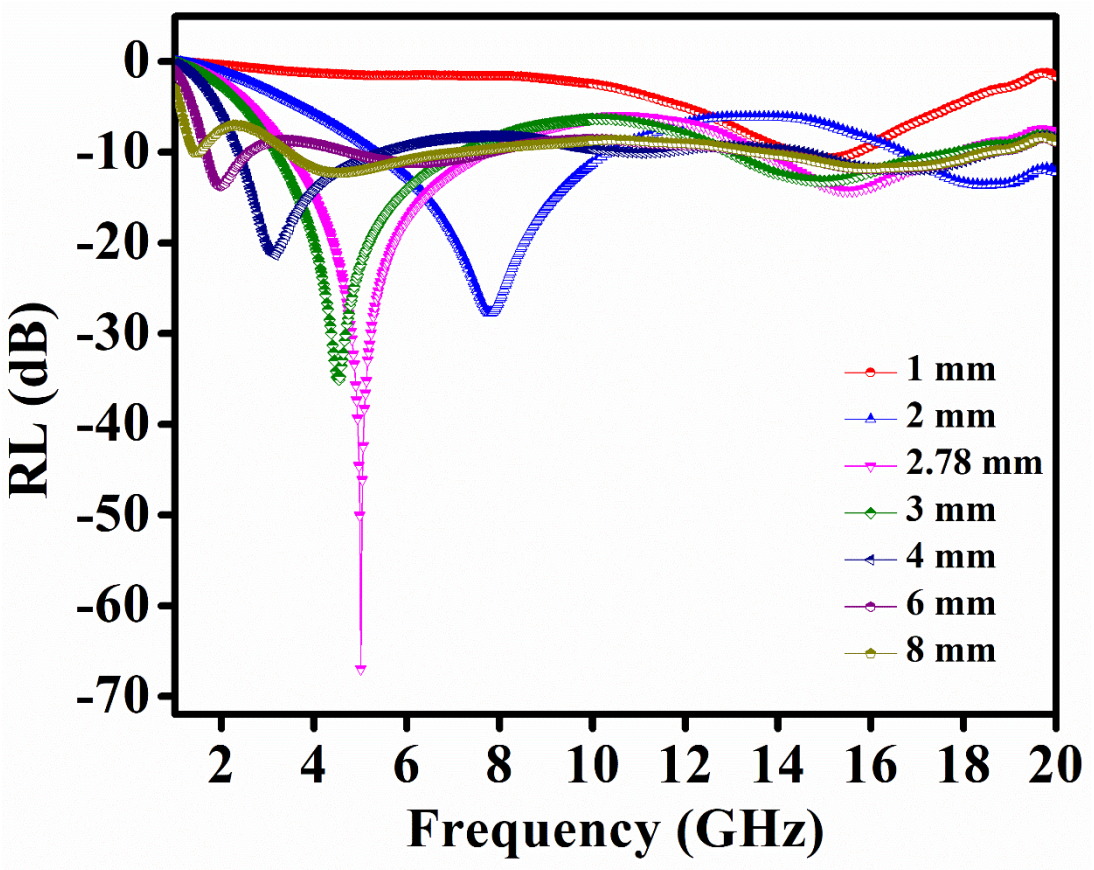

Figure 3.18: Frequency-dependent variation of reflection loss (RL) in the frequency range 1-20 GHz.

Table 3.3: Microwave absorption properties of magnetic metal, alloy and oxide-based MA materials

Sample	Matrix	Filler content (wt%)	D_{out} : d_{in} : t (mm)	RL (dB)	BW (GHz)
Porous Co/C nanocomposites[48]	Paraffin	15	3.01 : 6.99 : 1.82	− 38.8	5
Co-MnO_2 nanowires[49]	Paraffin	20	3 : 7 : 5	−24.8	1.2
Fe_3O_4 hollow nano-spheres[50]	Epoxy resin	68	7 : 3.04 : 6.9	−42.7	1
$MnFe_2O_4$@rGO nano-composites[51]	Polyvinylidene fluoride	5	7.0 : 3.04 : 3.0	−29.0	4.88
Sheet-shaped $ZnCo_2O_4$[52]	Paraffin	30	7.0 : 3.04 : 2.8	−43.61	7.12
CoNi alloy[53]	Paraffin	55	7.0 : 3.04 : 2.1	− 49.79	6.84
$Zn_{0.2}Fe_{2.8}O_4$ NHSs [This work]	Epoxy resin	25	3.5 : 1.5 : 2.78	−66.9	7.71

3.4. Conclusion

In conclusion, $Zn_xFe_{3-x}O_4$ nano hollow spheres were successfully prepared with higher value of saturation magnetization reaching a maximum at x=0.2. We found an increase in resistivity for the same Zn doping content due to reduction in spin hopping, which is effective in reducing eddy current, back-emf and other high frequency related negative effects. $Zn_{0.2}Fe_{2.8}O_4$ NHSs are found to show excellent microwave absorption properties with RL=−66.9 dB at 5.01 GHz for the composite thickness of only 2.78 mm, owing to its high value of the dielectric and magnetic loss, and EM wave trapping capacity inside the hollow cavity of NHSs. We believe these findings will lead to the potential application of this material in lightweight microwave attenuation devices. $Zn_{0.2}Fe_{2.8}O_4$ NHSs with highest magnetization can be an excellent material for magnetorheology as well.

Bibliography

1. Laurent, S. *et al.* Magnetic Iron Oxide Nanoparticles: Synthesis, Stabilization, Vectorization, Physicochemical Characterizations, and Biological Applications. *Chemical Reviews* **108**, 2064–2110 (2008).

2. Hong, J. P. *et al.* Room temperature formation of half-metallic Fe3O4 thin films for the application of spintronic devices. *Applied Physics Letters* **83**, 1590 (2003).

3. Liu, H. *et al.* Large room-temperature spin-dependent tunneling magnetoresistance in polycrystalline Fe3O4 films. *Applied Physics Letters* **83**, 3531 (2003).

4. Wang, X. *et al.* The application of Fe3O4 nanoparticles in cancer research: A new strategy to inhibit drug resistance. *Journal of Biomedical Materials Research Part A* **80A**, 852–860 (2007).

5. Ruan, X., Pei, L., Xuan, S., Yan, Q. & Gong, X. The rheological responds of the superparamagnetic fluid based on Fe3O4 hollow nanospheres. *Journal of Magnetism and Magnetic Materials* **429**, 1–10 (2017).

6. D. H. M. B. & Feldmann*, C. Nanoscale γ-AlO(OH) Hollow Spheres: Synthesis and Container-Type Functionality. *Nano Letters* **7**, 3489–3492 (2007).

7. Changwa Yao, † *et al.* ZnFe2O4 Nanocrystals: Synthesis and Magnetic Properties. *Journal of Physical Chemistry C* **111**, 12274–12278 (2007).

8. Jacintho, G. V. M., Brolo, A. G., Corio, P., Suarez, P. A. Z. & Rubim, J. C. Structural Investigation of MFe2O4 (M = Fe, Co) Magnetic Fluids. *Journal of Physical Chemistry C* **113**, 7684–7691 (2009).

9. He, Q., Wang, H. Z., Wen, G. H., Sun, Y. & Yao, B. Formation and properties of BaxFe3−xO4 with spinel structure by mechanochemical reaction of α-Fe2O3 and BaCO3. *Journal of Alloys and Compounds* **486**, 246–249 (2009).

10. Liping Li, †,§, Guangshe Li, *,†,‡, R. L. Smith, Jr. ,‡ and & Inomata‡, H. Microstructural Evolution and Magnetic Properties of NiFe2O4 Nanocrystals Dispersed in Amorphous Silica. *Chemistry of Materials* **12**, 3705–3714 (2000).

11. Mozaffari, M., Manouchehri, S., Yousefi, M. H. & Amighian, J. The effect of solution temperature on crystallite size and magnetic properties of Zn substituted Co ferrite nanoparticles. *Journal of Magnetism and Magnetic Materials* **322**, 383–388 (2010).

12. Irving, H. & Williams, R. J. P. 637. The stability of transition-metal complexes. *Journal of the Chemical Society (Resumed)* 3192–3210 (1953) doi:10.1039/JR9530003192.

13. Maaß, M., Griessner, A., Steixner, V. & Zierhofer, C. Reduction of eddy current losses in inductive transmission systems with ferrite sheets. *BioMedical Engineering OnLine 2017 16:1* **16**, 1–18 (2017).

14. Thompson, D. O. & Chimenti, D. E. Review of Progress in Quantitative Nondestructive Evaluation : Volume 2A. 1853 (1983).

15. Gorai, A., Mandal, D. & Mandal, K. Multi-layered nano-hollow spheres for efficient electromagnetic wave absorption. *Nanotechnology* **32**, 345707 (2021).

16. Takaobushi, J. *et al.* Electronic structures of <span class. *Physical Review B* **76**, 205108 (2007).

17. Takaobushi, J. *et al.* Fe3−xZnxO4 thin film as tunable high Curie temperature ferromagnetic semiconductor. *Applied Physics Letters* **89**, 242507 (2006).

18. Venkateshvaran, D. *et al.* Epitaxial <span class. *Physical Review B* **79**, 134405 (2009).

19. Liu, J., Bin, Y. & Matsuo, M. Magnetic Behavior of Zn-Doped Fe3O4 Nanoparticles

Estimated in Terms of Crystal Domain Size. *Journal of Physical Chemistry C* **116**, 134–143 (2011).

20. Das, A. R., Ananthan, V. S. & Khan, D. C. Lattice parameter variation and magnetization studies on titanium-, zirconium-, and tin-substituted nickel-zinc ferrites. *Journal of Applied Physics* **57**, 4189 (1998).

21. Z. R. Marand, M. H. R. F. N. S. Study of Magnetic and Structural and Optical Properties of Zn Doped Fe3O4 Nanoparticles Synthesized by Co-precipitation Method for Biomedical Application. *Nanomed Journal* **1**, 238 (2014).

22. Gupta, R., Sood, A. K., Metcalf, P. & Honig, J. M. Raman study of stoichiometric and Zn-doped <span class. *Physical Review B* **65**, 104430 (2002).

23. Clark, D. A. & Schmidt, P. W. Theoretical analysis of thermomagnetic properties, low-temperature hysteresis and domain structure of titanomagnetites. *Physics of the Earth and Planetary Interiors* **30**, 300–316 (1982).

24. Landi, G. T. *et al.* AC susceptibility as a tool to probe the dipolar interaction in magnetic nanoparticles. *Journal of Magnetism and Magnetic Materials* **421**, 138–151 (2017).

25. Dormann, J. L., Fiorani, D. & Tronc, E. Magnetic Relaxation in Fine-Particle Systems. 283–494 (2007) doi:10.1002/9780470141571.CH4.

26. Šimša, Z., Zounová, F. & Krupička, S. Initial permeability of single crystal magnetite and Mn-ferrite. *Czechoslovak Journal of Physics B 1985 35:11* **35**, 1271–1281 (1985).

27. Idzikowski, B., Rößler, U. K., Eckert, D., Nenkov, K. & Müller, K.-H. Spin-glass–like ordering in giant magnetoresistive CuCo. *EPL (Europhysics Letters)* **45**, 714 (1999).

28. Tholence, J. L. On the frequency dependence of the transition temperature in spin glasses. *Solid State Communications* **35**, 113–117 (1980).

29. Das, R., Sarkar, T. & Mandal, K. Multiferroic properties of Ba2+ and Gd3+ co-doped bismuth ferrite: magnetic, ferroelectric and impedance spectroscopic analysis. *Journal of Physics D: Applied Physics* **45**, 455002 (2012).

30. Gopalan, E. V. *et al.* Evidence for polaron conduction in nanostructured manganese ferrite. *Journal of Physics D: Applied Physics* **41**, 185005 (2008).

31. Jonscher, A. K. The 'universal' dielectric response. *Nature 1977 267:5613* **267**, 673–679 (1977).

32. Pandit, P., Satapathy, S. & Gupta, P. K. Effect of La substitution on conductivity and dielectric properties of Bi1−xLaxFeO3 ceramics: An impedance spectroscopy analysis. *Physica B: Condensed Matter* **406**, 2669–2677 (2011).

33. Meaz, T. M., Attia, S. M. & Abo El Ata, A. M. Effect of tetravalent titanium ions substitution on the dielectric properties of Co–Zn ferrites. *Journal of Magnetism and Magnetic Materials* **257**, 296–305 (2003).

34. Ghosh, A. ac conduction in iron bismuthate glassy semiconductors. *Physical Review B* **42**, 1388 (1990).

35. Fayek, M. K., Mostafa, M. F., Sayedahmed, F., Ata-Allah, S. S. & Kaiser, M. On the electrical behavior of nickel ferrite-gallates. *Journal of Magnetism and Magnetic Materials* **210**, 189–195 (2000).

36. He, J.-Z., Wang, X.-X., Zhang, Y.-L. & Cao, M.-S. Small magnetic nanoparticles decorating reduced graphene oxides to tune the electromagnetic attenuation capacity. *Journal of Materials Chemistry C* **4**, 7130–7140 (2016).

37. Liu, X. *et al.* Flexible nanocomposites with enhanced microwave absorption properties based on Fe3O4/SiO2 nanorods and polyvinylidene fluoride. *Journal of Materials Chemistry A* **3**, 12197–12204 (2015).

38. Liu, P., Huang, Y., Yan, J. & Zhao, Y. Magnetic graphene@PANI@porous TiO2 ternary composites for high-performance electromagnetic wave absorption. *Journal of Materials Chemistry C* **4**, 6362–6370 (2016).

39. Gilbert, T. L. & L., T. Classics in Magnetics A Phenomenological Theory of Damping in Ferromagnetic Materials. *ITM* **40**, 3443–3449 (2004).

40. Gorai, A., Mandal, D. & Mandal, K. Multi-layered nano-hollow spheres for efficient electromagnetic wave absorption. *Nanotechnology* **32**, 345707 (2021).

41. Zhang, Y. *et al.* Nanolayered Cobalt@Carbon Hybrids Derived from Metal–Organic Frameworks for Microwave Absorption. *ACS Applied Nano Materials* **2**, 2325–2335 (2019).

42. Han, M. *et al.* Graphene-wrapped ZnO hollow spheres with enhanced electromagnetic wave absorption properties. *Journal of Materials Chemistry A* **2**, 16403–16409 (2014).

43. Wang, D. J., Zhang, J. Y., He, P. & Hou, Z. L. Size-modulated electromagnetic properties and highly efficient microwave absorption of magnetic iron oxide ceramic opened-hollow microspheres. *Ceramics International* **45**, 23043–23049 (2019).

44. Xue, W., Yang, G., Bi, S., Zhang, J. & Hou, Z. L. Construction of caterpillar-like hierarchically structured Co/MnO/CNTs derived from MnO2/ZIF-8@ZIF-67 for electromagnetic wave absorption. *Carbon* **173**, 521–527 (2021).

45. Yang, Z., Li, Z., Yang, Y. & Xu, Z. J. Optimization of ZnxFe3–xO4 Hollow Spheres for Enhanced Microwave Attenuation. *ACS Applied Materials and Interfaces* **6**, 21911–21915 (2014).

46. Han, M. *et al.* Graphene-wrapped ZnO hollow spheres with enhanced electromagnetic wave absorption properties. *Journal of Materials Chemistry A* **2**, 16403–16409 (2014).

47. Wang, F. *et al.* Template free synthesis and electromagnetic wave absorption properties of monodispersed hollow magnetite nano-spheres. *Journal of Materials Chemistry* **21**, 4314–4320 (2011).

48. Xie, P. *et al.* Hierarchically porous Co/C nanocomposites for ultralight high-performance microwave absorption. *Advanced Composites and Hybrid Materials* **4**, 173–185 (2021).

49. Duan, Y., Liu, Z., Jing, H., Zhang, Y. & Li, S. Novel microwave dielectric response of Ni/Co-doped manganese dioxides and their microwave absorbing properties. *Journal of Materials Chemistry* **22**, 18291–18299 (2012).

50. Wang, F. *et al.* Template free synthesis and electromagnetic wave absorption properties of monodispersed hollow magnetite nano-spheres. *Journal of Materials Chemistry* **21**, 4314–4320 (2011).

51. Zhang, X. J. *et al.* Enhanced microwave absorption property of reduced graphene oxide (RGO)-MnFe2O4 nanocomposites and polyvinylidene fluoride. *ACS Applied Materials and Interfaces* **6**, 7471–7478 (2014).

52. Wang, J., Wang, B., Feng, A., Jia, Z. & Wu, G. Design of morphology-controlled and excellent electromagnetic wave absorption performance of sheet-shaped ZnCo2O4 with a special arrangement. *Journal of Alloys and Compounds* **834**, 155092 (2020).

53. Gu, W. *et al.* Extending effective microwave absorbing bandwidth of CoNi bimetallic alloy derived from binary hydroxides. *Scientific Reports 2020 10:1* **10**, 1–11 (2020).

Chapter 4

Magnetic, Dielectric, and Microwave Absorption Properties of Magnesium Ferrite Nano Hollow Spheres

This chapter demonstrates synthesis of $Mg_xFe_{3-x}O_4$ nano-hollow spheres with x=0.0, 0.2, 0.3, 0.4 and 1.0 doping content. Variation of structural, magnetic and dielectric responses of as-synthesized different $Zn_xFe_{3-x}O_4$ nano-hollow spheres with different doping content are studied in detail. Owing to the unique magnetic and dielectric response of $Mg_{0.3}Fe_{2.7}O_4$ broadband microwave absorption properties are obtained.

4. Unusual dielectric properties of $Mg_xFe_{3-x}O_4$ Magnetic Nano-Hollow Spheres: A Potential Lightweight Microwave Absorber

4.1. Preamble

Magnetic semiconductors are at the heart of modern devices and technological applications in material physics. These magnetic materials naturally provide spin-dependent bandgap, non-zero magnetic moment below the ordering temperature and spin polarization that originates from exchange-coupled magnetization[1–5]. Some of the strongly correlated spinel ferrites with low bandgap are amongst the most significant candidates for semiconductor spintronics[6,7]. $MgFe_2O_4$ is a magnetic semiconductor with unique magnetic and electrical properties, enabling it to be an excellent material for semiconductor spintronics[8,9]. Various studies have been carried out so far on the magnetic properties of $MgFe_2O_4$ with various morphologies[10–14], doping and cation distribution[15–17]. Wu et al. showed crystallographic defect mediated negative magnetoresistance in $MgFe_2O_4$ thin-film[8]. S. Rahman et al. recently reported Zn-doped $MgFe_2O_4$ exhibits insulators to metal transitions[18]. J. Sláma et al. showed metamagnetism in manganate magnesium ferrite[19]. However, detailed literature study reveals that less attention has been paid to understand the unique electrical properties of $MgFe_2O_4$. These findings led us to carry out a detailed study on the electrical and magnetic properties of $Mg_xFe_{3-x}O_4$ nano hollow-spheres (NHSs) with various doping concentrations of Mg to unravel the effect of morphology and doping on the electrical and magnetic properties.

Nano hollow spherical morphology has some special advantage over the solid counterpart owing to its low density, higher surface to volume ratio, better dispersibility in liquid. Moreover, due to the presence of two surfaces in the shell region, nano-hollow spheres (NHSs) can offer unique magnetic and electrical properties[20]. R. Rakshit et al. showed hollow-sphere induced ferromagnetism in antiferromagnetic Co_3O_4 in the micrometre length-scale[21]. Here $Mg_xFe_{3-x}O_4$ NHSs show temperature-dependent negative dielectric permittivity and it compliments them further for the potential application in wave absorbing, wave transmission in antennas, electromagnetic radiation shields. Negative permittivity is one of the key characteristics of the unique metamaterial or negative index

material (NIM). The permittivity of the NIM is not, or is just weakly, dependent on chemical structures and interactions among different components in the materials. In other words, the unusual properties of metamaterials are determined by their specially designed structures, rather than their compositions[22]. At present only very few materials are reported to show negative dielectric constant[23–29]. In general, it is difficult to obtain negative permittivity in natural materials. So far, various metamaterials have been artificially designed by physicists and electrical engineers to obtain negative permittivity, and in all these cases resonance is considered to be the main mechanism of negative permittivity. In contrast, the negative permittivity from innate physical properties of chemically synthesized materials has not yet achieved attention from material researchers. Moreover, among the very few works reported on metamaterials, all the research in this field is focused on metallic, ceramic, and polymer materials, and less attention has been paid to conventionally synthesized transition metal oxides. The observed negative permittivity in $Mg_xFe_{3-x}O_4$ NHSs is attributed to the surface effect of this special morphology in the vicinity of metamagnetic transition.

In this chapter, we bring together the structural, dielectric and magnetic properties of $Mg_xFe_{3-x}O_4$ nano-hollow spheres (NHSs), to unravel the effect of morphology and cationic order distribution on the electronic and magnetic response, along with the experimental evidence of negative dielectric permittivity and metamagnetism in $Mg_{0.3}Fe_{2.7}O_4$ NHSs. The correlation of the magnetic and dielectric properties with the origin of a high dielectric constant is analyzed. Finally, owing to the high magnetic permeability and dielectric permittivity, excellent electromagnetic wave absorption property is achieved for $Mg_{0.3}Fe_{2.7}O_4$ NHSs.

4.2. Experimental Section

4.2.1. Materials Used

The precursor salts, Magnesium Chloride ($MgCl_2$, $6H_2O$) and Ferric Chloride ($FeCl_3$, $6H_2O$), urea (CH_4N_2O) and surfactant oleylamine ($C_{18}H_{37}N$) are obtained from Sigma-Aldrich. All the reagents are of analytical grade and used without further purification. Ethylene glycol and ethyl alcohol are used as solvents.

4.2.2. Synthesis of Nano-Hollow Spheres

$Mg_xFe_{3-x}O_4$ (x=0.0, 0.2, 0.3, 0.4 & 1) NHSs are synthesized using a facile template free solvothermal method through proper variation of $MgCl_2,6H_2O$ and $FeCl_3$, 6H2O, to maintain the stoichiometry for different doping concentration. In the typical synthesis of $Mg_xFe_{3-x}O_4$ NHSs, y g of $FeCl_3.6H_2O$, z g of $MgCl_2,6H_2O$ and 0.43 g of urea are dissolved in 30 ml solvent mixture of 20 ml Ethylene glycol & 10 ml Ethanol, which are stirred until clear homogeneous solution was obtained. The amounts of used precursor salts are listed in Table 4.1. Thereafter, 1 ml of oleylamine which is a growth modifier as well as surface stabilizer is added to the solution mixture in order to restrict the particle growth in nanometer size range. The properly mixed final solution is transferred into 40 ml Teflon lined stainless steel autoclave and heated to 180°C for 20 h followed by natural cooling to room temperature. The resulting black precipitate is thoroughly washed with absolute ethanol and DI water to remove all residual reagents, and separated by centrifugation. The as-obtained product is dried at 60°C for 12 h. At the elevated temperature urea decomposed to ammonia which produced hydroxyl groups. These hydroxyl groups precipitated the hydroxides of magnesium and ferric ions and finally $Mg_xFe_{3-x}O_4$ NHSs formed.

Table 4.1: Amount of precursor salts used in the NHSs synthesis

x	$MgCl_2,6H_2O$ in g	$FeCl_3.6H_2O$ in g
0.0	0	1.35
0.2	0.135	1.17
0.3	0.21	1.09
0.4	0.28	1.05
1.0	0.69	0.81

4.2.3. Characterization

The phase of the prepared samples are characterized by a PANalytical X'Pert PRO X-ray diffractometer equipped with Cu Kα radiation (λ=1.5418 Å) radiation. To understand the morphology of the as-prepared MgxFe3-xO4 samples are analysed in FEG high-resolution transmission electron microscope (HRTEM) (80–200 kV) and a FEI QUANTA FEG 250 field-emission scanning electron microscope (FESEM) (0.2–30 kV). The magnetic

measurements are performed with a vibrating sample magnetometer (VSM), Lake Shore-7144. Local I-V characteristic to understand grain and grain boundary response of nanomaterial is studied using a Bruker (di INNOVA) conductive atomic force microscope (C-AFM). The electromagnetic (EM) wave absorption properties of $Mg_{0.3}Fe_{2.7}O_4$ NHSs are performed using an Anritsu MS46122B vector network analyzer and a coaxial airline (Maury Microwaves-8043S6). The composite sample for microwave measurements is prepared by loading 25 wt% powder samples in an epoxy resin matrix. The final composite is in a hollow cylindrical shape with inner diameter (d_{in}) = 1.5 mm, outer diameter (d_{out}) = 3.5 mm and thickness (d) = 3.12 mm. Analysis from 2-port scattering (S)-parameters measured in transmission line technique is performed using Nicholson-Ross-Weir algorithm.

4.3. Results and Discussion

4.3.1. Structural Properties

The X-ray diffraction patterns with Rietveld Refinement in Figure 4.1(a) confirm the formation of spinel $Mg_xFe_{3-x}O_4$ (x=0.0, 0.2, 0.3, 0.4 & 1) with face centered cubic structure (JCPDS card no. 42-0181), without any impurity or secondary phase. To understand the variation of lattice parameters with Mg doping, an enlarged version of the (311) x-ray diffraction peak is shown in Figure 4.1(b). This indicates that the lattice constant alternatively increases and decreases with increasing Mg doping concentration in $Mg_xFe_{3-x}O_4$. Figure 4.3(c) summarizes all the calculated values of lattice constant for different values of x. To identify the reason for the zigzag variation of lattice constant with Mg doping, we calculate the cation distribution through a full phase Rietveld refinement of XRD pattern in Fullprof software by considering the cubic space group of $Fd\bar{3}m$ in $Mg_xFe_{3-x}O_4$.

The Rietveld refinement data, as summarized in Table 4.2, shows the existence of mixed spinel structure with the cation distribution of $[Mg_{\delta}^{2+}Fe_{(1-\delta)}^{3+}]_A[Mg_{(x-\delta)}^{2+}Fe_{(1-\delta)}^{2+}Fe_{(1-x+2\delta)}^{3+}]_BO_4$, where δ is the inversion degree, defined as the amount Mg^{2+} ions entering the A site. For x=0.0, there is no inversion degree, indicating the traditional inverse spinel structure of Fe_3O_4. For x=0.2, an extremely small inversion degree of δ=0.003 is observed which indicates a major replacement of Fe_B^{3+} ion and minor replacement of Fe_A^{3+} ion by

Mg^{2+} ion followed by the simultaneous transformation of Fe_B^{2+} into Fe_B^{3+} ion for maintaining the charge neutrality. The overall increase in the lattice constant for x=0.2 is owed to the major replacement of Fe_B^{3+} ion with the ionic radius of 63 pm by Mg^{2+} ion of larger ionic radius (72 pm). For x=0.3, the inversion degree of δ=0.01 is observed, indicating that Mg^{2+} ion starts to replace Fe_B^{2+} ion significantly along with the replacement of Fe_B^{3+} and Fe_A^{3+}. Here the lattice constant decreases due to the replacement of Fe_B^{2+} ion of larger ionic radius (77 pm) by the Mg^{2+} ion which has a smaller ionic radius of 72 pm. The inversion degree becomes δ=0.02 for x=0.4 and Mg^{2+} starts replacing Fe_A^{3+} ions from the A site in a considerable amount along with the Fe_B^{3+} and Fe_B^{2+} ions replacements from the B site. As a whole, the lattice parameter increases due to the major replacement of Fe_A^{3+} (63 pm) by the Mg^{2+} (72 pm) and the system becomes similar to that of x=0.0. Finally, the lattice constant becomes minimum for $MgFe_2O_4$ (x=1.0), with δ=0.1 due to the major replacement of Fe_A^{2+} ions (63 pm) by Mg^{2+} (72 pm) and transformation of Fe_B^{2+} (77 pm) into Fe_B^{3+} (63 pm).

Table 4.2: List for doping concentration (x), inversion degree (δ), cation distribution, and lattice constant from Rietveld refinement of the XRD data of $Mg_xFe_{3-x}O_4$.

x	δ	$[Mg_{\delta}^{2+}Fe_{(1-\delta)}^{3+}]_A[Mg_{(x-\delta)}^{2+}Fe_{(1-\delta)}^{2+}Fe_{(1-x+2\delta)}^{3+}]_BO_4$	Lattice constant (Å)	Lattice spacing (nm)
0.0	0.0	$[Fe^{3+}]_A[Fe^{2+}Fe^{3+}]_BO_4$	8.3907±0.0008	0.253
0.2	0.003	$[Mg_{0.003}^{2+}Fe_{0.997}^{3+}]_A[Mg_{0.197}^{2+}Fe_{0.8}^{2+}Fe_{1.003}^{3+}]_BO_4$	8.4027±0.0006	0.2533
0.3	0.01	$[Mg_{0.01}^{2+}Fe_{0.99}^{3+}]_A[Mg_{0.29}^{2+}Fe_{0.7}^{2+}Fe_{1.01}^{3+}]_BO_4$	8.3718±0.0005	0.2524
0.4	0.02	$[Mg_{0.02}^{2+}Fe_{0.98}^{3+}]_A[Mg_{0.38}^{2+}Fe_{0.6}^{2+}Fe_{1.02}^{3+}]_BO_4$	8.3897±0.0007	0.2529
1.0	0.1	$[Mg_{0.1}^{2+}Fe_{0.9}^{3+}]_A[Mg_{0.9}^{2+}Fe_{1.1}^{3+}]_BO_4$	8.3668±0.0009	0.2523

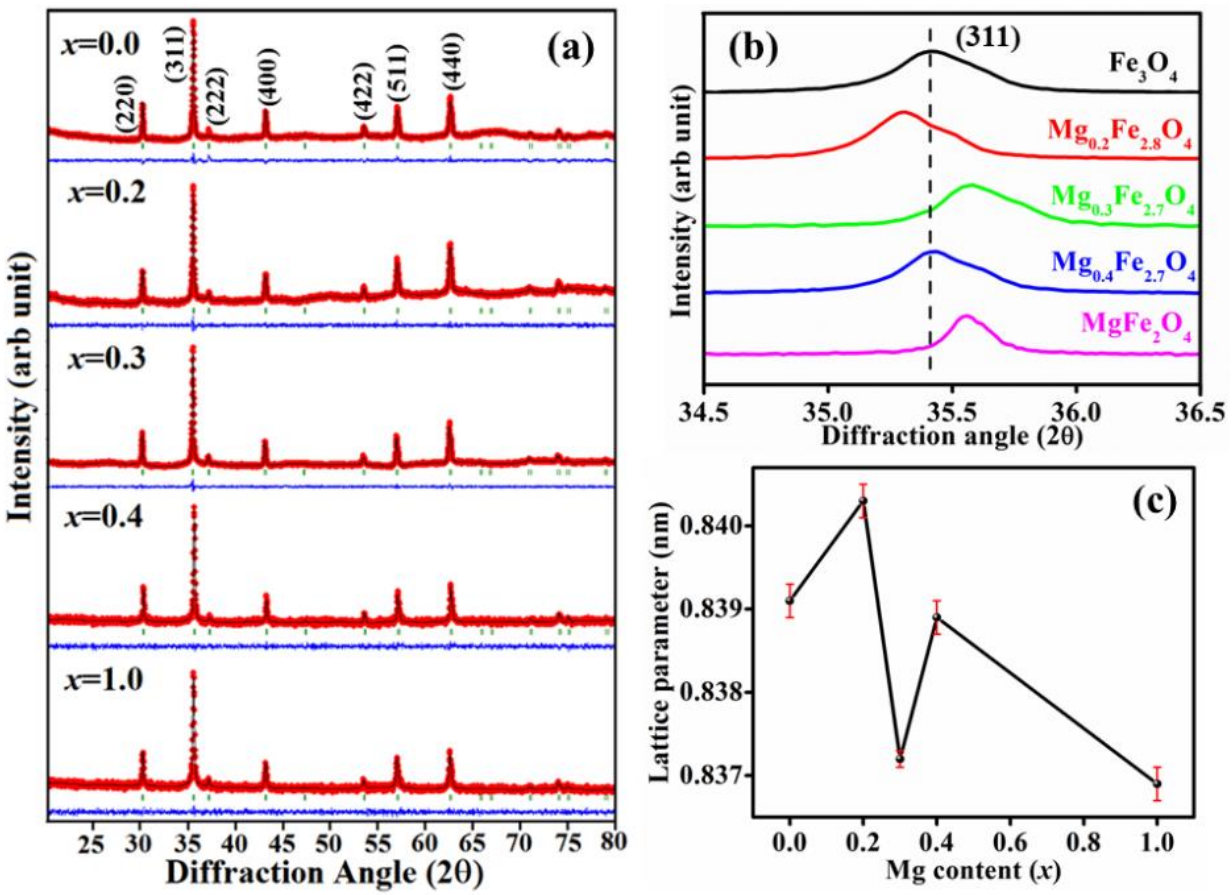

Figure 4.1: (a) XRD pattern with Rietveld refinement, (b) enlarged version of (311) diffraction peak, and (c) variation of lattice parameter with Mg doping content of $Mg_xFe_{3-x}O_4$ (x=0.0, 0.2, 0.3, 0.4 & 1) NHSs.

4.3.2. Morphological Properties

FESEM and TEM micrographs for all doping percentages of $Mg_xFe_{3-x}O_4$ samples are examined for morphological analysis, as shown in Figure 4.2. FESEM micrographs of all the samples are shown in Figure 4.2(a-e). From the surface morphology hollow spherical structure formation is confirmed with uniform size distribution. The average size of the NHSs calculated from FESEM images are 400 nm, as evident from the size distribution curves in Figure 4.2(k-o).

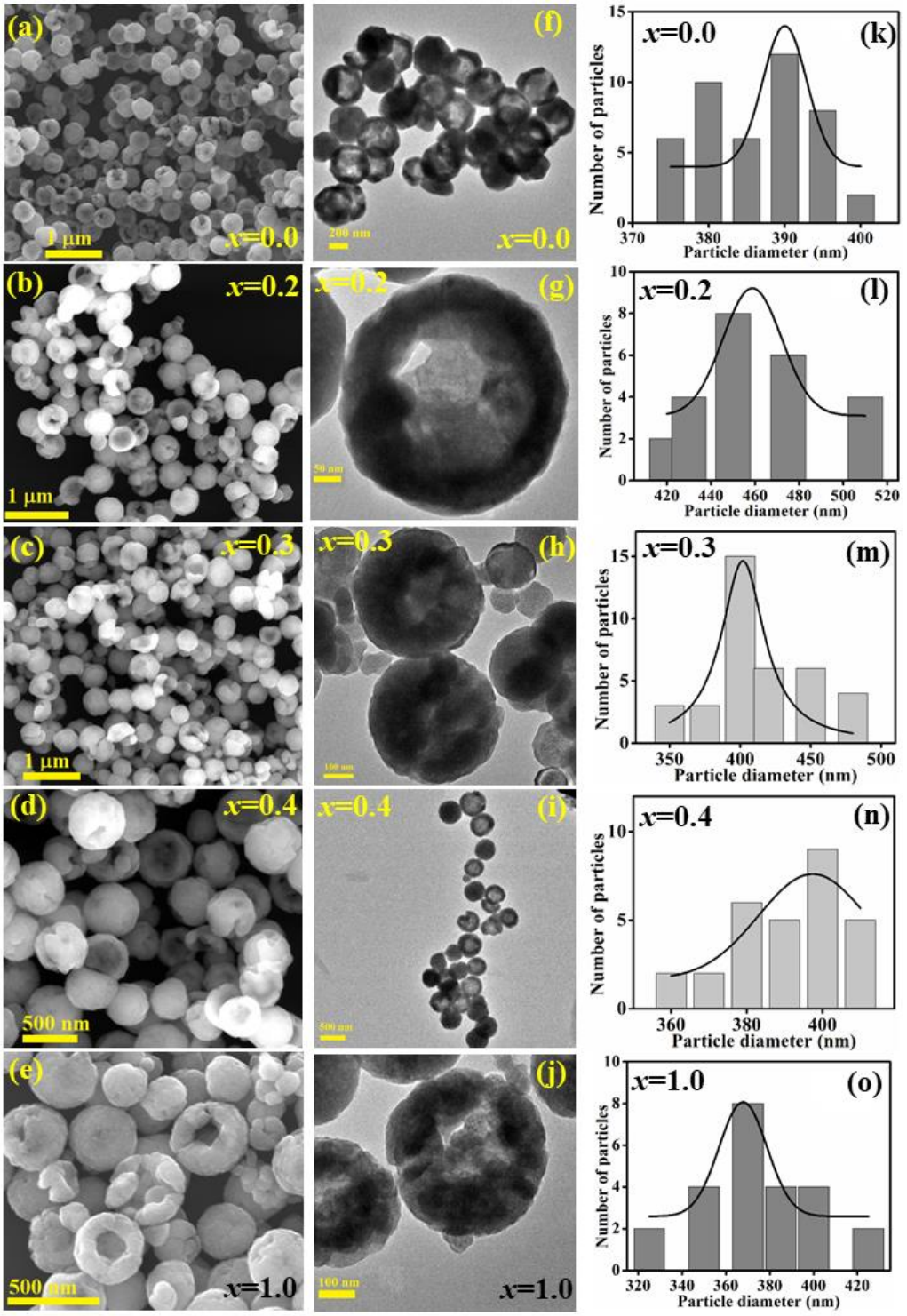

Figure 4.2: (a-e) FESEM micrographs, (f-j) TEM micrographs, and (k-o) size distribution curves calculated from FESEM images of $Mg_xFe_{3-x}O_4$ (x=0.0, 0.2, 0.3, 0.4 & 1) NHSs.

For detail analysis of the hollow interior TEM analysis is performed. TEM images of $Mg_xFe_{3-x}O_4$ NHSs are shown in Figure 4.2 (f-j). From the intensive contrast between the lighter inner region and darker outer edges of the TEM images the formation

of hollow spheres is confirmed for all doping concentrations. The formed NHSs are of shell thickness ~100 nm.

4.3.3. Dielectric Properties

Room temperature (RT) dielectric properties are investigated for $Mg_xFe_{3-x}O_4$ NHSs by studying the dielectric permittivity ε′ and dielectric tangent loss, tanδ. The frequency dispersion behavior of ε′ and tanδ, shown in Figure 4.3 (a) and (b) respectively, can be explained by the classical Debye type or Cole-Cole type dipole relaxation process. The origin of dipoles in the $Mg_xFe_{3-x}O_4$ cubic spinel system is attributed to the presence of mix valent Fe^{2+} and Fe^{3+} cations surrounded by oxygen anions in the octahedral site. Due to the action of the externally applied electric field, the center of the cations gets shifted with respect to the center of the anions in an alternating motion. As the frequency increases, the response of the dipoles to the oscillating external field reduces, leading to the decreased dielectric response. Dielectric spectra attain a maximum value of ε′ and a pronounced peak of tanδ for x=0.3. According to Koop's theory, the dielectric polarization is mainly attributed to the charge carrier fluctuation in the conducting grain regions and the accumulation of space charges at the highly resistive grain boundary (GB) regions. Therefore, the dielectric behavior for various doping concentrations can be well understood by studying the resistance and capacitance of the grains in $Mg_xFe_{3-x}O_4$ NHSs[30].

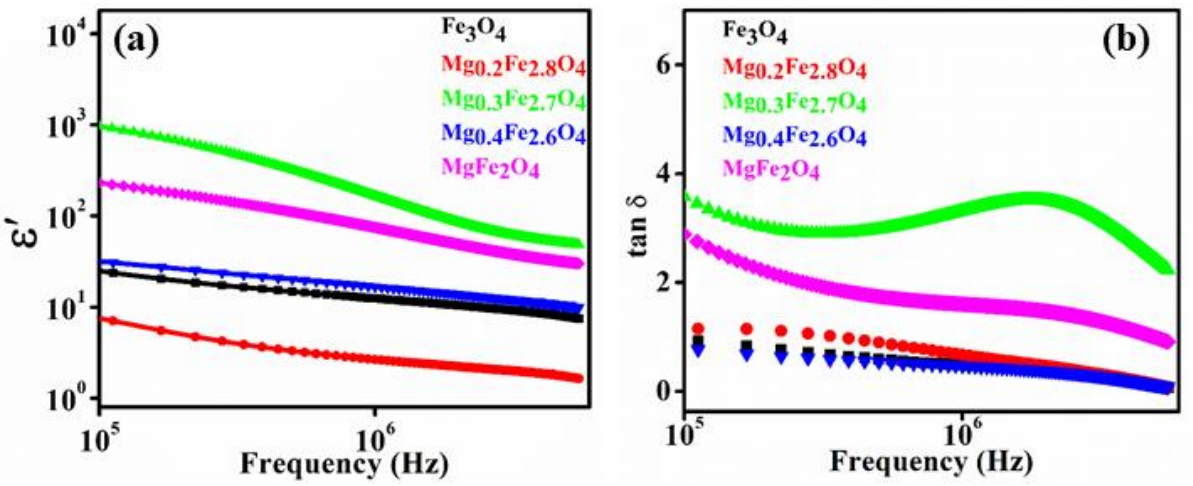

Figure 4.3: Frequency dependent variation of (a) ε′ and (b) tanδ for $Mg_xFe_{3-x}O_4$ NHSs at RT.

In order to explain the trend of ε′ and tanδ for various doping concentrations, we

calculate the resistance and capacitance of the grain by analyzing the Nyquist plot between the imaginary (-Z′′) and real part (Z′) of impedance, as shown in Figure 4.4(a-e) for $Mg_xFe_{3-x}O_4$ NHSs, fitted to equivalent circuit model, shown in the inset of Figure 4.4(c), consisting of two parallel RC circuits, $R_g||C_g$ (contribution from grain) and $R_{gb}||C_{gb}$ (contribution from GB) and R connected in series, which represents the contribution from measuring leads and electrodes. The variation of R_g and C_g with x is shown in Figure 4.3(f) and the inset of Figure 4.3(f) respectively. From Figure 4.3(a) and Figure 4.4(f), it is observed that ε′ varies complementarily with R_g for various doping concentrations (x). The dielectric polarization due to the oscillation of dipoles faces low restrain with the decrease in grain resistance, resulting in maximum ε′ for the minimum value of R_g in x=0.3. The increase in ε′ also increases the capacitive effect of the grain. This is mainly due to the accumulation of charges at the GB, termed as Maxwell-Wagner (MW) interfacial polarization. In the high-frequency region, the dipoles are unable to follow the applied frequency field reversal and thus results in a significant dielectric loss. The comparison of Figure 4.3(b) and the inset of Figure 4.4(f) reveals that tanδ shows a prominent peak for x=0.3 in the high-frequency region due to the pronounced capacitive effect and interfacial polarization. The absence of interfacial polarization for other doping concentrations leads to a low capacitive effect. Overall, the dielectric spectra of $Mg_xFe_{3-x}O_4$ NHSs reveal that the dipolar polarization contributes in the low-f region ($f<10^6$ Hz) whereas in the high-frequency region ($f>10^6$ Hz) the MW interfacial polarization is significant.

For the quantitative estimation of grain and grain boundary (GB) resistances, we have further studied the local electrical transport properties of nanoscale grain and GB for x=0.0 and x=0.3, showing the highest and lowest R_g and R_{gb} respectively from dielectric analysis, by using C-AFM. Figure 4.5(a) and (e) show the AFM micrographs of x=0 and 0.3 respectively, and Figure 4.5(b) and (f) represent the corresponding C-AFM images. Grain and GB regions are visible from the AFM micrographs.

To study the local I-V characteristics, the AFM tip is separately positioned on the bright conductive grain and darker grain boundary, as marked with a yellow circle in the C-AFM images. I-V curves of the grain and GB regions for x=0, shown in Figure 4.5(c) and (d) respectively, clearly indicate higher resistance for GB than the grain itself. A similar characteristic is also observed for x=0.3, shown in Figure 4.5(g) and (h), for grain and GB respectively. By comparing the local I-V curves associated with each sample, a higher C-

AFM signal is found to pass through the grain for x=0.3, indicating a lower R_g of $Mg_{0.3}Fe_{2.7}O_4$ compared to that of Fe_3O_4. Moreover, the I-V curves for GB regions indicate that the current can only pass through GB above the applied voltage of 4 V and 3.3 V for x=0.0 and 0.3 respectively, suggesting a lower R_{gb} of $Mg_{0.3}Fe_{2.7}O_4$, compared to that of Fe_3O_4. Therefore, the combined effect of low R_g and R_{gb} helps in dipolar and MW interfacial polarization and thus enhances the capacitance (C_g) of $Mg_{0.3}Fe_{2.7}O_4$ compared to that of Fe_3O_4. These C-AFM results are in accordance with that of Nyquist plots, as shown in Figure 4.4(f) and support the highest ε′ and tanδ for $Mg_{0.3}Fe_{2.7}O_4$, as shown in Figure 4.3(a) and (b) respectively.

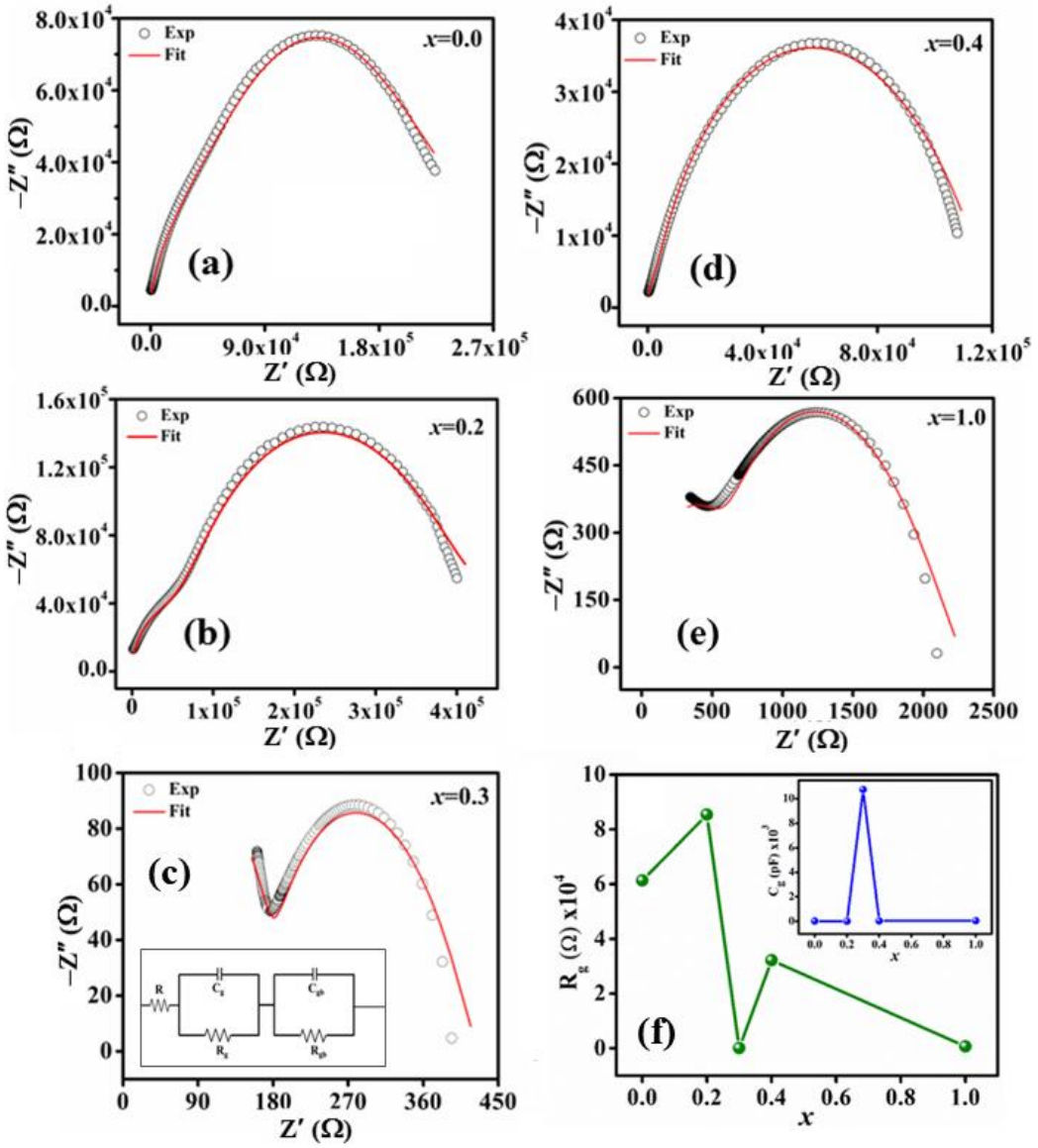

Figure 4.4: (a-e) Nyquist plot of $Mg_xFe_{3-x}O_4$ NHSs fitted with the equivalent circuit model shown in the inset of Figure (c). (f) Variation of grain resistance with Mg doping content (x), where the inset Figure shows the variation of grain capacitance with x.

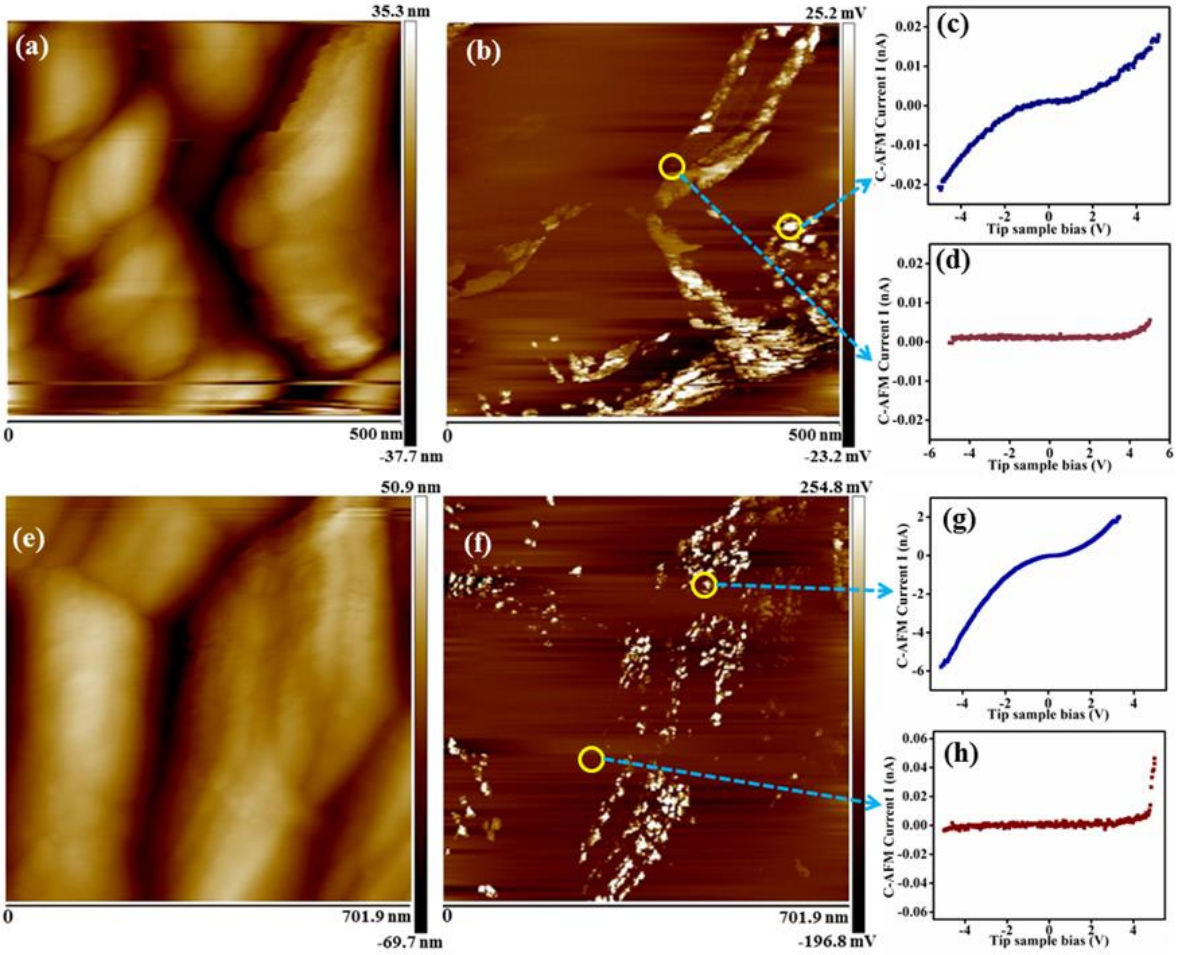

Figure 4.5: AFM image, C-AFM image, and local I-V characteristics of the grain and grain boundary regions respectively for (a-d) x=0.0 and (e-h) x=0.3.

To get a clear insight into the mechanism of dielectric polarization, the temperature-dependent dielectric response is studied over a wide temperature range of 373 K-573 K for $Mg_{0.3}Fe_{2.7}O_4$ NHSs which shows the highest RT dielectric response. The frequency dispersion of ε′ for $Mg_{0.3}Fe_{2.7}O_4$ NHSs can be divided into three temperature regions: (1) Region I (323 K-373 K): ε′ decrease with increase in frequency as evident from Figure 4.6(a), (2) Region II (383 K-473 K): This can be subdivided into three frequency zones where zone I: ε′ is positive and decrease with an increase in f, zone II: ε′ becomes negative and decreases with an increase in f, and zone III: ε′ is negative and start to increase with an increase in f as shown in Figure 4.6(b), and (3) Region III (503 K-573K): ε′ increases in the low f range (1kHz-3kHz) and attains saturation in the intermediate f range (10^4 Hz-10^5 Hz) followed by a decrease in the high f region (10^5-10^6 Hz), as evident from Figure 4.6(c).

In region I, ε′ decreases with an increase in f because the low characteristics dipolar frequency restricts the dipoles to follow the high-frequency field reversal. In region II, the positive decrease of ε′ with frequency in the zone I can be explained by the same reasoning as region I, while the negative decrease of ε′ with f in zone II and the negative increase in zone III cannot be explained in terms of ordinary frequency effect. To explain the peculiar frequency dispersion of negative ε′, temperature-dependent magnetization study (M-T) is performed on $Mg_{0.3}Fe_{2.7}O_4$ NHSs over the temperature range of 300 K-600 K, showing a gradual increase with temperature in the range 300-500 K and then reaches to saturation in the temperature range of 500K-600K, for an applied magnetic field value of 50 Oe, suggesting a metamagnetic transition[31], shown in Figure 4.3(d), due to the change in the spin arrangement of Fe^{3+} ions from antiferromagnetic to ferromagnetic alignment. This also suggests a strong spin-polaron coupling in $Mg_{0.3}Fe_{2.7}O_4$ NHSs[32]. Since the increase in ferromagnetism increases the metallicity of the material due to parallel spin alignment[33], the dipolar fluctuation significantly increases in the temperature range of 300 K-500 K. The negative decrease of ε′ with f in zone II is due to high dipolar fluctuation assisted backscattering from the GB while the negative increase in zone III is due to metallicity induced surface skin effect. The hollow spherical morphology with two surfaces in the shell region contributes more in the backscattering process compared to its solid counterpart, owing to the presence of GB on both surfaces. The surface skin effect significantly increases the effective resistance and helps ε′ transition from negative towards positive value in the high-frequency range. Overall, the competition between backscattering effect in the low-frequency region and skin effect in the high-frequency region results in a dip in negative ε′ across (10^5-10^6 Hz) and ε′ tries to approach towards positive value.

In addition to the frequency dispersion of ε′, Figures 4.6(a) and (b) also reveal that ε′ spectra decrease with an increase in temperature in the high-frequency range. The oscillation of cations with respect to the anions is better facilitated with an increase in temperature, resulting in an increase in ε′ spectra in the low-frequency range. However, the decrease in e¢ spectra with temperature in the high-frequency range is quite unexpected. This can be related to temperature-induced high dipolar fluctuation assisted backscattering from the GB and decreases e¢ with an increase in temperature in the high-f range. More interestingly, the frequency at which ε′ changes from positive

to negative value also shifts towards lower f with an increase in temperature. This is due to an increase in back-scattering which supports negative ε′ and thus can be easily achieved at low-frequency with the increase in temperature.

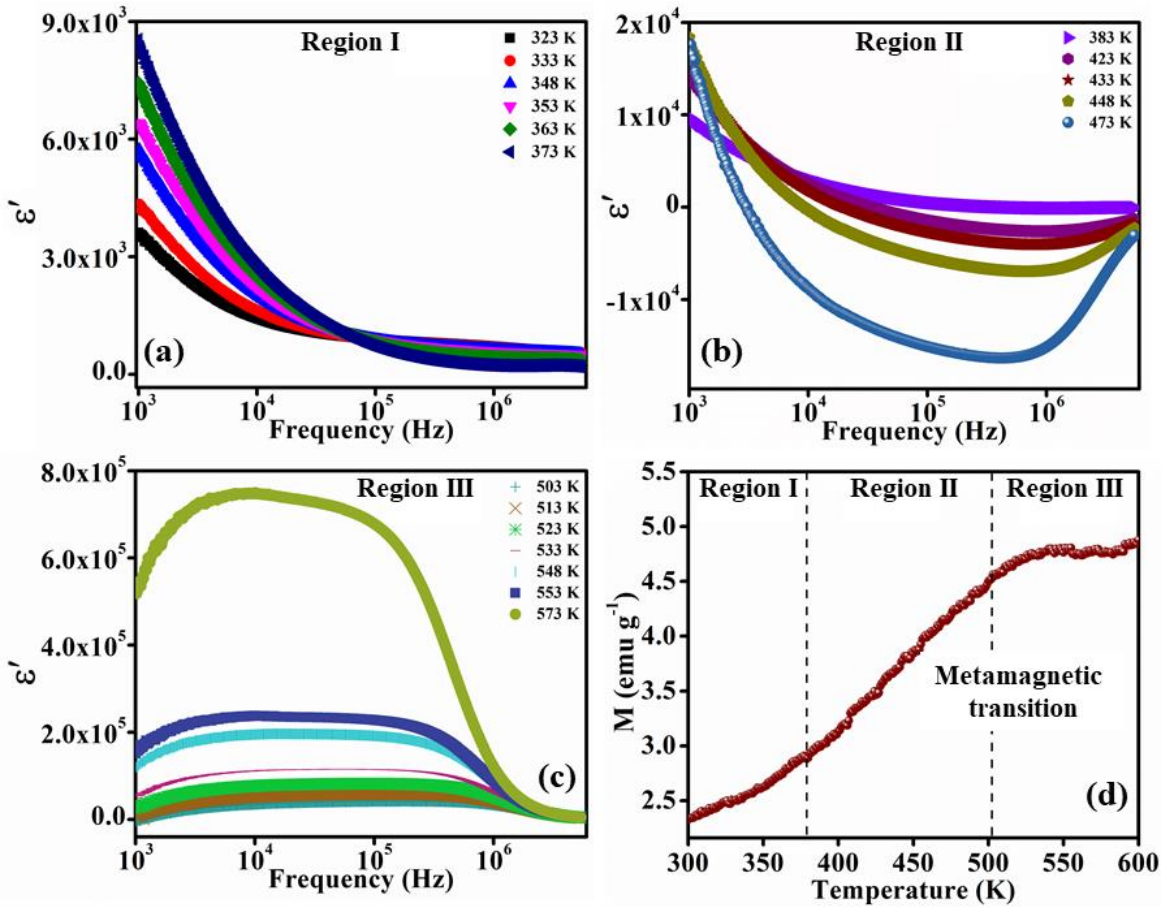

Figure 4.6: Variation of ε′ with frequency in temperature region (a) I, (b) II and (c) III, and (d) temperature-dependent magnetization curve of $Mg_{0.3}Fe_{2.7}O_4$ NHSs.

In region III, ε′ increases with frequency from 1 kHz-3 kHz and after remaining constant up to ~ 50 kHz, it decreases with frequency, as shown in Figure 4.6(c). The positive increasing trend of ε′ in the frequency range of 1 kHz-3 kHz indicates the dominant contribution of skin effect over back-scattering phenomena in region III. The constant ε′ in the frequency range of 3 kHz-50 kHz is due to saturation of skin effect with maximum possible metallicity in $Mg_{0.3}Fe_{2.7}O_4$ NHSs. This metallicity gives rise to strong dipolar fluctuation and significantly increases the characteristic dipolar frequency which results in resonance with a high constant ε′ in the frequency region (3 kHz - 50 kHz), as compared to region I and II. Beyond 50 kHz, ε′ decreases due to

growing mismatch between dipolar characteristic frequency and externally applied frequency.

Similar to ε′, the frequency-dependent dielectric loss (tanδ) for various temperatures in Figure 4.7 can also be separable into three temperature regions, (1) Region I (323 K-373 K), (2) Region II (383 K-473 K), and (3) Region III (503 K-573 K). In region I, tanδ decreases with frequency due to low characteristic dipolar frequency, shown in Figure 4.7(a). Moreover, the increase in tanδ with temperature is due to the enhancement of ε′ in region I. In region II, the unusual fluctuations in tanδ are observed, where the dielectric loss profile reaches a positive maximum followed by a negative minimum, suggesting some internal resonance. This positive to negative transition in tanδ takes place at the same frequency at which ε′ changes from positive to negative value, suggesting resonance due to backscattering of the dipole, as evident from Figure 4.7(b). Therefore, the higher value of dielectric loss in region II is due to the backscattering of dipoles from the GB, with maximum tanδ at 473 K (inset of Figure 4.7(b)), where maximum negative ε′ is obtained. Negative loss phenomenon is related to the fact that more energy must be released than absorbed. According to the principle of energy conservation, the total energy in the material must be conserved. Therefore, there must be some mechanism in this material that allows to store energy and release it only at certain temperatures and at certain frequencies. The negative loss phenomenon is attributed to local non-compensated charges, which are accumulated at the material interfaces or pores. The separation of charges leads to the accumulation of energy and this is a metastable state. This metastable state is eliminated under certain temperature and frequency, causing energy emission[34]. In region III, a steep change of tanδ with frequency is observed, unlike region I and it decreases with an increase in temperature, as shown in Figure 4.7(c). In general, dielectric loss occurs due to the resistance suffered by the dipole at the GB[35]. Since region III belongs to a high-temperature region, a strong dipolar fluctuation reduces the GB resistance, leading to a decrease in tanδ with the increase in frequency as well as temperature.

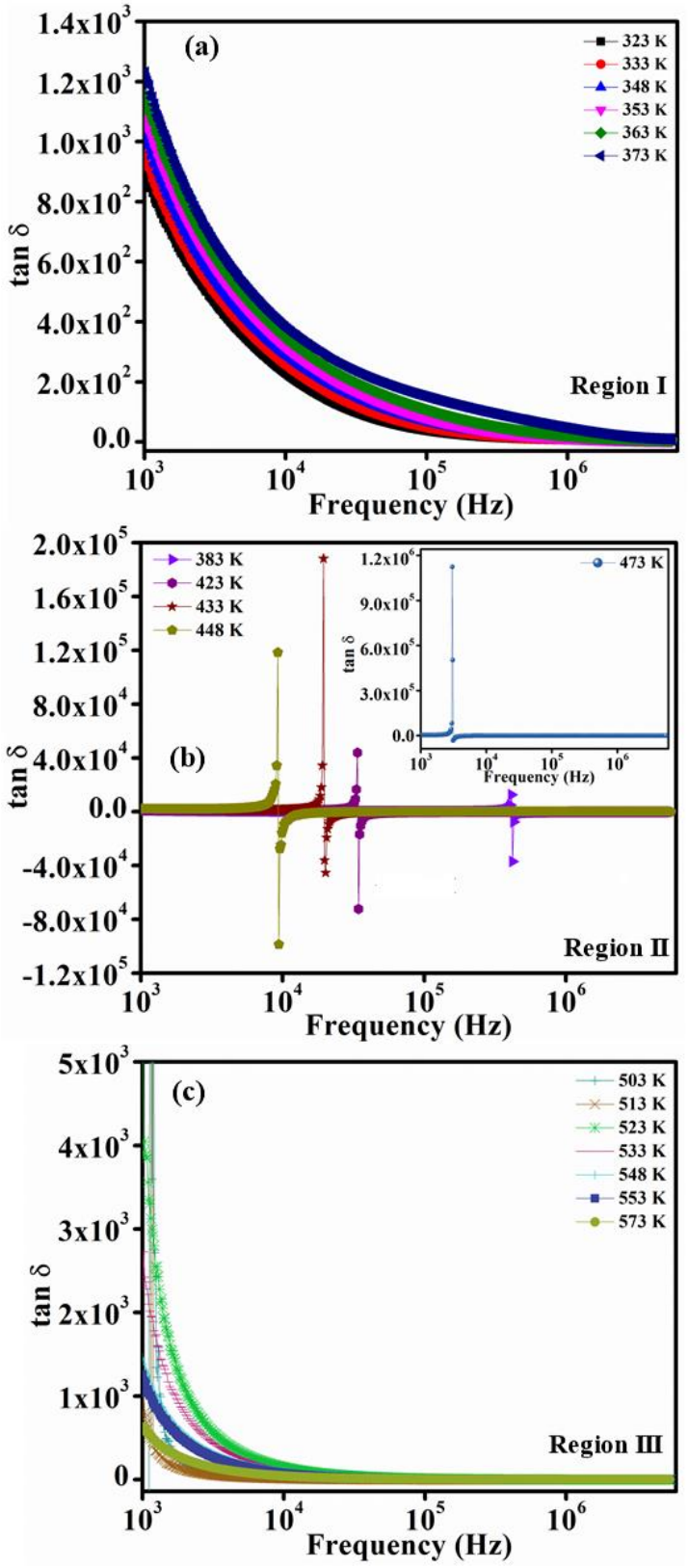

Figure 4.7: Variation of dielectric tangent loss with frequency for $Mg_{0.3}Fe_{2.7}O_4$ NHSs in temperature region (a) I, (b) II and (c) III.

4.3.4. Electrical Conduction Properties

Electrical conduction in ferrites occurs due to the hopping of charge carriers between $Fe_B^{2+} \leftrightarrow Fe_B^{3+}$. The RT ac conductivity (σ_{ac}) in $Mg_xFe_{3-x}O_4$ NHSs follow the same trend as RT dielectric polarization, with a maximum for x=0.3 and minimum for x=0.2, as evident from Figure 5 (a), which is due to the lowest and highest grain and GB resistances of x=0.3 and 0.2 respectively. At low-frequency, σ_{ac} increases slowly with f as the GB regions are more active due to its frequency-dependent capacitive behavior[32] and hopping between $Fe^{2+} \leftrightarrow Fe^{3+}$ ions is very much hindered within grain because of less energy. However, σ_{ac} increases rapidly at a higher frequency, when the conductive grains are very much active due to increased hopping between the neighboring ions. With further increase in frequency σ_{ac} decreases due to relaxation.

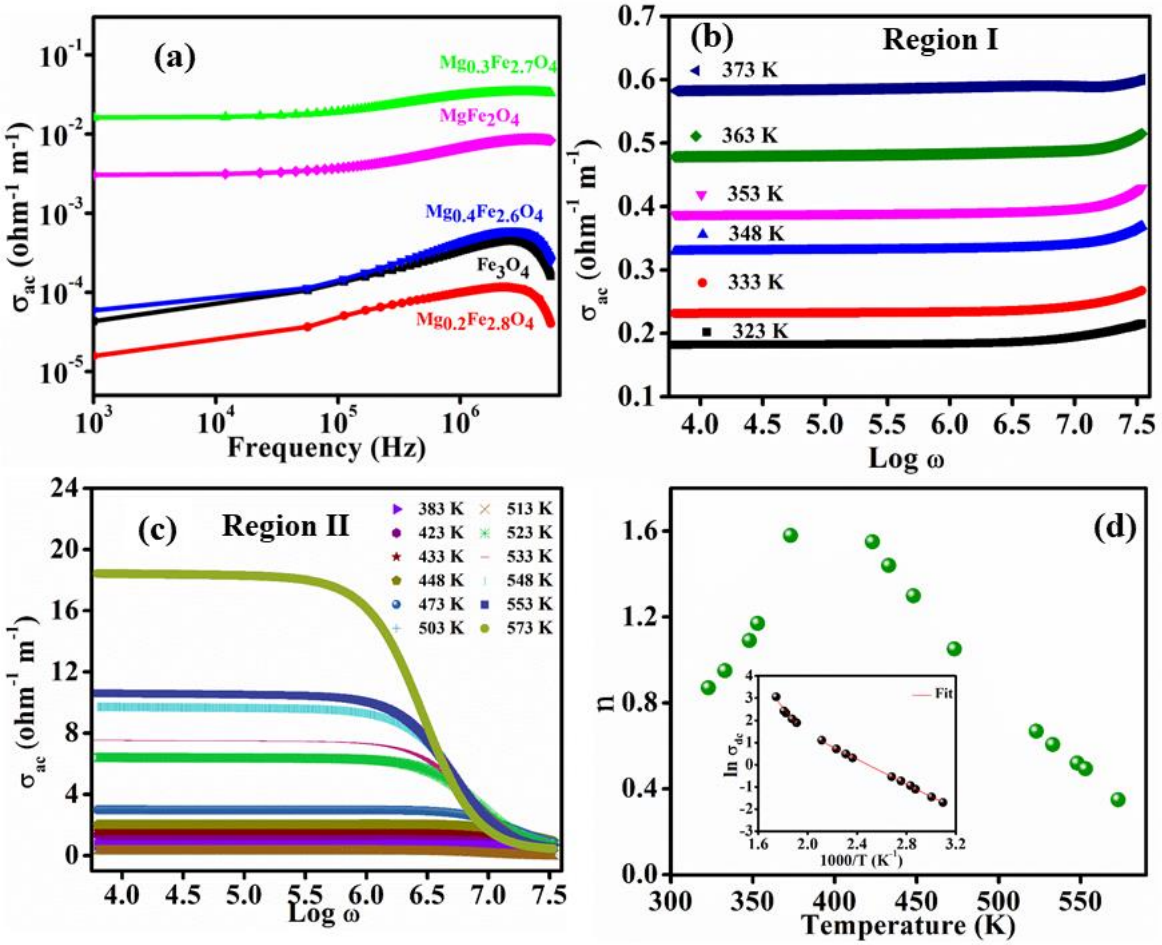

Figure 4.8: (a) Variation of σ_{ac} with frequency of $Mg_xFe_{3-x}O_4$ NHSs at RT. Frequency dependence of σ_{ac} in temperature region (b) I and (c) II. (d) Temperature dependence of n, where inset Figure shows the variation of σ_{dc} with temperature for $Mg_{0.3}Fe_{2.7}O_4$ NHSs.

For better understanding of the mechanism of ac conduction in $Mg_{0.3}Fe_{2.7}O_4$ NHSs with the highest ac conductivity, the frequency dependence of σ_{ac} over the temperature range of 373 K-573 K is shown in Figure 4.8(b-c). Variation of σ_{ac} with temperature can be divided into two regions, Region I (323 K-373 K) and region II (383 K-573 K). In region I σ_{ac} is found to increase at higher f from Figure 4.8(b) when the frequency of external electric field matches that of polaron hopping. At low-frequency, σ_{ac} remains nearly constant due to the inability of the charge carriers to cross the potential barrier. In region II, from Figure 4.8(c), after the frequency-independent plateau region, σ_{ac} decreases with f due to the appearance of skin effect and increased metallicity in x=0.3, as understood from the M-T curve in Figure 4.6(d).

The frequency-dependent behavior of σ_{ac} is explained by Jonscher's Power Law[36], governed by the Equation

$$\sigma_{ac} = \sigma_{dc} + A\omega^n \quad (4.1)$$

where σ_{dc} is dc conductivity (frequency-independent plateau region) and n is the power-law exponent. The σ_{ac} spectra are fitted with Equation 1. Figure 4.8(d) shows the variation of fitting parameter n with temperature, where the inset of Figure 4.8(d) displays the reciprocal temperature dependence of σ_{dc}. From the variation of n with temperature, the conduction mechanism in the $Mg_{0.3}Fe_{2.7}O_4$ NHSs system can be well understood. n increases rapidly with temperature up to 400 K, beyond which it reduces. The degree of interaction between the charge carriers and the lattice is represented by n, where n=1 implies pure Debye-type dielectric behavior, indicating negligible interaction between neighboring dipoles[37]. According to Jonscher's power law, n lies between $0<n<1$. However, we observed $n>1$ over the temperature range of 350-450 K. Experimentally obtained values of $n>1$ have been reported in lithium ferrite[38]. Values of $n>1$ represent a nearly linear increase of σ_{ac} with frequency and near-constant losses[39,40]. After 500 K, n reaches 0.4, indicating increased interaction between the charge carriers and lattice. From the nature of variation of n with temperature we can conclude that in the high-temperature region when n decreases with increase in temperature, correlated barrier hopping is the active conduction mechanism; whereas in low-temperature region small polaron conduction is predominant[41]. Variation of σ_{dc} with inverse temperature shows that it increases with the increase in temperature.

The increase is rapid after 500 K as observed from the slope of the fitted curves. Activation energy is calculated from the slopes and is found to be 0.589ev and 0.243ev from high and low-temperature regions respectively.

4.3.5. Magnetic Properties

The magnetization curves (M-H) at room temperature and 80 K are shown in Figure 4.9(a) and (b) respectively for $Mg_xFe_{3-x}O_4$ NHSs. Magnetization data show that with increasing Mg-doping saturation magnetization (M_s) reduces up to x=0.3 and then enhances again at x=0.4, followed by a further reduction for x=1.0. Variation of M_S with x is shown in the inset of Figure 4.9(b) for 300 K and 80 K, showing similar nature of variation with temperature change. The net magnetization in Fe_3O_4 is contributed from the Fe_B^{2+} ions, as the magnetic contribution from the antiferromagnetically coupled Fe^{3+} ions of A and B sites is nullified. At x=0.2, divalent Mg^{2+} replaces the trivalent Fe_B^{3+} ion from the octahedral B site and to maintain the overall charge neutrality Fe_B^{2+} transforms into Fe_B^{3+}. As the net magnetization in Mg-doped Fe_3O_4 is contributed from the Fe_B^{2+} ions, M_S decreases due to reduced Fe_B^{2+} ion density. For x=0.3, M_S decreases further due to the replacement of Fe_B^{2+} ions by Mg^{2+}. Along with the replacement of Fe_B^{2+} and Fe_B^{3+} ions from the octahedral B site, at x=0.4, Mg^{2+} starts replacing Fe_A^{3+} from the tetrahedrally coordinated A site in a considerable amount and transformation of Fe_B^{2+} to Fe_B^{3+} takes place. This in turn cancels out the nullification of magnetization from antiferromagnetically coupled Fe^{3+} ions between A and B sites and the magnetic contribution increases, becoming nearly equal to that of x=0. In $MgFe_2O_4$ (x=1.0) M_S becomes minimum due to the replacement of nearly all the Fe_A^{3+} ions by Mg^{2+}. M_S increases at 80K due to the reduced thermal vibration of the spins at lower temperature and thus better spin alignment along the applied field direction.

For better understanding of the nature of magnetic behavior, the temperature dependence of magnetization is performed following the zero-field cooled (ZFC) and field cooled (FC) procedure. The ZFC curves show certain maxima as evident from Figure 4.10(a-e) for x=0.0 and 0.3. The higher temperature peak (T_V) around 120 K corresponds to Verwey transition, which is a temperature-dependent structural transition from cubic (low resistive) to monoclinic (high resistive) state. Figure 4.10(f) shows the variation of T_V with x. With Mg^{2+} replacing Fe^{2+} / Fe^{3+}, a change in phonon vibration frequency is expected, which in

turn changes T_V[42]. T_V varies inversely with the frequency of phonon vibration ($\boldsymbol{\nu}$), which can be expressed as:

$$\boldsymbol{\nu} = \frac{\mathbf{1}}{\mathbf{2\pi}}\sqrt{\frac{\boldsymbol{k}}{\boldsymbol{m_r}}} \tag{4.2}$$

where k is the bond strength and m_r is the reduced mass of the system. Both k and m_r change with Mg doping; m_r decreases due to lower mass of Mg^{2+} compared to Fe^{2+} / Fe^{3+}, whereas k varies in the same fashion as the lattice parameter with x (Figure 4.1(c)). Figure 4.10(f) shows the resultant effect of Mg-doping on T_V. The 2nd cusp like maximum observed in each ZFC curve at low temperature represents the spin freezing temperature (T_F), at which the randomness of spins is frozen. T_F is determined by the thermal energy required to overcome the super-exchange interaction[43]. From the inset of Figure 4.10(f), T_F increases with Mg-doping, indicating stronger super-exchange interaction. For x=1.0 major amount of Fe_A^{3+} ions are replaced by Mg^{2+} and due to dilution of super-exchange interaction T_F decreases.

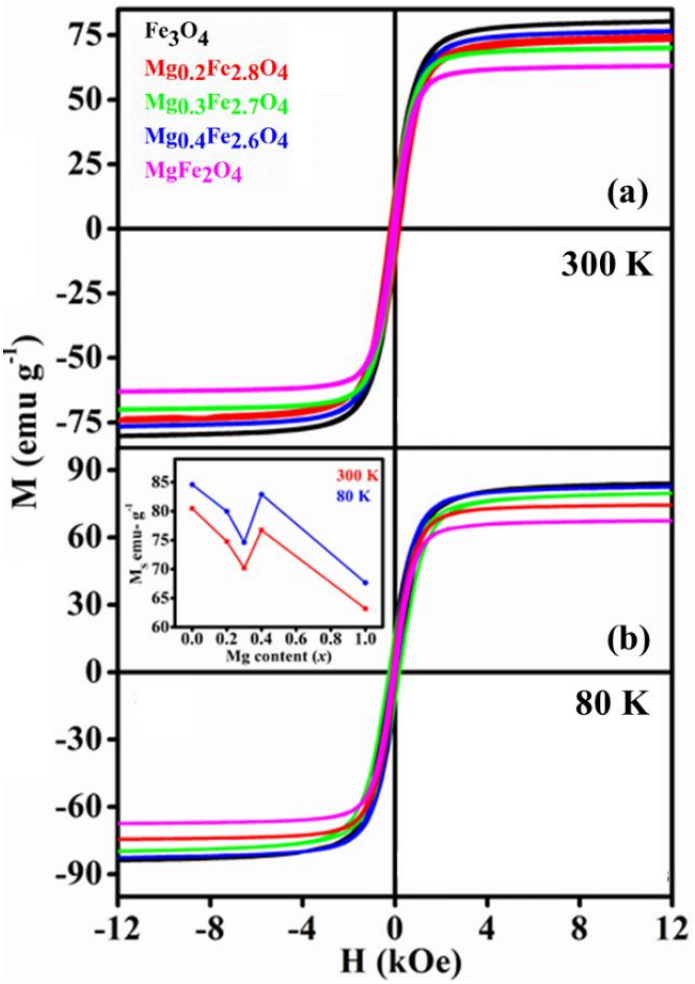

Figure 4.9: M-H curve of $Mg_xFe_{3-x}O_4$ NHSs at (a) 300 K and (b) 80 K.

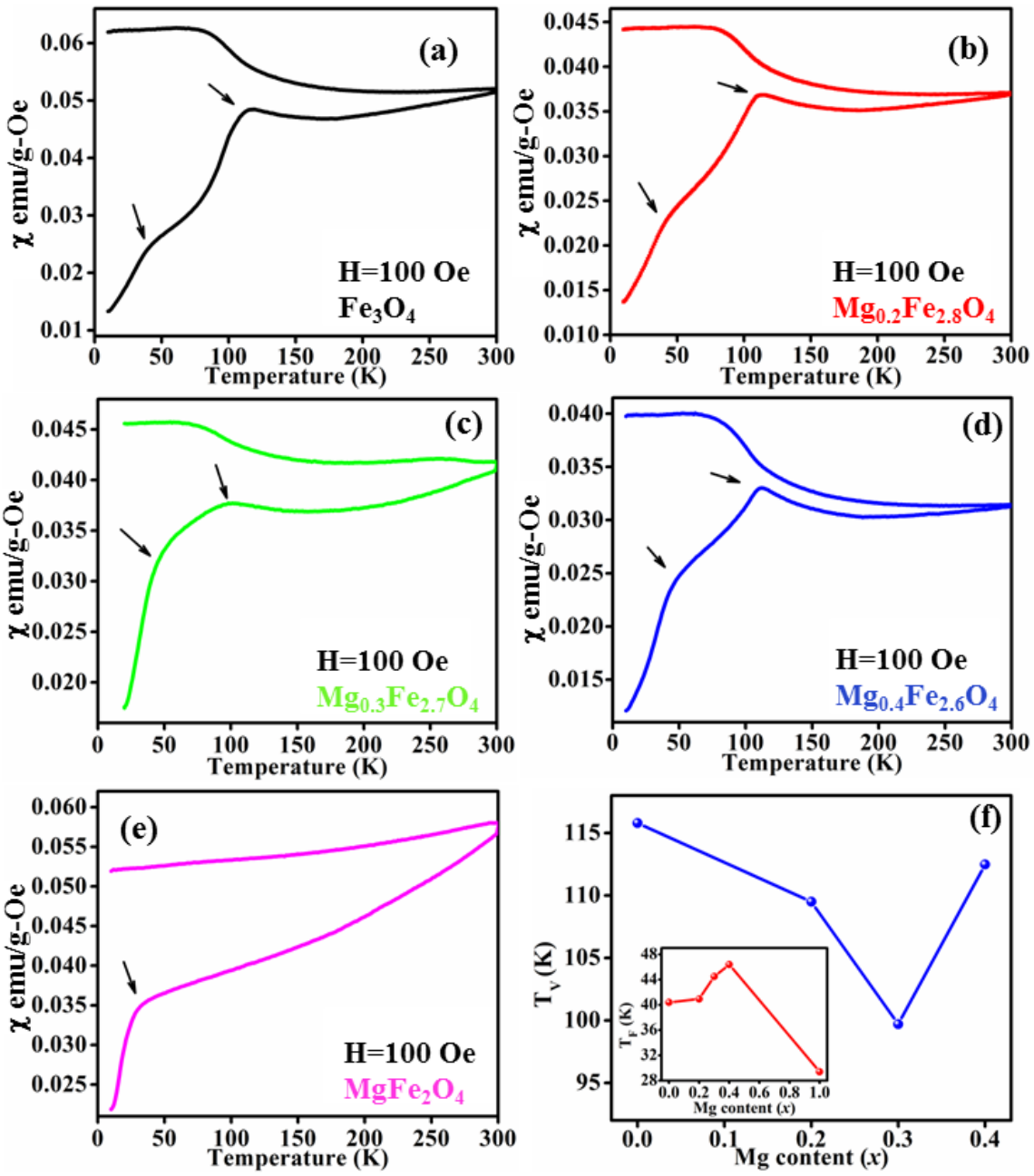

Figure 4.10: (a-e) ZFC-FC curves of $Mg_xFe_{3-x}O_4$ NHSs and (f) variation of T_v with Mg content x, where the inset Figure shows the variation of T_g with x.

4.3.6. Microwave Absorption Properties

Use of negative dielectric material can be a novel approach for making unique optical and microwave devices, such as absorbers, filters, and switches. The finding of this unique property in $Mg_{0.3}Fe_{2.7}O_4$ NHSs led us to study its microwave absorption (MA) properties. The transmit-line theory relates the MA properties of a material to the frequency, thickness of the material, relative complex permittivity ($\varepsilon_r = \varepsilon' - j\varepsilon''$) and relative complex

permeability ($\mu_r = \mu' - j\mu''$)). ε′ and μ′ represent the storage ability of electromagnetic (EM) energy, and ε″ and μ″ symbolize the dielectric and magnetic loss of the material. To study the MA properties of $Mg_{0.3}Fe_{2.7}O_4$ NHSs, the four EM parameters (ε′, ε″, μ′, and μ″) are measured at RT in the frequency range of 1–20 GHz. The f dependent variation of ε′, μ′ and the corresponding dielectric and magnetic tangent loss factors $\tan\delta_\varepsilon$ (=ε″/ε′), and $\tan\delta_\mu$ (=μ″/μ′) are shown in Figures 4.11(a-b). ε′ decreases with f and it increases again in the frequency range 16-20 GHz.

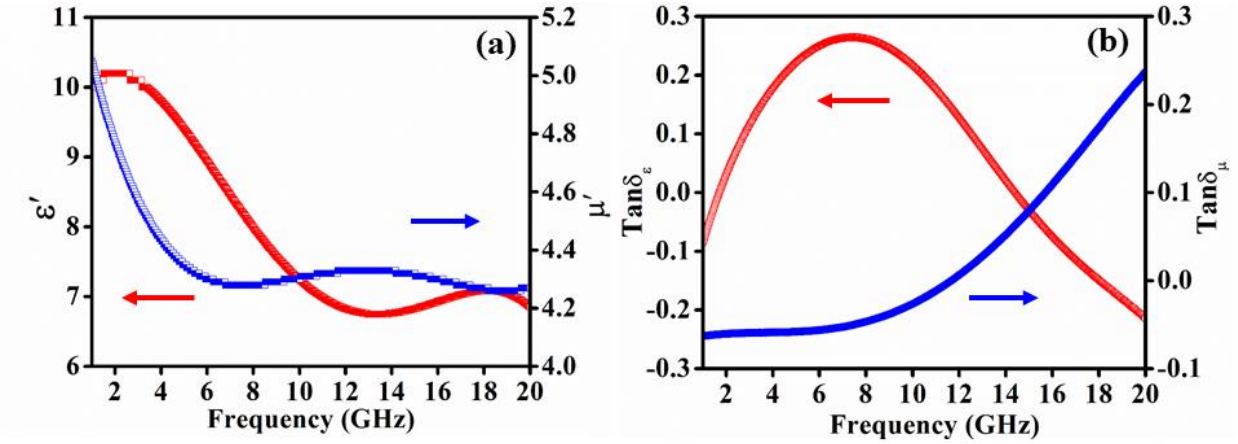

Figure 4.11: Frequency-dependent variation of (a) ε′, μ′, and (b) $\tan\delta_\varepsilon$, $\tan\delta_\mu$.

In the experimental frequency range, dielectric polarization is originated from dipolar and interfacial polarization. The occurrence of high-frequency peak at ~18GHz suggests the presence of atomic polarization[44] and thus ε′ increases. From the frequency-dependent variation of $\tan\delta_\varepsilon$ in Figure 4.11(b), a dielectric relaxation peak is observed at ~7GHz with a sufficiently high value of dielectric loss. From Figure 4.11(a), μ′ decreases up to a certain frequency and then it maintains an almost constant value, whereas $\tan\delta_\mu$ increases with an increase in frequency. Typical morphology of NHSs enhances the surface magnetic anisotropy than bulk ferrites, which helps to achieve higher magnetic loss and EM wave absorption in the NHSs system[45]. Dynamic magnetic loss arises from magnetic hysteresis, domain wall resonance, eddy current effects, and natural and exchange resonance. Due to the presence of a low field in this study, the first two contributions are less effective for $Mg_{0.3}Fe_{2.7}O_4$ NHSs in the high-frequency region[46].

Dynamic magnetic properties of the ferrimagnets are strongly related to the parameters such as magnetic anisotropy and Saturation magnetization (MS), according to

the Landau–Lifshitz–Gilbert (LLG) equation[47]. Moreover, the analysis from the Globus equation $\mu' \propto (M_S^2 D/K^{1/2})$ where K is the magnetocrystalline anisotropy constant. The contribution of eddy current loss to μ″ can be understood from the relation, connecting μ″ and electrical conductivity σ, expressed as $\mu'' \propto 2\pi\mu_0\mu'^2(d^2\sigma)f$, where d is the thickness of the sample (3.12 mm here) and μ_0 is the permeability of free space[48]. According to the above formula, if μ″ originates from eddy current loss, $\mu''(\mu')^{-2}f^{-1}$ vs f curve will show no peaks[49]. In order to understand the probable source of magnetic loss is our NHSs system frequency-dependent plot of $\mu''(\mu')^{-2}f^{-1}$ is shown in Figure 4.12 and no visible peak is found showing a nearly linear high-frequency variation, suggesting eddy current loss as the main mechanism of magnetic loss.

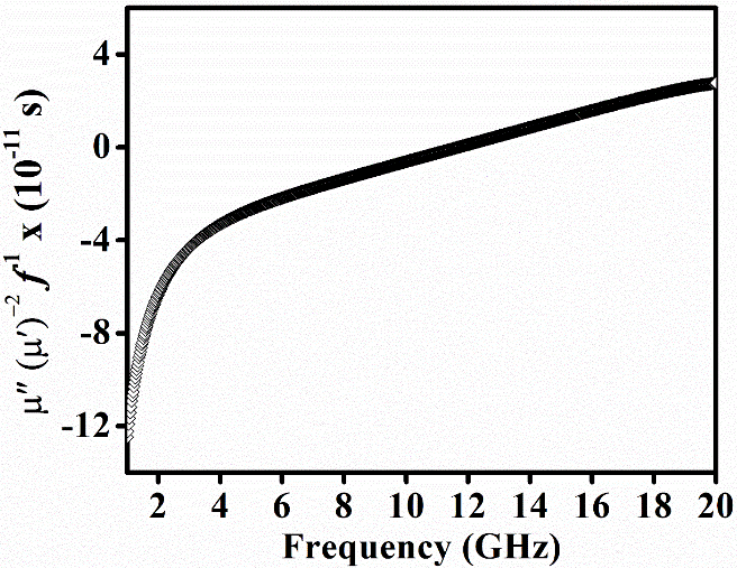

Figure 4.12: Frequency dependence of $\mu''(\mu')^{-2}f^{-1}$ in the frequency range 1-20GHz.

Reflection loss (RL) of EM waves gives insight towards the efficiency of a material to cut down the reflected waves and it is strongly correlated to the magnetic and electronic properties of the material. According to transmission line theory, RL of a microwave absorbing material can be calculated by the following formula[50,51]:

$$Z_{in} = Z_0\sqrt{\frac{\mu_r}{\varepsilon_r}}\tanh\left[j\left(\frac{2\pi ft}{c}\right)\sqrt{\mu_r\varepsilon_r}\right] \quad (4.3)$$

$$RL = 20\log\left|(Z_{in} - Z_0)/(Z_{in} + Z_0)\right| \quad (4.4)$$

where, *c* is the velocity of light in free space, *t*, thickness of the absorber composite, Z_0 and

Z_{in} are the impedance of free space and the input impedance of the absorber respectively. RL is calculated for different thicknesses varying from 1mm to 8 mm and a comparison between the simulated and experimental results, as a function of frequency is shown in Figure 4.13. The frequency (f_m) at which RL is minimum shifts with varying thickness (tm) and they are connected as[52]:

$$t_m = \frac{nc}{4f_m\sqrt{|\mu_r\varepsilon_r|}} \ (n = 1,3,5,7, \ldots \ldots) \qquad (4.5)$$

A good agreement between the experimental and simulated t_m can be well understood from Figure 4.13.

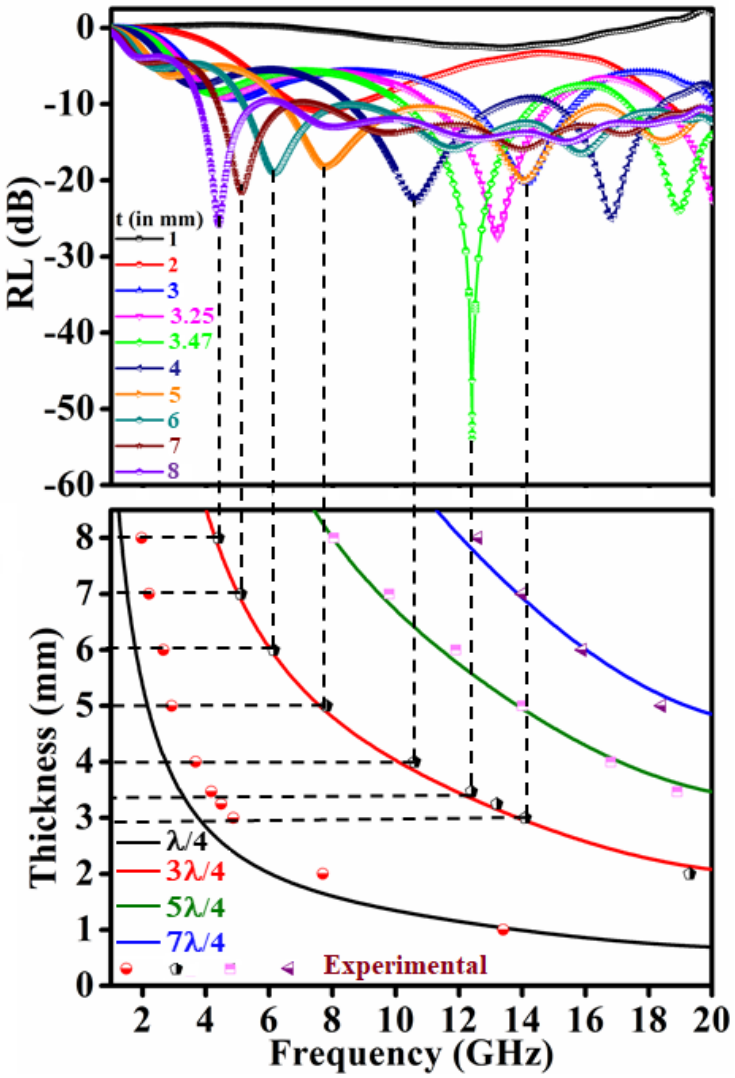

Figure 4.13: Frequency dependence of RL for various thicknesses of microwave composite with the experimental and simulated matching thickness in 1-20 GHz range.

$Mg_{0.3}Fe_{2.7}O_4$ NHSs exhibits stronger dissipation with RL= −53.8 dB at 12.4 GHz and an effective bandwidth (BW) of ~7 GHz (frequency region for RL < −10 dB) at t=3.47 mm. For t=8 mm an effective broad BW of ~ 15.45 GHz is obtained with RL=−25.9 dB at 4.4 GHz, shown in Figure 4.14(a). MA is strongly dependent on either (i) higher transmission and absorption of the incident wave that requires better impedance matching, i.e., $|Z_{in}/Z_0|$~1 or (ii) the dynamic combination of dielectric and magnetic loss[49,53]. The better MA property of $Mg_{0.3}Fe_{2.7}O_4$ NHSs is attributed to both the high dielectric and magnetic loss, as well as the best impedance matching achieved for t = 3.47 mm, as shown in Figure 4.14(b). Moreover, the incident EM waves form repeated oscillation inside the hollow cavity of the $Mg_{0.3}Fe_{2.7}O_4$ NHSs, giving rise to enhanced reflection loss due to enhancement of the total propagation path[54,55].

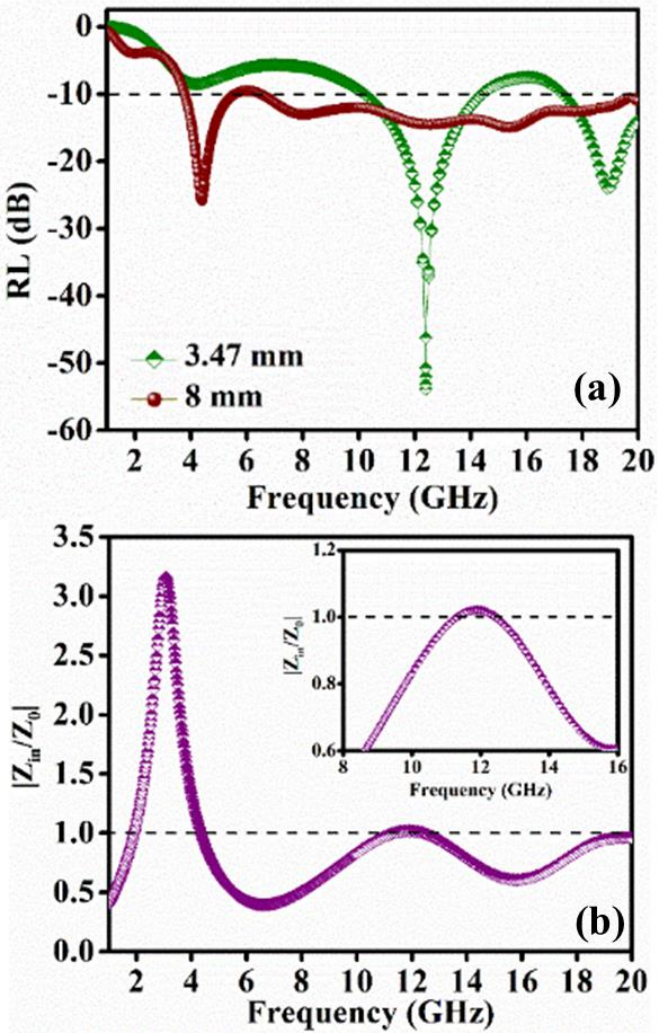

Figure 4.14: Frequency-dependent variation of (a) reflection loss (RL) and (b) $|Z_{in}/Z_0|$ ratio in the frequency range 1-20 GHz.

4.4. Conclusion

In conclusion, the room temperature dielectric response of $Mg_xFe_{3-x}O_4$ nano hollow structures shows improved dielectric permittivity and ac conductivity for x=0.3. More interestingly, the temperature-dependent negative dielectric permittivity observed for this particular doping content, over the temperature range of 383 K-473 K, is explained by backscattering of dipoles and surface skin effect, enhanced by hollow spherical morphology near the metamagnetic transition from ferrimagnetic to ferromagnetic phase. The enhanced metallicity due to ferromagnetic spin alignment shows its effects on both the dielectric and conductive properties. Magnetic measurements further confirmed how the cation distribution and the inversion degree parameter are modulating the magnetization, Verwey transition and the spin freezing temperature. $Mg_{0.3}Fe_{2.7}O_4$ NHSs are found to show excellent microwave absorption properties with RL=−53.8 dB at 12.4 GHz for the composite thickness of only 3.47 mm, owing to its high value of the dielectric and magnetic loss, and EM wave trapping inside the hollow cavity of NHSs. We believe these findings will lead to the potential application of this negative index material in lightweight and inexpensive waveguides.

Bibliography

1. Jansen, R. Silicon spintronics. *Nature Materials* vol. 11 400–408 (2012).
2. Hwang, H. Y. *et al.* Emergent phenomena at oxide interfaces. *Nature Publishing Group* **11**, (2012).
3. Moodera, J. S., Miao, G. X. & Santos, T. S. Frontiers in spin-polarized tunneling. *Physics Today* **63**, 46–51 (2010).
4. Caffrey, N. M., Fritsch, D., Archer, T., Sanvito, S. & Ederer, C. Spin-filtering efficiency of ferrimagnetic spinels CoFe2O 4 and NiFe2O4. *Physical Review B - Condensed Matter and Materials Physics* **87**, (2013).
5. Awschalom, D. D. & Flatté, M. E. Challenges for semiconductor spintronics. *Nature Physics* vol. 3 153–159 (2007).
6. Holinsworth, B. S. *et al.* Magnetic field tunability of spin-polarized excitations in a high-temperature magnet. *PHYSICAL REVIEW B* **96**, 94427 (2017).
7. Lüders, U. *et al.* Spin filtering through ferrimagnetic NiFe 2 O 4 tunnel barriers. *Applied Physics Letters* **88**, 82505 (2006).
8. Wu, H. C. *et al.* Magnetic and transport properties of epitaxial thin film MgFe2O4 grown on MgO (100) by molecular beam epitaxy. *Scientific Reports* **4**, 1–6 (2014).
9. Guo, J. *et al.* Spin-polarized electron transport in highly reduced MgFe2O4-δ. *Materials Research Express* **5**, 126301 (2018).
10. Pan, Y. *et al.* MgFe2O4 nanoparticles as anode materials for lithium-ion batteries. *Electrochimica Acta* **109**, 89–94 (2013).
11. Kim, D. H., Aimon, N. M., Sun, X. & Ross, C. A. Compositionally modulated magnetic epitaxial spinel/perovskite nanocomposite thin films. *Advanced Functional Materials* **24**, 2334–2342 (2014).
12. Sivakumar, N., Narayanasamy, A., Greneche, J. M., Murugaraj, R. & Lee, Y. S. Electrical and magnetic behaviour of nanostructured MgFe2O4 spinel ferrite. *Journal of Alloys and Compounds* **504**, 395–402 (2010).
13. Araújo, J. C. R. *et al.* Tuning structural, magnetic, electrical, and dielectric properties of MgFe2O4 synthesized by sol-gel followed by heat treatment. *Journal of Physics and Chemistry of Solids* **154**, 110051 (2021).
14. Sripriya, R. C., Mahendiran, M., Madahavan, J. & Victor Antony Raj, M. Enhanced magnetic Properties of MgFe2O4 nanoparticles. *Materials Today: Proceedings* **8**, 310–314 (2019).
15. Abraham, A. G. *et al.* Enhanced magneto-optical and photo-catalytic properties of transition metal cobalt (Co2+ ions) doped spinel MgFe2O4 ferrite nanocomposites. *Journal of Magnetism and Magnetic Materials* **452**, 380–388 (2018).
16. Wang, X. *et al.* Characterization of microstructure and magnetic properties for Co2+ ions doped MgFe2O4 spinel ferrites. *Materials Today Communications* **25**, 101414 (2020).
17. Manohar, A., Vijayakanth, V., Pallavolu, M. R. & Kim, K. H. Effects of Ni - substitution on structural, magnetic hyperthermia, photocatalytic and cytotoxicity study of MgFe2O4 nanoparticles. *Journal of Alloys and Compounds* **879**, 160515 (2021).
18. Rahman, S. *et al.* Pressure-induced structural evaluation and insulator-metal transition in the mixed spinel ferrite Z n0.2 M g0.8 F e2 O4. *Physical Review B* **95**, 024107 (2017).

19. Sláma, J., Pala, J., Šoka, M. & Lokaj, J. Metamagnetism in manganate magnesium ferrite. *Journal of Electrical Engineering* **70**, 78–81 (2019).
20. Sarkar, D., Mandal, M. & Mandal, K. Domain controlled magnetic and electric properties of variable sized magnetite nano-hollow spheres. *Journal of Applied Physics* **112**, 064318 (2012).
21. Rakshit, R. *et al.* Surface Electronic States Induced High Terahertz Conductivity of Co3O4 Microhollow Structure. *ACS Applied Materials and Interfaces* **10**, 19189–19196 (2018).
22. Li, B., Sui, G. & Zhong, W. H. Single negative metamaterials in unstructured polymer nanocomposites toward selectable and controllable Negative permittivity. *Advanced Materials* **21**, 4176–4180 (2009).
23. Lee, K. & Heeger, J. Crossover to negative dielectric response in the low-frequency spectra of metallic polymers. *Physical Review B - Condensed Matter and Materials Physics* **68**, 035201 (2003).
24. Hou, Q. *et al.* Ultrahigh dielectric loss of epsilon-negative copper granular composites. *Materials Letters* **169**, 86–89 (2016).
25. Yan, H. *et al.* Negative dielectric constant manifested by static electricity. *Applied Physics Letters* **102**, 062904 (2013).
26. Liu, R., Degiron, A., Mock, J. J. & Smith, D. R. Negative index material composed of electric and magnetic resonators. *Applied Physics Letters* **90**, 263504 (2007).
27. Schurig, D., Mock, J. J. & Smith, D. R. Electric-field-coupled resonators for negative permittivity metamaterials. *Applied Physics Letters* **88**, 1–3 (2006).
28. Chu, C. W. *et al.* A negative dielectric constant in nano-particle materials under an electric field at very low frequencies. *Strongly Correlated Electron Materials: Physics and Nanoengineering* **5932**, 59320X (2005).
29. Gajula, G. R., Buddiga, L. R., Chidambara, C. K., Ch., A. K. & Dasari, M. Dielectric, magnetic and magnetoelectric studies of lithium ferrite synthesized by solid state technique for wave propagation applications. *Journal of Science: Advanced Materials and Devices* **3**, 230–235 (2018).
30. Prakash, C. & Baijal, J. S. Electrical conductivity and dielectric behaviour of Fe2-2xSnxZn1 + xO4. *Journal of The Less-Common Metals* **114**, 241–248 (1985).
31. Rani, S., Sharma, Y. & Varma, G. D. Structurally Induced Spin Canting and Metamagnetism in CoFe2O4 Nanoparticles Synthesized via Co-precipitation Method. *Journal of Superconductivity and Novel Magnetism* **28**, 3633–3644 (2015).
32. Pradhan, D. K. *et al.* Correlation of dielectric, electrical and magnetic properties near the magnetic phase transition temperature of cobalt zinc ferrite. *Physical Chemistry Chemical Physics* **19**, 210–218 (2017).
33. Shlyk, L., Kryukov, S., Schüpp-Niewa, B., Niewa, R. & de Long, L. E. High-temperature ferromagnetism and tunable semiconductivity of (Ba, Sr)M2±xRu4±xO11 (M = Fe, Co): A new paradigm for spintronics. *Advanced Materials* **20**, 1315–1320 (2008).
34. Bartkowska, J. A. & Bochenek, D. Microstructure and dielectric properties of BF–PFN ceramics with negative dielectric loss. *Journal of Materials Science: Materials in Electronics* **29**, 17262–17268 (2018).
35. Rayssi, C., el Kossi, S., Dhahri, J. & Khirouni, K. Frequency and temperature-dependence of dielectric permittivity and electric modulus studies of the solid solution Ca0.85Er0.1Ti1-: XCo4 x /3O3 (0 ≤ x ≤ 0.1). *RSC Advances* **8**, 17139–17150 (2018).
36. Jonscher, A. K. The "universal" dielectric response. *Nature* vol. 267 673–679 (1977).
37. Lu, Z., Bonnet, J. P., Ravez, J. & Hagenmuller, P. Correlation between low frequency

dielectric dispersion (LFDD) and impedance relaxation in ferroelectric ceramic Pb2KNb4TaO15. *Solid State Ionics* **57**, 235–244 (1992).
38. Cheruku, R., Govindaraj, G. & Vijayan, L. Super-linear frequency dependence of ac conductivity in nanocrystalline lithium ferrite. *Materials Chemistry and Physics* **146**, 389–398 (2014).
39. Lee, W. K., Liu, J. F. & Nowick, A. S. Limiting behavior of ac conductivity in ionically conducting crystals and glasses: A new universality. *Physical Review Letters* **67**, 1559–1561 (1991).
40. Sidebottom, D. L., Green, P. F. & Brow, R. K. Two contributions to the ac conductivity of alkali oxide glasses. *Physical Review Letters* **74**, 5068–5071 (1995).
41. Pradhan, D. K. *et al.* Correlation of dielectric, electrical and magnetic properties near the magnetic phase transition temperature of cobalt zinc ferrite. *Physical Chemistry Chemical Physics* **19**, 210–218 (2017).
42. Gupta, R., Sood, A. K., Metcalf, P. & Honig, J. M. Raman study of stoichiometric and Zn-doped Fe3O4. *Physical Review B - Condensed Matter and Materials Physics* **65**, 1044301–1044308 (2002).
43. Silva, F. G. *et al.* 2th International Conference on Magnetic Fluids Exchange Bias Properties and Surface Spin Freezing in Magnetic Nanoparticles. *Physics Procedia* **00**, 0 (2009).
44. He, J.-Z., Wang, X.-X., Zhang, Y.-L. & Cao, M.-S. Small magnetic nanoparticles decorating reduced graphene oxides to tune the electromagnetic attenuation capacity. *Journal of Materials Chemistry C* **4**, 7130–7140 (2016).
45. Liu, X. *et al.* Flexible nanocomposites with enhanced microwave absorption properties based on Fe3O4/SiO2 nanorods and polyvinylidene fluoride. *Journal of Materials Chemistry A* **3**, 12197–12204 (2015).
46. Liu, P., Huang, Y., Yan, J. & Zhao, Y. Magnetic graphene@PANI@porous TiO2 ternary composites for high-performance electromagnetic wave absorption. *Journal of Materials Chemistry C* **4**, 6362–6370 (2016).
47. Gilbert, T. L. & L., T. Classics in Magnetics A Phenomenological Theory of Damping in Ferromagnetic Materials. *ITM* **40**, 3443–3449 (2004).
48. Gorai, A., Mandal, D. & Mandal, K. Multi-layered nano-hollow spheres for efficient electromagnetic wave absorption. *Nanotechnology* **32**, 345707 (2021).
49. Zhang, Y. *et al.* Nanolayered Cobalt@Carbon Hybrids Derived from Metal–Organic Frameworks for Microwave Absorption. *ACS Applied Nano Materials* **2**, 2325–2335 (2019).
50. Han, M. *et al.* Graphene-wrapped ZnO hollow spheres with enhanced electromagnetic wave absorption properties. *Journal of Materials Chemistry A* **2**, 16403–16409 (2014).
51. Li, X. *et al.* One-pot synthesis of CoFe2O4/graphene oxide hybrids and their conversion into FeCo/graphene hybrids for lightweight and highly efficient microwave absorber. *Journal of Materials Chemistry A* **3**, 5535–5546 (2015).
52. Panbo Liu, Ying Huang, Jing Yan & Yang Zhao. Magnetic graphene@PANI@porous TiO 2 ternary composites for high-performance electromagnetic wave absorption. *Journal of Materials Chemistry C* **4**, 6362–6370 (2016).
53. Yang, Z., Li, Z., Yang, Y. & Xu, Z. J. Optimization of ZnxFe3–xO4 Hollow Spheres for Enhanced Microwave Attenuation. *ACS Applied Materials and Interfaces* **6**, 21911–21915 (2014).
54. Han, M. *et al.* Graphene-wrapped ZnO hollow spheres with enhanced electromagnetic wave absorption properties. *Journal of Materials Chemistry A* **2**, 16403–16409 (2014).

55. Wang, F. *et al.* Template free synthesis and electromagnetic wave absorption properties of monodispersed hollow magnetite nano-spheres. *Journal of Materials Chemistry* **21**, 4314–4320 (2011).

Chapter 5

Magnetorheological Response of Magnetic Fluids Containing Fe_3O_4 Nano Structures

This chapter demonstrates preparation of Fe_3O_4 nano-hollow spheres and nanoparticles based magnetorheological fluids with silicone oil as base fluid. Nano-hollow spheres are found to be an excellent candidate for stable magnetorheological fluid.

A part of this chapter is already published in ***Journal of Magnetism and Magnetic Materials, 2019,*** *484, 324* and it is reproduced here.

5. Rheological Response of Magnetic Fluids Containing Fe_3O_4 Nano Structures

5.1. Preamble

Magnetorheological (MR) fluid is a smart material consisting of magnetic particles, with diameter within 0.01-20 μm, suspended in non-magnetic carrier fluid. Due to the rising dipolar interaction between the suspended magnetic particles they show typical MR effect, by forming chain-like structure and in turn changing the effective viscosity reversibly, under the externally applied magnetic field[1]. The unique magnetic property of MR fluids made them attractive in various field of application, such as vacuum sealing, magnetic resonance imaging, intelligent sensors, drug delivery, loud speaker and microphone centering, tunable dampers and clutches[2–6].

MR effects depend on disordered to ordered transition of the particles assembling under externally applied magnetic field. Therefore magnetic properties, size and morphology of the particles are important for better MR response. In last few years different groups used various structured materials such as particles, sheets, spheres, rods and wires[7–10] of Iron, Cobalt, Nickel, Carbonyl-Iron, transition metal alloys and their oxides[9–14]to improve the MR effect. Researchers have also enhanced the MR response by adding non-magnetic particles in the suspension[15]. Better MR response was observed for particles with rough surface and increased area of contact[16]. Besides particles with higher magnetization are preferable as the yielding point depends on magnetic saturation (M_s). For better understanding of the MR mechanism the particle size dependent magnetorheological property need to be studied, though very few have been reported so far. The mostly used magnetic particles in MR fluids is Carbonyl iron, with tunable size between few μm to 10 μm, anticipating higher yielding stress due to higher M_s value. However their high density makes them very unstable in carrier fluid, resulting their limitations for repeated use. There are several ways to improve the sedimentation stability, e.g. coating the surface of the particles with polymers to make them dispersible[17], make the interior of the particles porous to reduce density[18] etc., where the former process reduces the magnetization of the material. We prepared hollow submicron spheres of

Fe_3O_4, which makes it lighter keeping the magnetization unaltered. Though Fe_3O_4 show less magnetism over Fe and carbonyl iron, its tunable size and less density enable it to be more stable in carrier fluid and the magnetic saturation arising from Fe_3O_4 microstructures is sufficient for their use as MR materials.

In this chapter, to improve the stability and yield stress, magnetorheological properties of low density Fe_3O_4 nano hollow spheres (NHSs) are investigated, by dispersing them in silicon oil and the results are compared with corresponding solid nanoparticles (NPs). From the study NHSs are found to be better candidate for MR applications compared to their solid counterpart.

5.2. Experimental Section

5.2.1. Materials Used

The precursor salt Ferric Chloride ($FeCl_3$, $6H_2O$), urea (CH_4N_2O) and surfactant PVP (Polyvinylpyrrolidone $(C_6H_9NO)_n$) are obtained from Sigma-Aldrich. All the reagents are of analytical grade and used without further purification. Ethylene glycol is used as solvent.

5.2.2. Synthesis of NHSs and NPs in Solvothermal Method

Fe_3O_4 nanostructures are synthesized using a facile template free solvothermal method. In the typical synthesis of Fe_3O_4 NHSs, 1.015 g of $FeCl_3.6H_2O$ and 0.465 g of urea are dissolved in 30 ml Ethylene glycol, which are stirred until clear homogeneous solution was obtained. Thereafter, 37.5 mg of PVP is added to the solution mixture to synthesize NHSs of 700 nm diameter. PVP acts as a growth modifier as well as surface stabilizer, in order to restrict the particle growth in nanometer size range. The properly mixed final solution is transferred into 40 ml Teflon lined stainless steel autoclave and heated to 180°C for 20 h followed by natural cooling to room temperature. The resulting black precipitate is thoroughly washed with absolute ethanol to remove all residual reagents and separated by centrifugation. The as-obtained product is dried at 60°C for 12 h. To prepare NHSs of diameter 250 nm we only change the amount of PVP to 75 mg. For the NPs we added 200 mg of PVP and the reaction was conducted at a temperature 200°C for 4 h.

Due to hydrolysis of Fe^{2+} in the reaction, $Fe(OH)_2$ and FeOOH nanocrystals are formed, which are thermodynamically unstable because of their extreme nanoscale size. The nanocrystals aggregates to form solid spheres to reduce the surface energy and we can control the aggregation with the amount of growth modifier in the reaction. Following the 20 h reaction time at 180°C, the $Fe(OH)_2$ and FeOOH nanocrystals transform to Fe_3O_4 with irregular shaped small pores inside the solid sphere. As Fe_3O_4 is denser than $Fe(OH)_2$ and FeOOH, the pores are formed to maintain the effective density by removing material from the aggregates. The small pores merge together to form large pores following the Ostwald ripening process[19]. The PVP coating over individual nanocrystallite not only limits the aggregation, but also prevents them from collapsing. With increase in the amount of PVP and reduction of the reaction time small NPs are formed.

5.2.3. Preparation of NPs and NHSs Based MR Fluids

For preparing MR fluids the respective samples are mixed with silicon oil (purchased from MERCK) with 50% weight fraction. The powder samples and carrier oil are mixed with mechanical stirring followed by sonication until uniformity obtained. MR fluid containing NPs of diameter 100 nm is marked as MR100 and the other two MR fluids are marked as MR250 and MR700 containing NHSs of diameter 250 nm and 700 nm respectively.

5.2.4. Characterization

The prepared submicron structures are characterized using X-Ray Diffraction (XRD), Transmission electron (TEM) and Field emission scanning electron microscope (FESEM). Magnetic measurements are performed using Vibrating sample magnetometer (VSM). Commercial rheometer "MCR 301" is used for the magnetorheological measurements.

5.3. Results and Discussions

5.3.1. Structural and Morphological Analysis

Figure 5.1 shows the XRD patterns of the NHSs and NPs, confirming the formation of face centered cubic inverse spinel structure (JCPDS card np. 75-0033) of Fe_3O_4. For the morphological analysis of the as prepared NSs, FESEM and TEM analysis are performed.

Figure 5.2 (a) and (b) show the FESEM micrographs of NHSs of diameters 700 nm and 250 nm respectively. From FESEM images formation of cracked spheres of uniform distribution with hollow interior is confirmed.

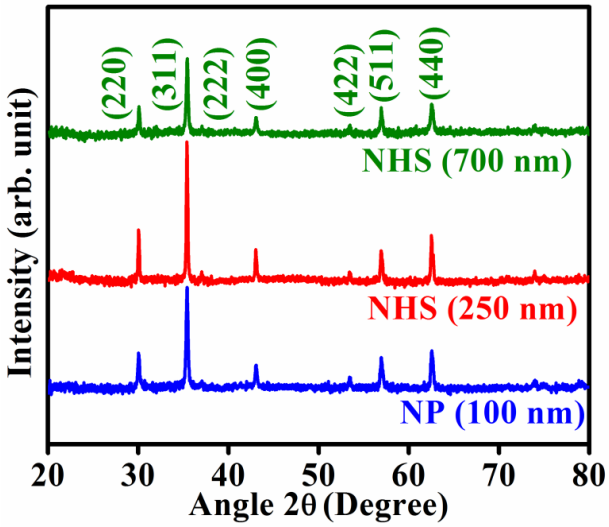

Figure 5.1: XRD patterns of the as prepared Fe_3O_4 NHSs and NPs.

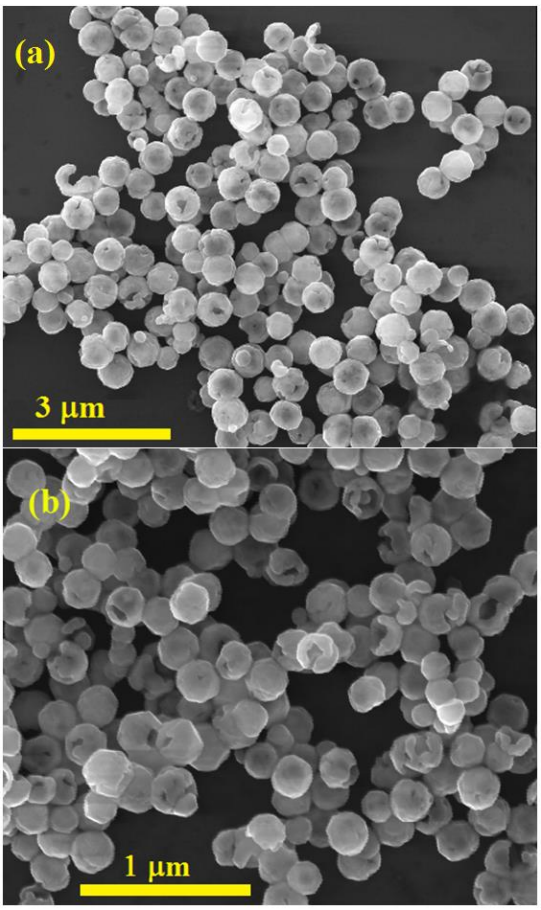

Figure 5.2: FESEM image of as prepared NHSs of diameter (a) 750 nm and (b) 250 nm.

Figure 5.3(a) and (b) show the TEM image of the NHSs, where from the dark and bright contrast between the outer line and center part, hollow structure formation is ensured. For better clarity only TEM image of the as prepared NPs is shown in Figure 5.3(c), confirming the formation of NPs of 100 nm diameter with uniform size distribution.

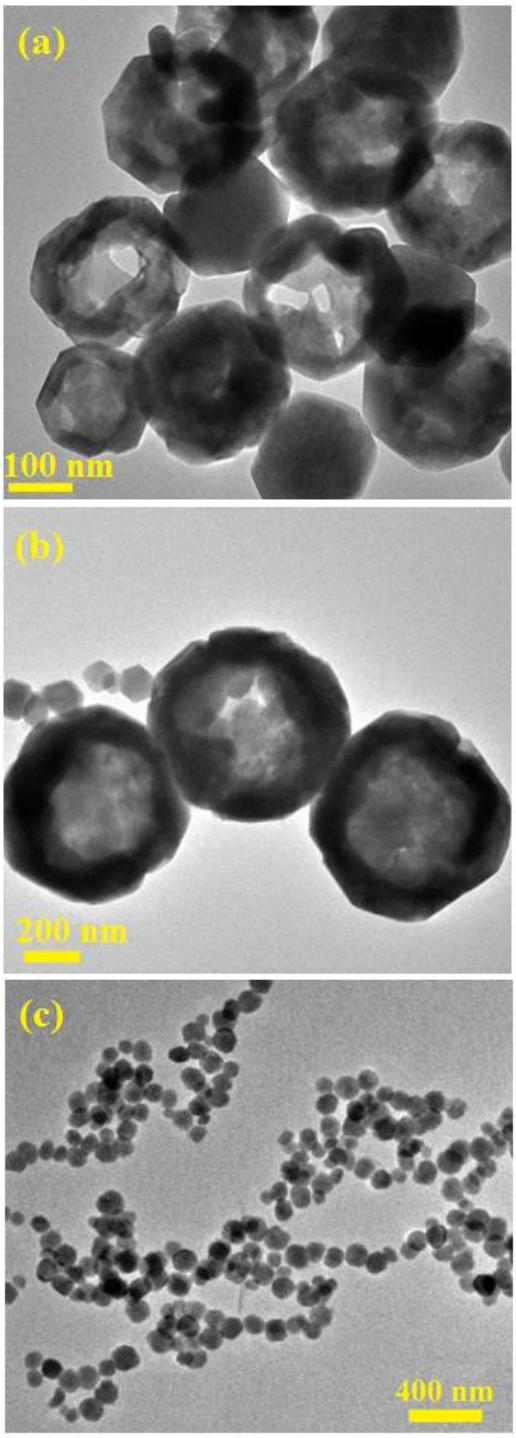

Figure 5.3: TEM image of the prepared Fe_3O_4 (a) NHSs of diameter 250 nm (b) NHSs of diameter 700 nm and (c) NPs of diameter 100 nm.

5.3.2. Magnetic Properties

The room temperature magnetic hysteresis loops (M-H) of NHSs and NPs are shown in Figure 5.4. NHSs with higher diameter show higher M_s (92.2 emu g^{-1} for 700 nm & 85.1 emu g^{-1} for 250 nm), whereas both of them exhibit better magnetization compared to that of NPs (79.4 emu g^{-1}). M_s values of NHSs and NPs suggest these NSs are suitable for MR studies. The inset of Figure 5.4 shows the enlarged version of the center region of M-H loop showing negligible remanence (M_r) and coercivity (H_c).

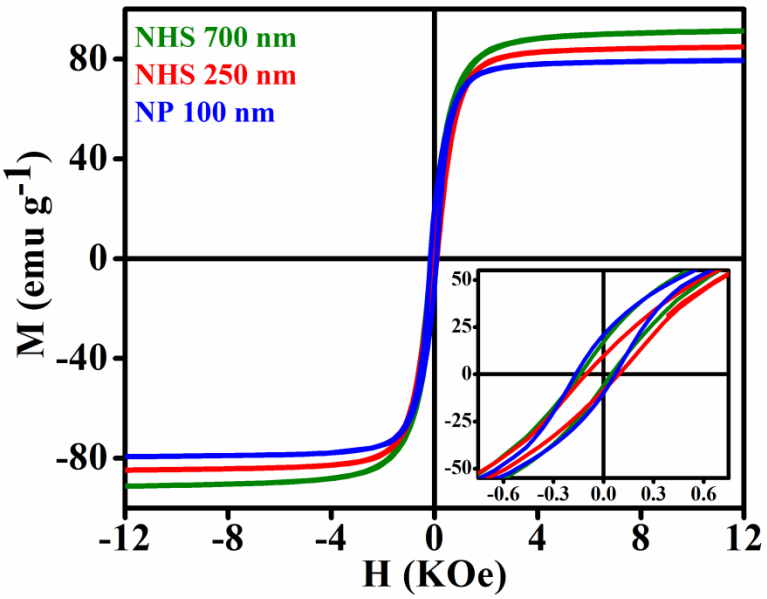

Figure 5.4: Room temperature M-H curve of Fe_3O_4 NPs and NHSs.

5.3.3. Magnetorheological Properties

Anticipating better MR property due to low density and higher magnetization two different MR fluids MR250 and MR700, as described in the experimental section, were investigated under external magnetic field varying from 0 to 0.4 T. To compare their results with that of solid particles, MR100 is also investigated under the same conditions. The shear rate dependence of shear stress of the MR fluids were studied with shear rate varying from 0.01 s^{-1} to 100 s^{-1} (shown in Figure 5.5), keeping the gap between the rotating plates of the rheometer fixed at 0.3 mm. These flow curves (shear stress vs shear rate

curves) are found to be non-linear, implying non-Newtonian behavior. To understand the MR behavior these curves are fitted with the Herschel-Bulkley (HB) fluid model[20]:

$$\tau = \tau_0 + k\dot{\gamma}^n \tag{5.1}$$

where, τ is the shear stress, τ_0, the yield stress value and $\dot{\gamma}$, the shear rate. k and n are model factors which are respectively the consistency index and flow index.

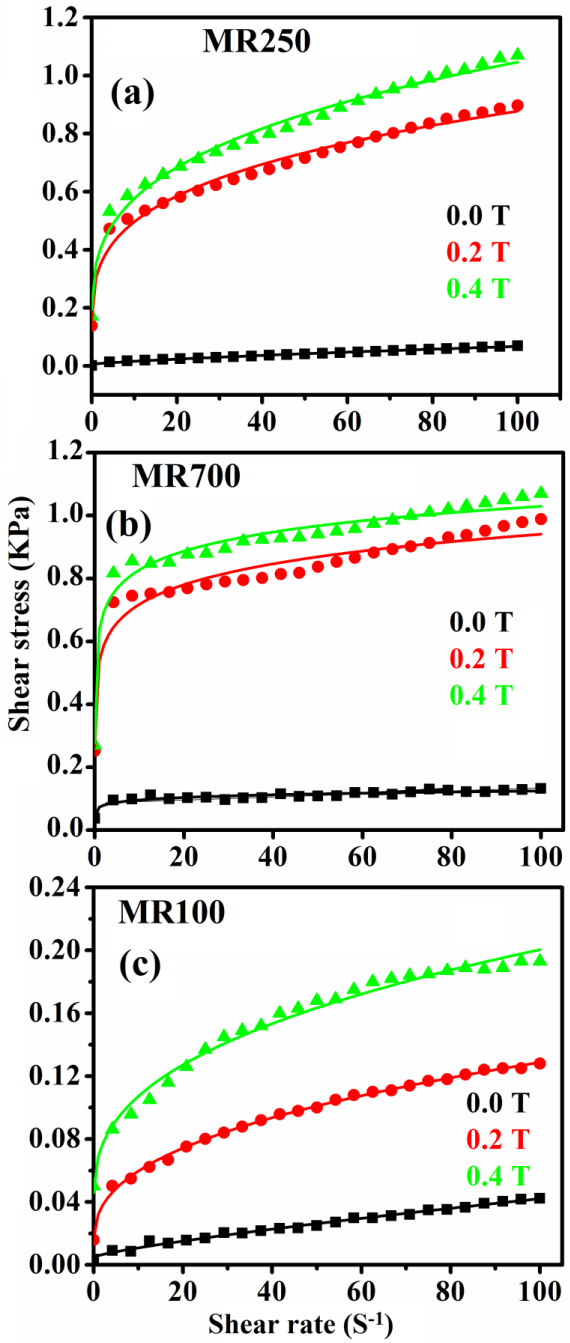

Figure 5.5: Shear rate dependent shear stress plot (flow curve) of (a) MR250 (b) MR700 and (c) MR100 fitted with HB fluid model.

Though the flow curves for MR250 and MR100 fit well with the HB fluid model, it is not appropriate for MR700, which is also reflected from the fitted parameters (Table 5.1), such as negative value of τ_0 and unacceptable values of n. Even for MR250 and MR100 the values of n are inconsistent, as n decreases with increase of magnetic field which is contrary to the behavior of MR fluids. Moreover, it is clear from Figure 5.5 that the shear behavior at a particular magnetic field is not similar for different MR fluids. Thus it is not possible to explain the MR behavior of all the samples by a simple power law such as HB model.

Table 5.1: Rheological behavior of MR fluids under different magnetic field from Herschel-Bulkley fitting

MR samples	Magnetic field (T)	τ_0 (Pa)	k (Pa S^n)	n
MR250	0	5.37 ± 0.001	0.002 ± 0.001	0.77 ± 0.03
	0.2	109.9 ± 0.03	0.19 ± 0.03	0.3 ± 0.02
	0.4	147.3 ± 0.03	0.21 ± 0.03	0.32 ± 0.02
MR700	0	-22.4 ± 0.06	0.1 ± 0.06	0.09 ± 0.05
	0.2	-275.2 ± 0.32	0.81 ± 0.33	0.09 ± 0.03
	0.4	-320.9 ± 4.5	3.85 ± 4.5	0.02 ± 0.02
MR100	0	4.98 ± 0.001	0.001 ± 0.002	0.8 ± 0.05
	0.2	13.4 ± 0.002	0.018 ± 0.001	0.39 ± 0.01
	0.4	41.3 ± 0.006	0.027 ± 0.004	0.38 ± 0.03

The higher shear rate region of the stress-shear rate curve behaves like a Bingham curve at all the applied magnetic fields. Bingham Plastic (BP) model[21] suggests that

$$\tau = \tau_B + \eta\dot{\gamma} \tag{5.2}$$

where, $\tau_B$is the Bingham yield stress and η is the field independent plastic viscosity defined as the slope of the shear stress curve at high value of $\dot{\gamma}$.

According to BP model, for $\tau < \tau_B$, the magnetic particle-oil suspension is in solid-like state and after the yielding point the magnetic fluid behaves like liquid state. Under the application of an external magnetic field, dipole moment arises in the suspended magnetic particles of MR fluid and they form chain like columnar structure in the applied field direction and on removal of the magnetic field the fluid reverses back to the initial state. In a parallel plate rheometer the MR fluid is placed in between two plates and a shear loading is applied by rotating the upper plate and keeping lower one fixed. MR fluids resist the flow by forming chain under applied field and with increasing shear rate the flow initiates again due to chain deformation. The point at which shear stress reaches the maximum is called the yielding point. Yield stress is the most important parameter of MR fluids in application point of view, which depends on the magnetic saturation, stability of the MR fluid, carrier fluid, and particle weight fraction. Flow curves fitted with BP model are shown in Figure 5.6. The fitting parameters are listed in Table 5.2.

As evident from Table 5.2, MR100 and MR250 show huge difference in MR response. The NPs of diameter 100 nm show M_s ~80 emu/g which is close to the magnetization of NHSs of diameter 250 nm (85 emu/g). Though the magnetization values are comparable for these particles, poor MR response of MR100 is due to the larger surface area as well as better stability (showed experimentally later on) of the NHSs in the carrier oil. The area of contact between two spheres of radius r is a small circle of radius *a* given by[22]:

$$\mathrm{a} = \frac{C}{\sqrt[3]{\frac{1}{r}+\frac{1}{r}}} \tag{5.3}$$

where, C is a constant which depends on the moduli of elasticity and Poisson's ratios of the spheres. It is obvious from Eq. 5.3 that the area of contact will increase with increasing r. Larger surface area gives rise to stronger magnetic interaction and frictional force among the particles.

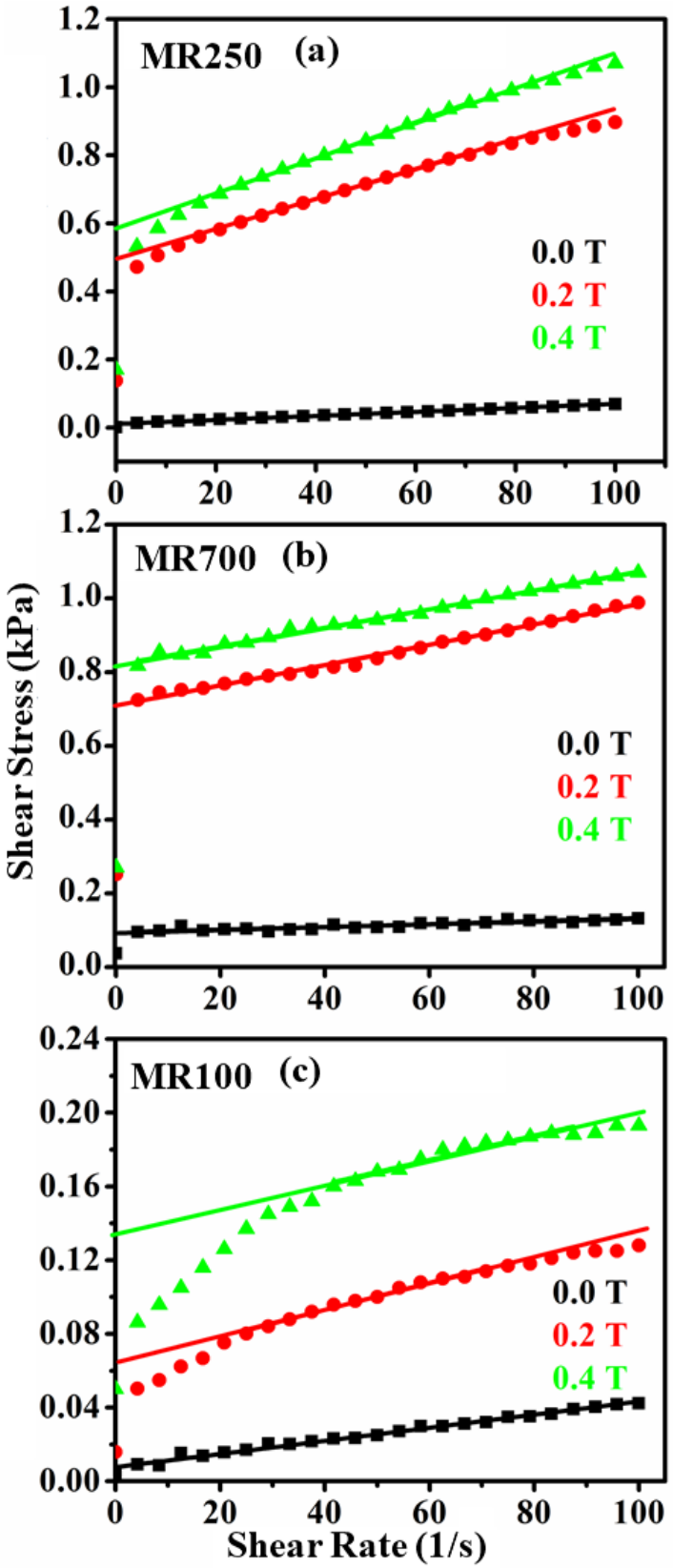

Figure 5.6: Shear rate dependent shear stress plot (flow curve) of (a) MR250 (b) MR700 and (c) MR100 fitted with BP model.

Table 5.2: Yield stress of the MR fluids from Bingham-Plastic model

Magnetic Field (T)	τ_B(Pa)		
	MR250	**MR700**	**MR100**
0	13.1	85.9	9.3
0.2	491.1	687.8	76.9
0.4	582.1	829.9	154

5.3.4. Sedimentation Stability

Density of the NSs are calculated before sedimentation test. The density of the NHSs of diameter 250 and 700 nm are 5.208x103 kg/m^3 and 5.214 x103 kg/m^3 respectively, whereas the solid NPs are of density 5.655 x103 kg/m^3.

Sedimentation tests are performed on all the three samples to compare the stability of the three different kinds of MR fluids. The sedimentation rate is calculated using the equation:

$$\text{Sedimentation percentage (S)} = \frac{\text{Volume of supernatant fluid}}{\text{Total volume of MR fluid}} \text{ X } 100\%$$

Figure 5.7 shows the sedimentation curves of the MR fluids. NHSs show much better stability than NPs in the MR fluid due to the lighter density of NHSs than NPs. MR250 shows slightly better stability over MR700, which is due to the higher density of NHSs with 700 nm diameter in comparison to NHSs of diameter 250 nm..

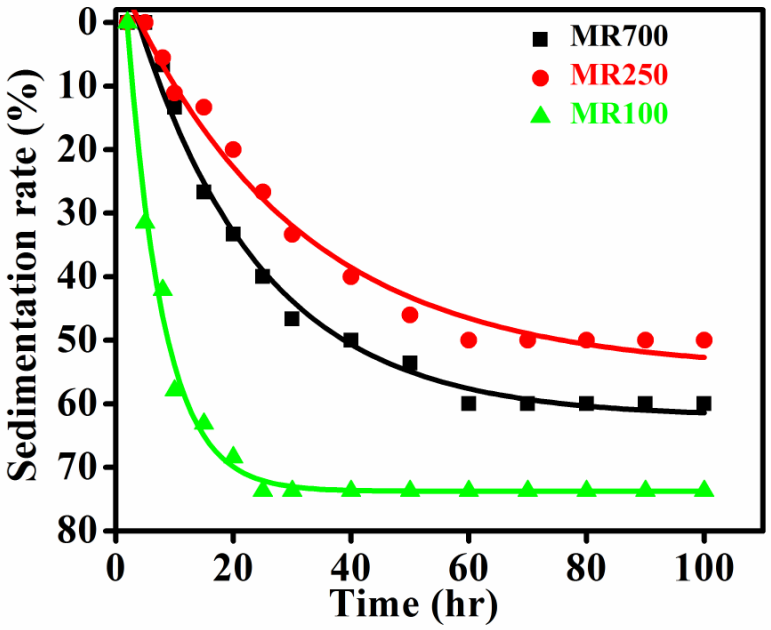

Figure 5.7: Sedimentation rate of the MR fluids.

5.4. Conclusion

In summary, magnetorheological fluid with high yield stress and better stability is successfully prepared by using hollow nano spheres in a facile method. The typical MR behavior of these fluids is successfully understood using Bingham Plastic model. Yield stress is found to be morphology dependent, suggesting not only the magnetic saturation, but the stability of the magnetic particles in carrier oil plays a crucial role in determining the MR response. Fe_3O_4 nano hollow structure based MR fluids with excellent sedimentation stability and high shear stress can be a good candidate for future MR fluids based technology.

Bibliography

1. Rabinow, J. The magnetic fluid clutch. *Electrical Engineering* **67**, 1167–1167 (2013).

2. Patel, J., Parekh, K. & Upadhyay, R. v. Maneuvering thermal conductivity of magnetic nanofluids by tunable magnetic fields. *Journal of Applied Physics* **117**, 243906 (2015).

3. Heine, M. C., de Vicente, J. & Klingenberg, D. J. Thermal transport in sheared electro- and magnetorheological fluids. *Physics of Fluids* **18**, 023301 (2006).

4. Liu, J., Flores, G. A. & Sheng, R. In-vitro investigation of blood embolization in cancer treatment using magnetorheological fluids. *Journal of Magnetism and Magnetic Materials* **225**, 209–217 (2001).

5. Kordonski, W. & Golini, D. Multiple Application of Magnetorheological Effect in High Precision Finishing: *http://dx.doi.org/10.1106/104538902026104* **13**, 401–404 (2016).

6. Read, D. H. & Martin, J. E. Field-Structured Chemiresistors. *Advanced Functional Materials* **20**, 1577–1584 (2010).

7. Park, B. J., Song, K. H. & Choi, H. J. Magnetic carbonyl iron nanoparticle based magnetorheological suspension and its characteristics. *Materials Letters* **63**, 1350–1352 (2009).

8. Arief, I. & Mukhopadhyay, P. K. Magnetorheological Payne effect in bidisperse MR fluids containing Fe nanorods and Fe3O4 nanospheres: A dynamic rheological study. *Journal of Alloys and Compounds* **696**, 1053–1058 (2017).

9. Ngatu, G. T., Wereley, N. M., Karli, J. O. & Bell, R. C. Dimorphic magnetorheological fluids: exploiting partial substitution of microspheres by nanowires. *Smart Materials and Structures* **17**, 045022 (2008).

10. Shah, K., Oh, J. S., Choi, S. B. & Upadhyay, R. v. Plate-like iron particles based bidisperse magnetorheological fluid. *Journal of Applied Physics* **114**, 213904 (2013).

11. Gómez-Ramírez, A., López-López, M. T., Durán, J. D. G. & González-Caballero, F. Influence of particle shape on the magnetic and magnetorheological properties of nanoparticle suspensions. *Soft Matter* **5**, 3888–3895 (2009).

12. Kim, M. S., Liu, Y. D., Park, B. J., You, C. Y. & Choi, H. J. Carbonyl iron particles dispersed in a polymer solution and their rheological characteristics under applied magnetic field. *Journal of Industrial and Engineering Chemistry* **18**, 664–667 (2012).

13. Katiyar, A., Dhar, P., Nandi, T. & Das, S. K. Magnetoviscoelastic characteristics of superparamagnetic oxides (Fe, Ni) based ferrofluids. *Journal of Magnetism and Magnetic Materials* **436**, 35–46 (2017).

14. Sedlacik, M., Pavlinek, V., Saha, P., Svrcinova, P. & Filip, P. The role of particles annealing temperature on magnetorheological effect. *Modern Physics Letters B* **26**, (2012).

15. Plachy, T., Cvek, M., Kozakova, Z., Sedlacik, M. & Moucka, R. The enhanced MR performance of dimorphic MR suspensions containing either magnetic rods or their non-magnetic analogs. *Smart Materials and Structures* **26**, (2017).

16. Zhang, P., Lee, K. H. & Lee, C. H. Friction behavior of magnetorheological fluids with different material types and magnetic field strength. *Chinese Journal of Mechanical Engineering 2016 29:1* **29**, 84–90 (2015).

17. Hajalilou, A., Kianvash, A., Shameli, K. & Lavvafi, H. Carbonyl iron based magnetorheological effects with silver nanoparticles via green-assisted coating. *Applied Physics Letters* **110**, 261902 (2017).

18. Zhang, K., Piao, S. H. & Choi, H. J. Hollow Structured Magnetic Particles of CoFe2O4 and Their Magnetorheological Characteristics. *IEEE Transactions on Magnetics* **51**, (2015).

19. Rakshit, R., Serita, K., Tonouchi, M. & Mandal, K. THz conductivity of semi-insulating and magnetic CoFe2O4 nano-hollow structures through thermally activated polaron. *Journal of Applied Physics* **120**, 203901 (2016).

20. Herschel, W. H. & Bulkley, R. Konsistenzmessungen von Gummi-Benzollösungen. *Kolloid-Zeitschrift 1926 39:4* **39**, 291–300 (1926).

21. Bingham, E. C. *AN INVESTIGATION OF THE LAWS OF PLASTIC FLOW*.

22. Zhu, X. Tutorial on Hertz Contact Stress. (2012).

Chapter 6

Magnetorheological Response of Magnetic Fluids Containing Zn Doped Fe_3O_4 Hollow Structures

This chapter shows the MR response, MR mechanism and viscoelastic properties of Zn doped Fe3O4 NHSs based MR fluids. Further, a theoretical model is developed to understand the yielding behavior and magnetorheological mechanism of ferrites NHSs based MR fluids depending on magnetic dipolar interaction.

A part of this chapter is already published in ***Journal of Applied Physics 2021***, *129, 033901* and it is reproduced here.

6. Shear response of magnetorheological fluid with $Zn_{0.2}Fe_{2.8}O_4$ sub-micron hollow spheres

6.1. Preamble

A magnetorheological (MR) fluid consists of a carrier liquid where nano to micron-sized magnetic particles are well dispersed and the fluid shows magnetic field responsive reversible change in viscosity from liquid state to solid-like state[1–3]. Till date, MR fluids have received considerable attention in technological applications such as, brake, clutch, dampers, seismic vibrations [4,5]etc. High concentration and large magnetic saturation (M_S) of the suspended magnetic particles in MR fluids improve the magnetorheological response. However, MR response is not always proportional to the particle concentration and rather deteriorates when the particle concentration goes beyond a certain limit[6]. Therefore, to improve MR response, the metallic magnetic particles with high M_S, such as Carbonyl Iron are used. But poor sedimentation stability in suspension due to their high density and poor oxidative stability recommend the use of additives[2,3] and coating[7–10]. Nonetheless due to the additives and coatings the MR response gets compromised[11] and noneconomic[12]. On the other hand, spinel ferrites with excellent chemical stability and low density are found to be stable MR material with good magnetorheological response comparable to metallic particles[13,14]. They can be even more advantageous if used in the form of hollow structures which can improve their stability further by reducing the density. MR fluids containing hollow spherical Fe_3O_4 particles were reported earlier[15,16]. Ferrite hollow spheres with good chemical, physical, and sedimentation stability make an excellent MR material both for application purpose and basic understanding of MR effect[17].

In *chapter 3*, we observed Zn-doping improves the magnetization of $Zn_xFe_{3-x}O_4$ hollow spheres up to a certain doping percentage (x=0.2)[18]. In this chapter, $Zn_{0.2}Fe_{2.8}O_4$ (ZFO) hollow spheres with diameter ~700 nm are synthesized via solvothermal method and the MR suspension is prepared using them. The steady-state shear response and the viscoelastic properties of the MR suspension is studied and explained in detail.

6.2. Experimental Section

ZFO hollow spheres are prepared following the synthesis procedure as mention in *chapter*

3. In brief, 1.015 g $FeCl_3.6H_2O$, 0.0315 g of $ZnCl_2$ and 0.46 g of Urea are added in 30 ml ethanol and stirred until homogeneous solution is obtained. 25 mg of PVP is added as surface stabilizer. The properly mixed solution is transferred into a 40 ml Teflon lined stainless steel autoclave and heated at 200°C for 20 h, followed by natural cooling. The resulting black precipitate is washed with absolute ethanol and dried overnight.

The structure and phase of ZFO hollow spheres are characterized by X-ray diffraction (XRD) while the morphology and elemental analysis are performed by scanning electron microscope (SEM) equipped with energy dispersive X-ray spectroscopy (EDX) and transmission electron microscope (TEM). The magnetic measurements are performed by using a vibrating sample magnetometer (VSM) at room temperature with maximum applied field of 10 kOe.

The MR fluid with 50 wt% particle fraction is prepared by adding ZFO hollow spheres in silicone oil (density 0.981 g/cc at room temperature) and henceforth named as ZFO-MR fluid. The mixture is homogenized by mechanical mixing followed by sonication. No additive is present in the prepared MR fluid. The MR measurements are performed in an Anton Parr parallel plate magnetorheometer MCR 301. The gap between two parallel plates is kept at 0.3 mm.

6.3. Results and discussion

6.3.1. Structural and Morphological Properties

The XRD pattern of as synthesized sample is shown in Figure 6.1(a), which confirms the formation of single phase face centered cubic spinel structure, where the EDX spectra in its inset confirms the element and purity of as synthesized material.

The FESEM image in Figure 6.2(a) shows the formation of regular and uniform ZFO spheres of average diameter of 700 nm and rough surface area. Some broken parts of the spheres can also be seen in the FESEM image, which confirm the hollow interior of the spheres. The hollow structure of the as synthesized sample becomes more prominent, from the intensive contrast between the black edge and bright center of the spheres, in the TEM image, as shown in Figure 6.2(b), with a shell thickness of 120 nm. Density of the hollow spheres is found to be ~4.9 g/cc, which is much less compared to the density (~5.3 g/cc) of $Zn_{0.2}Fe_{2.8}O_4$ solid spheres.

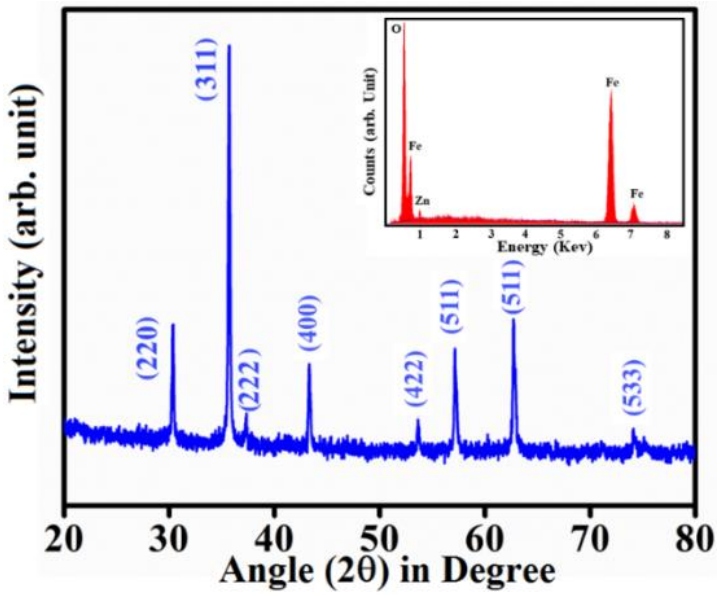

Figure 6.1: XRD pattern with EDX spectra (inset) of the as prepared $Zn_{0.2}Fe_{2.8}O_4$ hollow spheres.

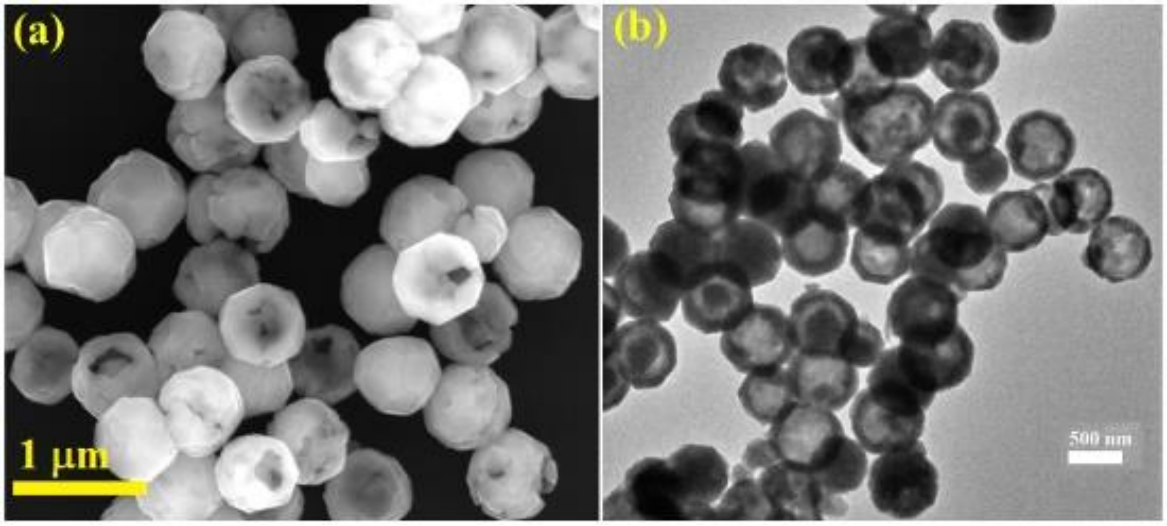

Figure 6.2: (a) FESEM image and (b) TEM image of the as prepared $Zn_{0.2}Fe_{2.8}O_4$ hollow spheres.

6.3.2. Magnetic Properties

The field dependent magnetization (M-H) loop in Figure 6.3 shows soft magnetic nature of ZFO hollow spheres M_S=96 emu/g, coercivity ~ 140 Oe and remanence ~ 14 emu/g. From the inset of Figure 6.3 the soft nature can be understood clearly. These magnetic properties suggest that ZFO hollow spheres based MR fluid will be quick in MR response and re-dispersible due to negligible remanence.

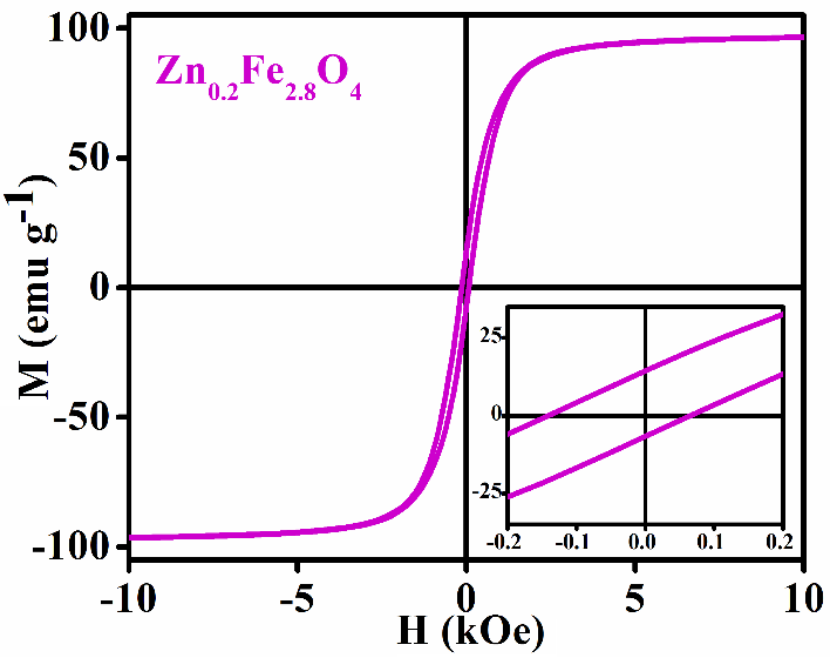

Figure 6.3: Room temperature M-H loop of $Zn_{0.2}Fe_{2.8}O_4$ hollow spheres with enlarged center region in the inset.

6.3.3. Magnetorheological Properties

Figure 6.4(a) exhibits the flow curve of ZFO-MR fluid and silicon oil only to understand the origin of high shear stress in the MR fluid. The high shear stress of ZFO-MR fluid even at zero field is due to the rough surface of the hollow spheres which can be observed in the SEM image (Figure 6.2(a)). The shear stress (τ) of the suspension increases in presence of magnetic field (H), with the appearance of dynamic yield stress, owing to the formation of magnetic field induced columnar structures. During the flow test, the measurement is repeated for a particular applied magnetic field and the flow curve follows the same path each time, proving negligible effect of remanence magnetization on MR response.

The sample represents a shear thinning behavior at a fixed applied magnetic field, as appeared from Figure 6.4(b), where with increase in shear rate ($\dot{\gamma}$), the columnar structures break and initiate flow in the MR fluid. All the curves show non-Newtonian behavior (Figure 6.4(a)) and the presence of yield stress under the application of magnetic field confirms Bingham plastic (BP) nature following the BP equation $\tau = \tau_y + \eta\dot{\gamma}$; where, τ_y represents the yield stress and η is the plastic viscosity. By extrapolating the shear rate to zero, the yield stress (τ_y) is estimated for different applied magnetic fields. A yield stress (τ_y) of ~1120 Pa is obtained for the maximum applied magnetic field of 400 mT for ZFO-MR

fluid, which is better as compared to the MR fluid with pure Fe_3O_4 hollow spheres[15]. Once the yielding point is reached, the flow curves show gradual increasing nature with increase in shear rate for all the applied magnetic fields. The slope of this linear region at higher $\dot{\gamma}$ represents the value of plastic viscosity (η), which changes with applied magnetic field, indicating the dependence of η on applied field.

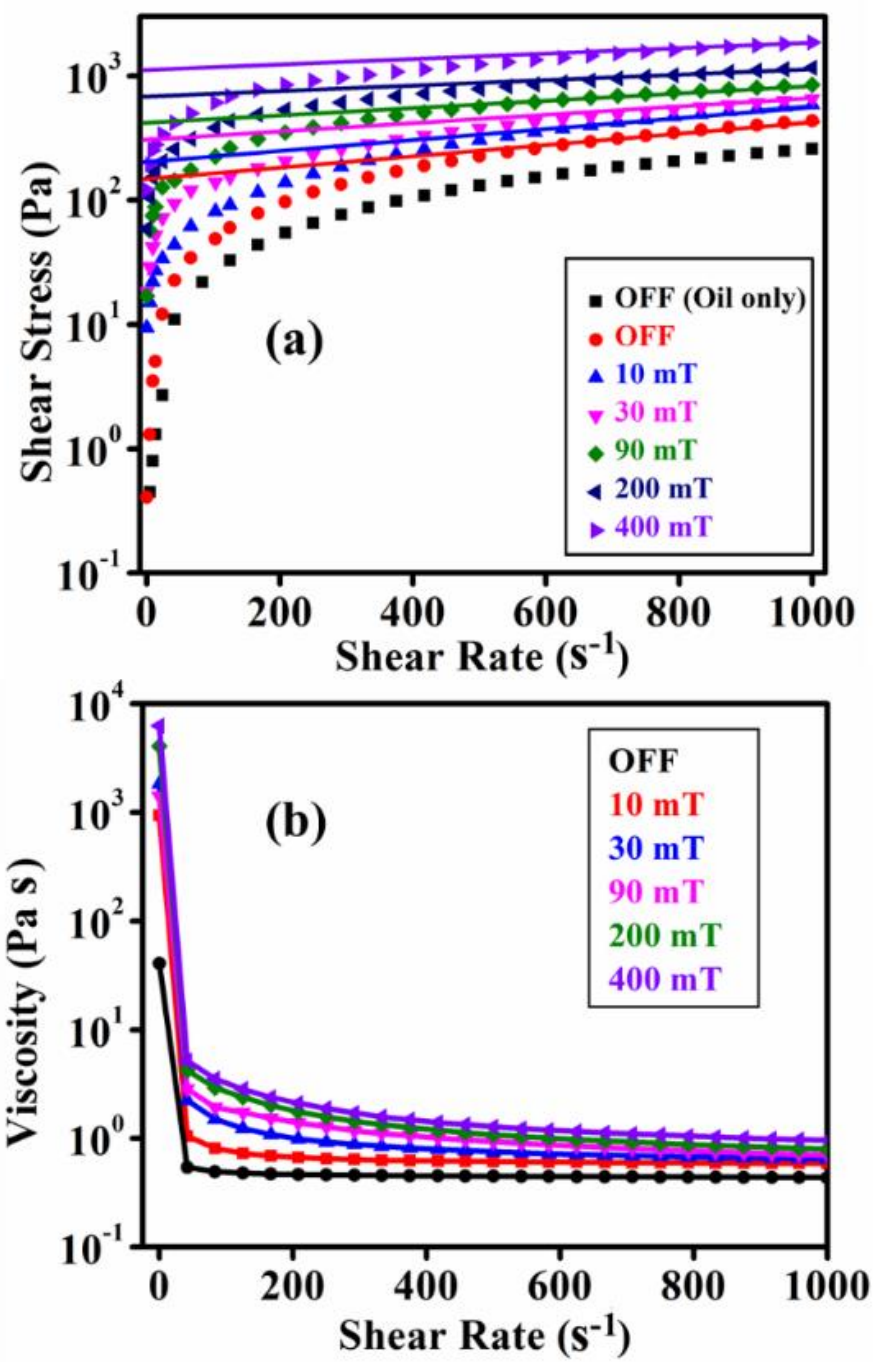

Figure 6.4: (a) Steady shear rate flow curve and (b) variation of viscosity with shear rate of the ZFO-MR fluid.

6.3.4. MR Mechanism

To understand the MR mechanism, the nature of variation of the yield stress with applied magnetic field needs to be studied. In MR fluids, under a weak applied magnetic field τ_y increases quadratically with increasing magnetic field strength, while at higher values of the applied magnetic field, τ_y is expressed as[19] $\tau_{y=}\sqrt{6}\phi\mu_0 M_S^{1/2} H^{3/2}$. In ZFO-MR fluid system, the yielding nature with different magnetic fields does not follow any previously established model as observed from Figure 6.5(a). With the externally applied magnetic field, each hollow sphere acts as an individual dipole and form chain. The nature of variation of τ_y with H is explained by considering frictional force between the hollow spheres and the plates of the magnetorheometer.

Frictional force is proportional to the normal reaction, which is composed of dipolar interaction force between the magnetic particles in the particle chains. Under applied magnetic field each sphere acts as a magnetic dipole. The dipolar interaction force between two dipoles can be expressed as

$$F_d = -\frac{3\mu_0 m^2}{2\pi l^4} \tag{6.1}$$

where, *m* is the magnetic dipole moment and *l* is the distance between the particles.

In MR fluid the suspended hollow spheres form chain in the direction of the applied magnetic field through dipolar interaction. Considering infinite number of particles in a chain from lower static plate to upper rotating plate, shown in Figure 6.5(b), the dipolar interaction force on the hollow sphere in contact with the rotating plate can be calculated as

$$F = -\frac{3\mu_0 m^2}{2\pi}\left[\frac{1}{(2r)^4} + \frac{1}{(4r)^4} + \frac{1}{(6r)^4} + \cdots\right] \tag{6.2}$$

where, r is the radius of ZFO hollow spheres.

By adding the infinite series of eq. (6.2), $F = -\frac{3\mu_0 m^2}{2^5 \pi r^4}\frac{\pi^4}{90}$ (6.2a)

If we consider a unit volume of length, breadth and height of unit scale and n number particles per unit length then there are n^2 number of particles per unit area and n^3 number of particles per unit volume, with n^2 number of particle chains per unit cell. So, the dipolar interaction force per unit area is

$$N = -\frac{3\mu_0 m^2 n^2}{2^5 \pi r^4}\frac{\pi^4}{90} \tag{6.2b}$$

N is also the normal reaction which is required for calculating the frictional force between the particle chains and upper plate of the magnetorheometer.

Eq. (6.2b) can be expressed as $N = -\frac{3\mu_0 M^2}{2^5 \pi r^4 n^4} \frac{\pi^4}{90}$ (6.3)

where, M is the magnetization of the particles defined as $M=mn^3$.

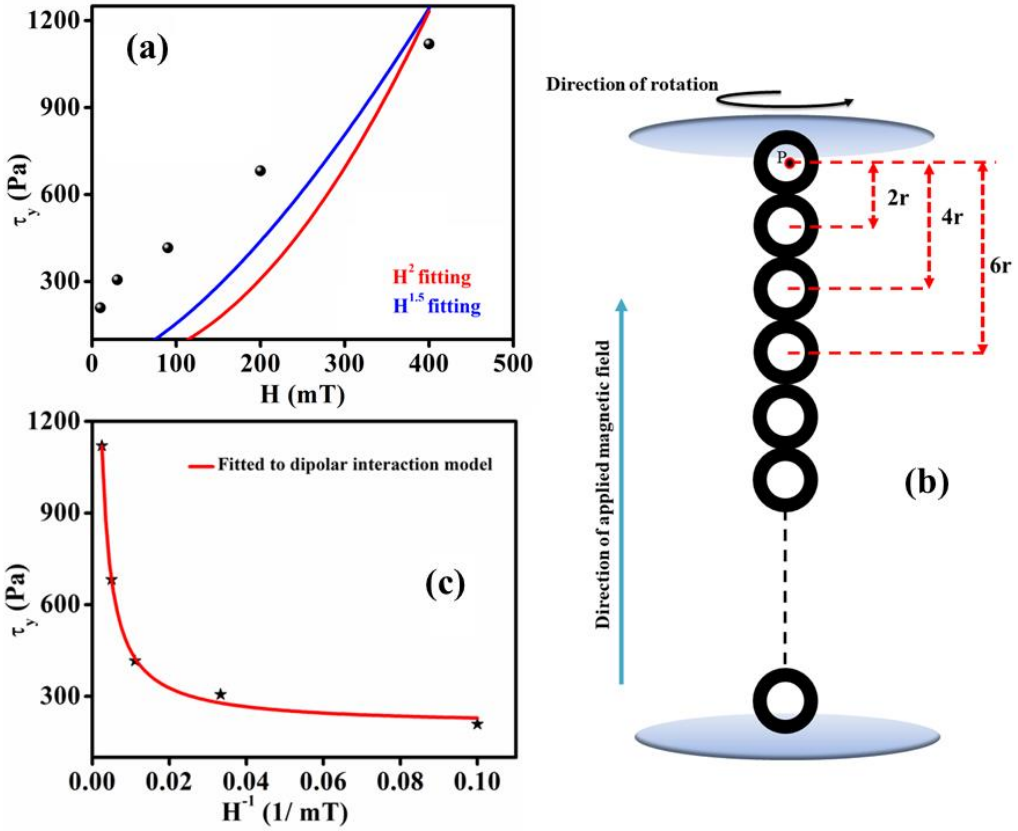

Figure 6.5: (a) Variation of yield stress with applied magnetic field of the ZFO-MR fluid fitted with previously established standard model, (b) Schematic of infinite particles chain formed due to arising dipole moment under the application of magnetic field and (c) variation of yield stress with applied magnetic field of the ZFO-MR fluid fitted with dipolar interaction model.

The normal reaction of eq. (6.3) gives rise to frictional force, which in turn develops shear in the ZFO-MR fluid. In the range of applied magnetic field (400 mT) the ZFO hollow spheres are in the approach to saturation region, where M can be written as[20,21]:

$$M=M_S\left(1-\frac{a}{H}-\frac{b}{H^2}-\cdots\right) \quad (6.4)$$

where, a and b are constants. Combining equations (6.3) and (6.4), and neglecting the higher order terms the field dependence of normal reaction in the approach to saturation region, N_{AS}, can be expressed as:

$$N_{AS}\,\alpha\;\; M_S^2(1-\frac{2a}{H}+\frac{a^2}{H^2}) \qquad (6.5)$$

As the normal reaction is the origin of shear stress, the yield stress τ_y should follow the same H dependency. The variation of τ_y with 1/H is shown in Figure 6.5(c). Plastic viscosity, η, also varies following the same pattern as τ_y with H, as shown in Figure 6.6(a). Viscosity values in our experiment are calculated for different values of shear rate 0.01, 41.7, 125, 500 and 1000 s^{-1} with applied magnetic field and is denoted as η_s. $\eta_s$is found to increase with magnetic field strength due to stronger chain formation in the MR fluid and their nature of variation with H is shown in Figure 6.6(b), fitted with eq. (6.5).

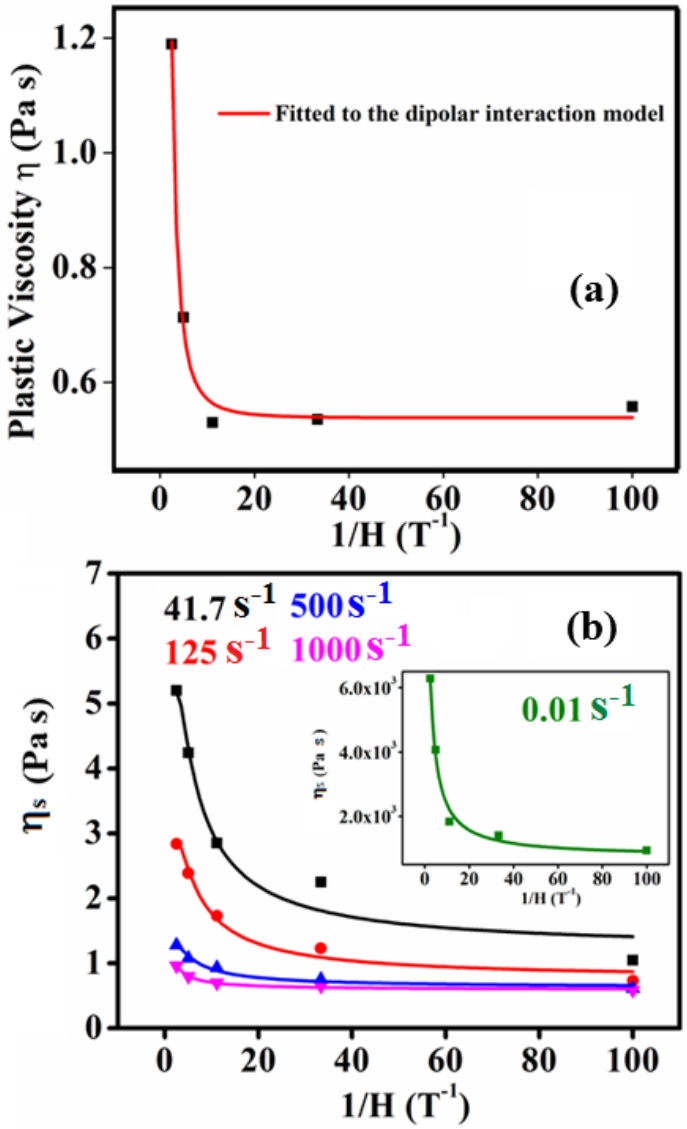

Figure 6.6: Nature of variation of (a) plastic viscosity with applied magnetic field intensity and (b) viscosity values at different shear rate $\eta_s$with applied magnetic field at different shear rate of the ZFO-MR fluid, inset Fig. shows the variation of η_s with 1/H for shear rate 0.01 s^{-1}.

6.3.5. Viscoelastic Properties

The viscoelastic properties of the ZFO MR fluid are analyzed by applying sinusoidal shear. Frequency dependent storage modulus (G′) and loss modulus (G″) at constant shear amplitude (0.5%) is shown in Figure 6.7. G′ increases with increase in magnetic field, suggesting strong solid-like behavior over liquid-like state, which indicates dominating elastic behavior over viscous nature. G″ also shows improvement under field stimuli, indicating enhanced dissipative response in addition to improved elasticity, which is a suitable characteristic for dynamic applications of MR fluids.

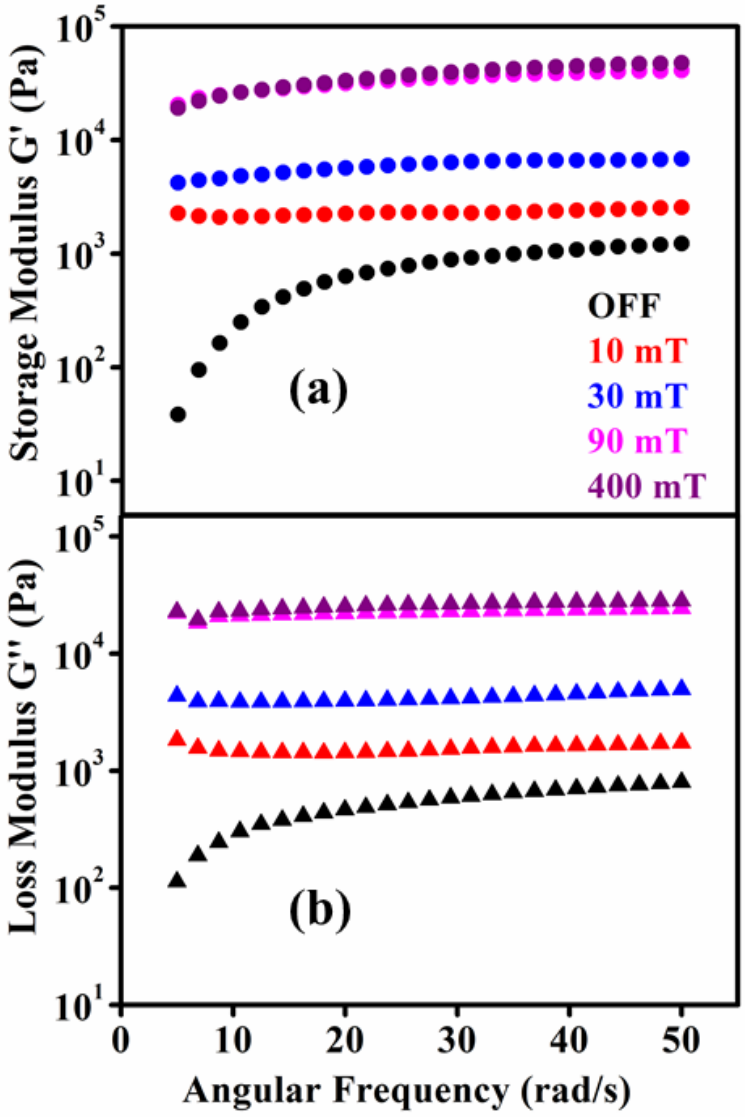

Figure 6.7: Variation of (a) storage modulus and (b) loss modulus with angular frequency of the oscillating strain at different applied magnetic fields.

6.3.6. Sedimentation Stability

Dispersion stability of the prepared MR fluid is shown in Figure 6.8 by plotting time dependent sedimentation rate. The MR fluid system is kept steady during the time of stability test. Sedimentation tests are performed on all the three samples to compare the stability of the three different kinds of MR fluids. The sedimentation rate is calculated using the equation:

$$\text{Sedimentation percentage (S)} = \frac{\text{Volume of supernatant fluid}}{\text{Total volume of MR fluid}} \text{ X } 100\%$$

The sedimentation rate is found to be slow as compared to the metallic magnetic particles[22], which is owed to the low density of ZFO hollow spheres.

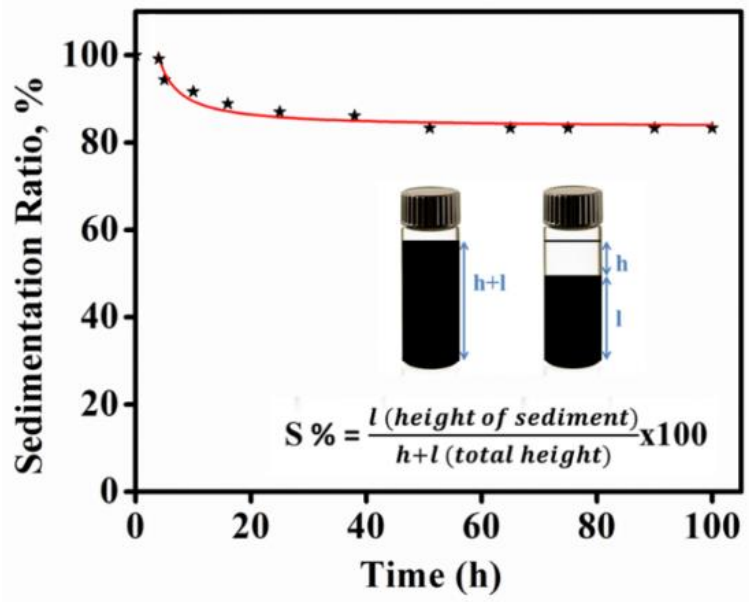

Figure 6.8: Sedimentation stability of ZFO-MR fluid with time.

6.4. Conclusion

In conclusion, MR fluid with $Zn_{0.2}Fe_{2.8}O_4$ hollow spheres is prepared and its MR effects and sedimentation behavior are studied in detail. The MR fluid not only shows good dispersion stability but achieve sufficient value of yield stress at a low applied field of 400 mT. Magnetic dipolar interaction is found to govern the MR behavior. This MR fluid with dominating elastic behavior over viscous nature in presence of an applied magnetic field and excellent MR response is suitable for commercial use such as brake, clutch, and MR damper.

Bibliography

1. Hajalilou, A., Amri Mazlan, S., Lavvafi, H. & Shameli, K. Field Responsive Fluids as Smart Materials. (2016) doi:10.1007/978-981-10-2495-5.
2. Park, B. J., Song, K. H. & Choi, H. J. Magnetic carbonyl iron nanoparticle based magnetorheological suspension and its characteristics. *Materials Letters* **63**, 1350–1352 (2009).
3. Hajalilou, A., Mazlan, S. A. & Shila, S. T. Magnetic carbonyl iron suspension with Ni-Zn ferrite additive and its magnetorheological properties. *Materials Letters* **181**, 196–199 (2016).
4. Carlson, J. D. & Jolly, M. R. MR fluid, foam and elastomer devices. *Mechatronics* **10**, 555–569 (2000).
5. Synthesis and Characterization of Antifriction Magnetorheological Fluids for Brake. doi:10.14429/dsj.63.2633.
6. Werely, N. Magnetorheology : advances and applications. 396 (2013).
7. Liu, Y. D. & Choi, H. J. Carbon nanotube-coated silicated soft magnetic carbonyl iron microspheres and their magnetorheology. *Journal of Applied Physics* **111**, 07B502 (2012).
8. Ko, S. W., Lim, J. Y., Park, B. J., Yang, M. S. & Choi, H. J. Magnetorheological carbonyl iron particles doubly wrapped with polymer and carbon nanotube. *Journal of Applied Physics* **105**, 07E703 (2009).
9. Jung, H. S. & Choi, H. J. Hydrothermal fabrication of octahedral-shaped Fe3O4 nanoparticles and their magnetorheological response. *Journal of Applied Physics* **117**, 17E708 (2015).
10. Hajalilou, A., Kianvash, A., Shameli, K. & Lavvafi, H. Carbonyl iron based magnetorheological effects with silver nanoparticles via green-assisted coating. *Applied Physics Letters* **110**, 261902 (2017).
11. Liu, Y. D., Fang, F. F. & Choi, H. J. Core-shell-structured silica-coated magnetic carbonyl iron microbead and its magnetorheology with anti-acidic characteristics. *Colloid and Polymer Science* **289**, 1295–1298 (2011).
12. Fang, F. F. & Choi, H. J. Noncovalent self-assembly of carbon nanotube wrapped carbonyl iron particles and their magnetorheology. *Journal of Applied Physics* **103**, 07A301 (2008).
13. Anupama, A. v., Khopkar, V. B., Kumaran, V. & Sahoo, B. Magnetic field dependent steady-state shear response of Fe3O4 micro-octahedron based magnetorheological fluids. *Physical Chemistry Chemical Physics* **20**, 20247–20256 (2018).
14. Fang, F. F., Kim, J. H. & Choi, H. J. Synthesis of core–shell structured PS/Fe3O4 microbeads and their magnetorheology. *Polymer* **50**, 2290–2293 (2009).
15. Saha, P., Mukherjee, S. & Mandal, K. Rheological response of magnetic fluid containing Fe3O4 nano structures. *Journal of Magnetism and Magnetic Materials* **484**, 324–328 (2019).
16. Xuan, S., Hao, L. & Leung, K. C. F. Shear disassembly of hierarchical superparamagnetic Fe3O4 hollow nanoparticle necklace chains. *New Journal of Chemistry* **38**, 6125–6132 (2014).
17. Shahrivar, K. *et al.* Rheological behavior of magnetic colloids in the borderline between ferrofluids and magnetorheological fluids. *Journal of Rheology* **63**, 547 (2019).
18. Saha, P., Rakshit, R., Alam, M. & Mandal, K. Magnetic and Electronic Properties of Zn - Doped Fe3 O4 Hollow Nanospheres. *Physical Review Applied* **11**, 024059 (2019).
19. Fang, F. F., Liu, Y. D., Choi, H. J. & Seo, Y. Core-shell structured carbonyl iron microspheres prepared via dual-step functionality coatings and their magnetorheological response. *ACS Applied Materials and Interfaces* **3**, 3487–3495 (2011).

20. Chen, C.-Wen. *Magnetism and Metallurgy of Soft Magnetic Materials.* (Dover Publications, 2013).
21. Chikazumi, S., Graham, C. D. (Chad D.) & Chikazumi, S. Physics of ferromagnetism. 655 (1997).
22. Tong, Y., Dong, X. & Qi, M. High performance magnetorheological fluids with flower-like cobalt particles. *Smart Materials and Structures* **26**, 025023 (2017).

Chapter 7

Application of Magnetic Fluids in Tuning The Dielectric, Electrical and Thermal Conduction Properties

This chapter demonstrates the effect of external magnetic stimuli on the dielectric, electrical conduction and thermal conduction properties of Fe_3O_4 NHSs based MR fluids. Improvement in magnetic field stimulated heat transfer property through the MR fluids along with direction controlled thermal conduction is presented is showed experimentally.

7. Magnetic Field Stimulated Dielectric, Electronic and Thermal Properties of Magnetite Nano-Hollow Spheres Based Magnetic Fluids

7.1. Preamble

Magnetorheological (MR) fluids are smart materials with magnetic particles (0.1 mm-10 mm) suspended in a carrier liquid, which can change their viscosity from liquid to solid-like state reversibly under an applied magnetic field. These fluids have fascinated a great interest among the researchers and various industrial applications such as solar thermal transportation[1], microelectronic[2], power plants[3] and defence[4,5]. For developing heat transfer equipment incorporating MR fluids various physical properties, such as thermal conductivity, viscosity, density and dielectric permittivity, act as the most influencing parameters of these fluids[6]. In response to external stimuli such as magnetic fields, these properties can be altered or controlled. MR fluids possess large magnetization in the presence of a magnetic field while retaining their fluid properties. Moreover, under the applied magnetic field interactions between magnetic nanoparticles lead to the formation of heterogeneous ordered structures along the field direction[7]. Due to the formation of field-assisted microstructures, the effective thermal conductivity of the medium changes while certain thermodynamic properties such as effective heat capacity remain unaffected[8]. An enhanced thermal conductivity of in-field magnetic fluids, when temperature and magnetic field gradients are parallel, is demonstrated by researchers through multiple experimental studies. In the case of the perpendicular orientation of the magnetic field to the temperature gradient, no change or relatively small increase in thermal conductivity is observed[9,10]. However, very few studies are reported on the magneto-dielectric effect in these MR fluids. Detailed literature survey reveals that few research works have been done on the dielectric response of magnetic nanofluids with constant applied magnetic field in parallel and appendicular orientation of the electric field[11,12]. However, the effect of varying magnetic field strength on the magneto-dielectric effect to understand the mechanism of dielectric polarization and relaxation phenomena of MR fluids is not reported so for. Besides, due to the formation and enhancement of the field-assisted microstructure, and the change of the overall viscosity of the MR materials to a solid-like state, the electrical conduction of the MR fluids enhances. Although very few research works have been carried out to understand

the electrical conduction in MR fluids[13–15]. This led us to divulge the dielectric relaxation and polarization behaviour of MR fluids, along with the augmentation of electrical and thermal conduction properties.

The heat exchange performance of heat transfer equipment is generally reliant on the heat transfer properties of the operating fluid, normally mentioned as Heat Transfer Fluids (HTFs), such as H_2O[16,17], ethylene glycol[18–20], solar glycol[21,22], propylene glycol[23], bio glycol[24], ionic liquid[25]. The heat conduction properties of these base fluids can upsurge with magnetic nanomaterials addition with high thermal conductivity, such as metallic magnetic particles. Nonetheless, various difficulties are faced by researchers due to the sedimentation of metallic magnetic particles blocking the flow channels, which restricts its use in practical applications. Fe_3O_4 nano-hollow spheres (NHSs) show remarkably good chemical and sedimentation stability in the base fluids[26], enabling these magnetic fluids for practical applications. Moreover, the soft magnetic nature of magnetite let it redisperse in the base fluids quickly after the field removal.

In this chapter, we aim to study the effect of external magnetic stimuli on the dielectric, electrical conduction and thermal conduction properties of Fe_3O_4 NHSs based MR fluids with DI water and ethylene glycol as carrier fluids. We experimentally demonstrate the effect of heterogeneous structures formation on the dielectric permittivity, dielectric relaxation mechanism and electrical conduction properties of MR fluids. The contribution of base fluids and particle concentration on these properties are investigated in detail. Finally, the improvement in magnetic field stimulated heat transfer property through the MR fluids along with direction controlled thermal conduction is presented.

7.2. Experimental Section

Fe_3O_4 NHSs are synthesized in a solvothermal method as mentioned in *chapter 3*. . The phase of the prepared samples are characterized by a PANalytical X'Pert PRO X-ray diffractometer equipped with Cu K_α radiation (λ=1.5418 Å) radiation. Morphological analysis are performed using FEG transmission electron microscope (TEM) (80–200 kV) and A FEI QUANTA FEG 250 field-emission scanning electron microscope (FESEM) (0.2–30 kV). The magnetic measurement is performed with a vibrating sample magnetometer (VSM), Lake Shore-7144. For preparing the DI water and ethylene glycol (EG) based MR fluids with 1% and 5% wt. concentration the respective amounts of Fe_3O_4 NHSs are added into the respective base

fluids. The DI water-based MR fluids with 1wt% and 5wt% particle concentrations are named as W1 and W5 respectively. Similarly, the EG based MR fluids are labelled as EG1 and EG5 containing 1wt % and 5wt % particles respectively.

For measuring the dielectric response of the prepared MR fluids in an impedance analyzer a dielectric cell is prepared in the laboratory. The lab-made dielectric setup is shown in *Chapter 2* (section 2.8.12). A laboratory-based experimental setup is prepared for conducting the heat transfer property measurements of the MR fluids, explained in detail in section 2.10 of *Chapter 2*.

7.3. Results and Discussions

7.3.1. Structural and Morphological properties

The X-ray diffraction (XRD) pattern shown in Figure 7.1 confirms the formation of spinel Fe_3O_4 with face centred cubic structure (JCPDS card number 19-0629) without any impurity or secondary phase. Both the TEM and FESEM images, shown in Figure 7.2(a) and (b) respectively, confirm the formation of nano-hollow structures with 250 nm diameter. The SEM micrograph confirms the formation of NHSs of uniform size distribution, whereas, from the dark and bright contrasts between the centre and edges of the spheres in the TEM image, the hollow structure is more prominent with a shell thickness of 60 nm.

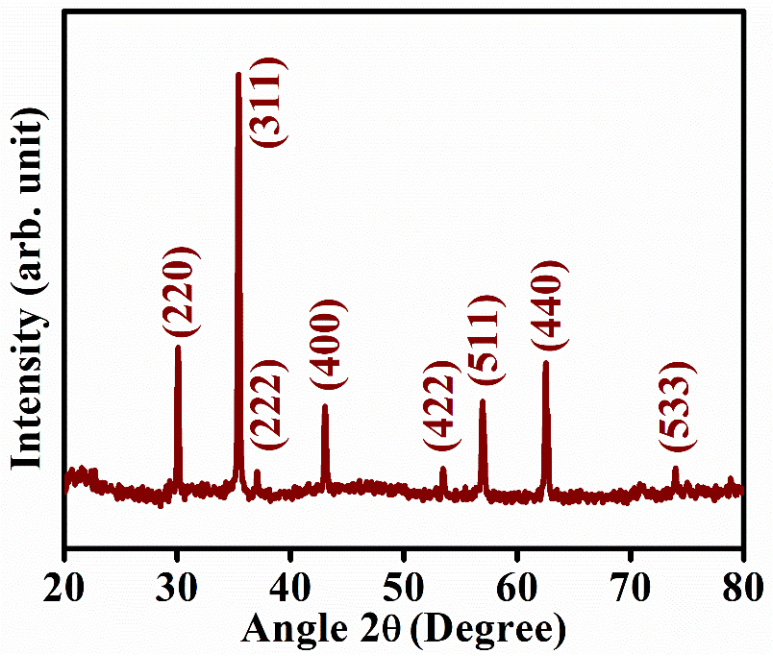

Figure 7.1: XRD pattern of the as-prepared Fe_3O_4 NHSs.

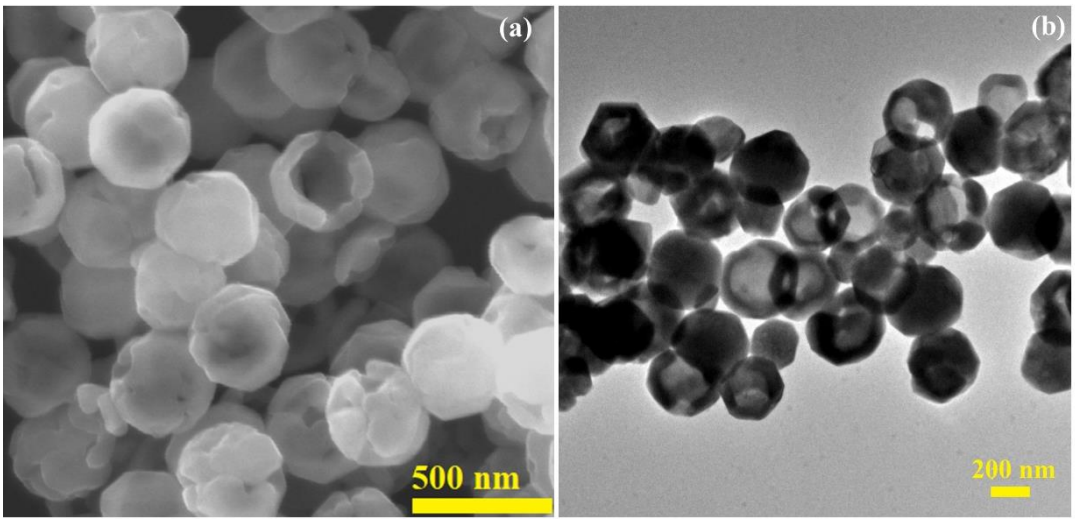

Figure 7.2: (a) FESEM and (b) TEM micrographs of the as-prepared Fe_3O_4 NHSs.

7.3.2. Magnetic Properties

From the room temperature M-H loop in Figure 7.3 the magnetic saturation of the Fe_3O_4 NHSs is found to be 79 emu/g with negligible values of remanent magnetization and coercivity, as evident from the inset of Figure 7.3, which makes this this NHSs a perfect candidate for in MR fluid-based applications.

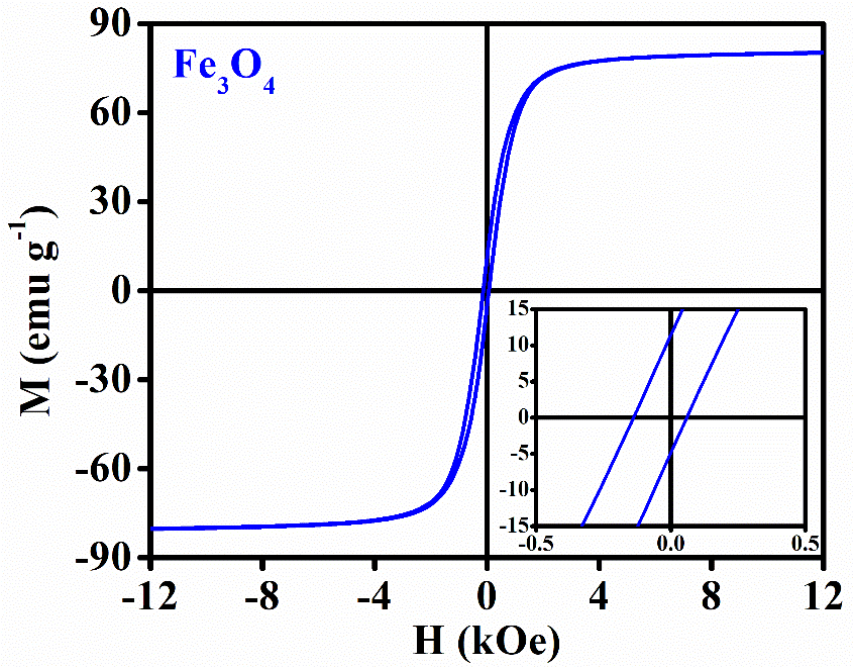

Figure 7.3: Room temperature M-H loop with an enlarged version of the center (inset) of the Fe_3O_4 NHSs.

7.3.3. Dielectric Properties

The dielectric properties of all the MR fluids are first measured in the absence of a magnetic field. It is observed that the addition of NHSs influences the dielectric response. Figure 7.4(a) and (b) show that with the addition of NHSs the dielectric permittivity (ε′) of the base fluids, DI water and EG, increase and with the increase in particle concentrations ε′ increase further. MR fluids act as a colloidal system with the suspended magnetic particles in carrier fluids. According to the Schwarz model[27], the colloidal particles are electrically charged with fixed or adsorbed ions, surrounded by counterions, forming an electric double layer on the surface of the particles. These counterions can move laterally, but not transversally on the surface of the suspended magnetic particles. On the surface of the Fe_3O_4 NHSs some $0H^-$ ions are adsorbed due to the synthesis procedure[28]. Polarization in MR fluids arises due to the displacement of these counterions relative to the fixed uncompensated surface charge, with the application of the electric field. With the addition of magnetic particles in carrier fluids the dielectric response increases due to the increase in electric double layers, which increases further with increased particle fraction, thus increasing ε′.

For both the fluids ε′ decreases with an increase in frequency (f) due to the mismatch between the characteristics frequency of the dipole and the applied ac electric field frequency[29]. From the tangent loss (tanδ) curves, in the inset of Figure 7.4(a), it is observed that the dielectric loss is decreasing with the addition of magnetic particles in the base fluid and the relaxation peak is shifting towards higher f with increasing particle concentrations for DI water-based MR fluids. For EG based MR fluids, dielectric relaxation amplitude increases with magnetic particle addition in base fluid with minimum shifting in peak position, as evident from the inset of Figure 7.4(b). Dielectric loss increases for EG1 and EG5 due to the high viscosity of EG, which obstructs the alignment of the dipoles with the applied electric field. It is observed that DI water-based MR fluids show better dielectric behaviour over those based on EG. Further, the effect of an external magnetic field is studied on the dielectric response of these MR fluids.

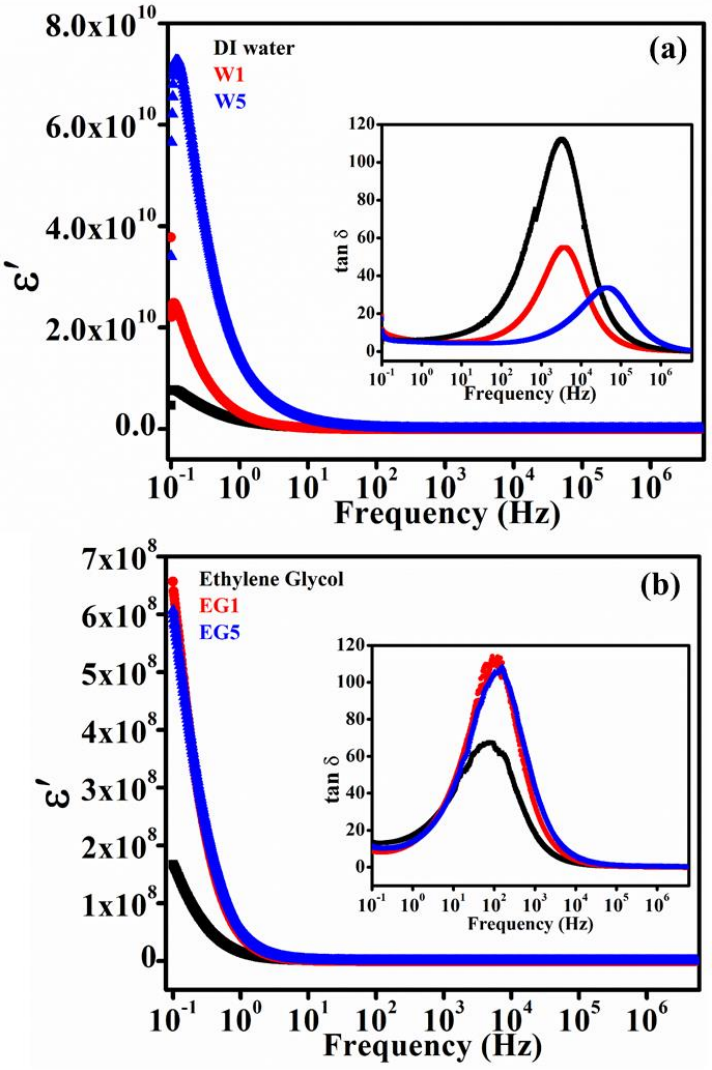

Figure 7.4: Variation of dielectric permittivity with frequency for (a) DI water-based MR fluids and plain DI water, and (b) EG based MR fluids and pure EG.

Dielectric response in MR fluids is contributed from i) the suspended magnetic particles, ii) the uncompensated surface charge and counter-ions, and iii) the water bridge between the magnetic particles. With an increase in H, not only the deflection of dipoles due to Lorentz force is decreasing, but also the water gap between two consecutive magnetic particles, forming chain due to the magnetic-dipolar force between them, reduces with increase in H and thus ε′ increases due to the prominent particle contribution. Dielectric relaxation curves of W1 and W5, originating from the long and/or short-range movement of the charge carriers such as space charge, various charge defects etc, are observed from the frequency dependence of tanδ in Figure 7.5(c) and (d) respectively, under applied H. Two types of dielectric relaxations are observed in both W1 and W5 at the low and high-

frequency regions, whereas for W1 at H=0 condition only one relaxation peak is visible ~10^3 Hz. The low f relaxation peak is originated from counterion polarization[27], whereas the high f relaxation is due to Maxwell-Wagner (MW) interfacial polarization. With the application of H, dielectric loss reduces significantly and the relaxation peaks move towards higher f giving rise to M-W relaxation for W1, as evident from Figure 7.5(c). The lower value of tanδ for W1 under applied magnetic field conditions is associated with low dissipation energy, due to easy alignment of the NHSs in the field direction. Figure 7.5(d) reveals both kinds of relaxations are present in W5 under no field and applied magnetic field conditions. When the particle concentration is low dielectric relaxation is predominantly arising from the base fluid under the H=0 condition, and with applied H due to the chain formation in the MR fluids, the contribution of NHSs in dielectric relaxation is dominating. In both types of MR fluids, W1 and W5, the dielectric relaxation amplitudes are increasing with increase in H due to the growing magnetic dipolar interaction between the magnetic particles and thus giving rise to higher dissipation, as evident from the inset images of Figure 7.5(c) and (d) respectively.

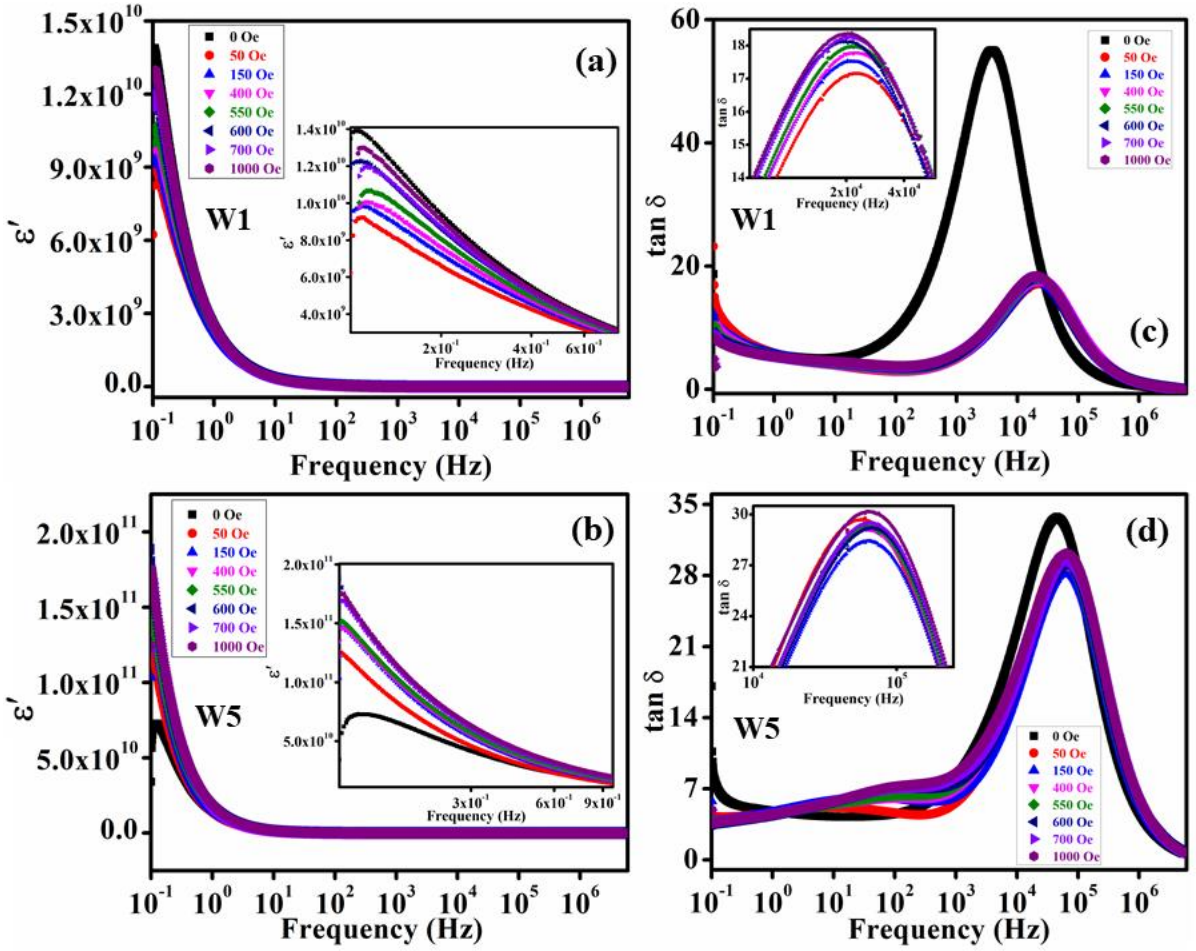

Figure 7.5: Frequency-dependent dielectric permittivity of (a) W1 and (b) W5. Frequency dependence of tangent loss of (c) W1 and (d) W5.

To understand the effect of base fluids on the magneto-dielectric effect of MR fluids the frequency-dependent complex dielectric spectra of EG1 and EG5 are studied under applied H (50 Oe-1000 Oe) and are shown in Figure 7.6. With the application of H, visible low-frequency the magneto-dielectric effect is observed in both EG1 and EG5, as evident from the frequency dependence of ε′ in Figure 7.6(a) and (b) respectively. In EG1, ε′ increases with increase in H initially and after 400 Oe of applied magnetic field ε′ decreases as a result of dipolar deflection due to Lorentz force. At H=1000 Oe, EG1 overcomes the effect of Lorentz force due to strong chain formation and ε′ increases, as evident from the inset of Figure 7.6(a). For EG as base fluid, the effect of Lorentz force is observed at a much higher value of H compared to that in DI water due to the higher viscosity of EG in comparison to water, which hinders the dipolar movement. Dielectric polarization in EG5 shows a continuous increase with an increase in H, as shown in the inset of Figure 7.6(b). Under H=0 condition, the value of ε′ is nearly equal at f=0.1 Hz for both EG1 and EG5, indicating a minimum effect of magnetic NHSs addition in dielectric polarization, and with the externally applied magnetic field the dielectric polarization in EG5 improves indicating the effect of particle chain formation on ε′ in MR fluids. The frequency dispersion of EG1 and EG5 are sharp compared to W1 and W5, as evident from Figure 7.6(a) and (b), and Figure 7.5(a) and (b) respectively. The tanδ curves of EG1 and EG5, from Figure 7.6(c) and (d) respectively, indicate with the application of H the dielectric loss amplitude decreases and it is more prominent in EG5 due to higher particle concentration. It is observed that the EG based MR fluids show only low-f counter-ion polarization relaxation peak at ~100 Hz. By comparing the dielectric relaxation spectra of Water and EG based MR fluids, it can be concluded that the dielectric behaviour of MR fluids depends not only on the particle concentration and the strength of chain formation, but the base fluids play a crucial role as well.

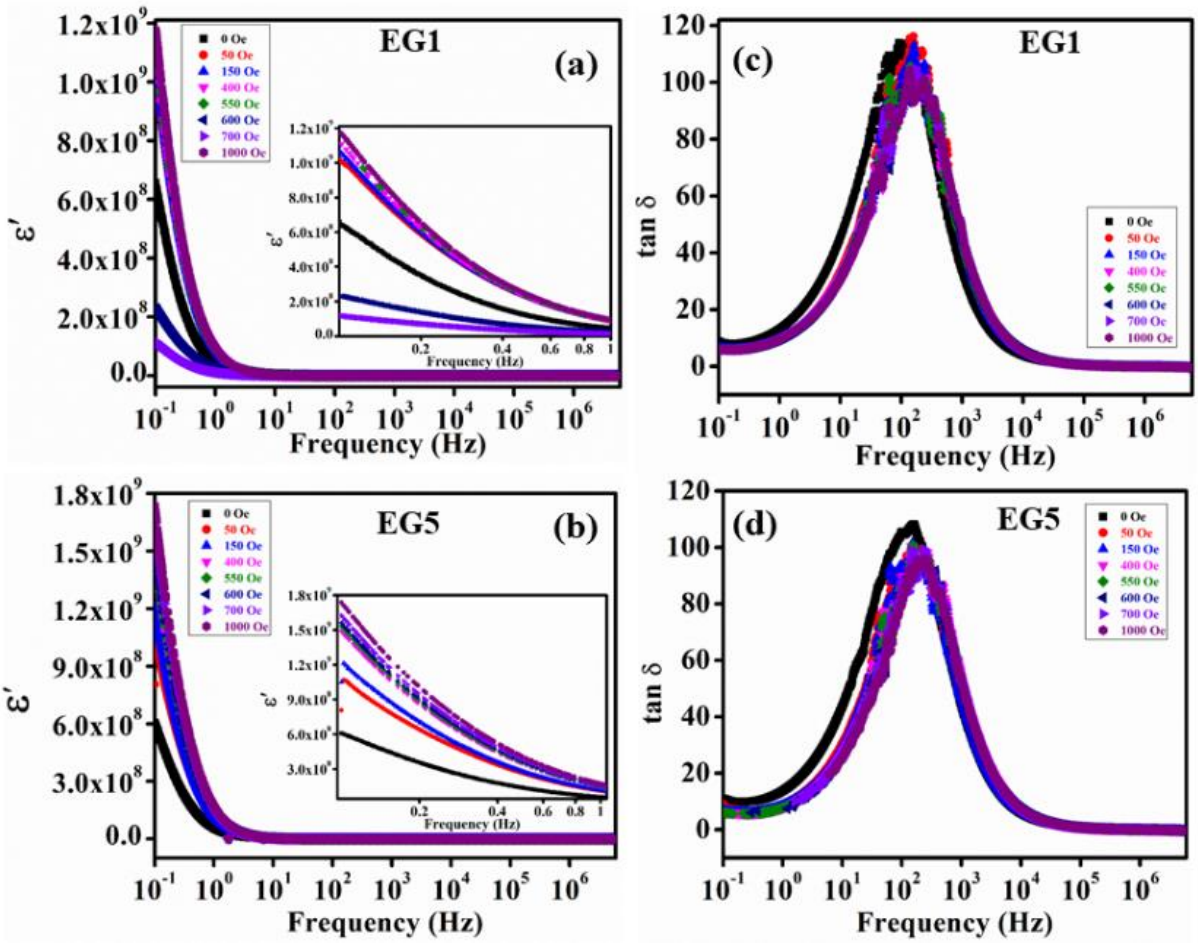

Figure 7.6: Frequency-dependent dielectric permittivity of (a) EG1 and (b) EG5. Frequency dependence of tangent loss of (c) EG1 and (d) EG5.

7.3.4. Electrical Conduction Properties

To divulge the role of particle chain formation in MR fluids on the electrical conduction properties of these smart materials, the ac conductivity (σ_{ac}) curves of these MR fluids are studied. To understand the effect of NHSs addition the conducting property of the base fluids, σ_{ac} of DI water, EG and the MR fluids based on these two fluids, W1, W5, EG1 and EG5, are studied at H=0 condition. Figure 7.7(a) and (b) show the σ_{ac} spectra of DI water and EG based MR fluids respectively, suggesting improvement in σ_{ac} with magnetic NHSs addition. σ_{ac} increases with an increase in f showing a peak at high-frequency region due to resonance between the characteristics frequency of the charge carriers and the applied electric field frequency, and, in the high-f region beyond ~10^6 Hz σ_{ac} decreases with f due to the frequency mismatch.

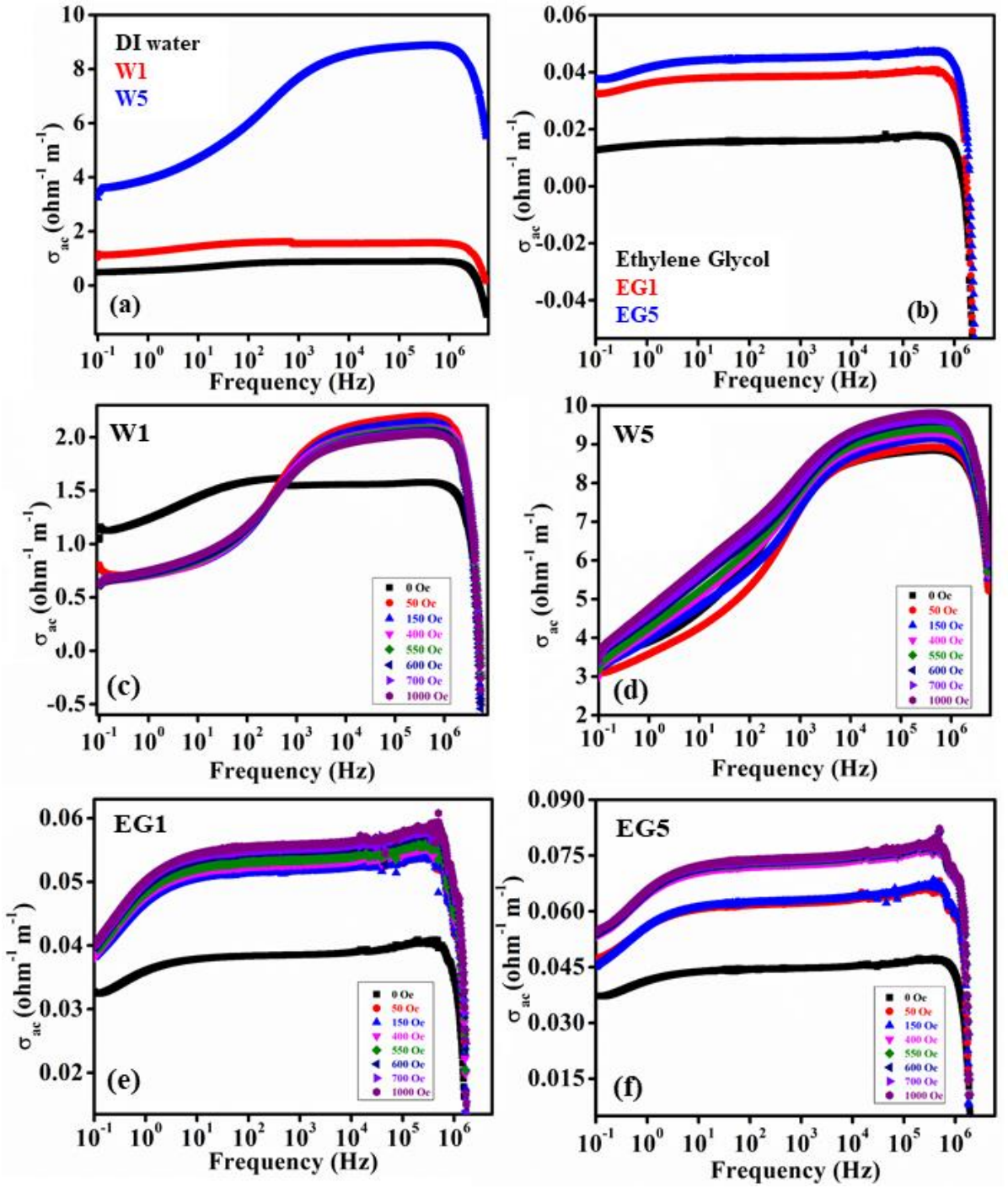

Figure 7.7: Frequency dependence of σ_{ac} at H=0 condition for (a) DI water, W1 and W5 (b) EG, EG1 and EG5. Frequency dependence of σ_{ac} under applied H for (c) W1, (d) W5, (e) EG1 and (f) EG5.

Further, the magnetic field dependent ac conductivity (σ_{ac}) data of these MR fluids are analysed as a function of frequency for various H. Figure 7.7(c) and (d) represent the σ_{ac} of W1 and W5 respectively under applied H. In W1 with the application H, the conductivity value decreases in comparison to the H=0 condition in the low-f region ($f<10^3$ Hz), whereas in the high-f region the situation reverses. Moreover, in the low-f region σ_{ac} increases with

an increase in H, but surprisingly in the high-f region with an increase in H, a decreasing trend in σ_{ac} is observed. This is probably due to the discontinuity in the particles chain formed under applied H in this low concentration MR fluid. This phenomenon is absent in W5 due to the continuity of particle chains in MR fluids. With the application of H the σ_{ac} values of W5 increase with the increase in H due to stronger chain formation. For both the fluids σ_{ac} increases with frequency, reaching a peak, and beyond 10^6 Hz it reduces with further increase in f, as the characteristic frequency of the carriers cannot follow the applied electrical frequency after 10^6 Hz. A similar increasing trend in σ_{ac} with applied H and frequency is observed for EG1 and EG5, as evident from Figure 7.7(e) and (f) respectively. Unlike σ_{ac} of W1 in Figure 7.7(c), σ_{ac} of EG1 do not show any peculiar behaviour, suggesting the continuity of NHSs chain in EG forming a conducting path between the two plates and also the dependency of MR fluids conductivity on the base fluids. In both kinds of MR fluids, σ_{ac} improves with the enhancement of magnetite NHSs wt% in base fluids.

7.3.5. Thermal Conduction Property

The heat conduction properties of all the MR fluids, W1, W5, EG1 and EG5, are measured using the lab-made setup as described earlier. Both the types of base fluids are compared with the respective MR fluids (1 wt% and 5 wt%) without the external magnetic field to understand the effect of Fe_3O_4 NHSs addition on the thermal conductivity of the base fluids. While performing the thermal property measurements a constant current of 1.75 amp is applied to the plate A. Figures 5(a) and (b) show the variation of temperature change (ΔT) of the plate B with time (t) for DI water and EG based MR fluids respectively. By comparing DT for the base fluids only, from Figure 7.8(a) and (b), the observed higher thermal conductivity of DI water compared to that of EG indicates the low measurement error of our setup. With the addition of Fe_3O_4 NHSs the thermal conductivity of the MR fluids increases and with the increase in particle concentration in base fluids, it enhances furthermore. Further to study the effect of magnetic field on thermal conduction properties of the MR fluids external magnetic field varying from 0 Oe-550 Oe is applied in the direction parallel to plates A and B so that the magnetite NHSs form chains between these two plates. Effect of H on ΔT for W1 and W5, and EG1 and EG5 are shown in Figure 7.8(c) and (d) respectively. Under the application of H, both W1 and W5 show improved heat transfer property from plate A to B with the increase in value of H, due to chain formation between the plates and with increased particle concentration ΔT increases more due to stronger chain

formation, evident from Figure 7.8(c). A similar enhancement in heat transfer property is observed for EG1 and EG5 under H as shown in Figure 7.8(d). Under applied H the Fe_3O_4 NHSs in the MR fluids enhances the overall viscosity of the material from liquid to solid-like state, forming a pathway between plates A and B and hence enhances the thermal conductivity of the MR materials.

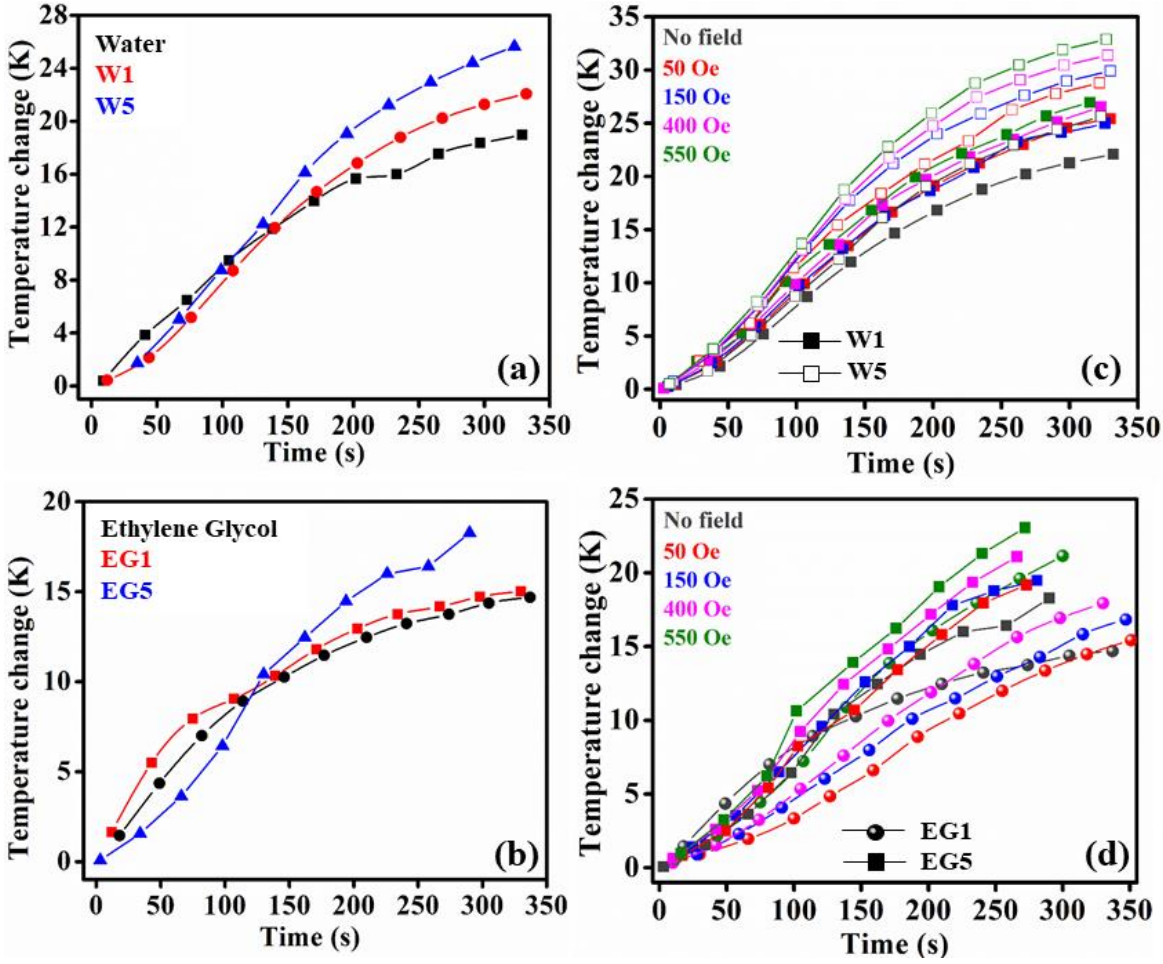

Figure 7.8: Change in temperature of plate B with time under no applied magnetic field for (a) only water, W1 and W5, (b) only ethylene glycol, EG1 and EG5. Change in temperature of plate B with time under applied magnetic field in parallel orientation with the plates for (c) W1 and W5, and (d) EG1 and EG5.

An evidence of chain formation in MR fluids with applied H of various strength is shown in Figure 7.9(a-d). With changing H from 150 to 500 Oe, the chains become wider, as evident from Figure 7.9(b) and (c). However, up on increasing H to 1000 Oe, the columns become more robust and restricted towards the field direction, evident from Figure 7.9(d).

To study the direction controlled heat transfer property of MR fluids, H varying from 0 Oe-550 Oe is applied in the perpendicular orientation of the Cu plate arrangement.

For this measurement we chose EG5 owing to the wide operating temperature of ethylene glycol compared to DI water. As evident from Figure 7.10, under low applied magnetic field, ΔT increases up to 50 Oe of applied field value, followed by a reduction in DT with the increase in H further, reducing the thermal conductivity in the direction of plate B to H=0 condition for the applied field value of 550 Oe. Under a low value of H (up to 50 Oe) the magnetic particles chains are small and distributed all over the volume of the liquid, thus some particles are in contact between plated A and B, hence increases ΔT. As the value of H increases (after 550 Oe) the magnetic particle chains become stronger and strictly oriented in the magnetic field direction, as evident from Figure 7.8, reducing the magnetic particle contact between the plates. Therefore, with an increasing value of H, heat conduction in the direction of plate B reduces.

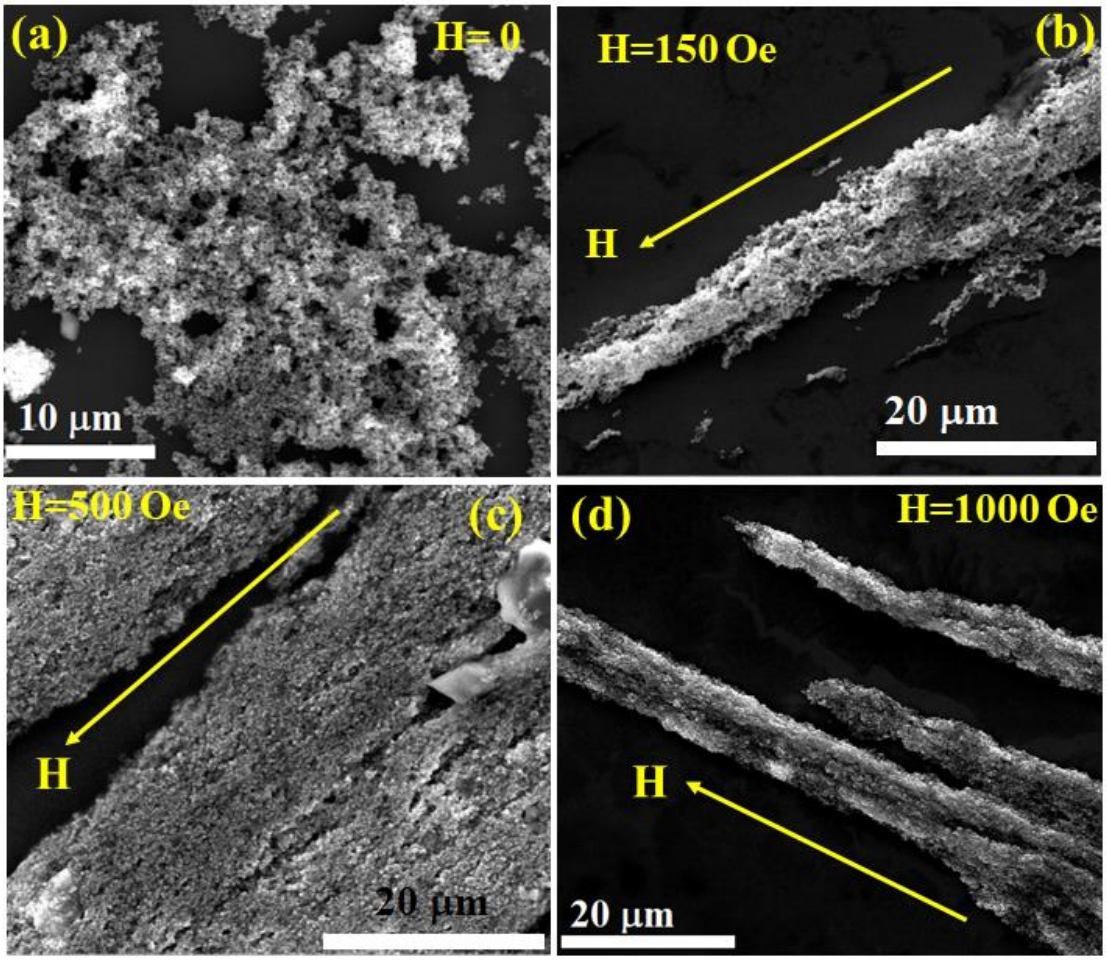

Figure 7.9: FESEM image of chain formation in Fe_3O_4 NHSs under H= (a) 0 Oe, (b) 150 Oe, (c) 500 Oe and (d) 1000 Oe conditions.

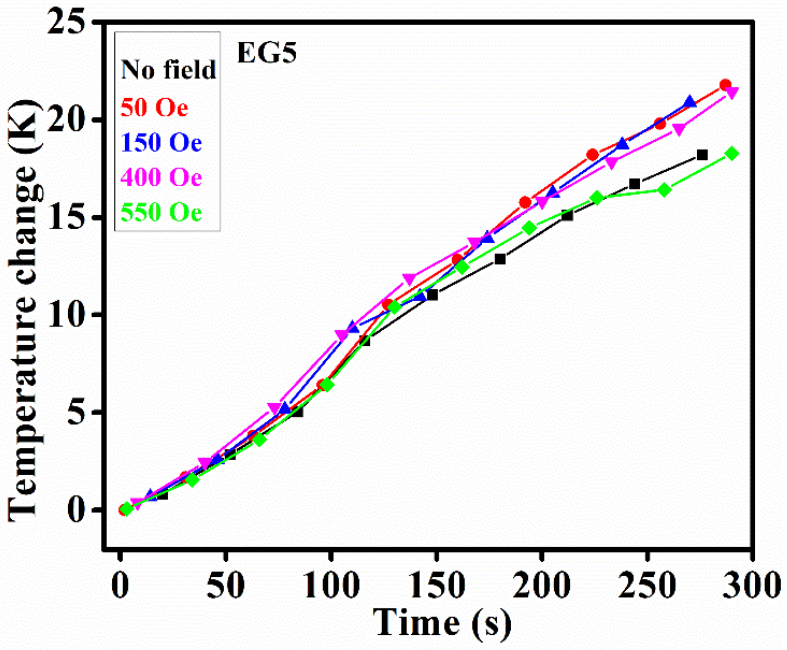

Figure 7.10: Change in temperature of plate B with time under applied magnetic field in a perpendicular orientation with the plates EG5.

7.4. Conclusion

In summary, a detailed analysis of the complex dielectric spectra of Fe_3O_4 NHSs based MR fluids in DI water reveals that in low concentrations of magnetic particles and the low applied field, low-frequency dielectric relaxation is observed due to electric double layer polarization. With an increase in particle wt. fraction and/or increases in magnetic field strength, along with low-frequency relaxation, high-frequency Maxwell-Wagner polarization is also visible in DI water-based MR fluids, indicating the effect of chain-like microstructures formation on the dielectric properties of MR fluids. Whereas in EG based MR fluids, only low-frequency polarization is visible due to the high density of EG obstructing the chain formation process under field stimuli. The dielectric permittivity of both kinds of MR fluids decreases initially with the applied magnetic field due to the Lorentz force effect. With stronger chain formation dipolar deflection due to Lorentz force decreases by increasing the permittivity value. An excellent upsurge is achieved in the electrical conduction of the MR fluids with magnetic stimuli, whereas σ_{ac} of W1 indicates that a minimum concentration of magnetic particles is required to form a continuous conduction path in base fluids under an external magnetic field. The thermal conduction properties of these smart materials not only improves with an increase in magnetic field strength but the conduction of heat in a certain direction can also be controlled by changing

the magnetic field orientation. These MR fluids can be recommended as heat transfer fluids in engine cooling, electronic cooling, solar thermal cooling in machining and other industrial applications.

Bibliography

1. Gupta, S. K. & Dixit, S. Progress and application of nanofluids in solar collectors: An overview of recent advances. *Materials Today: Proceedings* **44**, 250–259 (2021).

2. Kciuk, M. & Turczyn, R. Properties and application of magnetorheological fluids.

3. Salilih, E. M. *et al.* Annual performance analysis of small scale industrial waste heat assisted solar tower power plant and application of nanofluid. *Journal of the Taiwan Institute of Chemical Engineers* **124**, 216–227 (2021).

4. Kolekar, S., Venkatesh, K. & Choi, S. B. Application of semi-Active MRFluid sandwich beam for defence vehicles. *Journal of Mechanical Engineering Research and Developments* **40**, 639–649 (2017).

5. Ha, S. H., Seong, M. S. & Choi, S. B. Design and vibration control of military vehicle suspension system using magnetorheological damper and disc spring. *Smart Materials and Structures* **22**, 065006 (2013).

6. Wong, K. v. & de Leon, O. Applications of Nanofluids: Current and Future: *http://dx.doi.org/10.1155/2010/519659* **2010**, 11 (2010).

7. Patel, R. Mechanism of chain formation in nanofluid based MR fluids. *Journal of Magnetism and Magnetic Materials* **323**, 1360–1363 (2011).

8. Susan Mousavi, N. S. & Kumar, S. Effective heat capacity of ferrofluids – Analytical approach. *International Journal of Thermal Sciences* **84**, 267–274 (2014).

9. Reinecke, B. N., Shan, J. W., Suabedissen, K. K. & Cherkasova, A. S. On the anisotropic thermal conductivity of magnetorheological suspensions. *Journal of Applied Physics* **104**, 023507 (2008).

10. Li, Q., Xuan, Y. & Wang, J. Experimental investigations on transport properties of magnetic fluids. *Experimental Thermal and Fluid Science* **30**, 109–116 (2005).

11. Dong, M. *et al.* Insight into the dielectric response of transformer oil-based nanofluids. *AIP Advances* **7**, 025307 (2017).

12. Rajnak, M. *et al.* Dielectric response of transformer oil based ferrofluid in low frequency range. *Journal of Applied Physics* **114**, 034313 (2013).

13. Zakinyan, A. R., Kulgina, L. M., Zakinyan, A. A. & Turkin, S. D. Electrical Conductivity of Field-Structured Emulsions. *Fluids 2020, Vol. 5, Page 74* **5**, 74 (2020).

14. Zhou, F., Wang, Y., Wang, R. & Wang, R. Research on the Electrical and Thermal Conductivity of Magnetorheological Fluid. *Advanced Materials Research* **581–582**, 786–789 (2012).

15. Yang, X. *et al.* An experimental study of magnetorheological fluids on electrical conductivity property. *Journal of Materials Science: Materials in Electronics* **28**, 8130–8135 (2017).

16. Modi, A. & Haglind, F. Performance analysis of a Kalina cycle for a central receiver solar thermal power plant with direct steam generation. *Applied Thermal Engineering* **65**, 201–208 (2014).

17. Birnbaum, J. *et al.* Steam temperature stability in a direct steam generation solar power plant. *Solar Energy* **85**, 660–668 (2011).

18. Hayduk, W. & Malik, V. K. Density, viscosity, and carbon dioxide solubility and diffusivity in aqueous ethylene glycol solutions. *Journal of Chemical and Engineering Data* **16**, 143–146 (2002).

19. Colangelo, G., Favale, E., Miglietta, P. & de Risi, A. Innovation in flat solar thermal collectors: A review of the last ten years experimental results. *Renewable and Sustainable Energy Reviews* **57**, 1141–1159 (2016).

20. Duell, A. K., Pankow, J. F., Gillette, S. M. & Peyton, D. H. Boiling points of the propylene glycol + glycerol system at 1 atmosphere pressure: 188.6-292 °C without and with added water or nicotine. *Chemical engineering communications* **205**, 1691–1700 (2018).

21. Poongavanam, G. K., Panchabikesan, K., Murugesan, R., Duraisamy, S. & Ramalingam, V. Experimental investigation on heat transfer and pressure drop of MWCNT - Solar glycol based nanofluids in shot peened double pipe heat exchanger. *Powder Technology* **345**, 815–824 (2019).

22. Poongavanam, G. K., Kumar, B., Duraisamy, S., Panchabikesan, K. & Ramalingam, V. Heat transfer and pressure drop performance of solar glycol/activated carbon based nanofluids in shot peened double pipe heat exchanger. *Renewable Energy* **140**, 580–591 (2019).

23. Manikandan, S. & Rajan, K. S. Sand-propylene glycol-water nanofluids for improved solar energy collection. *Energy* **113**, 917–929 (2016).

24. Zainon, S. N. M. & Azmi, W. H. Stability and thermo-physical properties of green bio-glycol based TiO2-SiO2 nanofluids. *International Communications in Heat and Mass Transfer* **126**, 105402 (2021).

25. Liu, J., Ye, Z., Zhang, L., Fang, X. & Zhang, Z. A combined numerical and experimental study on graphene/ionic liquid nanofluid based direct absorption solar collector. *Solar Energy Materials and Solar Cells* **136**, 177–186 (2015).

26. Saha, P., Mukherjee, S. & Mandal, K. Rheological response of magnetic fluid containing Fe3O4 nano structures. *Journal of Magnetism and Magnetic Materials* **484**, 324–328 (2019).

27. Schwarz, G. A THEORY OF THE LOW-FREQUENCY DIELECTRIC DISPERSION OF COLLOIDAL PARTICLES IN ELECTROLYTE SOLUTION1,2. *Journal of Physical Chemistry* **66**, 2636–2642 (2002).

28. Ha, H. T., Phong, P. T. & Minh, T. D. Synthesis of Iron Oxide Nanoparticle Functionalized Activated Carbon and Its Applications in Arsenic Adsorption. *Journal of Analytical Methods in Chemistry* **2021**, (2021).

29. Hardoň, Š., Kúdelčík, J., Bury, P. & Gutten, M. Influence of Electric and Magnetic Fields on Dielectric Response of Oil-Based Ferrofluid. **133**, (2018).

Chapter 8 Conclusion and Scope for Future Work

This concludes of the work described so far and the scopes for further work in this specific field.

8.1. Epilogue

In this thesis, we have mainly focused our work on the synthesis of transition metal oxide (Fe_3O_4, $ZnFe_2O_4$, and $MgFe_2O_4$) based magnetic nanostructures (nanoparticles (NPs) and nano hollow spheres (NHSs)) by different chemical synthesis procedures with various doping concentrations of Zn and Mg in order to improve or tune their magnetic and dielectric properties, without going to the limit of critical diameter of the nanomaterials (NMs).

Very interestingly, Zn-doped Fe_3O_4 NHSs are found to show improved saturation magnetization (M_s) up to a certain doping percentage of Zn. In addition, for the same doping concentration (x=0.2), the electrical conductivity of these $Zn_xFe_{3-x}O_4$ NHSs also decreases. Owing to the improved magnetic permeability, high dielectric and magnetic loss, $Zn_{0.2}Fe_{2.8}O_4$ NHSs is found to an excellent microwave absorbing material. With Mg-doping the magnesium ferrites NHSs show unique electrical property, due to this special morphology, along with metamagnetic transition from antiferromagnetic to ferromagnetic transition. $Mg_{0.3}Fe_{2.7}O_4$ NHSs, with negative dielectric index, show outstanding microwave absorption properties as well, owing to its high dielectric and magnetic loss, and hollow interior. Further, these NHSs with enhanced magnetic properties and low density are utilized in magnetorheological (MR) fluids.

In general, properties of NMs required for an excellent MR material are, high M_s, low density and high oxidation stability. Interestingly, ferrite NHSs possess all these properties along with their low cost synthesis procedure, making the MR suspensions const effective and economic. In our study, we have showed Fe_3O_4 NHSs as an excellent candidate by comparing their MR response with Fe_3O_4 NPs, due to their hollow interior and thus low density. The MR response is improved further by using $Zn_{0.2}Fe_{2.8}O_4$ NHSs with enhanced M_s. All these MR fluids show excellent sedimentation stability. A model is established to explain the MR yielding behavior of these hollow spherical system based MR fluids based on the magnetic dipolar interactions between the suspended hollow spheres in base fluid.

In an attempt to apply these MR fluids in tuning the dielectric, electrical and thermal conduction properties of magnetite NHSs based MR fluids, with external magnetic stimuli, laboratory based set ups are developed. All these properties are found not to be only influenced by the type of base fluids, but also depend on the particle concentration in the MR fluids. The thermal conduction properties of these smart materials not only improves with an increase in magnetic field strength, but the conduction of heat in a certain direction can also be controlled by changing the magnetic field orientation. Ferrite NHSs based MR fluids can replace the metallic magnetic particle based MR suspensions as heat transfer fluids in engine cooling, electronic cooling, solar thermal cooling in machining and other industrial applications.

8.2. Scope of Future Work

Zn-doped Fe_3O_4 NHSs with improved magnetization and reduced conductivity can be an excellent material for high frequency communication technology and devices owing to its low eddy current loss. Besides, the enhancement of specific magnetic properties in non-toxic zinc ferrite NHSs has enhanced its effectiveness in bio-medical field such as biosensing, hyperthermia, targeted drug delivery, and magnetic resonance imaging.

The rapid enhancement of wireless communication, digital systems, and fast processors, considerable attention has been focused on the fabrication of materials that possess a broad absorption frequency, high absorption capacity, low weight, good thermal stability, and antioxidant property. The hollow NSs of these ferrite materials are found to absorb EM radiation more efficiently due to multiple internal reflections within the cavity. Therefore, high absorption capability of ferrite hollow NSs in the microwave frequency region may rise opportunities in the space, stealth technology, electromagnetism based electronic devices such as sensors, switches, and so on.

Moreover, the ferrite nano-hollow structures based MR fluids with sufficiently high magnetization, better stability and low remanence can be utilized in magnetic fluid based bio-medical applications due to its quick reversal to the initial equilibrium state. These MR fluids are fast in response with applied magnetic field and can be useful in MR fluid based applications such as brake, clutch, MR fluid based energy harvester, and thermal engineering.